



**INSTITUTO SUPERIOR TÉCNICO**  
Universidade Técnica de Lisboa

## **Non-standard events at Pierre Auger Observatory**

**João Pedro Canhoto Espadanal**

Dissertação para a obtenção de Grau de Mestre em  
**Engenharia Física Tecnológica**

### **Júri**

Presidente: João Carlos Carvalho de Sá Seixas  
Orientador: Mário João Martins Pimenta  
Coorientador: Bernardo Antonio Neto Gomes Baptista Tomé  
Vogal: Sofia Andringa Dias

**Novembro 2010**



To my Mother  
and my Grandmother



## Acknowledgements

I would like to start by thanking to all people who were involved directly or indirectly in this work and without whom this thesis would have never been completed.

My thanks to my supervisor Prof. Mario Pimenta, for his patience, support and valuable help.

Especially, I would like to thanks to Ruben Conceição and Sofia Andringa. Ruben give me a great help working with the simulation, in programming issues and to interpret phsysical problems. Thanks Sofia for all help in the analyses, when all things seemed to be wrong.

I would like to acknowledge the inestimable help I received in writing this thesis from all member of the Lisbon Auger group. They helped me in many different ways. Thanks to LIP (Laboratório de Instrumentação e Física Experimental de Partículas), where these thesis was developed and FCT for the given grants.

I would also like to thank all my friends and colleagues at MEFT, for their company during the course. Especially to David Soares and Maria Fialho, who heard my frustration over the course, but not only, they also shared all the good time in the past 5 years.

I have to thank to all my friend outside the IST, to their patience and understanding of all my geek comments and my disappearance in some periods for the IST.

And obviously thanks to my mother and my grandmother for all support. And thanks to the rest of the family that was always present.



## Resumo

Actualmente, com o Observatório Pierre Auger terminado, esperam-se cerca de 30 eventos com energias acima de  $10^{20}eV$  e muitos mais abaixo desta. Tendo em conta que o Observatório utiliza uma técnica híbrida, obtêm-se eventos com uma qualidade muito melhor do que experiências anteriores (e em maior quantidade). Assim, estamos em uma fase essencial para novos estudos aplicados aos raios cósmicos. Para além disto, ainda assistimos ao início do funcionamento do LHC (Large Hadron Collider), onde se poderem retirar grandes constrangimentos nas características das interações, facilitando o estudo de raios cósmicos.

Na primeira fase desta tese, faz-se uma síntese das principais características dos raios cósmicos, bem como dos principais problemas a eles associados. Como por exemplo, qual a sua composição, qual a sua origem e processos de produção e a sua propagação pelo espaço. Em seguida, descrevem-se a física das cascatas de partículas e formas de detecção. No capítulo 5 apresenta-se a descrição do observatório e os seus dados recentes.

No capítulo 4, faz-se uma breve descrição do estado actual dos modelos das interações hadronicas. Verifica-se que significativas extrapolações dos dados dos aceleradores são necessárias para descrever as energias das interações dos raios cósmicos. E existe uma grande desconfiança sobre as suas validades (devido às ambiguidades previstas, quando comparadas com os dados).

Neste âmbito, na fase inicial estuda-se a probabilidade do  $\chi^2$  do fit das cascatas com a função de Geisser-Hillas. Pretendendo-se extrair a fracção de eventos com flutuações acima das flutuações Gaussianas, que serão o ruído dos eventos de cenários exóticos e servirão de base para o principal objectivo da tese.

No último capítulo propõe-se um método para determinação da secção eficaz das primeiras leadings dos chuviros. Considera-se que o perfil longitudinal observado, é a soma de dois perfis (com a forma da equação de Geisser-Hillas), um correspondendo a uma leading e o outro ao conjunto das restantes partículas, produzidas na primeira interacção. A distribuição do espaçamento entre os dois perfis corresponderá ao comprimento de interacção da leading (retirando-se a secção eficaz). Aplica-se este método as chuviros simulados, estuda-se a validade, significado dos resultados e zonas onde o método funciona. Também se verifica a existência de eventos reais candidatos a serem descritos apenas por este método e não por uma Geisser-Hillas.

**Palavras-chave:** raios cósmicos de altas energias, Observatório Pierre Auger, cascatas atmosféricas de partículas, modelos hadronicos, secção eficaz a altas energias.



## Abstract

Nowadays, with the Pierre Auger Observatory completed, we expect about 30 events with energies above  $10^{20}eV$  and many more underneath it. Since the Observatory uses a hybrid technique, we obtain events with a much better quality than previous experiments (and in larger quantity). So we are in a crucial phase for further studies applied to cosmic rays. In addition, we still watching the start of operation of the LHC (Large Hadron Collider), which can give major constraints on the characteristics of interactions, facilitating the study of cosmic rays.

The first phase of this thesis is a summary of the main features of cosmic rays, as well as the main problems associated with them, as their composition, what are its sources and production processes, and their propagation through space. Then we describe the physics of particle cascades and forms of detection. Chapter 5 presents a description of the observatory and its recent data.

Chapter 4 is a brief description of the current state of hadronic models for interactions. It appears that significant extrapolations of the data from accelerators are needed to describe cosmic rays at the energies of their interactions. And there is great scepticism about their validity (due to ambiguities predicted, when compared with the data).

In this context, in the initial phase, we study the probability of  $\chi^2$  of the fit of cascades with the Geisser-Hillas function. With the purpose of extracting the fraction of events with fluctuations above the Gaussian fluctuations, which will be the background of events in exotic scenarios and will be the basis for the primary purpose of the thesis.

The last chapter proposes a method for determining the cross section of the first leadings of showers. It is considered that the observed longitudinal profile is the sum of two profiles (with the Hillas-Geisser equation shape), where one corresponds to a leading and the other to all the other particles produced in the first interaction. The distribution of the spacing between the two profiles correspond to the interaction length of the leading (taking out the cross section). We apply this method to simulated showers, study the validity, the results interpretation and areas where the method works. we also check in real events for candidates to be described only by this method and not by one Geisser-Hillas.

**Keywords:** ultra high energy cosmic rays, Pierre Auger Observatory, extensive air showers, hadronic models, cross section at high energies.



# Contents

Acknowledgements . . . . .	v
Resumo . . . . .	vii
Abstract . . . . .	ix
<b>Contents</b>	<b>xi</b>
<b>List of Tables</b>	<b>xiii</b>
<b>List of Figures</b>	<b>xv</b>
<b>List of Abbreviations</b>	<b>xix</b>
<b>1 Introduction</b>	<b>1</b>
<b>2 Ultra High Energy Cosmic Rays</b>	<b>3</b>
2.1 Energy spectrum . . . . .	3
2.2 Propagation . . . . .	4
2.3 Acceleration mechanisms and cosmic ray sources . . . . .	6
<b>3 Extensive Air Shower</b>	<b>9</b>
3.1 Physics of extensive air showers . . . . .	9
3.2 Longitudinal profile . . . . .	13
3.3 Lateral profile . . . . .	14
3.4 EAS detection . . . . .	14
<b>4 Hadronic models</b>	<b>21</b>
4.1 Introduction . . . . .	21
4.2 Hadronic Interaction . . . . .	23
4.3 Hadronic models . . . . .	28
<b>5 The Pierre Auger Observatory</b>	<b>35</b>
5.1 Southern Observatory . . . . .	36
5.2 Event reconstruction . . . . .	41
5.3 Recent results . . . . .	46
<b>6 How exotic are standard events</b>	<b>51</b>
6.1 Universal Shower Profile . . . . .	51
6.2 Tool to separate standard from exotic events . . . . .	52
6.3 Extreme fluctuations . . . . .	57
6.4 Full Simulation . . . . .	59
<b>7 Sensitivity to the leading particle</b>	<b>61</b>
7.1 Two Gaisser-Hillas approximation . . . . .	61
7.2 Two Gaisser-Hillas approach results . . . . .	64

7.3	Results interpretation . . . . .	69
7.4	Interaction length and Inelasticity . . . . .	72
7.5	Real Events . . . . .	77
<b>8</b>	<b>Conclusion and prospects</b>	<b>81</b>
	<b>Bibliography</b>	<b>83</b>
<b>A</b>	<b>Showers parametrizations</b>	<b>89</b>
<b>B</b>	<b>Two Gaisser-Hillas function fit test</b>	<b>93</b>
<b>C</b>	<b>Selection 3 analysis</b>	<b>97</b>

# List of Tables

7.1	Number of events selected with the selection rules. . . . .	66
7.2	Number of events of sub selections of selection 3 . . . . .	71
7.3	The efficiency and purity of the several steps in selection 3. . . . .	72
7.4	Leadings number per particle type. . . . .	73
7.5	The $\lambda$ and $\sigma$ effective for several selections. . . . .	74
7.6	Severals important $\lambda$ and corresponding $\sigma$ effective, from the input values. . . . .	75
7.7	The $\lambda$ and corresponding $\sigma$ effective for the new fitting equation (eq. 7.7) and corresponding meson/baryon fraction. . . . .	76
7.8	Values of the effective inelasticity $K$ . . . . .	78
A.1	Mean values for Shower Parameters . . . . .	91



# List of Figures

2.1	Data of the cosmic ray flux assembled by Gaisser, figure adapted from [8]. . . . .	4
2.2	Cosmic Ray spectrum from [8], for direct measurements (bellow $10^{15}eV$ ) and indirect measures with EAS (above $10^{15}eV$ ); the end of cosmic ray spectrum with galactic and extragalactic component. . . . .	5
2.3	Trajectories of 20 protons emanating from a point for several energies. The trajectories are follow until 40Mpc (from [15]). . . . .	5
2.4	The energy loss length for different processes at different energies, for the propagation of cosmic ray throughout the universe[15];the mean energy of a proton moving through the universe with CMB, with 3 initial energies.[26] . . . . .	7
2.5	Adapted Hillas diagram[19] from[23]; representation of the 2nd order Fermi mechanism of cosmic ray acceleration. . . . .	8
3.1	Symbolic representation of the evolution of a Extensive air shower from an hadronic primary particle	10
3.2	Schematic representation of an electromagnetic and hadronic shower within Heitler toys model. .	12
3.3	The atmospheric density as function of altitude with it's corresponding slant depth crossed; Example of longitudinal showers profiles for iron and proton at $10^{19}eV$ . . . . .	13
3.4	Draft of a shower development and it's detection with several types of detection techniques. . . .	15
3.5	Fluorescence spectrum of the atmospheric nitrogen; and fraction of the missing energy (in %) in a EAS. . . . .	16
3.6	Schematic representation of the image of a detection of a shower in a FD telescope. . . . .	18
3.7	scheme of a ground array with a detected event; and a scheme of severals showers fronts. . . . .	20
4.1	Deep inelastic scattering within the parton model and hadron-hadron interaction in QCD. . . . .	23
4.2	Firsts result from slac for DIS, with Bjorken scaling; and representation of the proton in the phase space ( $Q^2, x$ ) with the DGLAP and BFKL evolutions . . . . .	23
4.3	representation of an elementary interaction (in EPOS); multiscattering in EPOS; and pomeron re-scattering with soft and hard contributions (for QGSJET). . . . .	26
4.4	representation of the origin of produced particles (from projectile and target and ladder); The inner and outer contribution for several experiments; and particle production representation within string model . . . . .	26
4.5	Glauber formalism for a target hitting a nucleus with impact parameter b; the general pomeron in QGSJET-II as a combination of a soft and a semi-hard pomeron. . . . .	27
4.6	inelastic $h^{-1} 4N$ cross-section for QGSJET-II, QGSJET and SYBILL; The total and inelastic cross section of p-air and p-p for SYBILL . . . . .	30
4.7	interaction between two nucleus with cut and uncut pomerons; Inelastic and elastic splitting of a parton ladder, i.e. a re-scattering of a parton from parton ladder with a second extra parton from the target. . . . .	30
4.8	Inelastic cross section $p - Air$ for several models; Uncertainty of the extrapolation of $p - Air$ cross section from accelerator to CR energies, within the Glauber formalism. . . . .	32
4.9	Multiplicity and inelasticity for several models. . . . .	32
4.10	$X_{max}$ for several models in a wide energy range and predictions from recent hadronic model at ultra high energy . . . . .	33

4.11	number of muon over energy for several models; ratio of $\pi^0$ number over number of charge particles; and total CR energy over energy deposit in atmosphere for several models . . . . .	34
4.12	lateral profile for $\gamma$ , $e^\pm$ and $\mu^\pm$ ; and prediction of Cherenkov density in the tank for $10^{19}eV$ vertical proton in function of distance . . . . .	34
5.1	Configuration of the Pierre Auger Observatory southern detector from [68]. . . . .	36
5.2	A photograph of one of the tanks in the Pierre Auger surface array; the representation of the water Cherenkov detector used in PAO from [71] . . . . .	37
5.3	Layout of an FD eye building with 6 telescopes from [72]; and schematic representation of a telescope from [71]. . . . .	37
5.4	A photograph of PMT camera and aperture box and mirrors [75]; representation of six Mercedes stars positioned in order to form a the hexagonal pixel; photograph of some part of the camera with four PMTs and two Mercedes stars mounted together; and representation of a PMT and Mercedes star in degrees. . . . .	38
5.5	$(\beta, \alpha)$ coordinates in relation to the coordinates $(\theta, \phi)$ from [76]; representation of the camera with 440 pixels in the coordinates $(\beta, \alpha)$ . . . . .	39
5.6	Scheme of the geometry of the shower with the parameter settings; representation of the SD signal as a function of the distance to the core, and the optimum core distance in PAO. . . . .	41
5.7	Scheme of the geometry of the shower (with shower detector plane); and time of arrival of the light at each pixel in relation to the angle between the pointing direction of that pixel and the horizontal line. . . . .	42
5.8	Representation of direct fluorescence, Cherenkov light and scattered Cherenkov light received at diaphragm. . . . .	44
5.9	profile of light at aperture with reconstructed component of direct and scattered Cherenkov light from a simulated event with $10^{19}eV$ ; fit to the curve $CIC(\theta)$ relative to the signal $S_{1000}$ at zenith angle $38^\circ$ as a function of zenith and fit to the curve $CIC(\theta)$ in order to $\cos^2 \theta$ . . . . .	45
5.10	Precision in position and angle of the CLF laser reconstruction by monocular and hibrid reconstruction. . . . .	46
5.11	calibration between the parameter $S_{38}$ and FD energy $E_{FD}$ with 785 hybrid events (from [95]); The CR spectrum of HiRes and Auger. . . . .	47
5.12	CR spectrum of hybrid events and spectrum of SD events in Auger Data. . . . .	47
5.13	The 69 PAO events with $E \geq 55EeV$ until 31 December 2009 plotted in the sky with galactic coordinates; and the cumulative number of events as function of the angle $\Psi_A$ , with relation to the position of Centaurus A. . . . .	48
5.14	The sequential analysis of the likelihood ratio of CR with energy greater than $55EeV$ ; and the most likely value for the binomial parameter $p_{data} = k/N$ . . . . .	49
5.15	$\langle Xmax \rangle$ and RMS $(Xmax)$ from PAO data, from December 2004 until March 2009, compared with simulation predictions . . . . .	50
5.16	Upper limits on the photon fraction in the integral cosmic-ray flux for different experiments; and Differential and integrated upper limits for the flux of down-going $\nu$ and up-going $\nu_\tau$ . . . . .	50
6.1	Example of normal showers profiles and corresponding universal shower profiles at $10^{19}eV$ . . . .	53
6.2	Shower profiles varying $L$ and $R$ parameter . . . . .	53
6.3	$\chi^2$ distribution for one Geisser-Hillas at $10^{19}eV$ . . . . .	54
6.4	Shower profile in number of $e^+/e^-$ and $\mu$ ; and plot of $\chi_i^2$ terms at $10^{19}eV$ . . . . .	54
6.5	New $\chi^2$ distribution (with cuts in final and initial points) and corresponding $\chi_i^2$ as function of $X_i$ , at $10^{19}eV$ . . . . .	55
6.6	$\chi^2$ evolution with energy . . . . .	56
6.7	Draft of the $\chi^2$ probability . . . . .	57
6.8	$\chi^2$ distribution with new error definition and $\chi^2$ probability at $10^{19}eV$ . . . . .	58
6.9	$\chi^2$ distribution with new error definition and $\chi^2$ probability at $10^{19}eV$ . . . . .	58
6.10	Zoom of the low $\chi^2$ probability region at $10^{19}eV$ . . . . .	59
6.11	Profiles and mean profiles for samples with different $\chi^2$ probability . . . . .	59

6.12	Two simulated event with detector simulation and corresponding fits to one and two Geisser-Hillas function. . . . .	60
7.1	Schematic representation of the first interactions and decomposition into two Geisser-Hillas function. . . . .	62
7.2	Two examples of the fit of two Geisser-Hillas to one known Geisser-Hillas. . . . .	63
7.3	Reconstruction of knowns profile with sum of two Geisser-Hillas. . . . .	63
7.4	Rate of events as a function of the difference between the first and second interaction; and $\chi^2$ distribution for one and two Geisser-Hillas function. . . . .	64
7.5	$(\Delta X_{Rec} - \Delta X_{Gen})/\Delta X_{Gen}$ as function of $\Delta X_{Rec}$ and $\Delta X_{Gen}$ . . . . .	66
7.6	$(\Delta X_{Rec} - \Delta X_{Gen})/\Delta X_{Gen}$ as function of $\Delta X_{Gen}$ and $K_{Gen}$ . . . . .	66
7.7	$(\Delta X_{Rec} - \Delta X_{Gen})/\Delta X_{Gen}$ as function of $\Delta X_{Rec}$ and $K_{Rec}$ . . . . .	67
7.8	$(\Delta X_{Rec} - \Delta X_{Gen})/\Delta X_{Gen}$ as function of $\chi^2_{1GH}$ and $\chi^2_{2GH}$ . . . . .	67
7.9	$\Delta X_{Rec}/\Delta X_{Gen}$ distribution and $K_{Rec}/K_{Gen}$ distribution. . . . .	67
7.10	$\Delta X_{Rec}$ as function of $\Delta X_{Gen}$ and $K_{Rec}$ as function of $K_{Gen}$ , for selection 2 and 4. . . . .	68
7.11	$\Delta X$ distributions for all events and events of selection 3 . . . . .	68
7.12	The inelasticity ( $K$ ) distribution for all events and for selection 3. . . . .	69
7.13	Examples of two events with $10^{18}eV$ and corresponding fit to one GH and two GH. . . . .	70
7.14	Particle type of the leadings; $\Delta X_{Gen}$ and $\Delta X_{Gen} + \Delta X_{L2,Gen}$ distributions. . . . .	74
7.15	The new fit (of eq. 7.14) to the $\Delta X$ distributions of all reconstructed events and selection 3. . . . .	77
7.16	Plot of the events: EventId 7274947; and EventId 7274947. With corresponding fits. . . . .	78
7.17	Plot of the events: EventId 7269175; and EventId 7270194. With corresponding fits. . . . .	79
7.18	Draft of the camera pixels and the detected light at the camera of the events EventId 7269175 and EventId 7270194 . . . . .	79
A.1	$N_{Max}$ distributions and $N_{Max}$ parametrization with energy . . . . .	90
A.2	$X_{Max}$ distribution and $X_{Max}$ parametrization with energy . . . . .	90
A.3	$L$ distributions and $L$ parametrization with energy. . . . .	91
A.4	$R$ dsitributions and $R$ parametrization with energy. . . . .	91
A.5	$\chi^2$ ) distribution for several energies and $\chi^2$ ) parametrization with energy . . . . .	92
A.6	$\chi^2$ ) distribution for several energies and $\chi^2$ ) parametrization with energy (with cuts in the initial and final points of the profile.) . . . . .	92
B.1	$\Delta X_{Rec}$ (reconstructed) as a function of $\Delta X_{Gen}$ (input value) and $K_{Rec}$ as a function of $K_{Gen}$ . These events are made using 2GH with parameters equals the typical mean values without fluctuations. . . . .	94
B.2	$\Delta X_{Rec}$ as a function of $\Delta X_{Gen}$ , $K_{Rec}$ as a function of $K_{Gen}$ . These events are made using GH with parameters equals the typical mean values with gaussian fluctuations. . . . .	94
B.3	$\Delta X_{Rec}/\Delta X_{Gen}$ distribution, $K_{Rec}/K_{Gen}$ distribution. . . . .	95
B.4	$\chi^2$ for one GH of the consider events, divided into events with $0.2 < K_{Rec} < 0.8$ and $\Delta X_{Rec} > 200g/cm^2$ and the rest; $\chi^2$ plot in function of $\Delta X_{Rec}$ and divided into groups of $K$ . . . . .	95
B.5	Two examples of a two GH fit. . . . .	96
B.6	More two examples of a two GH fit . . . . .	96
C.1	$\Delta X_{Rec}$ and inelasticity $K$ distribution for several sub selections 3 . . . . .	97
C.2	$\chi^2_{1GH}$ and the $\chi^2_{2GH}$ distribution for several sub selections 3. . . . .	97
C.3	$X_{max,1}$ distribution for two GH and $X_{max,2}$ distribution for two GH for several sub selections 3. . . . .	98
C.4	$L_1$ distribution for two GH and $L_2$ distribution for two GH for several sub selections. . . . .	98
C.5	$L_1$ distribution for two GH and $L_2$ distribution for two GH for several sub selections. . . . .	98



# List of Abbreviations

AGASA	Akeno Giant Air Shower Array
AGN	Active galactic nucleus
CDAS	Central Data Acquisition System
CLF	Central Laser Facility
CMB	Cosmic Microwave Background
CORSIKA	COsmic Ray SIMulations for KAscade
CR	Cosmic Ray
DIS	Deep Inelastic Scattering
DPM	Dual Parton Model
EAS	Extensive Air Shower
EGCR	ExtraGalactic Cosmic Rays
EPOS	Energy conserving quantum mechanical multiple scattering approach, based on Partons (parton ladders), Off-shell remnants, and Splitting of parton ladders
FD	Fluorescence Detector
GCR	Galactic Cosmic Ray
GH	Geisser-Hillas function
GPS	Global Positioning System
GRT	Gribov-Regge Theory
GZK	Greisen-Zatsepin-Kuzmin
HiRes	High Resolution Fly's Eye
LDF	Lateral Distribution Function
LIDAR	LIGHT Detection And Ranging
MAGIC	Major Atmospheric Gamma-ray Imaging Cherenkov (telescope)
NKG	Nishimura-Kamata-Greisen
PAO	Pierre Auger Observatory
PDF	Parton Density Function

PMT	Photomultiplier Tubes
pQCD	perturbative Quantum Chromodynamics
QCD	Quantum Chromodynamics
QED	Quantum Electrodynamics
QGS	Quark Gluon String model
QGSJET	Quark Gluon String model with jets
SD	Surface Detector
SDP	Shower Detector Plane
SNR	Supernova Remnants
UHE	Ultra High Energy
UHECR	Ultra High Energy Cosmic Ray
USP	Universal Shower Profile
UV	Ultraviolet
VCV	Véron-Cetty and Véron catalogue
VEM	Vertical Equivalent Muon
XLF	second Central Laser Facility

# Chapter 1

## Introduction

Our planet is constantly being bombarded by extraterrestrial particles called cosmic rays (CR). They consist mainly of charged particles, such as ionized nuclei, protons and other particles like electrons and gammas. On the surface, we continue to receive the secondary particles of the CR. This natural radiation is on average about  $0.4\text{ mSv}$  (average annual effective dose) of the total  $2.4\text{ mSv}$ .

It was from this natural radiation that the CR story begins, at about 100 years ago. In 1912, Hess[1] and successively Kolhorster, using balloons, found that the average ionization increases with altitude (even overnight). This could indicate that part of the radiation came from abroad and not just from radioactive isotopes on the ground. Later, Millikan called this radiation cosmic rays, since they considered them to be high energetic gammas.

With more sophisticated instruments such as Geiger-Muller detectors, it was found that the CR were mostly charged and have energies of about  $10^9\text{ eV}$ , due to larger interaction lengths with matter. With that, Bruno Rossi studied the secondary particles of the CR and verified that there were strange coincidences between different spaced detectors [2]. In 1937, using the first coincidence circuit with a resolution of  $\sim 10 \times 10^{-6}\text{ s}$ , Pierre Auger discovered coincidences in detectors spaced up to 300m [3]. Those would be the secondary particles of a CR forming a cascade of particles, which he called Extensive Air Auger Shower (EAS). Using the new model of Bhabha and Heitler [4], Auger showed that the original CR should have energies above  $10^{15}\text{ eV}$ , which astonished the scientific community.

With cosmic rays, the elementary particle physics begins. Using cloud chambers, the discover of a wide variety of particles started. In 1933, the positron was discovered, which was predicted by Dirac. In 1936, the muon was found [6], which was initially believed to be the Yukawa particle of his theory of the nuclear force, but close measurements, shows that this particle was significantly lighter and interacts weakly with atomic nuclei, unlike Yukawa particle. However, in 1947 the pion was discover as the real Yukawa particle[5], at the Pyrenees, and later at the Andes Mountains. By mid-60's, thanks to the CR, many particles have been discovered, which became known as the particle zoo.

In 1961, MIT installed 19 detectors of  $3.3\text{ m}^2$  plastic scintillators on the surface and detected the first ultra high energy cosmic ray (UHECR) with about  $\sim 10^{20}\text{ eV}$ [7]. This corresponds approximately to the energy of a tennis ball, but in a particle with dimensions on the order of fermi ( $10^{-15}\text{ m}$ ).

Over the next forty years there were several experiments dedicated to CR as AGASA, Fly's Eye and Haverah Park. However, the study of CR has proved to be extremely difficult due to the small particle fluxes. For a particle with  $10^{20}\text{ eV}$ , we have a flow of 1 particle per  $\text{km}^2$  per century. This means that these experiments at the ultra high energy (UHE) will be dominated by statistical uncertainties.

At energies above  $10^{15}\text{ eV}$ , the reduced flux does not allow to detect directly the CR, but only through the EAS. Thus, in UHE, the composition of the CR spectrum is not known. In addition, there are problems related with the difficulty of find cosmological structures and processes that can produce such energies. And, there are even contradictory evidences on the possible GZK cutoff. Another very difficult challenge, and related to the composition of the spectrum, comes from the lack of theories capable of describing satisfactorily hadronic interactions (with the strong force) at these energies. So, extrapolations are needed, which will probably lead to biases in the analysis of the initial development of a shower. Nowadays, there are challenges from the

sources and propagation of CR throughout the universe, until the composition and characterization of the ends of the energy spectrum.

In order to solve these challenges, in 2007 the construction of the Pierre Auger Observatory (PAO) was completed. The PAO is the largest experience, allowing detection of much more UHECR than before. The observatory uses a hybrid technique that combines the detection with surface detectors (SD) for the lateral profile and fluorescence detectors (FD) for the longitudinal profile. Still, there has several additional systems, mainly for control of the atmosphere to better determine the systematic.

With the new PAO results in bigger quantity and better quality than ever, we are in a very exciting step for further studies and apply methods to data. Therefore, it will arise many implications in several areas of physics, like particle physics, astrophysics and cosmology.

In this context, this thesis aims to study the events with extreme fluctuations, using a new method for obtaining the interaction length (or a cross-section) of the first particles of an EAS, from a CR with energy between  $10^{18}$  and  $10^{19}eV$  (in the laboratory frame). Basically, the new method consider an independent development of the leadings (from first interactions), that carries an high fraction of the CR primary energy, from the remaining particles. Consequently, we will have two EAS, instead of one. If we can recover the two showers, we will be able to recover the distance travel by the leading and therefore, obtain a interaction length.

The thesis is structured as follow. The second chapter is an introduction of the main characteristics and problems existing in CR, with the description of the spectrum, composition, propagation, production and sources. In chapter 3, we will explain the physics of extensive air showers and the main detection techniques. Chapter 4 is devoted to hadronic interactions. Although some problems of the perturbative QCD and a brief summary of the models that describe those interactions at UHE are described, I will mention some features of most popular Monte Carlo models (for hadronic interaction). The fifth chapter will begin by describing the observatory and then the reconstruction methods. Finally, we describe the current state of the results with PAO. In Chapter 6, we determine the number of events with extreme fluctuations, which are preferably used in Chapter 7 to use the new method. In chapter 7, we want to find an effective cross section and a fraction of mesons to baryons in simulation, that could greatly constrain the hadronic models, when applied to data.

## Chapter 2

# Ultra High Energy Cosmic Rays

The Cosmic Ray term is somewhat misleading, since it is a radiation that consists mainly of ionized atomic nuclei. The term was assigned by Robert Millikan, after V. Hess prove it came from space. Millikan believed that throughout the universe, there was the release of binding energy of atoms in the form of gamma rays, and this would be the cosmic rays.

This radiation is simply particles that collide with earth, have various compositions and a wide range of energies. In this chapter, we will describe the spectra, composition, origin and propagation of cosmic rays.

### 2.1 Energy spectrum

The detected cosmic rays spectrum extends over several orders of magnitude both in energy and in flux on Earth. In figure 2.1 is shown a compilation of data from the cosmic rays spectrum made by Thomas Gaisser in [8].

In the figure, we see a variation in flux of 33 orders of magnitude, and can be detected about 15 orders in energy ( $10^6$ eV to  $10^{21}$ eV at least). For example, at  $10^{11}$ eV we have a rate of  $1 \text{ m}^{-2}\text{s}^{-1}$ , while for  $10^{20}$ eV, we have about  $1/\text{km}^2/\text{century}$  [9]. With this decrease in flux is only possible to directly detect the particles of energy up to  $10^{14-15}$ eV (with balloons and satellites). Above these energies would require very large areas of detectors to identify something and is no longer possible to detect directly. Thus, from there, we use the atmosphere as a calorimeter and cosmic rays are detected in the atmosphere as cascades of particles (which will be described in the following chapter 3). It is interesting that the spectrum can be described with a simple power law:

$$J(E) = \frac{dN}{dE} \propto E^{-\gamma_s} \quad (2.1)$$

Where  $\gamma_s$  is the spectral index and has a value near 3. The spectrum has some features, the index changes at  $3 \cdot 10^{15}$ eV, called the knee, and for  $\log E = 18.45$ , the ankle. For  $E < 3 \cdot 10^{15}$ eV, the flux is proportional to  $E^{-2.7}$  [8]. In this region the particles are derived primarily from the sun and other galactic sources such as supernova remnants (SNR). Its composition is mainly protons, but with significant amounts of He, C, N, O, Si and Fe nuclei [10], there are still small amounts of nuclei heavier than Fe [9].

Between the knee and ankle ( $\log E = 18.45$ ), the flux becomes  $J(E) \propto E^{-3.32}$  [13]. This value means that in this region the number of particles reaching the earth decreases more rapidly with energy than for energies below the knee. Apart from the change in flux between the knee and ankle, the composition will become heavier with E, because the particles are no longer confined to galaxy.

A particle of charge q and mass m, on the action of a magnetic field B perpendicular to the particle velocity v experiences a radial force given by  $F = |q|vB = \gamma m \frac{v^2}{r}$ , where r is the radius of the trajectory, and can be written by

$$r = \frac{\sqrt{E^2 - m^2c^4}}{|q|B} \cong \frac{E}{|q|B} \quad (2.2)$$

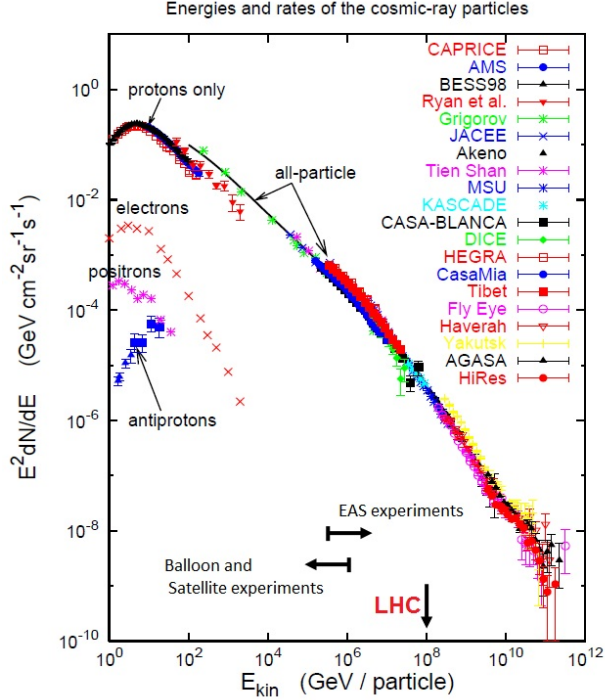


Figure 2.1: Data of the cosmic ray flux assembled by Gaisser, figure adapted from [8].

where  $\gamma$  is  $\gamma = 1/\sqrt{1-\beta^2}$ ,  $\beta = \frac{v}{c}$ . we use  $p = \gamma mv$  e  $E^2 = p^2 c^2 + m^2 c^4$ , for  $E \gg mc^2$  and therefore the maximum energy that particles can have before escaping the galaxy is about  $E \propto Z$ , ie depend on the rigidity  $\frac{E}{|q|}$ , as the proton has the smallest charge, it will be the first type of particle to escape from the galaxy, followed by the other particles until they reach the iron. According to [8], the proton will fall near  $3 \cdot 10^{15}$  eV, and the other nucleons will drop at  $E \approx 3Z \cdot 10^{15}$  eV.

It is interesting to note that part of the spectrum measured directly overlaps in the right place with the spectrum measured indirectly, figure 2.2a). Even if indirect measurements do not allow the full separation of protons and other nuclei, the figure shows that with several models, we can predict a the various nuclei fluxes, consistently with direct measures.

Following the line that represents the galactic cosmic rays (GCR) (see fig. 2.2b) with blue dashed line, we see that there is an excess flux that is due to extragalactic cosmic rays (EGCR). There are several models for the composition in this region, based on sources of mixed composition or only proton and both can equally reproduce the data.[14].

Nevertheless, the determination of the composition by indirect techniques such as  $RMS(X_{max})$  and  $X_{max}$  (which will be seen in the following chapter 3) indicate that the region of the ankle is practically compound of protons. Above the ankles there are many uncertainties, what is certain is that, at these energy, cosmic rays are EGCR. The spectrum is again  $J(E) \propto E^{-2.85} \sim E^{-2.7}$  see [13], similar to the energies below the knee. From around  $10^{19.5}$  eV, we see a sharp decline resulting from the GZK limit.

## 2.2 Propagation

As indicated, for energies below  $\sim 10^{17}$  eV, cosmic rays are confined to the galaxy with a diffusion coefficient. The galactic magnetic fields are the order of  $\mu G$  [19], the Larmor radius in more appropriate units is,

$$R_{pc} \approx 10^{21} \frac{E_{eV}}{q_e B_G} \quad (2.3)$$

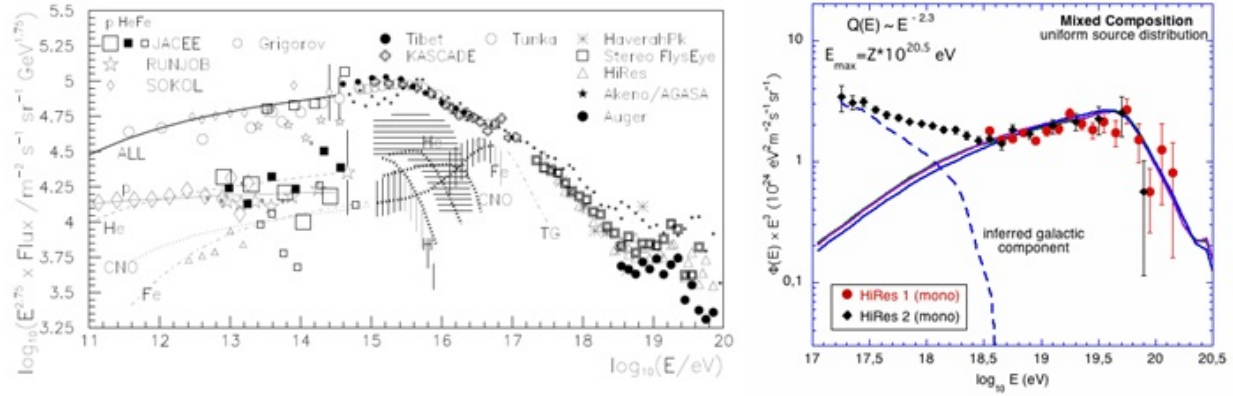


Figure 2.2: a: Cosmic Ray spectrum from [8], for energies below  $10^{15} \text{ eV}$ , the data are obtained by direct measurement techniques and above it, we have indirect measures with EAS. Above  $10^{15} \text{ eV}$  we can't know the composition, so the various bands that appear come from models and we can see that they coincide with direct measures. b: we have the end of cosmic ray spectrum [14], the blue dashed line corresponds to the inferred galactic cosmic ray (GCR) component, while the blue line represents the extra galactic cosmic ray (GCR) to fit the data

For protons with energy of  $10^{19} \text{ eV}$ , and magnetic field  $1 \mu\text{G}$  have a Larmor radius of  $10 \text{ kpc}$ , very wide in comparison with the thickness of the galaxy. For energies of  $10^{15} \text{ eV}$ , the Larmor radius is about  $1 \text{ pc}$  (much smaller than the galaxy). In figure 2.3 from [15], the proton trajectories are represented for various energies, considering magnetic fields close to nanogauss (typical intergalactic value) and areas with randomly oriented field. For  $E = 10^{20} \text{ eV}$ , the trajectories are almost rectilinear and even with realistic magnetic fields, we can do astronomy with cosmic rays.

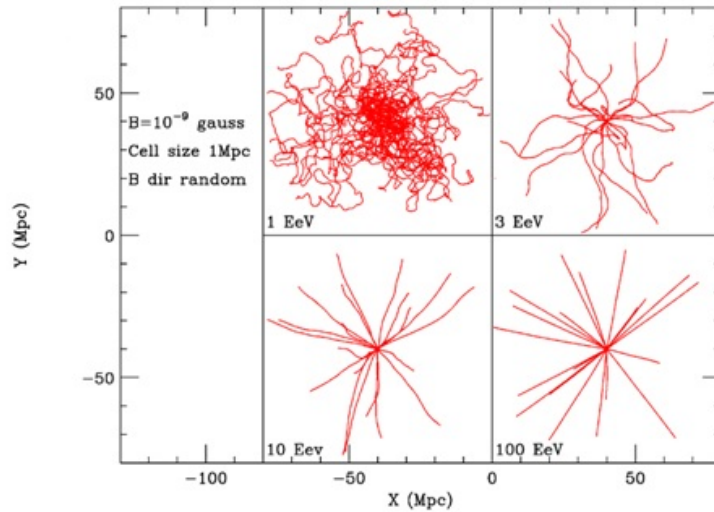


Figure 2.3: Trajectories of 20 protons emanating from a point for several energies. The trajectories are followed until  $40 \text{ Mpc}$  (from [15]).

### 2.2.1 GZK limit and losses

Above, it was considered that the propagation of the proton happen without energy losses, however, throughout its propagation in space, there will be losses.

In 1966, A. Penzias and R. Wilson discovered a cosmic microwave background (CMB) in the universe. The CMB is like a blackbody spectrum with  $T_{CMB} \simeq 2.73K$ , which means photons with  $\langle \lambda_{CMB} \rangle \simeq 1.96mm$ , which means with an energy  $\langle E_{CMB} \rangle = hc / \langle \lambda_{CMB} \rangle \simeq 6.34 \cdot 10^{-4}$  eV. This radiation resulting from the Big Bang is isotropic through the universe, and may interact with cosmic rays. After the discovery of the CMB, K. G. Greisen [16] and independently Zatsepin and V. Kuzmin [17], predicted that above a certain energy, protons would interact with the CMB and produce pions, causing a big decrease in the CR flux arriving the Earth (GZK cutoff). The main reactions involved are of type,



The threshold condition for the reaction occur is in the center of mass frame,  $s = (m_p + m_{\pi^0})^2$ . Being  $p_{CMB} = \langle E_{CMB} \rangle$  and  $p_p = \beta_p E_p$  (where  $\beta_p = \frac{v_p}{c} = v_p$  in units of c) we can write,

$$s = (p_{CMB} + p_p)^\mu (p_{CMB} + p_p)_\mu = (\langle E_{CMB} \rangle + E_p)^2 - (p_{CMB} \vec{p} + \vec{p}_p)^2 = m_p^2 + 2 \langle E_{CMB} \rangle E_p (1 - \beta_p \cos \theta) \quad (2.5)$$

where  $\theta$  is the angle between the initial proton and CMB photon. Together with the threshold condition, we obtain the GZK cutoff:

$$E_p^{GZK} = \frac{m_{\pi^0}^2 + 2m_p m_{\pi^0}}{2 \langle E_{CMB} \rangle (1 - \beta_p \cos \theta)} \quad (2.6)$$

For frontal collisions with  $\theta = \pi$ , and  $\beta_p \sim 1$ , we get  $E_p^{GZK} \simeq 1.07 \cdot 10^{20}$  eV. The energy in the center of mass is  $\sqrt{s} = m_p + m_{\pi^0} = 1073$  MeV, which was already achieved by accelerator by the time of the publication of the GZK [16][17], the cross section is  $\sigma(p\gamma \rightarrow p\pi^0) \simeq 200\mu b = 2 \cdot 10^{28} cm^2$ . According to [11], the density of CMB photons is  $n_{CMB} \simeq 411 cm^{-3}$ , we can use  $L_p = n_{CMB} \cdot \sigma(p\gamma \rightarrow p\pi^0)^{-1}$  to calculate the mean free path and we obtain  $L_p \simeq 1.22 \cdot 10^{23} m \approx 4Mpc$ . This means that for each 4Mpc, protons with energy close to the threshold will lose its power by a factor of 0.13, according to [16].

We can also calculate the threshold for the production of electron positron pairs  $E_p^{GZK} \simeq 4.8 \cdot 10^{17}$  eV, however, this effect is not so important, since the proton energy loss is negligible in this process. On the other hand, for gamma rays to produce  $e^+e^-$  pairs the threshold is very low, about  $E_p^{GZK} \simeq 2.6 \cdot 10^{14}$  eV and there is a large energy attenuation (with no  $\gamma$  rays detected above this energy). In figure 2.4left depicts the loss lengths for some of the most important reactions.

It should be noted that the spectrum of the CMB is a broader spectrum, so we have several threshold for the numerous energies of CMB photons, but even so, it makes sense to consider an average value for the energy of the CMB. Another source of loss is the expansion of the universe and other reactions such as the resonance  $\Delta^+$ ,  $p + \gamma_{CMB} \rightarrow \Delta^+ \rightarrow p + \pi^0$ , but are not as important as the production of pions.

In figure 2.4 right, we can see the energy loss of several protons above the GZK limit, along their trajectories. We conclude that the proton above the GZK cutoff can not travel more than about 100Mpc.

There is also a cosmic neutrino background with  $\langle E_{\nu_r} \rangle \sim 10^{-4}$  eV [18], which will interact with high-energy neutrino by  $\nu_r + \nu \rightarrow Z^0$ , with a cutoff  $E_\nu^{GZK} \simeq 2.08 \cdot 10^{25}$  eV.

Today have been detected cosmic rays above the GZK cutoff, however, there is no candidate for a source at a distance less than 100Mpc. This means that either there are sources that we do not know, or that the cosmic ray could have much more energy (since they leave from far away). In fact, neither for protons with energies in the limit, we can easily find sources of production.

## 2.3 Acceleration mechanisms and cosmic ray sources

The mechanisms of acceleration of UHECR are a subject of controversy with still open questions, there are two major types of acceleration, the bottom-up and top-down. The bottom-up mechanisms, assume that

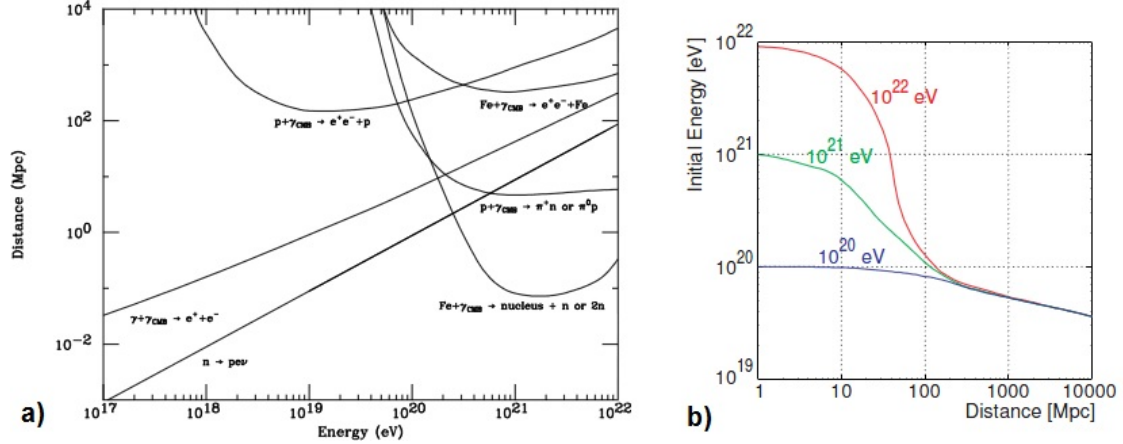


Figure 2.4: left:figure adapted from[15], the curves  $p + \gamma_{CMB} \rightarrow e^+e^- + p$  and  $Fe + \gamma_{CMB} \rightarrow e^+e^- + p$  represent the energy loss length for different energies, this length is the distance for which the proton,photon or iron loses  $1/e$  of its energy.The curve  $n \rightarrow pev$  is for the mean decay length of a neutron, the dashed line is the length for loses due to the red shift. The other curves represents the mean free path for the same loses.Rigth:the mean energy of a proton moving through the universe with CMB, with 3 initial energies.[26]

the particles are accelerated directly from low to high energies. We can have acceleration by electric fields, although it is easy to accelerate charged particles with electric fields, for these energies it would require a high density of particles in order to produce the fields. This would cause large energy losses of the accelerated particles, making it difficult to try to reproduce the spectrum [20], and today it is not very accepted. Another bottom-up was proposed by Fermi [21] in 1949, which consisted in statistical acceleration, since the particles could be accelerated each time they interact with magnetized plasma. The problem is that both models need to get a spectrum index greater than that observed to contain the energy losses of particles.

### 2.3.1 Fermi acceleration mechanism

In [21], Fermi proposed a mechanism of statistical acceleration, in which cosmic rays were scattered by magnetized plasma. In figure 2.5 right, is represented the diffusion of cosmic rays in a plasma. A particle with energy  $E_i$  and  $p_i$  in the laboratory reference frame S, enters in a magnetized zone. In the plasma reference frame  $S'$  the energy of the particle is,

$$E'_i = \gamma(E_i - \beta_{pl} \cdot \vec{P}_i) \simeq \gamma E_i (1 - \beta_{pl} \cos \theta_i) \quad (2.7)$$

where  $\beta_{pl}$  is the plasma velocity in relation to the frame S and  $\theta_i$  is the angle between  $\vec{\beta}_{pl}$  and  $\vec{P}_i$ . In frame S' we consider  $E'_i = E'_f$ .

When the particle leaves the magnetic zone, we have

$$E_f = \gamma(E'_f + \beta_{pl} \cdot \vec{P}'_f) \simeq \gamma E'_f (1 + \beta_{pl} \cos \theta'_f) \quad (2.8)$$

Putting equation 2.7 with equation 2.8, we get,

$$\frac{\Delta E}{E} = \frac{E_f - E_i}{E_i} = \frac{1 - \beta \cos \theta_i + \beta \cos \theta'_f - \beta^2 \cos \theta_i \cos \theta'_f}{1 - \beta^2} - 1 \quad (2.9)$$

As the particles are distributed randomly  $\langle \cos \theta_f \rangle = 0$ , but  $\theta_i$  depends on the speed between the cloud and the particle. The probability P per solid angle  $\Omega$ , having a collision at  $\theta_i$  is  $\frac{dP}{d\Omega} \propto (a - \beta \cos \theta_i)$ . So  $\langle \cos \theta_f \rangle = \frac{-\beta}{3}$ . With  $\beta \ll 1$ , we get

$$\frac{\langle \Delta E \rangle}{E} = \frac{1 + \beta^2/3}{1 - \beta^2} - 1 \approx \frac{4}{3} \beta^2 \quad (2.10)$$

This is the 2nd order Fermi mechanism, which has a very slow acceleration, and so, later have been proposed a 1st order mechanism to present a greater acceleration efficiency [24]. According to [24], with these methods, you can find an index of about 2, which taking into account the losses, which can fit more or less the spectrum.

### 2.3.2 Hillas Diagram

For the above mechanisms, it is necessary that cosmic rays are confined within the area of acceleration, if the region has a radius R, then the maximum energy obtained is,

$$E_{max}(EeV) = \frac{1}{2} Z \beta B(\mu G) R(kpc) \quad (2.11)$$

Where  $\beta$  is the speed of diffusion center, B in  $\mu G$ , R in parsec and E in EeV. Hillas made a diagram using this equation and considering the existing structures in the universe, figure 2.5 left. As we can see, it is possible to accelerate protons to  $10^{20}$ eV, but only considering the non realistic case of  $\beta = 1$ , ie, the magnetized plasma with the speed of light. If we consider the more realistic value of  $\beta = 1/300$  no known cosmological structure could produce such energies.

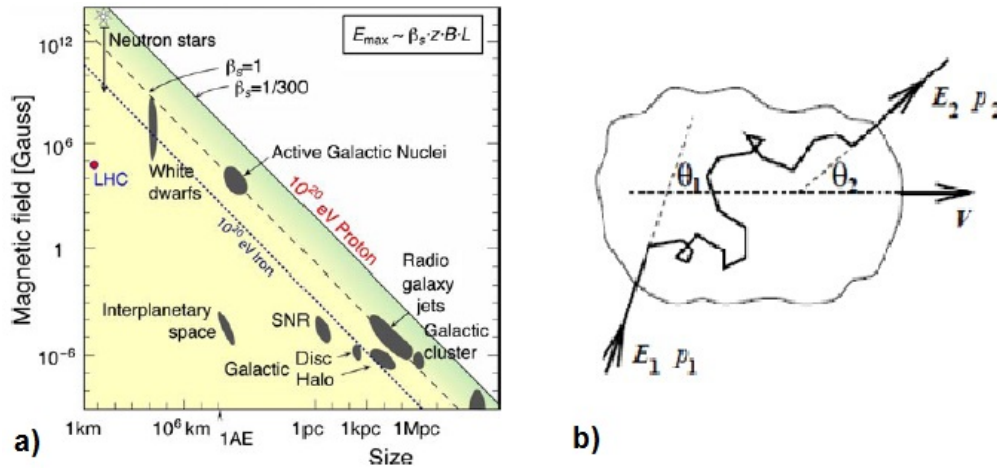


Figure 2.5: left:we have an adapted Hillas diagram[19] from[23], astronomical objects that are bellow the diagonal line can not accelerate the corresponding particle at the energy indicated. rigth: representation of the 2nd order Fermi mechanism in a moving magnetized plasma, 1 is the index for arrival particles and 2 for leaving particles (from [25])

### 2.3.3 Top-down models

Another type is the top-down model, whereby super-massive particles would decay producing UHECR. The decay of these particles would produce leptons and hadrons, the pions in turn produce muons, electrons photons and positrons. This would cause a spectrum dominated by photons at high energies. In addition the initial particle would have energies far above  $10^{20}$  and have a sufficient density to maintain the CR flux. These particles could be relics of the early universe at GUTs energies (for details see [22]).

Another model is the Z-burst, where UHE neutrinos interact with cosmic neutrinos background producing Z which in turn would decay into protons, neutrinos and photons. These neutrinos would come from even more energetic particles, which is difficult to explain. Besides, the flux of photons and high energy neutrinos would be very high, the current limits are major constraints in this scenario (see [22]).

## Chapter 3

# Extensive Air Shower

In 1938, Pierre Auger and Roland Maze showed that cosmic rays (CRs) separated by more than 20m were simultaneously detected, proving that they are originated from a single high energy cosmic ray. In 1939, they already had proven the existence of particles to  $10^{15}$ eV [3]. At these energies, as we saw in the previous chapter, the flux of CR is too low to be detected directly. Large areas were needed for detect them, which is impossible in space.

The atmosphere acts as a calorimeter <sup>1</sup> where CR disintegrates forming an Extensive air shower (EAS). There are several methods of studying EAS and that is what this chapter is about.

### 3.1 Physics of extensive air showers

The high energy CR will interact at the top of the atmosphere, producing particles, these, in turn have sufficient energy to re-produce new particles and so on, producing a cascade called Extensive air shower (EAS). These showers will depend on atmospheric conditions, which are now well vertically parametrized, but this characteristics vary widely over time (such as pressure, temperature and others). It is then necessary, a good control of the atmosphere. Since the CR may come from any angle and not necessarily in the vertical direction, the altitude is not a good variable to measure the development of the shower. The number of interactions that have occurred in the shower depends on the matter traversed and not the altitude. The good variable is the slant depth  $X$  measured in  $gcm^{-2}$ :

$$X(\vec{r}_0, \vec{r}) = \int_{\vec{r}_0}^{\vec{r}} \rho(\vec{r}') d\vec{r}' \quad (3.1)$$

Where  $\rho$  is the density of the atmosphere and  $\vec{r}_0$  is the point where the particle made first contact with the atmosphere. Generally the slant depth is defined by  $X_v$  and we have:

$$X \approx \frac{\int_h^\infty \rho(\vec{h}) dh}{\cos \theta} = \frac{X_v}{\cos \theta} \quad (3.2)$$

Where  $\theta$  is the angle from the vertical. For vertical showers at sea level,  $X \sim 1000gcm^{-2}$  for horizontal showers  $X \sim 36000 g/cm^{-2}$ .

In EAS, the primary particle produces secondary particles, which in turn will have interactions and decays producing more particles (and their energies will decrease). So the number of particles  $N(X)$  will increase until it reaches a maximum, where the energy per particle is on average equal to the ionization energy. The number of particles produced is equal to the number lost by ionization. From the  $N(X)$  maximum, particles are being absorbed and  $N(X)$  decreases.

---

<sup>1</sup>The atmosphere provides approximately a vertical thickness of 26 radiation length for electron and 15 interaction length for a proton, very similar to the values for the CMS at LHC [27]

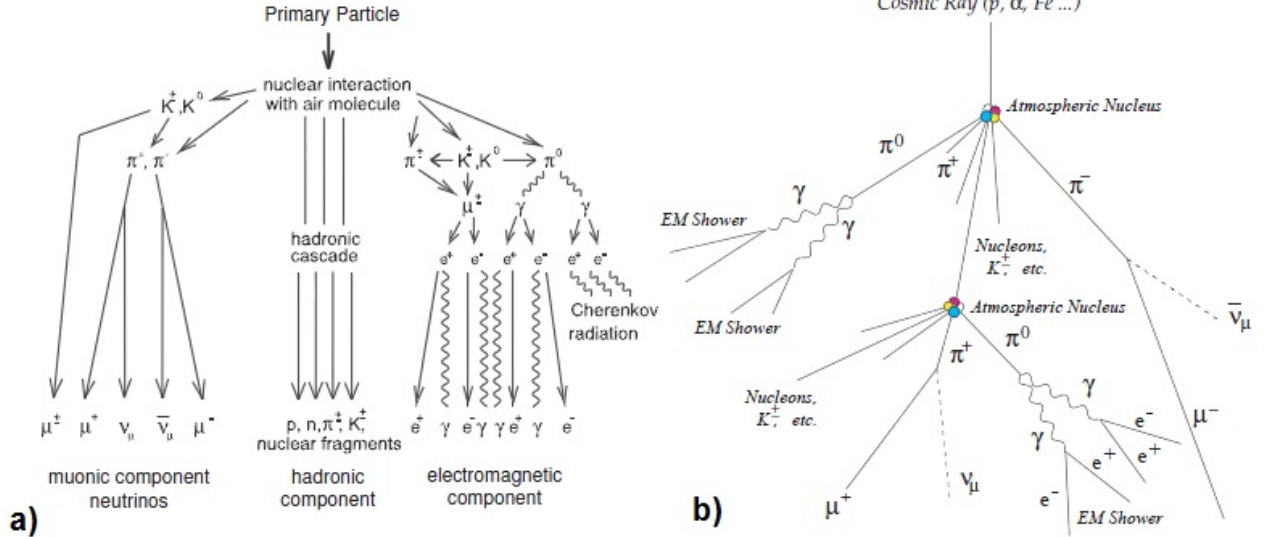


Figure 3.1: a) Symbolic representation of the evolution of an Extensive air shower from a hadronic primary particle [28] and b) from [71].

The EAS can be divided into three components: the hadronic; the muonic, and the electromagnetic component. The hadronic component comes from the interaction of CRs or secondary particles with the molecules of the atmosphere and are mostly mesons like pions and kaons. The muonic component contains the muons and neutrinos, while the electromagnetic component have the electrons, positrons and photons. According to [29], a vertical shower of a proton with  $10^{19}\text{eV}$ , at ground, has  $10^{11}$  secondary particles with energy above 90 keV and a shower core of  $\sim 10\text{km}$ . About 99% are photons, electrons and positrons, with 90% of the primary particle energy being dissipated by the electromagnetic component.

### 3.1.1 Photon showers and Electromagnetic component

The CRs interacts with air molecules in the top of the atmosphere, and there produces secondary particles and so on. If the particles produced are neutral pions, then they will decay by,

$$\pi^0 \rightarrow \gamma + \gamma \quad (3.3)$$

This decay has 98.798% [30] branching ration and thus, it is the most common reaction. Then, can also occur  $\pi^0 \rightarrow e^+e^-\gamma$  with 1.198%. This means, that the pions will produce mainly photons (and possibly a few electrons). Photons will convert into  $e^+e^-$  pairs, these by their turn will radiate photons by bremsstrahlung feeding the cycle in a chain reaction, while there is enough energy. So we get a cascade of particles composed of electrons, positrons and photons. For each reaction, the energy per particle decreases, the minimum energy required for pair production is  $2m_e \simeq 1022\text{keV}$ . When the energy begins to be small, the main mechanism of energy loss is through ionization and collisions, rather than by bremsstrahlung or pair production, then the atmosphere will absorb the particles and the cascade begins to decrease. The critical energy for the absorption of particles is roughly defined as the energy at which the ionization loss is equal to the bremsstrahlung loss, from [29],

$$E_C = \frac{710\text{MeV}}{Z_{eff} + 0.92} \approx 86\text{MeV} \quad (3.4)$$

Where is the  $Z_{eff}$  is the effective atomic charge, with  $Z_{eff} = 7.3$  [31], which considers that the atmosphere consists of 78.09%  $N_2$ , 20.95%  $O_2$  and 0.96% other gases. The profile of particle number grows up until the energy per particle is approximately  $E_C$  and from there the number of particles decreases.

If the primary particle is a proton, it is considered that on average every hadronic interaction produces one third of  $\pi^0$  from all particles(see next section). These will produce electromagnetic cascades of particles,

feeding the electromagnetic component.

In the case of the primary particle being a photon, it is considered that it produces basically the electromagnetic component. The cross section of Bethe-Heitler [38], which corresponds to the cross section for pair production and bremsstrahlung, for UHE 10EeV is about 500mb [32]. Moreover, the photonuclear cross section for these energies on [30] is about 1mb, and extrapolations to other more exotic scenarios gives  $\sim 10$  mb (see [32] [40]), so the ratio of the photohadronic cross-section to the pair production cross-section will be,

$$Q = \frac{\sigma_{\gamma \rightarrow \text{hadrons}}}{\sigma_{\gamma \rightarrow e^+e^-}} \simeq \frac{1(10)}{500} \simeq 0.2\%(2\%) \quad (3.5)$$

Where can we see that the hadronic interactions in  $\gamma$  are unlikely and photons produce mainly electromagnetic cascades. Now, if the first photon interaction is hadronic, the shower development will be more like to the proton shower [32].

For UHE, there are two effects that change the cross section of photons. On the one hand, there is the Landau-Pomeranchuk-Migdal effect, which suppresses the cross sections for pair production and bremsstrahlung above roughly 10EeV. On the other hand, we have pair production and magnetic Bremsstrahlung (pre-showering) effect, which make the photon produce the cascade before reaching the atmosphere (only interacting with the magnetic field of the earth). (See for instance and [32] [29]).

### 3.1.2 Heitler model

The first models for the EAS were proposed by Rossi and Greissen in 1941. But most of the main features of EAS may be deduced by the toy model due to Heitler [33]. I will follow the derivation by J. Mathews, from [34].

Heitler's model is a simple model, as shown by the figure 3.2. Here, the photon interacts after a set distance  $d$ , producing  $e^-e^+$  pairs, the two in turn after another distance  $d$ , will again be divided into two particles, in this case  $e^- \rightarrow e^- + \gamma$  and  $e^+ \rightarrow e^+ + \gamma$  respectively. At each distance  $d$ , each particle splits into two new particles.  $d$  is the distance at which the particle loses on average half the energy and is written as  $d = \lambda_r \ln 2$ , where  $\lambda_r$  is the radiation length. It is supposed that in the process of bremsstrahlung, the photon and  $e^-$  ( $e^+$ ) share the power of initial  $e^-$  ( $e^+$ ), the cascade is one-dimensional and all splitting occur after the same distance  $d$ .

After  $n$  splitting length, the cascade travel  $x = n\lambda_r \ln 2$  and the number of particles is  $N = 2^n = e^{x/\lambda_r}$ . The condition of the maximum of EAS is that the particles have a critical energy  $\xi_c^e$  (how as been said before), so

$$E_0 = \xi_c^e N_{max} \quad (3.6)$$

Where  $E_0$  is the energy of primary particles,  $N_{max}$  is the number maximum of particles through the development of EAS and  $n$  is the number of splitting.  $N_{max}$  is also obtained by  $N_{max} = 2^{n_c}$ , where  $n_c$  is the number of radiation length until the maximum. Together with the equation 3.6, we get  $n_c = \frac{\ln[E_0/\xi_c^e]}{\ln 2}$ . The maximum depth is then

$$X_{max}^\gamma = n_c \lambda_r \ln 2 = \lambda_r \ln[E_0/\xi_c^e] \quad (3.7)$$

As shown in [34] the result of the model for  $X_{max}^\gamma$  is very similar to that obtained by simulation, however we get an excess of particles, since in reality the particles begin to be absorbed before the maximum. The model provides a photon ratio of 1/3, while 9/10 is more realistic, because during the bremsstrahlung are emitted more than one photon.

It is now interesting to define the elongation rate  $\Lambda$ , which describes the increase of  $X_{max}$  with  $E_0$ :

$$\Lambda \equiv \frac{dX_{max}}{d \log_{10} E_0} \quad (3.8)$$

With the equation 3.7 we have  $\Lambda = 2.3\lambda_r = 85 \text{ gcm}^{-2}$  per decade of primary energy, which means that we have the mean length of interaction  $\sim 37 \text{ gcm}^{-2}$  (for  $E_0 < 1EeV$ ) and between  $45 - 60 \text{ gcm}^{-2}$  for  $E_0 > 1EeV$  [29]. With this we can obtain the cross section of the first interaction, which is not directly available in detectors.

One of the most important contributions of the model is providing the maximum number of particles proportional to  $\propto E_0$  for photon showers and  $X_{max} \propto \ln E_0$ .

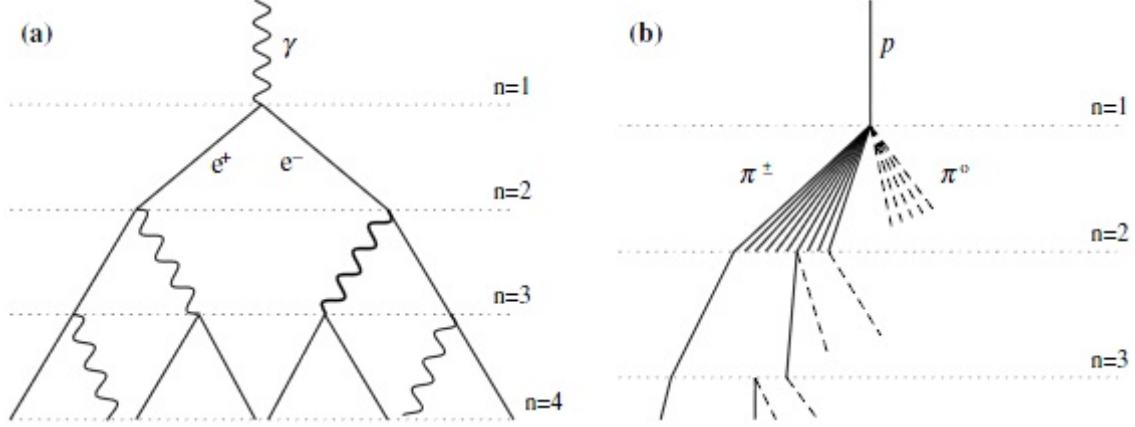


Figure 3.2: Schematic representation two showers within Heitler model, for an electromagnetic shower, initiated by a photon a) and an hadronic shower initiated by a proton. At each level  $n$  the particles interacts producing more particle. The electromagnetic shower duplicate the number of particles at each  $n$ , while in hadronic shower the multiplicity in each interaction is higher.[34]

### 3.1.3 Hadronic component

The hadronic component originates from the interaction of primary nuclei (such as protons and iron and very rarely of photons) with atmospheric nuclei. These interactions are the major source of error in the analysis of EAS, since the energies of the CR are several orders of magnitude above the data we currently have from accelerator (this will be discussed in this chapter 4 ).

At this stage, we can consider that in hadronic interactions, part of the energy is converted to mesons and the rest goes to a new nucleon that, after about an iteration length, will interact and produce a second generation of mesons, and successively. These mesons in turn will also interact producing more mesons (up to a critical energy, again). We consider the interaction of a proton with the atmosphere as

$$p + p \longrightarrow p + p + N(\pi^0 + \pi^+ + \pi^-) \quad (3.9)$$

And we can neglect the production of  $K$ ,  $\Lambda$ ,  $\eta$ ,  $\Omega$ ,  $\Sigma$ ..., because they are small in quantity compared to pions. We can see that in each generation, on average, the neutral pions carry one third of energy and charged pions about 2/3.

Nor all pions will interact, some of them will simply decay. The interaction length for pion in air is  $X \sim 120 gcm^{-2}$  for  $E < 10^{14} eV$  [11] ( $X$  is the slant depth, eq 3.2). Now, if the interaction length is larger than the decay length, then the pion interacts, if it's not the case the pion decays. The decay length depends on the energy of the pion, since the pions have a mean life time ( $\tau$ ) in their's reference frame. If it have a great energy (or velocity in relation to another reference frame), then by Lorentz equations, we know that in the other reference frame the pions will live more (time dilation). If they live more, then they can travel more and the decay length is larger. The decay length is the mean free path travelled by the pions until it decay and is given by (using Lorentz equations):

$$L_{decay} = x = \gamma(x^0 + v.t^0) = \gamma\tau c \quad (3.10)$$

where  $L_{decay}$  is the decay length (in laboratory reference frame),  $x^0$  and  $t^0$  are in the proper reference frame, so  $x^0 = 0$  and  $t^0 = \tau$ . The velocity of the proper reference frame to the laboratory reference frame is  $v$ , and we can use  $v \simeq c$ .

Since the interaction length is about  $120 gcm^{-2}$ , if we know the density of the atmosphere we know the distance needed for pions to interact. In the figure 3.3a), we can see the density of the atmosphere provided by the U.S. Standard atmosphere. At the altitude of 16km, the EAS has already gone through about  $100 gcm^2$  of depth, the average density between 16km and 11km is  $\rho = 2.55 \cdot 10^{-04} gcm^{-3}$ , so it takes about 4698m to cross  $\sim 120 gcm^{-2}$ , ie the pions travel something like  $\sim 4700m$  to interact. If we are between 0 and 1 km, the

average density is  $\rho = 1.11 \text{gcm}^{-2}$  and the distance will be  $\sim 1 \text{km}$  to interact. Now, we just need to compare these, to the values of the decay length.

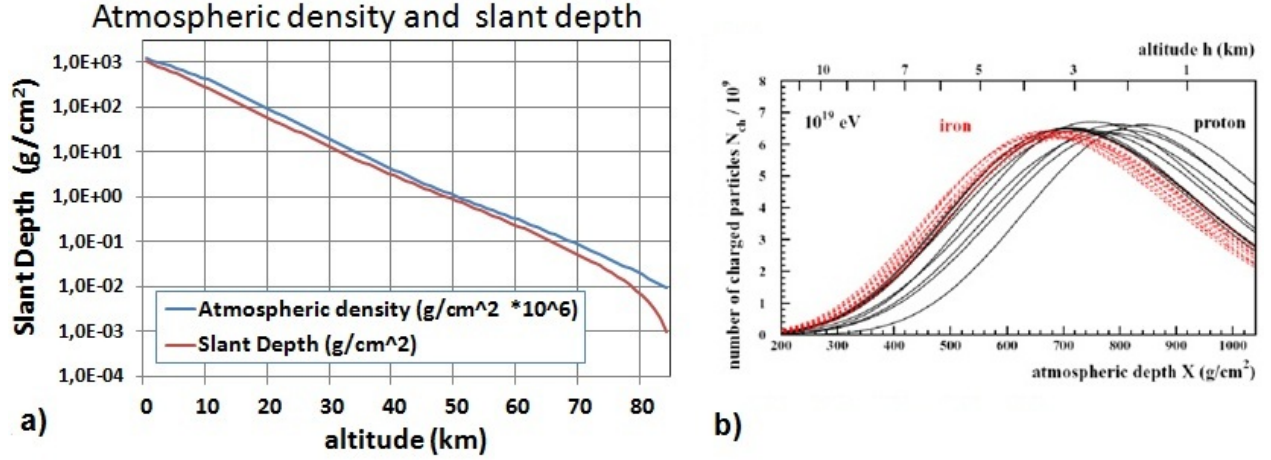


Figure 3.3: a) The atmospheric density as function of altitude with its corresponding slant depth crossed. This plot comes from the US standard atmosphere data, from [12]. b) Example of longitudinal showers profiles for iron (red) and proton (black) at  $10^{19} \text{eV}$  from [35].

The lifetime of the neutral pions is  $\tau_{\pi^0} = 8.4 \cdot 10^{-17} \text{s}$ , so at about  $\sim 13 \text{km}$  would require at least an energy of  $E \sim 2.5 \cdot 10^{19} \text{eV}$  for the neutral pion interact. This is a too extreme energy and we conclude that it will not interact but decay into two photons. Even at  $1 \text{km}$ , would require an energy  $\sim 5.4 \cdot 10^{18} \text{eV}$ , in order to the pion cross  $\sim 1000 \text{m}$ , it is concluded that the  $\pi^0$  always decays. For charged pions the case is different, since the average lifetime is  $\tau_{\pi^{+/-}} = 2.6 \cdot 10^{-8} \text{s}$ , so at  $\sim 13 \text{km}$ , with approximately  $E \sim 8.4 \cdot 10^{10} \text{eV}$ , these pions can cross  $4700 \text{m}$ . At  $\sim 1 \text{km}$ , the charged pions could cross  $1000$ , with an energy of about  $\sim 1.8 \cdot 10^{10} \text{eV}$ . If the pions have energy above a threshold that will be around  $\sim 10^{10} \text{eV}$ , then they can interact, producing again one third of  $\pi^0$  and two thirds of  $\pi^{+/-}$ . If their energy is below this limit, the charged pions will decay to produce muons in the reaction,



Due to the bust of hadron particle, the hadronic component remains very close to the axis of the cascade in relation to  $e^-$ ,  $e^+$ , photons and muons. You can also use an adapted Heitler model for Hadronic showers (fig 3.2 [34]).

### 3.1.4 Muonic component

The muonic component, comes from the decay of charged pions with lower energies. The muon has a lifetime larger than the charged pions, so few decays. However, they also have a very small cross section for radiation and pair production. Thus, muons don't produce cascades and are detected in the ground. The quantities of muons depend heavily on hadronic models and the composition of the primary particle and can be used to constrain models and composition. For the same energy, a solid prediction that can be obtained with simple models is that the number of muons for iron as a primary particle is 80% higher than for proton [34].

## 3.2 Longitudinal profile

Today, instead of the Heitler model, the parametrization most used to describe the number of particles in the longitudinal profile is the Gaisser-Hillas function (GH):

$$N_e(X; N_{max}, X_{max}, X_0, \lambda_{GH}) = N_{max} \left( \frac{x - X_0}{X_{max} - X_0} \right)^{\frac{X_{max} - X_0}{\lambda_{GH}}} e^{-\frac{X_{max} - X}{\lambda_{GH}}} \quad (3.12)$$

Where  $N_{max}$  is the maximum number of particles in the shower maximum at  $X = X_{max}$  in depth.  $X_0$  is associated with the first point of interaction, however, is not directly correlated, since after fitting the Gaisser-Hillas, the value of  $X_0$  can be negative. Indeed, the value  $X_{max} - X_0$  is associated to the composition and cross sections. In the figure 3.3b), are represented EAS for some protons in red and iron in black at an energy of  $E = 10^{19} eV$ . As we can see, the proton showers present higher fluctuations than iron, as expected, because iron is considered as being similar to 56 protons with an energy  $E/56$ , so we have 56 simultaneous showers of protons reducing the fluctuations and as the effective energy is lower we will also have a smaller  $X_{max}$  for iron.

### 3.3 Lateral profile

The particles of EAS suffer multiple Coulomb Scattering in the nuclei of the atmosphere, this causes the particles to gain transverse momentum. The lateral development of the cascades was parametrized by Nishimura, Kamata and Greisen [36][37] and takes the form for pure electromagnetic showers:

$$\rho(r) = c(s) \frac{N_e}{r_0^2} \left(\frac{r}{r_0}\right)^{s-2} \left(1 + \frac{r}{r_0}\right)^{s-45} \quad (3.13)$$

Where  $c(s) = 0.366 \cdot s^2 (2.07 - s^{1.25})$ ,  $\rho(r)$  is the density of particles with respect do the distance  $r$  of the axis shower.  $N_e$  is the total number of electrons,  $s$  is the age parameter and  $r_0$  is the Molière radius ( $r_0 = \lambda E_s / E_c$ , where  $\lambda$  is the radiation length,  $E_s = 21 MeV$  and  $E_c$  is the critical energy). In such showers, only about 10% of energy is contained in particles outside the cylinder with radius  $r_0$ . Greisen [36] also proposed a correction to the formula to parametrize Hadronic showers.

$$\rho(r) = \frac{C_1(s) N_e}{2\pi r_0^2} \left(\frac{r}{r_0}\right)^{s-2} \left(1 + \frac{r}{r_0}\right)^{s-45} \left(1 + C_2 \left(\frac{r}{r_1}\right)^\delta\right) \quad (3.14)$$

The Shower age parameter is given by  $s = \frac{3}{1 + 2 \frac{X_{max}}{X}}$ .

### 3.4 EAS detection

The study of the EAS can be done through two types of detection techniques. On the one hand, we can detect the particles that hits the ground with arrays in the grounds, on the other, we can detect the emission of light during the development of cascades in the atmosphere (with light detectors). In figure 3.4, are represented some of the possible detectors of EAS. As technical grounds arrays, we have the squares on the surface that detect the particles in the electromagnetic component on the ground (usually also muons). The squares inside the earth, only detect muons, the deeper the detector is, the greater is the energy of muons that have managed to get there. The house represents the surface detectors for hadrons which eventually reach the ground. On the right, the structure represents the detection of the light emitted by showers. With this we can obtain the lateral and longitudinal profiles of EAS, the muons content and others to analyse the features of EAS physics.

#### 3.4.1 Light detection

We can not detect directly the particles of the EAS during their development in the atmosphere, so we use indirect detection methods, based on the features of EAS. The development of the cascades, along the atmosphere, produces fluorescence light and Cherenkov light that can be detected by optical detectors installed in the ground. In addition, one can also detect the radio emissions of electrons from the cascades.

The light emissions are very dependent on the atmosphere and one still has to take into account the attenuation of light emitted into the atmosphere. The attenuation depends heavily on the composition and characteristics of the atmosphere, so it is strictly necessary, to manage day to day the atmospheric parameters. Currently, there is the U.S. standard atmosphere, a model of atmosphere in the U.S. region, which parametrizes the atmosphere very well, but variations in clouds, dust and pollutants vary very quickly and



energies [41]). If we consider photons with 350nm, then  $E \sim 44eV$  and therefore the fraction of energy emitted is  $44 \cdot \frac{17.6}{10^6} \sim 0.1\%$ . This is very low, but as the energies of the CR is much larger than MeV, then it is possible to have many photons. The method for the fluorescence light is thus more accurate for higher energies. It should be noted that the emission of photons is isotropic, so it is still necessary to have the issue of the 3D emission and not the direct fluorescence yield.

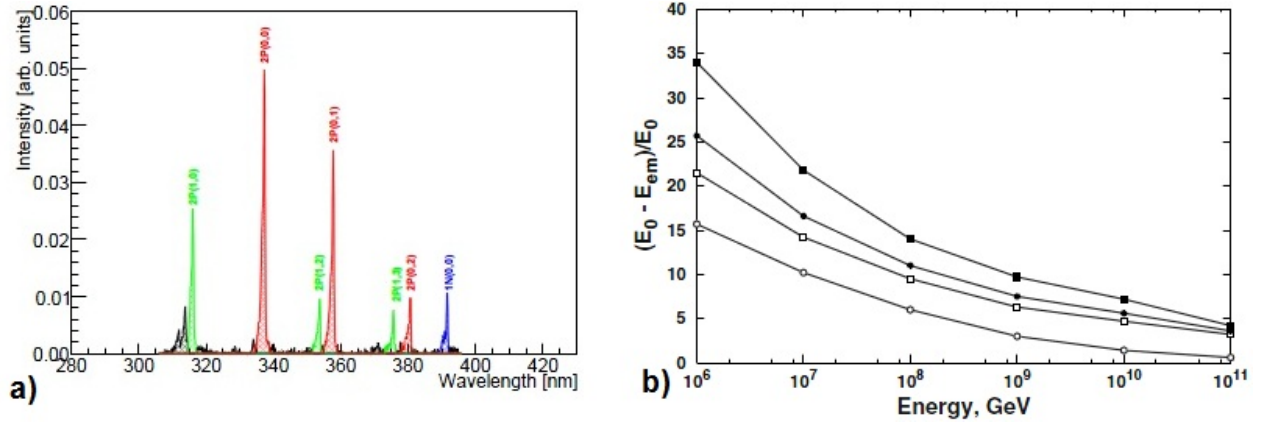


Figure 3.5: a) Fluorescence spectrum of the atmospheric nitrogen from [71], measured by A. Ulrich. b) Fraction of the missing energy (in %) in a EAS. With circles we have proton showers, in squares He, in dots CNO and filled squares for Fe. [11]

### 3.4.1.2 Cherenkov radiation

The Cherenkov radiation is emitted when charged particles traverse a medium of refractive index  $n > 1$ , with a higher speed than the speed of light in that medium  $v_{light} = c/n$  (where  $c$  is the speed of light in vacuum). It works like shock waves in the sound, but in this case for electromagnetic waves. The minimum velocity for the emission is,

$$\beta n > 1 \quad \rightarrow \quad E_{thr} = m\sqrt{1 - 1/n^2} \quad (3.17)$$

$m$  is the mass of the particle and  $\beta$  is the velocity. The radiation consists of photons emitted in a cone along the direction of propagation with an angle given by,

$$\cos \theta = \frac{1}{\beta n} + q \quad (3.18)$$

where  $q$  is a quantum correction without much importance. The refractive index of air is about  $n = 1,00029$  [42], so the Cherenkov angle is  $\sim 1.4^\circ$ . This is the maximum refractive index for the sea level, for higher altitudes, the index decreases and the angle too. The threshold energy for electrons is about  $\sim 21MeV$ . Approximately  $\sim 10^5$  photons are emitted by the electron at sea level. This is a large intensity compared to the intensity of fluorescence light. The Cherenkov radiation is only emitted very close to the axis of propagation, with angles generally less than  $25^\circ$  (due to transverse momentum). These photons are also attenuated by the Rayleigh scattering in the atmosphere. So even if the Cherenkov light is directional, light can be scattered into other directions.

### 3.4.1.3 Rayleigh scattering

The photons are scattered by molecules of the atmosphere, if the size of the scattering centers are small compared to the wavelength  $\lambda$  of photons, then we have the Rayleigh scattering, which is proportional to  $\lambda^{-4}$ . If we have  $dN_\gamma$  photons undergoing a thickness  $dl$  of the atmosphere, the Rayleigh scattering is given by,

$$\frac{dN_\gamma}{dl} = -\frac{\rho N_\gamma}{X_R} \left(\frac{400nm}{\lambda}\right)^4 \quad (3.19)$$

where  $X_R = 2974gcm^{-2}$  is the characteristic Rayleigh path length [44]. The radiation is scattered preferentially in the forward and backward direction as shown by,

$$\frac{d^2 N_\gamma}{dl d\Omega} = \frac{3}{16\pi} (1 - \cos^2 \theta) \left| \frac{dN_\gamma}{dl} \right| \quad (3.20)$$

Using  $dX = \rho dl$  (3.2) and integrating, we obtain  $N_\gamma(X_2) = N_\gamma(X_1) e^{-\frac{|X_1 - X_2|}{X_R} (\frac{400nm}{\lambda})^4}$ , that in terms of transmission coefficient is [43],

$$T_R = e^{-\frac{|X_1 - X_2|}{X_R} (\frac{400nm}{\lambda})^4} \quad (3.21)$$

#### 3.4.1.4 Mie scattering

If the wavelength of the photons is similar to the size of molecules, these will be spread by Mie scattering. The particles that diffuse fluorescence photons by this process are pollutants and aerosols, clouds and dust. The cross section is given by [44],

$$\frac{dN_\gamma}{dl} = -\frac{N_\gamma}{L_M} e^{-h/H_M} \quad (3.22)$$

where  $h$  is the height and  $h_M$  and  $L_M$  are characteristics for the aerosol distributions. Taking into account the angular distribution, we have

$$\frac{d^2 N_\gamma}{dl d\Omega} = a_M \cdot e^{\theta/\theta_M} \left| \frac{dN_\gamma}{dl} \right| \approx \frac{dN_\gamma}{dl} 0.802^{-\theta/\theta_M} \quad (3.23)$$

$\theta_M = 26.7^\circ$ ,  $a_M, \theta_M, h_M$  and  $L_M$ , are parameters, and they correspond to mean values for aerosol conditions. The diffusion is mainly driven forward. The coefficient of transmission [43] is,

$$T_M = e^{\frac{1}{L_M(\lambda)} \left| \int_1^2 e^{-h/h_M} dl \right|} \quad (3.24)$$

Using the approach  $dl = dh / \cos \theta'$  ( $\theta'$  being the angle between the vertical and the path of photons) and we get,

$$T_M = e^{\frac{h_M}{L_M(\lambda) \cos \theta'} \left| e^{-h_1/h_M} - e^{-h_2/h_M} \right|} \quad (3.25)$$

We should note that  $a_M, \theta_M, h_M$  and  $L_M$  strongly depend on the composition of the atmosphere and therefore is again needed a good control of the atmosphere. From [43], we have  $h_M \simeq 1.2km$  and  $L_M \simeq 14km$  at  $\lambda = 360nm$ .

#### 3.4.1.5 Attenuation

The fluorescent light that reaches the detector must be corrected by the geometry and the attenuation of the diffusion of Mie and Rayleigh. Thus,  $I_0$  being the intensity of photon emission, we get a photon intensity at the detectors given by,

$$I = I_0 \cdot T_R \cdot T_M \cdot (1 + \varepsilon) \frac{\Delta\Omega}{4\pi} \quad (3.26)$$

where  $\Delta\Omega$  is the angular interval and  $\varepsilon$  corresponds to higher order correction due to multiple scatterings.

#### 3.4.1.6 Cherenkov experiments

As mentioned, the Cherenkov radiation is emitted into the air in a cone with a very small angle of aperture and it is delivered very close to the axis of the shower. Thus, the optical detectors must be aligned with the showers in order to detect direct Cherenkov. If we are not oriented with the axis, we will only detect fluorescence light and Mie and Rayleigh scattering light (if sensitive enough). The big advantage comes from the high density of photons emitted, but is difficult to reconstruct the features of EAS and is necessary Monte Carlo simulation to estimate the  $X_{max}$  or primary energy.

Currently, this type of detectors (system of Imaging Atmospheric Cherenkov Telescopes) are used primarily to detect gamma-rays and two examples are the Major Atmospheric Gamma-ray Imaging Cherenkov (MAGIC), in the island of La Palma, Canary Islands, Spain and the High Energy Stereoscopic System (HESS).

### 3.4.1.7 Fluorescence technique

As the fluorescence intensity is lower than the Cherenkov radiation, then the detectors should not be placed in the direction of showers. Since radiation is isotropic and the fluorescence yield with the attenuations, is very low, it is only possible to detect very high energy EAS, usually for energies above  $10^{17}eV$ . The showers may develop far from the detector, since the intensity of photons is sufficient. If  $10^6$  electrons pass by 700 m of atmosphere, at about 20km from the detector, it will produce  $2.8 \cdot 10^{12}$  photons [11], but as the area of the  $\sim 20km$  sphere is  $\sim 5 \cdot 10^{13}cm^2$ , then the density of photons in the detector will be  $\sim 0.056\gamma/cm^2$ . Thus, we use mirrors to concentrate the amount of photons at an acceptable level. The concentrated light is collected by a PMT camera that divides the image into pixels (fig 3.6) and record the density of photons. We can thus obtain the longitudinal profile of the showers.

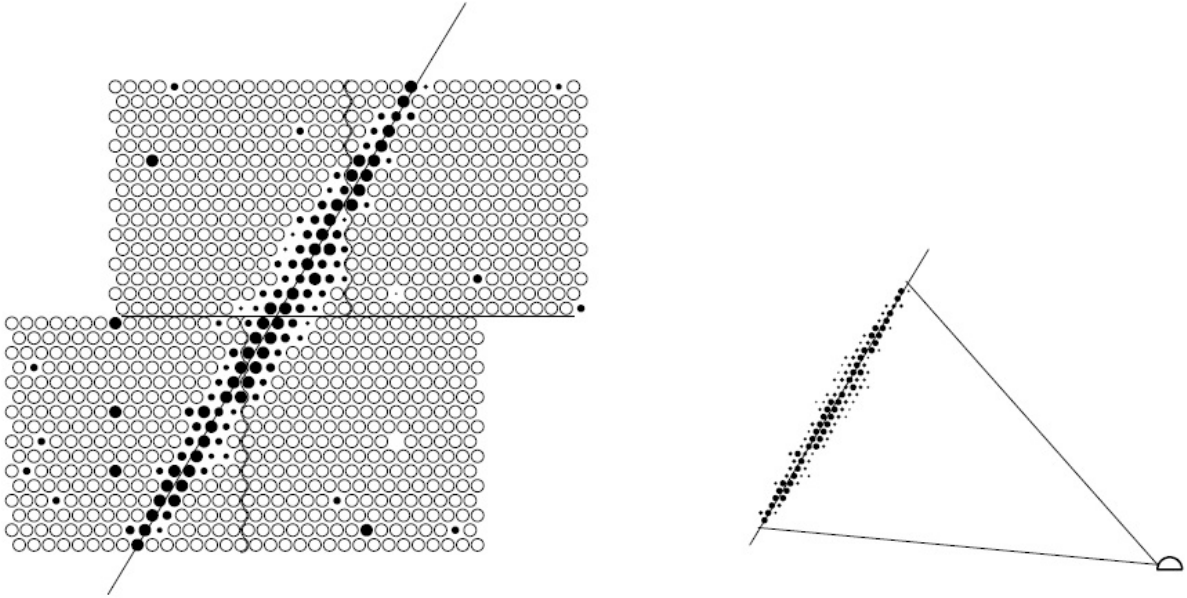


Figure 3.6: Schematic representation of the image of a detection of a shower in a FD telescope. [11]

The detector sees the shower as a point moving at the speed of light in the atmosphere. In order to take the longitudinal profile, it is necessary to reconstruct the geometry of the event. The first step is to define the shower-detector plane (SDP). If two detectors observe the event, we have a stereoscopic reconstruction of the EAS and the axis corresponds to the intersection of the SDP of both detectors. If only one detector has observed the event, then it is more complicated to determine the geometry, but knowing the SDP and the time of arrival is possible to recover the trajectory of showers along the SDP. For example, at 20km, the EAS takes about  $2.3\mu s$  to cross about 700m ( $\sim 2^\circ$  in the chamber), if the shower is 10km takes half the time for that route.

After knowing the geometry, as fluorescence emission is isotropic, then we know the amount of photons that passes through the atmosphere towards the detector, in addition we also account for the Rayleigh and Mie attenuation for these photons, and also direct Cherenkov and indirect Cherenkov (Cherenkov diffused by Rayleigh). All this is subtracted from the signal at a given the geometry. At this stage it is very important to know exactly the conditions of the atmosphere. After the reconstruction, we know the longitudinal profile in  $dE/dX$  and number of charge particles, the  $N_{max}$  and  $X_{max}$ .

To know the energy of primary particle, we have  $E_p = \alpha \int_0^\infty N_e(X)dX$ , where the constant is  $\alpha \sim 2.2MeV/g/cm^2$  [11] and expresses the average ionization energy loss rate for the shower. The value of the constant is the energy losses of the shower particles in atmosphere but it came mainly from electron, positrons and gammas while hadrons, muons, neutrinos hardly excite the air producing fluorescence radiation. This mean that same part of the primary energy will not excite the air and it continues in the hadronic and muonic component until the ground. So the total energy integrated will be approximately 90% of the primaries energy, the

remaining energy is called the missing energy. The missing energy is calculated by Monte Carlo simulation and is therefore dependent on the model. Moreover, it still depends on the composition of the primary particle (figure 3.5b). We can see that for higher energies the quantity of missing energy is less, this is due to the fact that the primary particle has more energy, then the pions also have more energy and therefore will interact to create more electromagnetic component. If the energy of pions is lower, they would decay into muons and neutrinos, which would leave more energy undetected. For larger nuclei than the proton occurs the same. Another feature is that the energy per nucleon for iron for example is lower than for protons (considering the same energy of primary particle), so iron shower will have more muons. This effect vanishes for higher energies.

The biggest problem with this method is that only runs on moonless nights and good weather, which leads to a duty cycle of  $\sim 10\%$ .

An experience of this type is the High Resolution Fly's Eye detector (HiRes). HiRes is located on hilltops above the desert in Utah, USA and operated from 1981 to 1993. In the initial phase, the detector, consisted of 67 spherical mirrors with  $\sim 1.6m$  in diameter and between 12 to 14 PMTs each, with a total of 880 PMTs. The PMTs have a time resolution of 25ns. With this system the detector covered the entire sky (each PMT was  $5^\circ \times 5^\circ$  of the sky). Later in 1986, has installed a second detector with 36 mirrors at 3.4km away from the original to make stereoscopic reconstructions. Until the Pierre Auger Observatory (PAO), this was the most important experience of this type.

### 3.4.1.8 EAS detection in other frequencies

The EAS also can be study at radio frequencies. It is believed that radio waves have geosynchronous origin. When the electron-positron pairs propagate in the atmosphere, they feel the Earth's magnetic field, which curve the trajectories in the opposite direction, this creates an electric dipole that propagates at the speed of light and generate radio waves with  $\sim 100MHz$ . The atmosphere is very clean for these frequencies and the detectors can be very effective in detection, even so we can not use them for themselves but as a complement to other methods. Electric storms may overlap measurements. One example is the Low-Frequency Array (LOFAR) in Nederland.

Another area which is currently being study for possible detection, is in the microwave. These come from the plasma in the atmosphere created by the passage of EAS (is not seen yet).

## 3.4.2 Ground array

The experiences of the ground arrays type, measure the particles of the EAS that reach the ground, where the system is installed. The altitude where these detectors are installed, depend on energy to be measured. If we want to measure energies of  $10^{15}eV$ , we can not put detectors at sea level since they would detect very few particles. If the altitude was high, we could be above  $X_{max}$  development of the EAS of UHECR and therefore we would not be sensitive to these showers. Typically, the detectors are scintillators and/or Cherenkov tank that allow us to detect photons, electrons, muons and hadrons and are spread at regular distances in a region.

In figure 3.7, is represented a possible event where each number expresses the density of particles detected by each of the detectors. The circles joins detectors with the same density and  $x$  represents the core of the shower. If the event is vertical, we can fit the lateral profile with the equation 3.14, however, for events oblique need to know the geometry of events, because the lateral profiles are perpendicular to the propagation.

To obtain the geometry, at first, we can consider that the EAS propagates as a front of particles with the shape of a flat disc, relatively thin. Thus, the detection time difference between consecutive detectors would give us the geometry. If this was so simple we would need only three detectors to determine the direction. But, as shown in the figure 3.7, the front of the EAS is curved instead of flat and its thickness increases with distance from the axis of the event. Fluctuations in the tanks further away from the core will increase and there is still the background from particle simultaneously detected with the EAS. Each experiment uses different parametrizations for these effects in reconstruction and they depend on the installed structure. To find the geometry, we fit the parametrizations for all points and we ignore the points with worse  $\chi^2$  until the solution stabilizes. Do not forget that there are no completely analytical models for the distributions and so it is necessary to use Monte Carlo to predict the results.

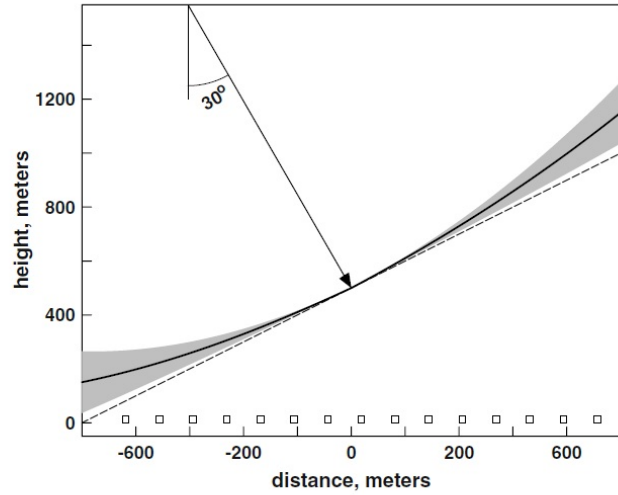
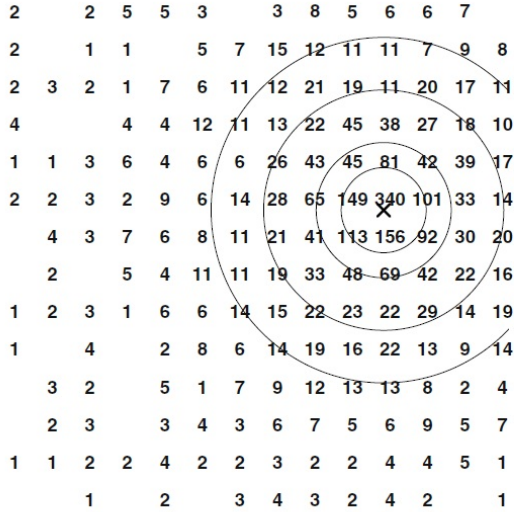


Figure 3.7: In left we have a scheme of a ground array with a detected event. The numbers are the intensity of the signal in each detector, which circles equals density and since the signal fluctuate with Gaussian distribution, some detectors are not triggered. In right, we have a scheme of a plane front in dashed line, in the grey shadow we have a realistic front and in the black line curved front.[11]

With the geometry established we obtain a lateral profile, and then we can estimate the energy of primary particle and composition, it will be related to the relative abundance between electrons and muons. Although it is not possible to recover the longitudinal profile, currently, we study the muon distribution profile taking into account the arrival time of muons.

This method is also dependent on hadronic models in Monte Carlo, as in the case of fluorescence methods. The advantage of this method compared to previous ones is that does not depend on the parameters of the atmosphere or background light, having a duty cycle of 100%.

One of the most important experiences of this type was the Akeno Giant Air Shower Array (AGASA), operated by the Institute for Cosmic Ray Research, University of Tokyo at the Akeno Observatory, in Japan. It covered an area of  $100km^2$  and consisted of 111 surface detectors for electrons and 27 detectors under absorbers for muon. The detectors were spaced with 1 km and as HiRes, it allowed the study of the end of the CR spectrum.

## Chapter 4

# Hadronic models

The ultra-energetic cosmic rays (UHECR) are mainly hadrons that interact with the atmosphere. Thus, the hadronic interactions are very important being the first to occur in the development of a cascade, they may alter considerably the shape of the longitudinal and lateral shower distribution of particles. The biggest problem is that the shower develops forward, ie in the regime of forward physics, which the theory can not describe and accelerators can't give us data. To make it even more difficult, the energies that occur in cosmic rays are several orders of magnitude higher than in accelerators, ie well above the available data. The models of these interactions, have to make extrapolations and cosmic rays results are sometimes contradictory.

In this section we'll talk a little about the models used in Monte Carlo simulations to describe the hadronic interactions. I'll start to see the hadronic interactions in terms of perturbative (QCD), and then talk about some of the foundations of phenomenology of the models and compare the results in comic rays with various models.

### 4.1 Introduction

A very important process in the study of QCD is the Deep Inelastic Scattering (DIS). This consists of scattering of a lepton by a hadron. In figure 4.1a), the DIS is represented and we should set the following variables:

$$q = k - k'; \quad Q^2 = -q^2; \quad \nu = \frac{p \cdot q}{M}; \quad x = \frac{Q^2}{2p \cdot q}; \quad (4.1)$$

where,  $Q^2$  is the momentum transferred in the reaction and  $x$  is the momentum fraction of the parton (inside the hadron) that interacts. We can distinguish different regimes depending on the value of  $Q^2$ . At very low  $Q^2$ , the photon exchanged at DIS has a resolution too small ( $1/Q^2$  is too big) and hadrons are seen as point particles. In this regime, Mott equations works. With increasing  $Q^2$ , the resolution  $1/Q^2$  increases (the Mott cross section is less true) and the hadrons appear as particles with finite size. In this context, most interactions are elastic, but now we can study some features of hadrons through the Rosenbluth cross section (see [45]). The most interesting thing occurs when the energy increases further. In this regime, with  $(p + q)^2 = -Q^2 + 2\nu + M^2 \gg M^2$  the resolution allows studying the internal constitution of hadrons, the cross section is dominated by inelastic interactions (with the destruction of the initial hadrons). The great importance of that process, is that we only need the energy of initial and final lepton and the mass of the hadron to know all variables in Eq 4.1. To study the cross section of this process we need to calculate the amplitude of the process, as we do not know the structure of hadrons (in figure 4.1a as a circle) then we parametrize it by the most general symmetric tensor  $W^{\mu\nu}$ . The amplitude is given by:

$$|\bar{M}|^2 = \frac{e^4}{q^4} L_{\mu\nu} W^{\mu\nu} \quad (4.2)$$

$L_{\mu\nu}$  is the leptonic tensor of QED. Then, with the generalization  $W^{\mu\nu} = -W_1 g^{\mu\nu} + \frac{W_2}{M^2} p^\mu p^\nu + \frac{W_3}{M^2} q^\mu q^\nu + \frac{W_4}{M^2} (p^\mu q^\nu + q^\mu p^\nu)$ , we can simplify the cross section in term of  $W_i$  (see [45]). One of the most important DIS

experiment was held at SLAC [66] in the 60s, which gives them the Nobel Prize at 1990 (see fig. 4.2a). Here they found the Bjorken scaling, where the form factors ( $F_1(x)$  and  $F_2(x)$ ) don't depend on  $Q^2$  but only on  $x$ . The form factors comes from the contraction of the previous amplitude and it contains the information about the structure of the proton. By the time, Bjorken and Feynman created the parton model which serve as the basis for QCD, and we have  $F_2(x) = 2xF_1(x) = \nu W_2(x) = \sum_i f_i^h(x) e_i^2 x$ , where  $f_i^h(x)$  is the distribution function of the parton  $i$  with charge  $e_i$ . In this model, the proton was constituted by partons (fermions with electric charge that interacts with strong force). Since partons are point-like particle and loosely bound, it is easy to obtain Bjorken scaling, however the DIS experiments say that these partons only carry  $\sim 54\%$  of the total energy. The QCD solved this problem with the gluon vector boson. The gluons are exchanged between the quarks (previously partons) mediating the strong force. The gluons can also fluctuate producing quark anti-quark pairs (called the sea quarks). Since they can have arbitrary moment, therefore it can be created quarks of any family but they exists in very small time scales. So  $\sim 46\%$  of the energy is in the sea quarks more gluons, and the previous  $\sim 54\%$  are the valence quarks. Each hadron has 3 valence quarks and DIS form factor can give us the parton distribution function (PDF)  $f_i^h(x)$  (for further detail see [45])

### 4.1.1 Asymptotic freedom and confinement

The Bjorken Scaling is easily obtained considering that quarks are loosely bound, but if the gluons exchanged between them take about 46% of total moment (directly or indirectly), this suggests that the interactions between quarks are really important.

The QED is also a quantum field theory like QCD. So if you think now in an electric charge in a vacuum, we know from QED that the electron radiates photons constantly and they will produce electron-positron pairs. The positrons are attracted towards the electron (opposite charges attract each other) and the electrons will be repelled. This causes that the vacuum will be polarized around the electron as a dielectric, causing an effect of screening. Basically, if we measure the charge, the effect of screening causes the increase of measured charge as we approach the electron. If the charge increases then the coupling constant increases. Closer to the electron the virtuality  $Q^2$  is higher and so the electromagnetic coupling constant increases with energy. In the case of QCD, quarks will emit gluons which in turn emit  $q - \bar{q}$  pairs, in addition to these, the gluons can also produce more gluons (increasing the effect). The big difference here is that the quarks with the same color attract each other, it creates an anti-screening, ie if we measure the actual color of a quark, as we walk away we would see an increasing amount of color. As the strong force is greater, then this effect dominates and the coupling constant increases with distance, which is the same as decrease virtuality or energy. The coupling constant  $\alpha_S$  of strong force with a loop is given by:

$$\alpha_S(\mu^2) = \frac{4\pi}{(11 - \frac{2}{3}n_f) \log \frac{\mu^2}{\Lambda_{QCD}^2}} \quad (4.3)$$

where  $n_f$  is the number of quark flavours and  $\Lambda_{QCD}^2$  is the scale bellow the coupling constant diverges. Experimentally,  $\Lambda_{QCD} \sim 200 MeV$  and tells us the typical time scale of strong interactions (using the Heisenberg's Uncertainty relation):  $T_S \sim \frac{1}{\Lambda_{QCD}}$ . Most of the gluon virtualities will be of this order, with many gluons inside the hadron, due to the intensity of the strong force. In DIS experiments, we are in a regime of high virtualities (greater than GeV) and therefore the time scale of interaction between the virtual photon and the quark is  $T_{int} \sim 1/Q$  ( $Q$  is the virtuality of photon). If  $T_{int} \ll T_s$ , then the process of scattering occurs at a time scale much smaller than the scale of the strong force and quarks can thus be viewed as loosely bound partons (the initial assumption of the parton model is correct). This phenomenon is called asymptotic freedom. We should note that if the virtualities were low, the coupling constant would increase and diverge (for low  $Q^2$ ) and this is the big problem of QCD.

Finally, another interesting phenomenon is that if we have a quark pair (with the sum of colours equal to zero) and try to separate the two quarks then the observed color in each one will increase (by the anti-screening effect). If the color around quarks increases, the coupling constant also increases and hence the potential energy grows very quickly. If we continue to increase the distance between the quarks we get to a point where the potential energy is enough to produce real quarks. These new quarks bind to old quarks creating two sets of diquarks without color. This make it impossible to have single free quarks or hadrons with color in nature (they have never been detected). This is called confinement.

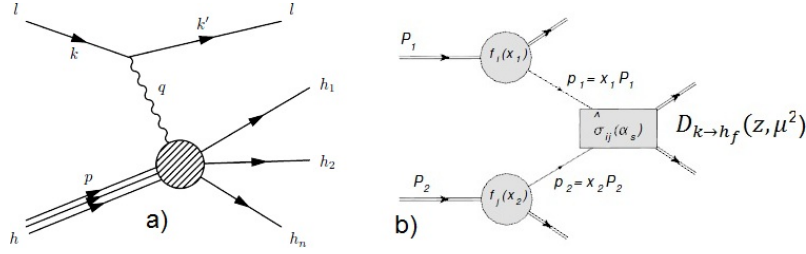


Figure 4.1: a) Deep inelastic scattering within the parton model, b) hadron-hadron interaction in QCD.

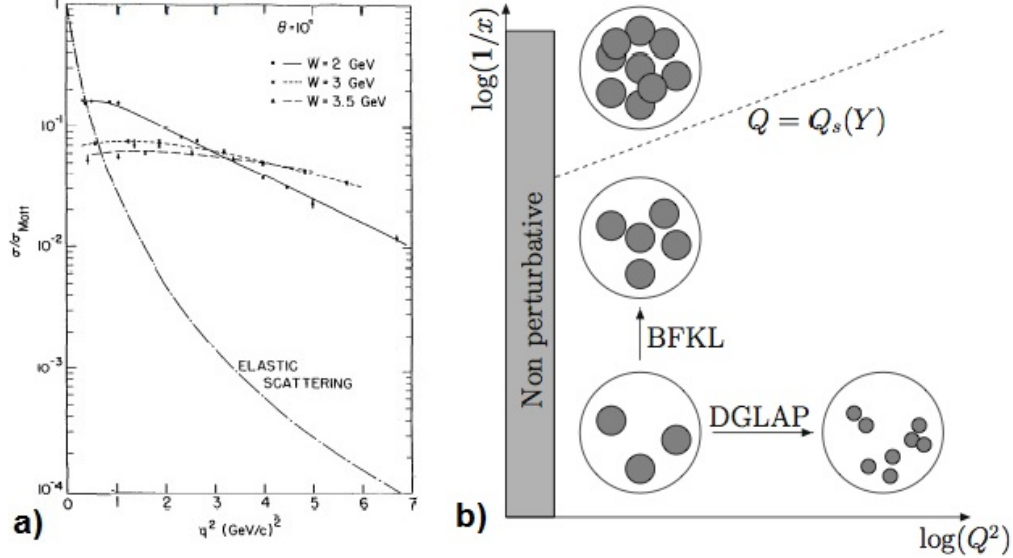


Figure 4.2: a) first result from slac for DIS, the  $\sigma/\sigma_{Mott}$  is proportional to the form factor, then we see the Bjorken scaling with  $q^2$ . [66] b) representation of the proton in the phase space  $(Q^2, x)$  with the DGLAP and BFKL evolutions, above  $Q = Q_s(Y)$  the size of the partons are bigger than the total size of the proton, and then we need non-linear effects of superposition of parton wave function.

## 4.2 Hadronic Interaction

At high energies, what happens when a proton interacts with another proton in an accelerator or when a cosmic ray interacts with atoms in the atmosphere is highly dependent on how they interact. The way to study these interactions relies heavily on energy and impact parameter between hadrons and is not always possible to directly use quantum chromodynamics. With QCD, we have the vertices of interaction, ie we have probabilities of interaction and from DIS we have the distribution functions of partons in protons, so we would expect that we can calculate cross sections and other quantities (this is the hard regime). However, it is not possible to solve exactly the QCD equations, but it is possible to do perturbation theory as in QED, since the coupling constant of the strong force is small we can neglect higher order terms. The problem happens when  $Q^2 \approx \Lambda_{QCD}^2 \rightarrow \alpha_s \approx 1$ , in this case, we can not disregard the higher order terms, and therefore we can not use pQCD. This is the soft regime, which is based on Gribov-Regge theory. The hard cases, should have an impact parameter much smaller than the soft one.

### 4.2.1 Evolution Equations

In the previous section, we considered that the quarks were practically free in the DIS experiments, however, despite the asymptotic freedom, the coupling constant only decreases logarithmically with increasing energy.

The quarks are not completely free. This causes a violation of Bjorken scaling and there is a small dependence of the structure functions with  $Q^2$ . This variation can be predicted by pQCD and it is very important for testing the theory.

In this context, the way we see a proton changes with transferred energy  $Q^2$  and the energy of the proton relatively to the center mass frame. As we can see in figure 4.2b), for low  $Q^2$  and energy (still in the perturbative regime) the proton is viewed as consisting of three quarks. Around this three quarks there are very weak fluctuations (like in the vacuum) producing  $q - \bar{q}$  pairs and gluons. By enhancing the  $Q^2$ , we improve the resolution with which we look to the proton and so we start to see more and more of these fluctuations, increasing the number of quarks. However, the density of partons decreases, since the size of partons is falling faster than the increase in the number of quarks. The number of partons increases with the  $Q^2$  logarithm, while the size decreases with  $1/Q^2$ . We can conclude that what was once a quark is now a set of quarks that are very close. These type of evolution equations is obtained by DGLAP (Dokshitzer, Gribov, Lipatov, Altarelli and Parisi).

If we increase the energy by keeping the value of  $Q^2$  constant, the number of partons grows very quickly, but the resolution size remains the same and then the density of partons becomes ever greater. The equations BFKL (Balitsky, Fadin, Kuraev and Lipatov) represent this evolution.

This growth was observed in HERA, however, due to the finite size of protons, the number of partons can not grow indefinitely, then we will have a saturation level  $Q_s$ . Above this scale we have overlap between partons and recombination or multiple diffusion, so we need nonlinear effects that are far from being understood. The formalism to describe this latest scheme is called Colour Glass Condensate.

## 4.2.2 Perturbative QCD

Perturbative QCD is based on the existence of asymptotic freedom, ie, because the coupling constant decreases for small distances, we can use perturbation theory. We can use the theory in situations where we have large energy transfers or in which the distances between partons are small. As mentioned, a large energy transfer means that the time scale of interaction is very small and we can ignore the other spectator partons. The cross section of two hadrons interacting (called inclusive cross section) can be factorized into several terms (figure 4.1b)) and has the form:

$$\sigma_{incl}^{h_1, h_2}(P_1, P_2) = \sum_{i,j,k} \int dx_1 dx_2 f_i^{h_1}(x_i, \mu^2) f_j^{h_2}(x_j, \mu^2) \hat{\sigma}_{i,j}(x_i P_1, x_j P_2, Q^2/\mu^2) D_{k \rightarrow h_f}(z, \mu^2) \quad (4.4)$$

where  $f_i^{h_1}$  is the PDF for the hadron  $h_1$  with total momentum  $P_1$  in order to momentum fraction  $x_i$  of parton  $i$  that interacts. As we do not know exactly the quarks moment in question, we integrate over the all distributions  $f_i^{h_k}(x_k, \mu^2)$ , where  $\mu^2$  is the factorization scale at which the PDFs are defined. This represents the initial conditions considering that the partons inside one hadron are independent from the others hadron's parton.  $\hat{\sigma}_{i,j}$  is the short distance (perturbative) cross-section for the interaction between the two partons. It depends on the momentum fraction of the parton  $x_i P_k$  and energy transferred between them. It can be computed using the Feynman rules for QCD. Some processes occur at tree level, while others are only possible at higher order of  $\alpha_s$ , just as in QED calculations. The question is that it can only be used in the perturbative regime.

Finally,  $D_{k \rightarrow h_f}(z, \mu^2)$  represents the hadronization of a final parton  $k$  to a hadron  $h$  of the final state carrying the fraction  $z$  of the parton momentum  $k$ , at the energy scale of  $Q^2$ . This is described by fragmentations functions, however, we should note that this occurs in the non perturbative regime and is therefore not possible to calculate from first principles, being obtained experimentally. The hadron-hadron interaction (such as proton-proton) are very complex, so hadronization is usually studied through the process of  $e^+e^-$  annihilation with the production of  $q - \bar{q}$  pairs. Since it is a purely non-perturbative process that happens at the  $Q_0$  scale and for which there are only models. Several models exists, of which the most successful ones are the (Lund) String model and the Cluster model based on which Monte Carlo simulation programs were build.

Despite the possible calculations, at high energies ( $\sqrt{s} \gg 10 GeV$ ) the inclusive cross section in proton-(anti)proton scattering exceeds the total one. This is due to the multiple scattering reactions and to include

this multiple reaction, we need an eikonalization of the form [46]:

$$\sigma_{inel}^{h_1, h_2}(s) = \int d^2b \{1 - \exp(-A(b)\sigma_{incl}^{h_1, h_2}(s))\} = \Sigma \sigma_m^{h_1, h_2}(s) \quad (4.5)$$

with  $\sigma_m^{h_1, h_2}(s)$  being the cross section for  $m$  scatterings,  $A(b)$  the proton-proton overlap function of the two profiles and:

$$\sigma_m^{h_1, h_2}(s) = \int d^2b \frac{(A(b)\sigma_{incl}^{h_1, h_2}(s))^m}{m!} \exp(-A(b)\sigma_{incl}^{h_1, h_2}(s)) \quad (4.6)$$

This picture, can recover the data results but we don't have any clue how to proceed for nucleos-nucleos collisions.

### 4.2.3 Soft interaction

In the regime where perturbation theory can not be used, we utilize phenomenological hadronic models based on the Gribov-Regge theory (GRT)[46][47]. The soft interactions with low  $Q^2$  are the interactions with a large impact parameter, far from pQCD. Thus, we can not have interactions according to the vertices of QCD (can not have an exchange of gluons or partons), since the confinement will not allow that a gluon or a parton could leave the first hadron to the second (it won't have enough energy). But is an interaction, something has to be exchanged, so it's considered that it exchanges pomerons, imaginary particles that have the vacuum quantum numbers (basically no color), like pions or glueballs.

According to the optical theorem we have  $\sigma_{tot} = \frac{1}{2s} 2ImT(s, t)$  where  $s$  and  $t$  are the Mandelstam variables and  $T$  is the elastic amplitude parametrize by (ref. [46]):

$$T(s, t) \sim i s^{\alpha_0 + \alpha' t} \quad (4.7)$$

with few parameters, where  $\alpha_0$  is the intersect and  $\alpha'$  is the slope of regge trajectory. The inelastic cross section is:

$$\sigma_{inel}^{h_1 h_2} = \int d^2b \{1 - \exp(-G(s, b))\} \quad (4.8)$$

$G(s, b)$  is the eikonal proportional to the Fourier transform of  $T(s, t)$ .

Interactions with soft pomerons are also known as diffractive processes. We have to refer that to include the jet production we need to include equation 4.4 in the GRT approach called GRT+minijets. However, the eikonalized parton model and GRT+minijets in the end are almost the same thing but with different starting point.

The models have introduced semi-hard interactions, since in an interaction viewed as a ladder or a cascade (see next section) some part of the cascade can develop in low virtualities parametrized by the soft pomeron and partly develops at high virtuality region (with pQCD). In this way, we can consider that ladder/cascade as one pomeron.

### 4.2.4 Parton ladder and multi-scattering

As we can only use pQCD above a threshold in  $Q^2$ , then the hadronic models treat these interactions as the exchange of hadrons parton ladder (figure 4.3a). These diagrams represent the perturbative interaction or hard. In newer models, it is considered that the parton ladder corresponds to an hard component and a soft component (b and c). This is due to the fact that even in high energy we can have peripheral interactions that have low virtualities.

The partons interact and leave behind remnant particles from the original two hadrons (figure 4.3a and 4.4a). Thus we have three types of origin of the particles, they may come from the target or projectile (outer Contributions), and they may originate from the ladders (inner Contributions). In figure 4.4 b, is depicts the two contributions in various experiments.

One can also consider the splitting of the ladder. The ladder will be re-scattered with the hadrons. This process can be elastic or inelastic (figure 4.3). The elastic part will make a screening effect decreasing the cross section, while the inelastic will greatly increase the number of particles produced. The ladder can be closed,

ie it is as if there were two ladders, with opposite effect, not altering the constitution of original hadrons. This ladder is very important because it makes a major contribution to effective elastic cross section. In the calculations of cross sections, for the same number of inelastic scattering, we must account any number of elastic multi-scattering, which leave the same final result.

The effects of multi scattering are present in the above description but not consistently because the energy shared between many pomerons is taken into account, but the energy conservations is not taken care in a consistent way in the cross section calculations.

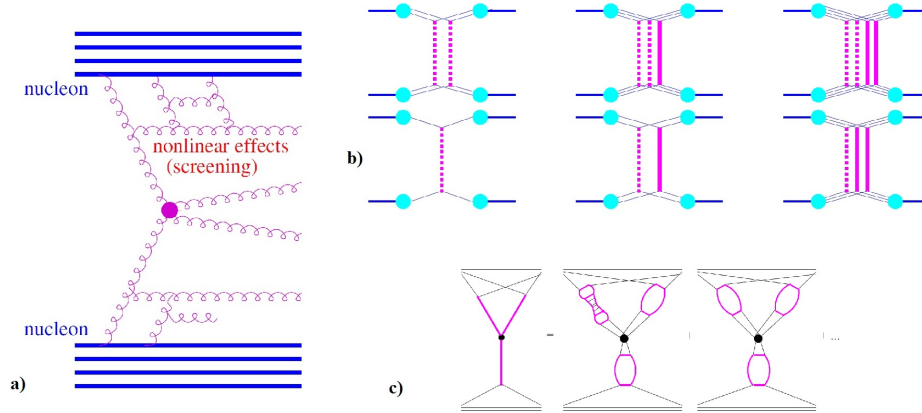


Figure 4.3: a)representation of an elementary interaction (in EPOS), we can see closed parton ladders (providing screening) and open parton ladders [48], b) multiscattering in EPOS, above one inelastic interaction (cut pomeron) with various numbers of inelastic interactions (uncut pomeron), in EPOS, for each cut pomeron we have to sum all terms with different uncut pomerons that have the same final result [49]. In QGSJET-II we have re-scattering of the pomeron, and we can have a triple pomeron vertex represented in c), with the contributions of soft and semi-hard pomerons [50].

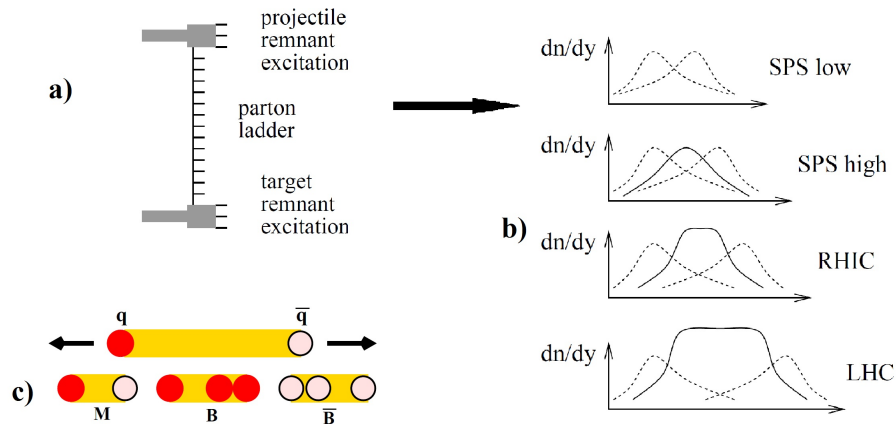


Figure 4.4: a) representation of the origin of produced particles. Some particles come from the projectile and target (outer contribution), and from the ladder (inner contribution). b) The inner and outer contribution (full and dashed lines respectively) for several experiments, the inner part grows with energy (since pQCD is more important and mini-jet cross-section can be used) [52]. c) particle production representation within string model [53].

## 4.2.5 String model

After having calculated the interactions, the ladder and pomerons will break up producing particles, and the partons spectators too. The model most used in the hadronic codes for hadronic interactions calculation is the model of the strings[49] (and see detail in [51]). Basically, different quarks that are moving create a color field between each other called string. If these quarks move apart, then the potential energy of the string will increase. This is due to the confinement effect. With increasing distances between quarks, the potential energy increases and then we could have energy to create new quarks, which will move apart again until new production. We can create pairs quark-antiquark or diquark-anti diquark, producing meson or barions respectively. In figure 4.4c) are represented string breaks in  $e^-e^+$  annihilation in virtual photon, that decay into  $q - \bar{q}$  pair.

## 4.2.6 Glauber formalism

One way to extrapolate data from accelerators is through the Glauber formalism [54] (figure 4.5). He noted that the scattering amplitude as a function of impact parameter and energy in the center of mass can be viewed similarly to a diffraction in optics, using a change phase relation:

$$a(s, b) = 1 - e^{i\chi(s, b)} \quad (4.9)$$

where  $a(s, b)$  is the Fourier transformation of the elastic amplitude (previously denoted in eq.4.7 by  $T(s, t)$ ),  $s$  is the energy in the center of mass,  $b$  the impact parameter and  $\chi$  the eikonal function (like previously seen). For multi-scattering (hadron-nucleus A) we have:

$$\begin{aligned} a_{hA}(s, b) &= 1 - e^{i\chi_{mult}(s, b)} \\ &= 1 - e^{i\sum_j \chi_j(s, b)} = 1 - \prod_j e^{i\chi_j(s, b)} = 1 - \prod_j (1 - a_j(s, b_j)) \end{aligned} \quad (4.10)$$

where  $\chi_{mult}$  is the sum of each phase sifts  $\chi_j(s, b)$  for each scattering nucleon, so that  $j$  is the sum over all nucleons A. The total cross section is then:

$$\sigma_{tot}^{hA} = 2Re \int \Gamma_{hA}(\vec{b}) d^2b \quad (4.11)$$

and  $\Gamma_{hA}(\vec{b}) = 1 - \prod_j^A [1 - \int a_j(\vec{b} - \vec{b}_j) \rho_j(\vec{r}_j) d^3r_j]$ , where we consider that the nucleons was not correlated so  $\psi * (\vec{r}_1, \dots, \vec{r}_A) \psi(\vec{r}_1, \dots, \vec{r}_A) = \prod_j^A \rho_j(\vec{r}_j)$ .  $\psi$  is the wave function of nucleons and  $\vec{r}_j$  is the position of nucleon  $j$  and  $\int \rho_j(\vec{r}_j) d^3r_j = 1$ . In the picture 4.8b) we see the proton-air cross section with a few data points of accelerators and their extrapolation to higher energies by Glauber and extrapolations of various models. The shadow in blue, represents the uncertainty of extrapolations.

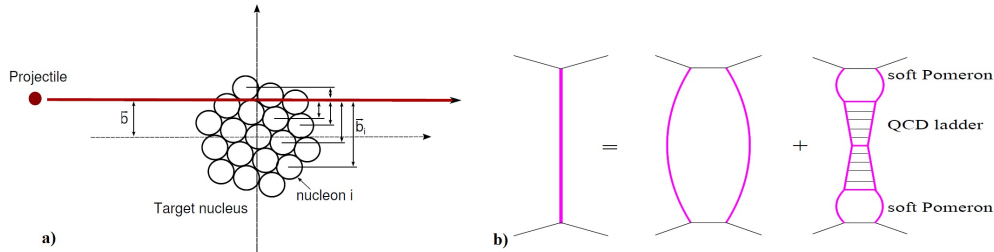


Figure 4.5: a) the picture represents a target hitting a nucleus with impact parameter  $b$  and we also have the relative impact parameter for each of the nucleons, most of the models consider individual separated nucleons in the interactions [54]. b) the general pomeron in QGSJET-II consists of a soft and a semi-hard pomeron [57].

### 4.3 Hadronic models

In this section, I will speak of the main hadron model in simulation of cosmic rays, as QGSJET-II, SIBYLL and EPOS. These models use the accelerators data to extrapolate to much higher energies, based on some physical assumptions. There are some problems in doing that. In accelerator, the physics studied have basically large transverse moments, while in cosmic ray the forward physics is very important (and little studied). In addition there are the problems of diffractive processes, where we do not have any true theory, which implies that the assumptions used in phenomenological models may not be the most certain. And finally we must extrapolate the data to several orders of magnitude higher.

One way to extrapolate data from accelerators is through the formalism of Glauber, see the previous section.

#### 4.3.1 QGSJET

The QGSJET model [55] [56] [50] appeared in the 90s based on the Quark-Gluon-String model (QGS model). The QGS model is a model based on GRT formalism and the eikonal of the probability of interaction between a hadron  $i$  and  $j$  is:

$$\chi_{ij}^P(s, b) = \frac{\gamma_i \gamma_j}{R_{ij}^2} \exp(\Delta y - \frac{b^2}{4R_{ij}^2}) \quad (4.12)$$

Where  $s$  is the energy of center of mass,  $b$  the impact parameter,  $\Delta = \alpha_p(0) - 1$ ,  $y = \ln s$  and  $R_{ij}^2 = R_i^2 + R_j^2 + \alpha'_p(0)y$ .  $\Delta$  and  $\alpha'_p(0)$  are parameters of the pomeron trajectory, while  $y$  and  $R$  are parameters to describe the vertices hadron-pomeron. The  $\chi_{ij}^P$  is the  $G(s, b)$  in equation 4.8, and parametrizes the soft interactions. These values are determined from experimental results.

The QGS had difficulty implementing minijets and then, the QGSJET (Quark-gluon string model with jets) was created to solve the problem. The QGSJET considers, in addition to the soft component (pomeron), one semi-hard component. In the model, for  $Q^2 < Q_0^2$ , it is used the non perturbative theory for pomerons. If  $Q^2 > Q_0^2$  is considered perturbative theory. The value is  $Q_0^2 = 2GeV$ . The eikonal approximation is now (see pomeron in figure 4.5b):

$$\sigma_{ij}(s, b) = \chi_{ij}^{soft}(s, b) + \chi_{ij}^{hard}(s, b) \quad (4.13)$$

where  $\chi_{ij}^{soft}(s, b)$  is the soft part given by the formula above and  $\chi_{ij}^{hard}(s, b)$  is the part of semi-hard. In the regime of the second term we have a cascade that partially develops with low virtuality and partly with high virtuality, then we have:

$$\chi_{ij}^{hard}(s, b) = r^2 \int dy_1 \int dy_2 \chi_{ij}^{soft}(e^{y_i+y_j}, b) \frac{1}{2} \sigma_{hard}(e^{y-y_1-y_2}, Q_0) \quad (4.14)$$

$y$  is the rapidity,  $y_1$  and  $y_2$  represent the extreme rapidity of the pomeron,  $\sigma_{hard}$  is the hard cross section and  $r^2$  is a fitting parameter related to the partons density. Therefore we get  $\chi_{ij}^{soft}$  for  $Q^2 < Q_0^2$  and  $\chi_{ij}$  for  $Q^2 > Q_0^2$ . The total cross section is given by:

$$\sigma_{ij}^{(tot)}(s) = \frac{1}{C_{ij}} \int d^2b \{1 - \exp[-C_{ij}(\chi_{ij}^{soft}(s, b) + \chi_{ij}^{hard}(s, b))]\} \quad (4.15)$$

$C_{ij}$  is the shower enhancement coefficient and takes the value  $C_{pp} = 1.5$ . We can also write the cross section in function of the number of  $n$  pomerons and  $m$  semihard block exchange in the interaction as:

$$\sigma_{ij}^{(n,m)}(s) = \frac{1}{C_{ij}} \int d^2b \left\{ \frac{(2C_{ij}\chi_{ij}^{soft}(s, b))^n}{n!} \times \frac{(2C_{ij}\chi_{ij}^{hard}(s, b))^m}{m!} \times \exp[-2C_{ij}(\chi_{ij}^{soft}(s, b) + \chi_{ij}^{hard}(s, b))] \right\} \quad (4.16)$$

The production of particles is obtained through the model of the strings.

The QGSJET was made with the assumption that the exchange of a parton ladders and pomerons occur independently. However, in the regime of high energies and small impact parameters there are many partons and therefore there are also many scattering processes, leading to the overlap and interaction of ladders and pomerons. These types of interactions are shown in figure 4.3c).

To introduce this nonlinear effects in QGSJET comes the QGSJET-II. Although it was considered that these

nonlinear effects occur mainly at low virtualities (ie  $Q^2 < Q_0^2$ ). This new model also includes parameterizations of realistic nuclear density of each nucleus and the parameters were updated with the latest results from HERA [56].

In references [56] and [58] we see the comparison between the latest and older version of QGSJET model. Since in this version there is interaction between pomerons, then the inelasticity will be lower because it is more likely to have elastic scattering (see fig. 4.6a). And as we do not have individual pomerons producing particles but rather the result of interaction between them, then we now have lower multiplicities. With lower multiplicities and inelasticities, particles with more energy will be produced. Thus are produced  $\pi^- \pi^+$  with more energy, so they are more likely to interact (because they live longer). If these pions interact, they will produce neutral and charged pions. The neutral pions (with a very short life) will decay into photons which in turn produce electrons. Thus, the showers produced with QGSJET-II will present a larger electronic component and a smaller muonic component than the version QGSJET-I.

### 4.3.2 SYBILL

The SYBILL model[59][60] is a model based on the Dual Parton Model (DPM) with minijet production superimposed. The current version is 2.1 which replaces the 1.7 version that could not reproduce many of the recent data. The 1.7 version had p-p cross sections with a larger increase than measured and for example on average the multiplicities are too low at high energies.

The DPM considers that nucleons consist of a quark and a diquark and thus, in a pp interaction, there is a gluon exchange between these two constituents (with the reorganization of color). With this, the quark/diquark combines with the quark/diquark of the other proton forming a string. Each string will then split up according to the string model, producing particles. The distribution of the quark in the nucleon as a function of the momentum fraction  $x$  is:

$$f_q(x) = \frac{(1-x)^\alpha}{(x^2 - \mu^2/s)^{1/4}} \quad (4.17)$$

Where  $\alpha = 3.0$  and  $\mu = 0.35 GeV$  is the effective mass of quark. The distribution of the diquark will be  $f_{qq}(x) = 1 - f_q(x)$ .

This was more or less the simplified model of DPM, however already in accelerators with energy in the center of mass around 100GeV, the model was not able to reproduce the high multiplicity, the increase of transverse momentum, the increase in transverse jets and increase in the central rapidity with energy. In order to solve these problems in the hard regime, the model is improved based on minijets with the cross section given by equation 4.4. The version 2.1 now uses the distributions results from HERA.

This cross section can not rise indefinitely with energy, because of the size of the proton. Thus, when the number of gluons/quarks multiplied by the resolution of the interaction ( $\sim 1/p_T$ ) is approximately equal to the size of the proton, we can not neglect the nonlinear effects and therefore in the model is considered that the cross section stops being valid. The minimum  $p_T$  where you can use the previous equations grows with energy. The 1.7 version used a cutoff  $p_T^{min} = \sqrt{5} GeV$ , where above this value we could use the minijet model. This cutoff independent of energy does not help to reproduce the data. So the new version has the cutoff:

$$p_T^{min}(s) = p_T^0 + \Lambda \exp(c\sqrt{\ln(s/GeV^2)}) \quad (4.18)$$

$p_T^0 = 1 GeV$ ,  $\Lambda = 0.0065 GeV$  and  $c = 0.9$ . This cut comes from geometric arguments based on the condition:

$$\frac{\alpha_s(p_T^2)}{p_T^2} \cdot xg(x, p_T^2) \leq \pi R_p^2 \quad (4.19)$$

$\alpha_s$  is the strong force coupling,  $g(x, p_T^2)$  is the gluon density and  $R_p$  is the proton radius. The  $g$  value is obtain by Hera results,  $g(x) \sim 1/x^{0.4}$  (the previous version uses  $\sim 1/x$ ). The minijet cross section (as was told before) quickly rises exceeding the total one, so the model consider that it is formed more than one minijet at a collision. The number of hard interaction is then  $n_{hard}(b, s) = A(b)\sigma_{QCD}(s)$  like we see in section 4.2.2,  $A(b)$  is the profile function. The cross section is then given by:

$$\begin{aligned} \sigma_{tot} &= 2\pi \int db^2 (1 - e^{-\chi(b,s)}) \\ \sigma_{ine} &= \pi \int db^2 (1 - e^{-2\chi(b,s)}) \end{aligned} \quad (4.20)$$

where the iekonal has the form:

$$\chi(b, s) = \chi_{hard}(b, s) + \chi_{soft}(b, s) \quad (4.21)$$

The hard iekonal is  $\chi_{hard}(b, s) = \frac{1}{2}n_{hard}(b, s)$ . In version 1.7, the soft part was  $\chi_{soft}(b) = \frac{1}{2}CA(b)$  (C is a parameter). In new version, to account for energy dependence, we have  $\chi_{soft}(b, s) = \frac{1}{2}A(b)\sigma_{soft}(s)$ , and:

$$\sigma_{soft}(s) = X\left(\frac{s}{s_0}\right)^{\Delta_{eff}} + Y\left(\frac{s}{s_0}\right)^{-\epsilon} \quad (4.22)$$

$\epsilon$  is a parameter for reggeon exchange and  $\Delta_{eff}$  parametrize in some way the subdivision of pomeron term into soft and hard component. All those parameters are fitted to the data. See fig. 4.6b) for compare the version 1.7 with 2.1. The nucleus-nucleus interaction still does not have the Glauber formalism completely implemented and needs to be improved.

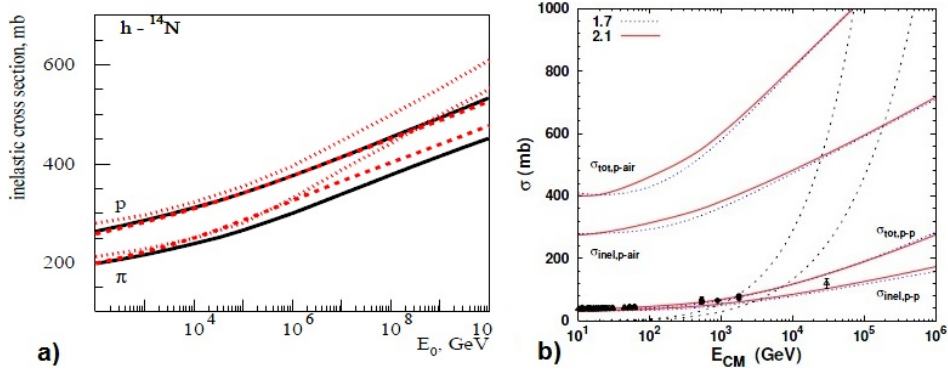


Figure 4.6: a) inelastic  $h-^{14}N$  cross-section for QGSJET-II, QGSJET and SYBILL (full, dashed, and dotted curves correspondingly).[58] b)The total and inelastic cross section of p-air and p-p for SYBILL, in red and dotted line if the version 2.1 and 1.7, and with dashed line the minijet cross section(which diverges).[60]

### 4.3.3 EPOS

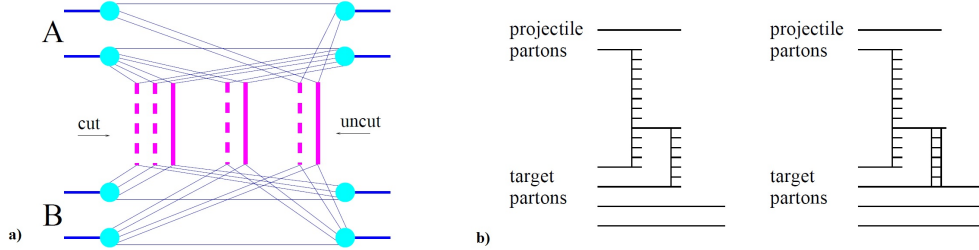


Figure 4.7: a) interaction between two nucleus with cut and uncut pomerons [49], b)Inelastic and elastic splitting of a parton ladder, i.e. a re-scattering of a parton from parton ladder with a second extra parton from the target [61].

EPOS [48][52] is a model founded on the parton based Gribov-Regge theory[46]. An elementary interactions is given by a parton ladder exchange. This parton ladder is a cascade of particles like in figure 4.3. At moderate energies, this ladder was considered to contain two parts: the hard part, where the cascade develops following pQCD, and the soft part where they follow the GRT. Like in the previous models, the soft amplitude is parametrized, and has the form:

$$T_{soft}(s, t) = 8\pi s_0 \eta \gamma_{part}^2 (s/s_0)^{\alpha_{soft}(0)} \exp(\lambda_{soft}^{(2)}(s/s_0)t) \quad (4.23)$$

with  $\lambda_{soft}^{(n)} = nR_{part}^2 + \alpha'_{soft} \ln z$ .  $\alpha_{soft}(0)$  and  $\alpha'_{soft}$  are the intercept and the slope of the pomeron trajectory,  $\gamma_{part}^2$  and  $R_{part}^2$  are the vertex value and the slope for the pomeron-parton coupling, and  $s_0 \simeq 1\text{GeV}$  like previous is the hadronic mass scale. The hard contribution follows the equation 4.4

The interesting feature of EPOS approach is the way it deals with multi-scattering. One of the problems of hadronic models is to treat consistently the energy conservation in interaction (principally in more than one). So EPOS has tried to consider energy conservation in each individual interaction, contrary to QGSJET that accounts for it in the end of the multi-scatter calculation, so there are no energy conservation between each interaction but only in the final result. This is due to the fact that, EPOS consider the interactions between partons whereas QGSJET considers the interactions between hadrons.

If we have an inelastic interaction (the cut pomeron at figure 4.7a) in dashed line) we have to sum the contribution of one elastic scattering (the uncut pomeron), two elastic scattering and so on, because the elastic interaction does not change the final state, but corrects the cross-section. If we had two or more inelastic interaction we follow the same thing. In this context, we define  $m$  as the number of inelastic interaction and for  $m=1$  we have  $x_1^+$  and  $x_1^-$  that is the traditional  $x$ , but referring to the two partons that interact from each hadron.

For nucleus-nucleus interaction we still have the  $m$  inelastic interaction, but now we have also the multi interaction coming from the various nucleus. Consider the nucleus A and B, we have  $X^- = \{x_{k,\mu}^-\}$  and  $X^+ = \{x_{k,\mu}^+\}$ , where we have  $k$  nucleons and  $\mu$  is the number of inelastic interaction in each nucleon (see fig. 4.7). In this way the inelastic cross section is:

$$\sigma_{inel}(s) = \Sigma_m \int db^2 \Omega_{AB}^{(s,b)}(m, X^+, X^-) \quad (4.24)$$

Here  $m$  is a vector like  $X^\pm$  and is  $m = m_k$ , where  $m_k$  is the number of inelastic interaction for each nucleon. Therefore in cross section we have to sum over all possible  $m$  inelastic interactions (with different final state). If we want a partial cross section we don't sum and  $\Omega_{AB}^{(s,b)}(m, X^+, X^-)$  is the probability of that reaction.

$$\Omega_{AB}^{(s,b)}(m, X^+, X^-) = \Pi_{k=1}^{AB} \left\{ \frac{1}{m_k!} \Pi_{\mu=1}^{m_k} G(x_{k,\mu}^+, x_{k,\mu}^-, s, b_k) \right\} \Phi_{AB}(x_{proj}, x_{targ}, s, b) \quad (4.25)$$

where  $\Phi_{AB}$  represents the sum over all elastic interactions (uncut pomerons, see ref. [46]).

When two parton interacts, we can have third parton very close so the parton ladder between the first two parton will split and interacts with the third one (figure 4.7). This effect increases with the mass of hadron/nucleus involved, since there will be a bigger chance to have some parton very close to the parton ladder. These ladders can be again elastic or inelastic (closed or open), the addition of closed ladder, in the splitting of the first ladder or in the ladder re-scattering will decrease the partial cross section. In hadronization we have to care that since one parton of the ladder is close to a parton of the splitting, and the splitting is attached to the original ladder, then we have to do a collective hadronization. Particle production are made within the string model approach.

### 4.3.4 Comparison between models

In this part, we will compare the models at the level of multiplicities, inelastic and cross sections, and the results obtained from air shower simulations. The models compared are QGSJET-II, Sybill 2.1 and EPOS 1.9.

#### 4.3.4.1 Cross section

In the figure 4.8, we can see the inelastic cross section and total one for several models compared with some data. In the total one, it is represented the uncertainty of the extrapolation of  $\sigma^{p-air}$  from accelerators within the Glauber formalism. The cross section is very important and can change many observables in CR. It's interesting to note, that the cross section for EPOS 1.6 is much higher than the version 1.9. This fact is due to the introduction of the non linear effect in the last version, i.e. the last version considers the re-scattering and multi-scattering with closed and open ladder. The closed ladder will decrease the partial

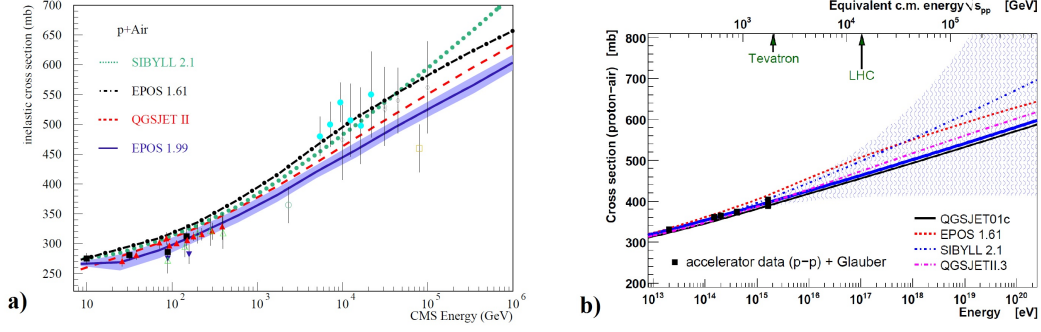


Figure 4.8: a) Inelastic cross section  $p - Air$  from [62]. b) Uncertainty of the extrapolation of  $p - Air$  cross section from accelerator to CR energies [54].

cross section and than the inelastic one decreases too. The QGSJET-II is lower too, since it also have the non-linear effects (due to saturation). The SIBYLL is a more simple model and is more dependent on minijet cross section, so it presents higher values that comes from the higher growth of the minijet cross section.

#### 4.3.4.2 Inelasticity and Multiplicity

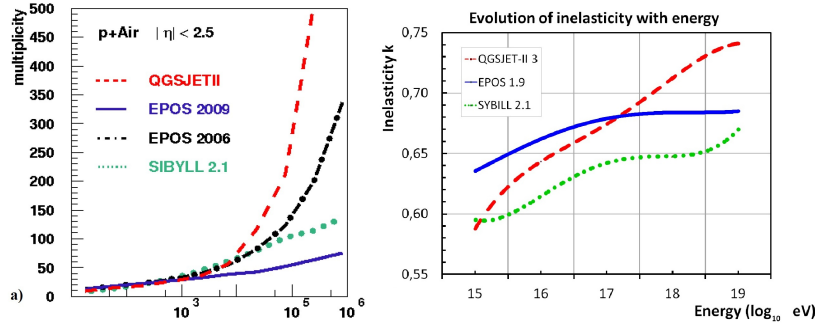


Figure 4.9: a) Multiplicity of the interactions from [62], b) inelasticity  $k$ .

The inelasticity ( $k$ ) is defined as  $k = 1 - \frac{E_L}{E_p}$ , with  $E_L$  being the energy of the most energetic particle (leading particle) produced in the reaction and  $E_p$  the energy of the primary particle. If the inelasticity is small, it means that the leading particle carries much energy, and can leave the shower to develop more deeply.

We can see the inelasticity for the three models in the figure 4.9b). The results are very close, but the QGSJET has the larger changes. In the graphic at low energy it has the smallest inelasticity, and at higher energies it has the higher inelasticity. This change is due to the non-linear screening corrections introduced in version II. In ref. [58], we can see the QGSJET version II compared with version I, and at smaller energies non-linear corrections will decrease the interaction inekonal reducing the inelasticity. At higher energy this effect is less important compared with a steeper parton momentum distribution.

The multiplicity is the number of particles produced in one interaction. If the inelasticity is high, the leading particle carries less energy and then the multiplicity should be high, but it is not completely necessary. In figure 4.9a), we can see that the QGSJET-II have a much higher multiplicity than the others models and so, the leading is less energetic (is energy has to be distributed for more particles). The new version of EPOS has a much lower multiplicity than the previous version and even the other models because the re-scattering with closed ladder decreases the production of particles, and so the leading can have high energy. The interesting case in SIBYLL is that it produces more particles than EPOS, but the leading particle is more energetic

than in EPOS. This is due to the fact that SIBYLL like many other models treats the first scattering much different from the subsequent process. First it makes the first interaction alone, and after that it makes the following scatters. We became with a less democratic distribution of energy in the produced particles, since many of them could go to the first scatter.

#### 4.3.4.3 Shower maximum

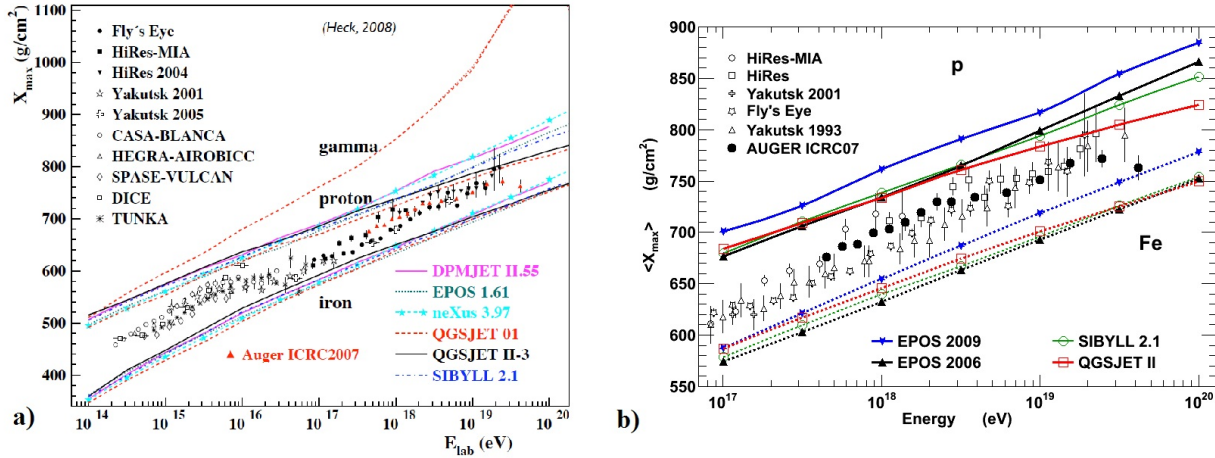


Figure 4.10: a)  $X_{max}$  for a wide energy range [63], b)  $X_{max}$  predictions from recent hadronic model at ultra high energy [62].

The results commented before, are the main variable that control the shower development. They give us if the shower develops quickly or slowly, and so more or less deeper, for example. In figure 4.10, we show the average shower maximum  $X_{max}$  obtained with the several hadronic models and compared to data. In left, we see the evolution of  $\langle X_{max} \rangle$  from  $10^{14} eV$  to  $10^{20} eV$ , like we said in section 2.1, the composition goes from light to heavier composition until ankle energy. After that, the composition becomes again lighter. From the result from simulation, we can see that the shower maximum is deeper for protons than iron at same energy, this is due to the fact that an iron CR with the same energy will divide that energy over it's nucleons, so each nucleon will have less energy and will travel less through atmosphere. Moreover, the iron with many nucleons, will produce a big number of particle, and then the shower develops quickly.

If we look at proton predictions, we can see that the EPOS 1.9 shower develops more deeply than version 1.6, it have a big  $\langle X_{max} \rangle$ . Since 1.9 EPOS has lower multiplicity, than the produced particles will have more energy, living more and travelling more into the atmosphere.

The QGSJET model has the higher multiplicities and inelasticities, then it produces many low energy particles, causing a quick shower development and as a result, it have the smallest  $X_{max}$ . For the same reason the EPOS have the bigger  $X_{max}$ .

#### 4.3.5 Muon and electron numbers

The muon number predicted by hadronic models is very important, since the energy reconstruction is based on the total energy deposit in atmosphere by the electromagnetic component and the muons practically do not deposit energy. If the muon number is higher, then total energy deposit will be smaller then the CR energy.

In the figure 4.11 a), we see that the number of muon is very different between the models. The EPOS is the model that produces more muons, it even produces more muons with a proton primary then the others two models for an iron primary. If this high value is correct it can change the results, from energy reconstruction to lateral profile studies. It's interesting to note that PAO claims a possible lack of muons in air showers

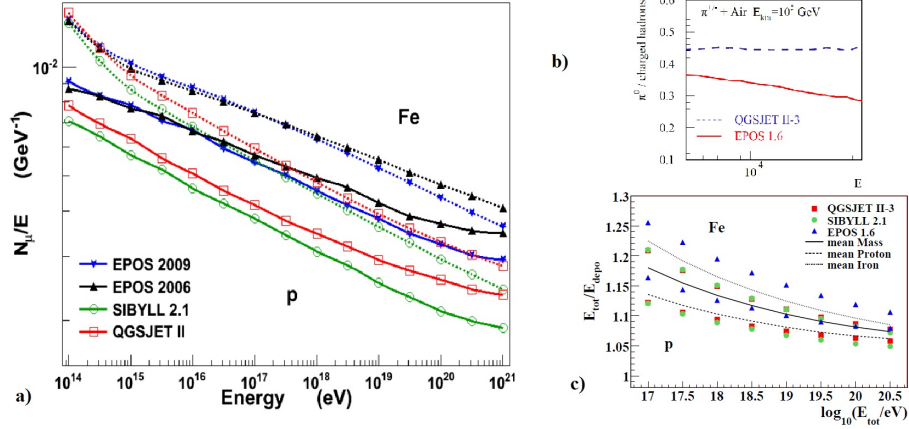


Figure 4.11: a) number of muon over energy for several models [62], b) ratio of  $\pi^0$  number over number of charge particles [61], c) total CR energy over energy deposit in atmosphere for several models [64].

simulated with the current hadronic interaction [61] (so EPOS could go in the good way).

The EPOS produces more muons because especially in  $\pi - Air$  interactions, it creates less  $\pi^0$  than the other models, since  $\pi^0$  feed the electromagnetic cascade, then EPOS makes a more important muonic component (from charge pions decay) than other models (see figure 4.11b)).

The EPOS muonic component is bigger and so the the fraction of CR energy that can be deposit in atmosphere will be smaller. In figure 4.11 c) is plotted the fraction between the total and the deposit energy as a function of energy. At  $10^{17}eV$  EPOS predicts that the original CR proton will have  $\sim 17\%$  more energy than the total energy deposit, while QGSJET and SIBYLL have  $\sim 13\%$  more. At energy higher this differences get less important (less than 10%), but it's crucial to have a good estimate of the missing energy into muonic component to make accurate energies reconstructions. With more muons, we could have higher energy reconstruction.

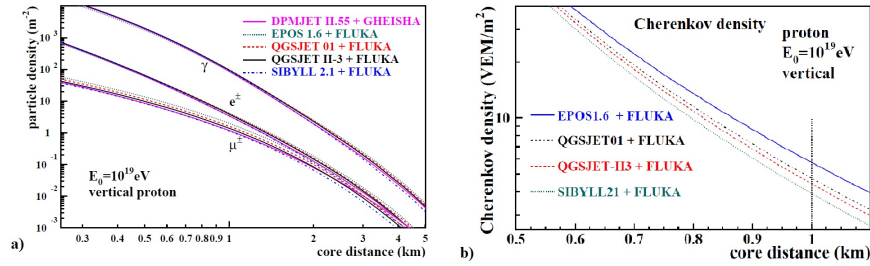


Figure 4.12: a) lateral profile for  $\gamma$ ,  $e^\pm$  and  $\mu^\pm$  [65], b) prediction of Cherenkov density in the tank for  $10^{19}eV$  vertical proton in function of distance [64].

Concerning the lateral profile (fig. 4.12) we see that  $\gamma$  and  $e^\pm$  have very similar result for the models, the only different more prominent is the number of muons as was been said. The density of muons at 1km shows an excess of about 30 to 40% from EPOS compared with QGSJET. This excess from EPOS could decrease the energy reconstructed from lateral densities.

## Chapter 5

# The Pierre Auger Observatory

The Pierre Auger Observatory (PAO), is the largest cosmic ray experiment at the present. The project was presented to the scientific community in 1992 by James Cronin and Alan Watson. The name of the observatory came from the French Physicist that discovered the EAS (chapter 1). It consists in two different zones, one in southern Argentina (The Southern Observatory) and another in USA (The Northern Observatory). In this chapter, we describe the Observatory and the current state of the results of ultra high energy cosmic ray (UHECR).

There was many reasons to built this experiment. For example, the results for the end of the spectrum were not consistent. In AGASA [67], there was an overflow, while in HiRes there was a smaller flux consistent with the GZK effect [69]. But the error bars could accept both values, since for very high energies there is a very low statistics. It was also not possible to do a statistical analysis for other matters as the composition, sources and study of anisotropy and intergalactic magnetic fields. With this experiment, it was expected about 30 events per year at energies of  $10^{20} eV$ .

The Southern Observatory is located on Pampa Amarilla, next to Mallargue, Province of Mendoza, Argentina ( $35^\circ$  South). While the Northern is to be located at Lamar, Colorado, USA ( $38^\circ$  North). With these two locations, we can cover the full sky. PAO, uses a hybrid technique, where we incorporate the two most successful past techniques, the fluorescence detector (FD) and the surface detector (SD).

The Southern consists of an array of water Cherenkov detectors, covering about  $3000 km^2$  with 1600 detectors spaced by 1.5 kilometres in a triangular grid. They are located at an altitude of around 1400m ( $875 gcm^{-2}$  in atmospheric depth), with differences between them of  $\sim 1\%$ . The ground array is similar to the one in Haverah Park. On the border of the ground array, we have four fluorescence detectors, each with six telescopes. In the figure 5.1, we can see a representation of the observatory.

The Northern site has not yet been built, but the Southern part was completed in May 2008 and began to record data since January 2004, with the parts of experiment that were already operational.

### 5.0.5.1 Hybrid technique

This is the most important feature of the project. Here we detect events in both SD and FD. Both techniques are well developed, and measure completely different variables. FD observes the longitudinal profile, while the SD sees the lateral profile. Using the two techniques is possible to do a inter-calibration between the methods (unlike AGASA and HiRes, which could gives their's differences), then we calibrate the measurements of energy, and use the variables of both together to determine the composition. This is very important, since the reconstruction of energy through fluorescence is much more independent of the models than the SD. However, we still have 100% duty cycle for SD and 10% duty cycle where we can use hybrid techniques.

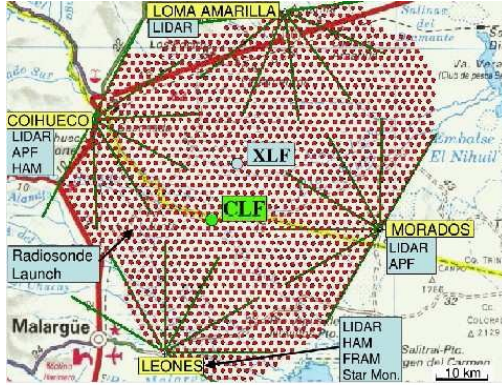


Figure 5.1: Configuration of the Pierre Auger Observatory southern detector from [68].

## 5.1 Southern Observatory

### 5.1.1 Surface detector

As noted before, the SD has 1600 detector spacing of 1.5km in a triangular grid, covering an area of  $300\text{km}^2$ . The grid spacing was chosen to maximize the efficiency of events to  $\sim 10^{19}\text{eV}$  (triggered with five tanks). There is a wireless local area network (LAN) which is used to communicate the tanks with four antennas at each fluorescence site. After that, the data are sent through a high capacity microwave link to the Central Data Acquisition System (CDAS). The synchronization and position is provided by the standard GPS system. The CDAS is located in the Central Campus, in Malargüe.

Each detector is a ground Cherenkov tank, a cylinder with a diameter of 3.6m ( $10\text{m}^2$  base) and 1.2m high, filled with approximately  $12\text{m}^3$  of purified water. The Cherenkov light is collected by three PMTs of 9 inches, placed on top of the tank and in steps of  $120^\circ$  (see figure 5.2). In addition, the inner surface of the tank, in tyvek, has a large reflectivity to increase the light collected. Each tank also has a solar panel, two 12V batteries (powered by solar panel), a GPS to control the time and location and a GSM, which is a wireless communications unit [70].

The Auger Collaboration has chosen Cherenkov tanks, since this allows to study very inclined showers, they are still much cheaper compared with other techniques, for the same performance and are expected to have a duration of 20 years, holding out the extreme weather of the zone. On average, we expect the possibility of distinguishing between the muonic and electromagnetic components.

When the muons and electrons or positrons pass through the tanks, they emit Cherenkov radiation which is detected. Photons will interact in the water producing pairs that will emit Cherenkov. The radiation of photons is  $\sim 37\text{g}/\text{cm}^2$  length, the tank has  $1\text{gcm}^{-3} * 120\text{cm} = 120\text{gcm}^2$ , then there are about 3 radiation lengths and photons interact.

The Cherenkov light is detected and analysed in terms of Vertical Equivalent Muon (VEM), which is defined as the average charge deposited by a vertical down-going muon. In cumulative data, is possible to distinguish between muons and electrons, because muons interact less, will have an higher energy and will have a larger signal in the tank. But in event-by-event, we only know that in tanks very far from the core, the particle will be mainly muons.

### 5.1.2 Fluorescence detector

The fluorescence detector (FD) consists in facilities at the top of small hills on the edge of the SD array: Los Leones, Los Morados, Loma Amarilla and Coihueco (see fig. 5.1). The FD was built with the aim of measuring the energy of the shower (since this method is practically independent of Hadronic models) and to have a resolution of  $20\text{gcm}^{-2}$ , since the difference between  $X_{max}$  in iron and protons in the models is about  $100\text{g}/\text{cm}^2$  (and thus would be possible to distinguish between the two).

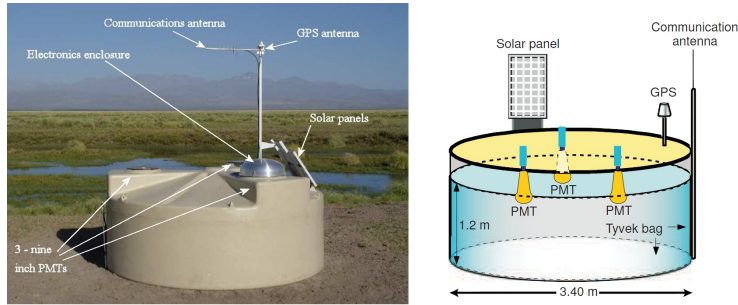


Figure 5.2: Left: a photograph of one of the tanks in the Pierre Auger surface array. Right: the representation of the water Cherenkov detector used in PAO from [71].

The FD consists of four stations called "eyes". Each eye has a field of view of  $180^\circ \times 30^\circ$  [71] and is divided in six telescopes, each with  $30^\circ \times 28.6^\circ$  field of view, and has an inclination of 16 degrees to the horizontal. In figure 5.3, is depicted the layout of an eye, the building is a semicircle with 14m, each telescope pointing radially, with a window of 3m(w) by 2.5m(h). Each eye has an antenna that communicates with part of the SD array and sends the data from the SD and FD for the CDAS.

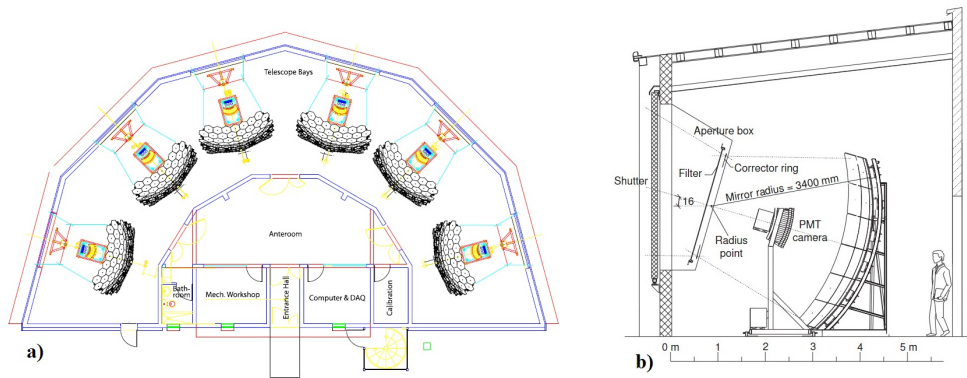


Figure 5.3: a) Layout of an FD eye building with 6 telescopes from [72]. b) Schematic representation of a telescope from [71].

### 5.1.2.1 Optics

The telescopes use Schmidt optics [73] to eliminate coma aberration. In figure 5.3, is represented the schema of each telescope. As we can see, outside each telescope, there is a shutter to protect the system from rain, wind and adverse external conditions.

After the shutter, we have the aperture box, here we have a ultraviolet (UV) filter on the outer side of the diaphragm, with  $80\text{cm} \times 40\text{cm}$ . The filter serves to reduce the intensity of the dark night background in relation to the fluorescence light. The filter sheets are MUG6glass with 3.25mm thick, having a transmission of 85% for wavelength of 350nm and decreases to 20% at 300nm and 400nm (in the area of fluorescent emissions see 3.5).

Still in the box aperture, UV radiation not absorbed will pass through a diaphragm with 0.85m radius, which eliminates the coma aberration and ensures a nearly uniform spot of about  $0.5^\circ$ . Around the diaphragm there is an adjustment ring between 0.85m and 1.10m. This ring increases the effective aperture of the telescope by a factor of 2 and is divided into 24 sectors with the appropriate spherical profile to compensate for the aberration and not increase the size of the spot.

The light is collected by a 3.5m by 3.5m spherical mirror, with a radius of 3.4m. Due to the large size of the mirror, this is divided into several smaller segments, overlapping with hexagonal shapes and squared-shape to improve the light collection. There are 49 segments of mirrors made of aluminum with AlMgSi in backing and coverage with a protective SiO<sub>2</sub> layer. The final average reflectivity is approximately 90% in the band 300-400nm [70].

Between the mirror and the aperture box, we have the PMT camera. This camera has 440PMT (20columns × 22rows) with 6cm × 94cm(w) × 86cm(h). It is in the focal plane with spherical shape and concentric with the mirror, having a radius of 1.743 m (see figures 5.3b and 5.4a).

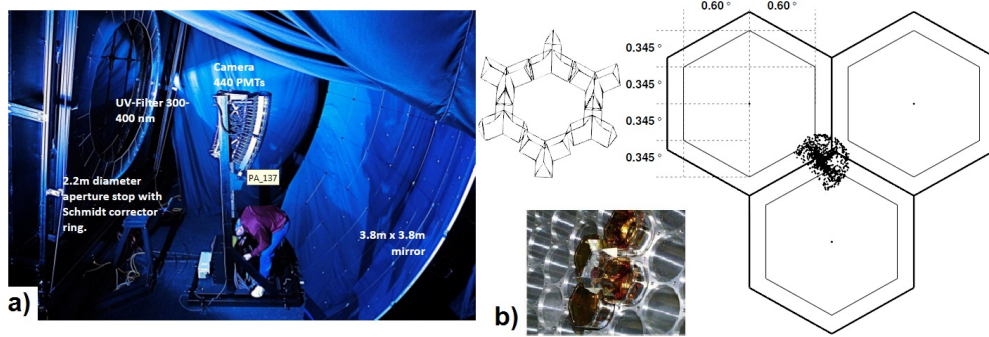


Figure 5.4: a) a photograph of PMT camera and aperture box and mirrors [75]. b) top left is represented six Mercedes stars positioned in order to form a the hexagonal pixel, down left is a photograph of some part of the camera with four PMTs and two Mercedes stars mounted together, the big holes is to mount the PMTs and the small one to mount Mercedes, in right is represented the dimension in degrees of a PMT and a Mercedes star, the hexagon is a PMT and the region between the parallel lines is for Mercedes, the point in the center represents the size of the spot [74] [72].

Each photomultiplier has a hexagonal shape to better cover the camera. It is needed some space between the PMT for a safe mechanical packing. So for better efficiency of light collection and to have a smooth transition of efficiency between the pixels, each PMT is surrounded by a simplified version of the classical "Winston cones", which is called the Mercedes star (see figure 5.4b). These reflective surfaces are inclined, to reflect about 90% of the light into the PMT.

To analyze the data, we use a coordinate system  $(\beta, \alpha)$  where the camera is rectangular and pixels are regular [76]. These new coordinates are obtained from the spherical coordinates  $(\theta, \phi)$ (see figure 5.5) by:

$$\beta = \arcsin(\phi_t - \phi) \sin(\theta) \alpha = \alpha_c - \alpha_m + \arcsin\left(\frac{\cos \theta}{\cos \beta}\right) \quad (5.1)$$

where  $\phi_t$  is the azimuth of the telescope center,  $\alpha_m = 16^\circ$  is the telescope elevation angle with respect to horizontal axis and  $\alpha_c = \frac{\sqrt{30}}{2}$  is the offset angle between the camera center and the telescope axis. In these coordinates, each pixel is a regular hexagon with radius  $r_{pix} = \frac{\sqrt{30}}{2}$ , with sides length of  $l_{pix} = \frac{\sqrt{30}}{2}$  and a width between the sides  $d_{pix} = 1.5^\circ$ . The position of 440 pixels is given by:

$$\beta_{ij} = \begin{cases} 1.5^\circ \cdot (10 - i), & \text{if } j \text{ is odd} \\ 1.5^\circ \cdot (10 - i) + 0.75^\circ, & \text{if } j \text{ is even} \end{cases} \quad (5.2)$$

$$\alpha_{ij} = 1.5^\circ \frac{\sqrt{30}}{2} \cdot (j - 11)$$

Where  $i \in [1, 20]$  is the number of column and  $j \in [1, 22]$  is the number of rows. The  $\beta$  ranges from  $-15.75^\circ$  to  $15^\circ$  and  $\alpha$  ranges from  $-13.86^\circ$  to  $15.16^\circ$ . The camera has a field of view of  $30.75^\circ \times 29.01^\circ$  in  $\beta$  and  $\alpha$  respectively. Also, we can define the pixels sorted from 1 to 440 with  $N_{pix} = 22 \cdot (i - 1) + j$  (in the figure 5.5 is depicted the camera in these coordinates).

The spot indicated above is the circle of least confusion, ie, due to aberrations, photons entering the telescope can be seen in the camera with a displacement from the original position and so the spot is a circle where

a photon can be detected with center being the original direction. The Schmidt optics was chosen in order to maintain this constant distance. The spot has an angular size of  $0.5^\circ$  ( $0.25^\circ$  radius) which corresponds to about one third of the pixels of the opening angle of  $1.5^\circ$ . This means that the effects of aberrations are not very significant, taking into account the size of these pixels.

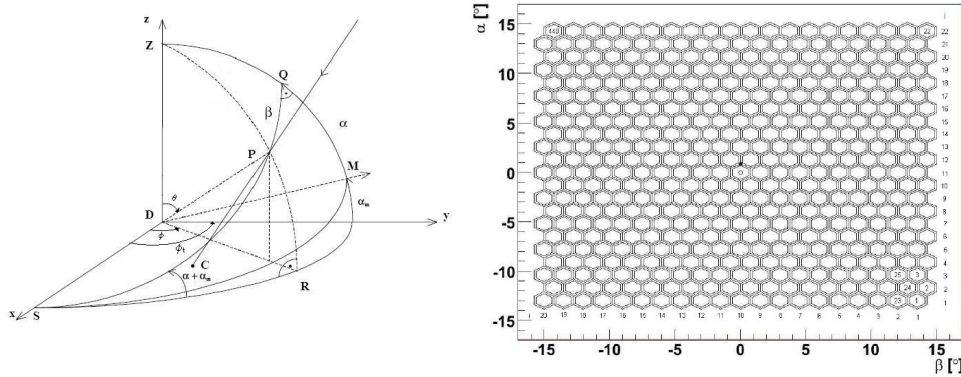


Figure 5.5: a:  $(\beta, \alpha)$  coordinates in relation to the coordinates  $(\theta, \phi)$  from [76]; b: representation of the camera with 440 pixels in the coordinates  $(\beta, \alpha)$ .

### 5.1.3 Atmospheric monitoring

As previously stated, the fluorescence technique is very sensitive to conditions of the atmosphere (because the atmosphere acts as a calorimeter) and thus the experiments requires a good control of their parameters. As noted in the equation 3.26, the intensity of photons reaching the detector depends on Rayleigh and Mie scattering, then is needed an accurate characterization of aerosols, clouds, dust, smoke, temperature, density and pressure of the atmosphere. These weather conditions varies on a small time scale requiring monitoring routines.

For most realistic atmospheric models of the site, there were campaigns of meteorological radio soundings with helium balloons equipped with radiosondes to measure temperature, pressure and humidity as a function of altitude for several seasons. In [77], we can see the of measurements of the atmosphere in PAO in comparison with the U.S. standard atmosphere.

In [77] [78], we can see the influences of the parameters of the atmosphere in some measurements, such as energy and the reconstructed  $X_{max}$  value.

Basically, in Auger, the atmospheric monitoring systems include LIDARs, cloud monitors, Horizontal Attenuation Length Monitor, phase function monitors, meteorological stations, and radiosondes [79] and I will describe that.

#### 5.1.3.1 LIDAR stations

The LIDAR (Light Detection And Ranging) is a device designed to study the aerosols in the atmosphere through the backscattered light signal. The LIDAR consists of a 355nm laser and a telescope with three mirrors, each with a gated, high-speed photon detector [80] and there is a system in each eye. After the laser is fired, the telescope sees the elastic backscattered light signal (measuring light intensity and position), so we can measure the aerosol optical depth towards the firing direction [81]. The LIDAR can operate continuously (regularly pointing to directions covering all sky) or in "shoot the shower, when the laser pulses are triggered by FD events, so we know the composition of aerosols for a given shower. Raman LIDAR (in LIDAR stations too) detects the backscattered light by Raman scattering, this allows a higher accuracy in measurements and identification of the constitution of the atmosphere, however, requires very intense lasers that would affect the FD (operate few times).

### 5.1.3.2 Horizontal Attenuation Length Monitor

This system serves to measure the aerosol attenuation length in horizontal path between FD sites, it measures several wavelengths near the acceptance of the Fluorescence detectors. The system has a DC light as a light source and a camera sensitive to UV. The measurements are made with a 365nm, 405nm, 436nm and 542nm filters. The total attenuation is then the ratio of the flux at large distances ( $\sim 50km$ ) and the flux measured at short distances (calibration point).

### 5.1.3.3 Aerosol Phase Function Monitor

This system measures the normalized aerosol differential scattering cross section as a function of the scattering angle from the initial light direction [82], which means that we measure the Mie scattering cross section, which allows to infer the Cherenkov light scattered.

Measurements are performed using a pulse of light directed through the horizontal field of view of one of the FD eye. The system uses three xenon flash tube sources which emit  $1\mu s$  light pulses covering the full range of wavelengths of the FD sensitivity and the distance from the source to the FD eye is about 1.3 km, which means that we have small atmospheric attenuation.

### 5.1.3.4 Cloud cameras and others

The clouds have a large optical depth and a very irregular shapes, causing unpredictable effects on scattering and transmission properties. As the clouds emit infrared, it is possible to detect them on a much cleaner background infrared. The cloud cameras are located in the FD eye and consist of digital cameras with infrared spectrum between 7 and 14  $\mu m$ . The cameras have a field of view  $45^\circ \times 35^\circ$ .

In each of the FD eyes there are weather stations that measure temperature, humidity, pressure, direction and wind speed. As mentioned above, meteorological radiosondes on balloons are sent to make measurements of atmosphere with altitude and being able to better characterize the atmosphere.

There is also a very important system, the central laser facilities which I describe below.

## 5.1.4 Central Laser facilities

At the Pierre Auger observatory, there are two laser facilities (see figure 5.1): Central Laser Facility (CLF) and Extreme Laser Facility (XLF). CLF is in the middle of the SD array at a distance of 26 to 39km to the buildings FD and became operational in 2003 (see article [84]). The XLF is a second laser facility very similar to the CLF and was built with the aim of improving the calibration of the CLF.

The CLF is based on the HiRes laser devices and is situated 26 km away from Los Leones, 30 km from Los Morados and Coihueco and 40 km from Loma Amarilla. It is an independent unit controlled by wireless, has his own weather station, to determine the temperature, pressure, humidity and wind. It is connected by a optical fiber cable to the closest SD tank, Celeste, where we can inject a fraction of the laser light.

The CLF has a linearly polarized laser with 355 nm wavelength, which is ideal for fluorescence techniques (there are a set of mirrors that reflect in 355nm to reduce the contributions of other frequencies). The laser can be fired in pulses 7ns up to a maximum energy of 7mJ, values that mimic an EAS of  $10^{20}eV$ . Moreover, we can direct the laser to an accuracy of  $0.2^\circ$ .

The assembly of the CLF is very important and it was constructed with various purposes. With this facility, we can monitor the atmosphere and measure the amounts of aerosols as a function of time through the analysis of vertical track of laser beams seen by the FD. As we know the direction of the CLF laser with an accuracy greater than the reconstruction, then we can use that information to confirm a correct alignment of telescopes, useful for the geometrical reconstruction of the shower directions. We also know the number of photons emitted by which we can study the atmosphere so we can compare the reconstruction of energy with the real energy of the laser.

Another important objective is to study the synchronization of the four eyes and determine the time offset between the SD and FD. From [83] we have  $289 \pm 45ns$  for Los Leones,  $363 \pm 43ns$  for Los Morados and  $307 \pm 49ns$  for Coihueco (in a sample), the SD being the last to record the event. Lastly, we can still study the efficiency of the trigger, knowing the fraction of events that is or is not registered by the eyes.

There are several redundant measurements among the atmospheric systems, however this is very important for a better control of systematics. The PAO is therefore different from other experiments in the area for a much better control of systematics.

## 5.2 Event reconstruction

### 5.2.1 SD reconstruction

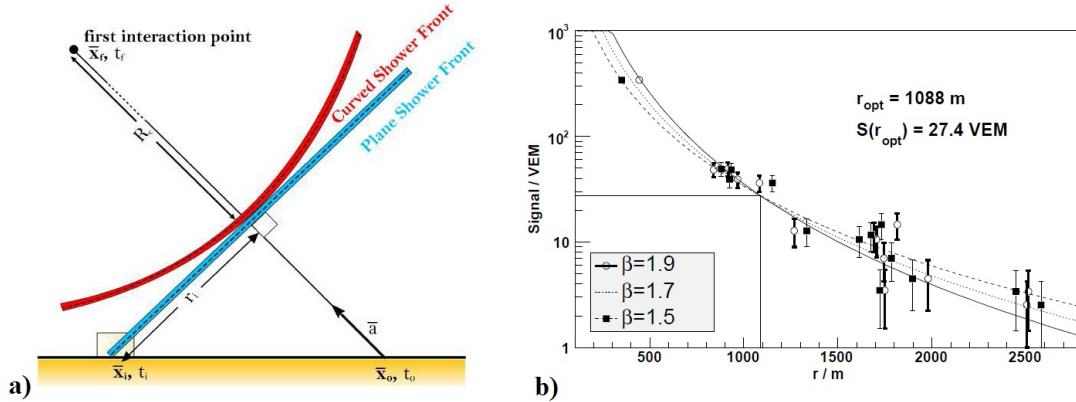


Figure 5.6: a) Scheme of the geometry of the shower with the parameter settings, b) is represented the signal as a function of the distance to the core compared with three LDF parametrizations of NKG type with different  $\beta$  slope and can be seen that the signal is more robust at  $r \sim 1000$ m (from [88])

The surface Detectors (SD) will always have a background for the equipment, to record the signals of interest, it is necessary selection rules at the level of PMTs and stations, which are called triggers, the triggers are explained in detail in [85]. These triggers are related to the total signal measured (in VEM) in a typical shower. After detecting an EAS, it is necessary to recover the geometry of the event. As mentioned in section 3.4, the simplest model considers a plane wave front and the geometry is obtained from the arrival times when the wave front passes through the tank leaving SD signal. From figure 5.6, we observe easily that the time  $t_i$ , which tank  $i$  detects signal is given by:

$$t'_i = \frac{1}{c}(ct_0 - (\vec{x}_i - \vec{x}_b) \cdot \vec{a}) \quad (5.3)$$

Where  $\vec{x}_b$  is a first estimate of the point where the core of the shower hits the floor ( $\vec{x}_0$ ),  $t_0$  is the time of arrival at  $x_0$  and  $\vec{a}$  is the vector direction of the shower axis. To determine the geometry, we compare the value of  $t'_i$  obtained from 5.3 with the measured value  $t_i$ , by minimizing the standard  $\chi^2$ :

$$\chi^2 = \sum_i \left[ \frac{t_i - t'_i}{\sigma_{t_i}} \right]^2 \quad (5.4)$$

Where the variance was parameterized in [86], doing a fit with three parameters, two from  $\vec{a}$  and  $t_0$ . However, the shower front is curved and we need a better descriptions of 5.3, thus assuming a radius of curvature  $R_C$  we have:

$$t'_i = \frac{1}{c} \left( ct_0 - (\vec{x}_i - \vec{x}_b) \cdot \vec{a} + \frac{r_i^2}{eR_C} \right) \quad (5.5)$$

where  $r_i = |\vec{a} \times (\vec{x}_i - \vec{x}_b)|$ . And we minimize equation 5.4, but now with the definitions of 5.5. Other models for the shower front can be used, for example in [89], where they use parabolic fronts, with that they obtain an angular resolution less than  $2^\circ$  for events with signal in three tanks, less than  $1.2^\circ$  for events with signal

in 4 or 5 tanks and less than  $0.9^\circ$  for larger tank multiplicities.

After determining the geometry, it is necessary to recover the size of the shower, or rather the energy of the shower. With the tank's signal, we can get the lateral profile of the shower (see section 3.3). This profile for reconstruction purposes have the form:

$$S(r) = S_{1000} f_{LDF}(r) \quad (5.6)$$

Where  $r$  is the distance to the axis shower,  $S_{1000}$  is the signal value at a distance of 1000m from the shower core and  $f_{LDF}(r)$  is the lateral distribution function, with  $f_{LDF}(1000) = 1$ , and:

$$f_{LDF}(r) = \begin{cases} \left(\frac{r}{r_{1000}}\right)^{\beta+\gamma \ln(r/r_{1000})}, & \text{if } r \geq r_{300} \\ \left(\frac{r}{r_{1000}}\right)^{\beta+\gamma \ln(r_{300}/r_{1000})}, & \text{if } r < r_{300} \end{cases} \quad (5.7)$$

$r_{300}$  e  $r_{1000}$  are 300m and 1000m respectively,  $\beta$  and  $\gamma$  are parameters that depends on zenite angle  $\theta$ . The  $S_{1000}$  is the value used to estimate the energy and according to [88], given the spacing between the SD tanks of about 1.5km, at a distance of 1000m the SD signal is considered to be robust and with few fluctuations allowing an estimate of energy with greater accuracy. Despite the many variations that  $f_{LDF}$  parametrization may have, it is considered that the value of  $S_{1000}$  has a precision less than 5%.

The lateral distribution is usually a variation of the NKG formula (see equation 3.13) and frequently has the form:

$$f_{LDF}(r) = \left(\frac{r}{r_{1000}}\right)^\beta \left(\frac{r - r_{700}}{r_{700} + r_{1000}}\right)^{\beta+\gamma} \quad (5.8)$$

Where  $\beta$  and  $\gamma$  are parameters that depends on zenite angle  $\theta$  and  $r_{700} = 700m$ . Then we just do a  $\chi^2$  minimization to obtain the  $S_{1000}$ , the energy is  $E = a(S_{1000})^b$  from [85]. Hybrid reconstructions does not use the  $S_{1000}$ , but rather the parameter  $S_{38}$  which will be explained later.

## 5.2.2 FD reconstruction

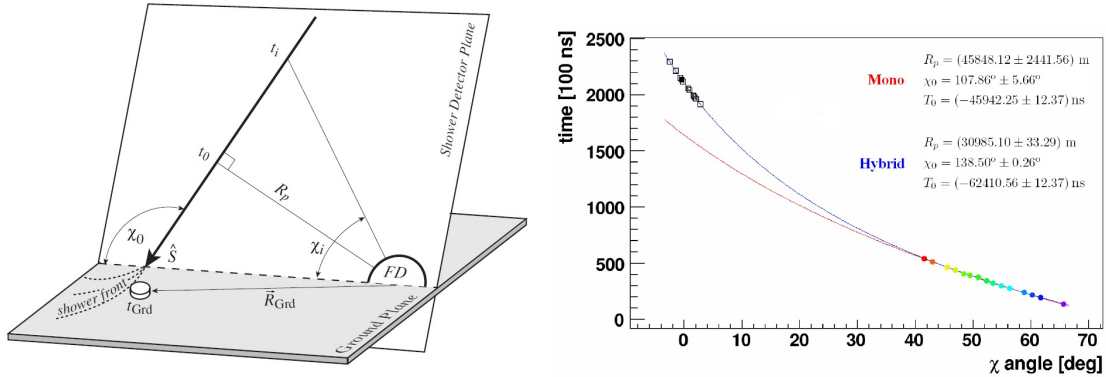


Figure 5.7: a) Scheme of the geometry of the shower with the parameter definitions (from [90]), b) time of arrival of the light at each pixel in relation to the angle between the pointing direction of that pixel and the horizontal line. The color points came from FD data and the black squares from SD, we can see the monocular (red line) and hybrid (blue line) reconstruction fits to equation 5.9 (from [72]).

In the reconstruction from the fluorescence detectors as in SD, first, we determine the geometry of the shower, and after that we get the longitudinal profile. As mentioned on section 3.4 the geometry reconstruction in FD, begins by finding the shower detector plane (SDP), represented in figure 5.7. Each camera pixel sees in a direction  $r_i$ , so the shower plan will intersect the FD on the corresponding pixels that have been triggered. The normal to the shower  $n_{SDP}$  can be found by minimizing the amount  $\chi^2 = \sum_i (\vec{r}_i \cdot n_{SDP}) w_i$  [70], we  $w_i$  is a weight proportional to the signal. This method has been verified by reconstructed CLF events

and obtain accuracies of  $\sim 0.5^\circ$  [70], as seen previously.

Knowing the SDP, it is necessary to determine the axis of the shower in the SDP. If the event is monocular (only seen by one FDeye) then based on arrival times we know the geometry. Considering that the shower front propagates at speed of light, the expected time  $t_i$  at which the pixel  $i$  is triggered is [70] [91]:

$$t_i = t_0 + \frac{R_p}{c} \tan[(\chi_0 - \chi_i)/2] \quad (5.9)$$

Where  $t_0$  is the time where the shower is at the nearest FD distance  $R_p$ ,  $\chi_i$  is the direction that the pixel sees and  $\chi_0$  is the angle of the shower in the SDP (see figure 5.7). We can find the geometry minimizing  $\chi^2 = \sum_i w_i (t_i - t_{th})^2$ , with three degrees of freedom ( $t_0$ ,  $R_p$  and  $\chi_0$ ). If the position of the shower to the FD eye is such that it is only possible to detect one short track, then  $(\chi_0 - \chi_i)/2$  could be small and may not be sensitive to the curvature of  $tg(\frac{\chi_0 - \chi_i}{2})$ . The values  $R_p$  and  $\chi_0$  would cover a wide range and the reconstruction would not be satisfactory. If the event is detected for more than one FDeye, then it is not necessary to take into account time and we just need to intersect the various SDP (like in section 3.4).

With the geometry fixed, we can reconstruct the longitudinal profile. Firstly, it is necessary to convert the ADC counts of PMTs into number of photons that pass through the diaphragm of the detector. From [74], the conversion factor between ADC and the number of equivalent photons at 370 nm in the camera is  $C_{pmt}^{370} \simeq 5ADC^{-1}$  [70] (determined in the calibration of the FD, with detector efficiency). Due to the size of the spot, for a given time  $t_k$ , we will not have all signal on the same pixel but in more than one pixel, and so considering the background signal, we define  $d_{pmt} = \arccos(\vec{R}_{pmt} \cdot \vec{R}(t)) < d_{cut}$ , being  $d_{cut}$  the distance that maximizes the signal to noise ratio,  $\vec{R}_{pmt}$  is the pixel pointing direction and  $\vec{R}(t)$  points the direction of the shower. We are only interested in the signal of the pixels that point close to the directions of the shower, i.e. pixels that point less than  $d_{cut}$  degree from the shower. The number of equivalent photons as a function of time is:

$$n_\gamma(t_k) = \sum_i n_{\gamma,ik} = \sum_i C_{pmt}^{370} \cdot (n_{ADC,i}(t_k) - n_{ped,i}) \quad (5.10)$$

Where  $n_{ADC,i}$  is the number of ADC counts in the pixel  $i$  at time  $t_k$  and  $n_{ped,i} = 100ADC$  is considered the baseline for the background. Thus we get the reconstruction of the longitudinal profile. Nevertheless, the profile will contain a direct mixture of fluorescence, Cherenkov and scattered Cherenkov light. In old versions, we take all signal as fluorescence component, we uses Rayleigh and Mie processes and the geometry to determine the real photon emission of the shower. After that, using the fluorescence yield we make the first approximation of the longitudinal profile  $N_e$  for charged particles (mainly electrons and positrons). With this approach and taking into account the geometry, we expect a particular component of direct Cherenkov and with that, we again expect Rayleigh and Mie scattered Cherenkov (see figure 5.8). The three light contamination is subtracted from the signal original, getting a new fluorescence profile. Next, we iterate once more the new values until the results converge (up to four times). If Cherenkov is reduced this method works, but if it is too high the Cherenkov method does not converge [74]. The previous description was the old approach, nowadays we uses a more sophisticated one, which is suppose to accounts the same things.

To study the energy of primary particle, we are interested in knowing the energy that was deposited in the atmosphere, so it's helpful to know the  $\frac{dE}{dX}(X)$  instead of  $N_e$ , but the Cherenkov emission depends on the profile of  $e^+e^-$  and we need to have  $N_e$ . So we must relate  $\frac{dE}{dX}(X)$  with  $N_e$  on the form ([87] and [92]):

$$\frac{dE}{dX}(X_i) = N_e(X_i) \alpha_{eff,i} \quad (5.11)$$

where  $\alpha_{eff}$  is the mean ionisation loss rate, from [93],  $\alpha_{eff,i}(s_i) = \frac{c_1}{(c_2 + s_i)^{\frac{2}{3}}} + c_4 + c_5 \cdot s_i MeV/gcm^{-2}$ , where  $c_1 \dots c_5$  are parameter from [93], and  $s_i = \frac{3}{1 + 2X_{max}/X_i}$  is the shower age parameter.

According to [87] and [92], we must bear in mind that at a given moment, the fluorescence light reaches the pixels with some of Cherenkov light too, before that moment, no light arrives at any pixel (see equation 5.13). However, after this instant, fluorescent light stops reaching the pixel, but Cherenkov light still gets there, from the development of the cascade in another location. Being  $x \equiv \frac{dE}{dX}(X)$ , and  $y$  the light reaching the diaphragm, it will only be necessary to reverse the equation:

$$y = Cx \quad (5.12)$$

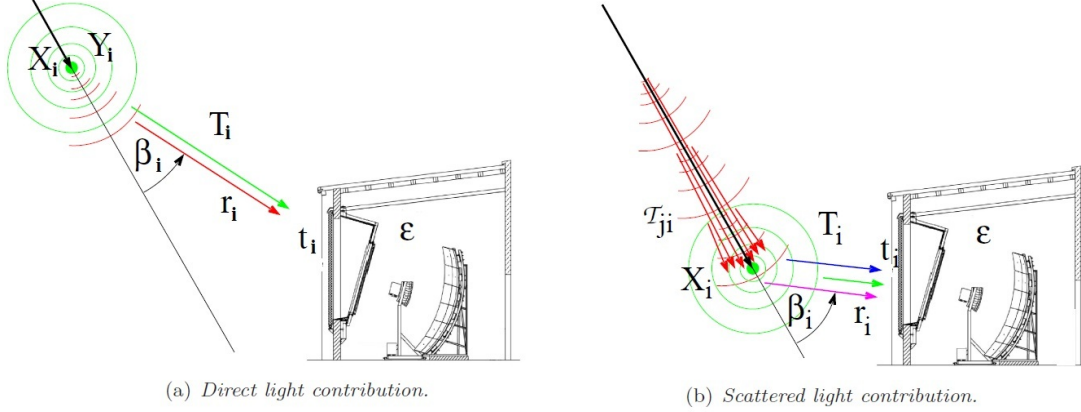


Figure 5.8: Representation of direct fluorescence and Cherenkov light (a) and scattered Cherenkov light (b) received at diaphragm. Isotropic fluorescence light in green, direct Cherenkov light in red, Rayleigh-scattered Cherenkov light in blue and Mie-scattered Cherenkov light in magenta (taken from [87]).

where  $C$  is the matrix given by:

$$C = \begin{cases} 0, & \text{if } i < j \\ c_i^d + c_{ii}^s, & \text{if } i = j \\ c_{ij}^s, & \text{if } i > j \end{cases} \quad (5.13)$$

where  $c_i^d$  is the direct light contribution from fluorescence and Cherenkov at time slot  $i$  and  $c_{ij}^s$  is the scattered Cherenkov due to Rayleigh and Mie scatterings detected at time slot  $i$  but emitted in slant depth  $X_j$ . The  $\frac{dE}{dX}(X)$  is found by inverting the equation 5.12, with that we can fit the Gaisser-Hillas formula too, but instead of being in particle number, it is in energy deposited.

The estimated power is calculated simply by integrating the profile of energy deposited:

$$E = \int_{X_0}^{\text{inf}} \frac{dE}{dX}(X) dX \quad (5.14)$$

Instead of using equation 5.14 from  $\frac{dE}{dX}$  profile, we could estimate the energy from the  $N_e$  profile and we have:

$$E \simeq \langle \frac{dE}{dX} \rangle \int_{X_0}^{\text{inf}} N_e(X) dX \quad (5.15)$$

where  $\langle \frac{dE}{dX} \rangle \simeq \frac{\varepsilon_0}{X_i} \simeq 2.2 \frac{MeV}{gcm^{-2}}$  is the mean energy deposit. We should not forget that this energy is  $\sim 90\%$  of the actual energy of an EAS due to missing energy (see section 3.4.1.7).

### 5.2.3 Hybrid reconstruction

The hybrid reconstruction is a technique that was used for the first time in the Pierre Auger Observatory. This technique combines the detection in SD with the detection in FD and it is very important in order to calibrate the reconstruction of energy in SD and improve the reconstructed geometry. To get hybrid reconstruction beyond FD measurements, we just need one SD tank to be triggered. Given a monocular event, we will use the equation 5.9 for the arrival time of shower front to find the geometry, if one SD tank is triggered, we can constrain the parameter  $t_0$  through [90]:

$$t_0 = t_{GND} - (R_{GND} \cdot \hat{S})/c \quad (5.16)$$

here,  $R_{GND}$  is the direction of SD tank from FDeye that was triggered at time  $t_{GND}$  and  $\hat{S}$  is the unit vector of shower axis (see figure 5.7).

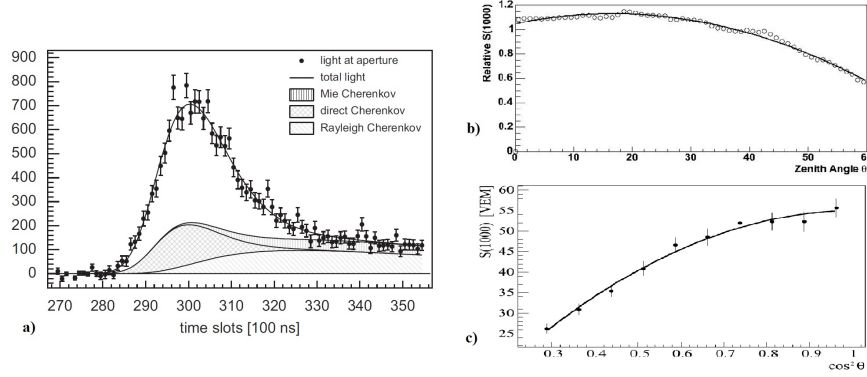


Figure 5.9: a) profile of light at aperture with reconstructed component of direct and scattered Cherenkov light from a simulated event with  $10^{19}eV$  (from [92]). b) fit to the curve  $CIC(\theta)$ , the values are relative to the signal  $S_{1000}$  at zenith angle  $38^\circ$  (from [94]). c) fit to the curve  $CIC(\theta)$  in order to  $\cos^2 \theta$  (from [95]).

This constraint allows to improve considerably the reconstructed geometry of the shower. If many SD stations are triggered, then the accuracy will improve even more, and may eventually constrain the position of the core of the cascade. Now, instead of three parameters, we have only  $R_p$  and  $\chi_0$  as parameters (equation 5.9). For example, in figure 5.7 we can see the fit to equation 5.9 for monocular and hybrid techniques. The hybrid has more data points to fit, so the result is much better. The values for  $R_p$  in monocular have an error of 2441.56m (precision of 5.3%, fig. 5.10), while in hybrid we have an error of 33,29m (precision of 1.0%), values for this particular event. If we look for the absolute values, the two reconstruction have very different results (but still inside error bar). With this, we can conclude that hybrid as a much better reconstruction with equation 5.9.

The duty cycle of SD is 100% and almost all events of FD will be hybrids, we will have about 10% of SD events which are hybrids. Interestingly, the hybrid technique, can detect events with lower energy than the SD, since only one SD tank needs to be triggered. With this technique, we do not need to know the lateral profile, not even the sign of the SD tank triggered, just need the time that the tank was triggered. As we mentioned before, to test the reconstruction, we use the laser CLF (section 5.1.4). This laser beam has a well known geometry position with 5m error in  $R_p$  and  $\chi_0 = 90^\circ \pm 0.01^\circ$ . The CLF is connected to a tank in order to make hybrid reconstruction (see section ref). In figure 5.10, we can see the monocular and hybrid reconstruction of the CLF laser [96]. It can be concluded that the resolution in  $R_p$  and  $\chi_0$  is about 10 times better in hybrid than in monocular and hybrid practically shows no systematic shift. In this way, this reconstruction is very good to carry out future studies of anisotropies.

The most important feature of the hybrid reconstruction is to be able to calibrate the energy of the SD. Although the value  $S_{1000}$  be appropriate to estimate the energy of the shower [88], for a fixed energy, it varies with the zenith angle ( $\theta$ ) of the shower. In PAO, the depth ranges from approximately  $870g/cm^2$  at  $\theta = 0^\circ$  up to  $1740g/cm^2$  for  $\theta = 60^\circ$ . Since the signal  $S_{1000}$  change with increasing depth, this means that the  $S_{1000}$ , should be replaced by a variable with zenith dependence. As we can see in [97] [94] for the same energy, the signal  $S_{1000}$  varies with the zenith angle and can be parameterized. The median zenith angle is  $\sim 38^\circ$ , so we describe the signal at any angle in relation to signal at  $38^\circ$  (figure 5.9). The variation of  $S_{1000}(\theta)$  with  $\theta$  with respect to the value  $S_{1000}$  at  $38^\circ$  is given by  $CIC(\theta)$  where  $CIC(38^\circ) = 1$  and then for any incidence angle of a shower we have the new parameter  $S_{38}$  defined as:

$$S_{38^\circ} \equiv S_{1000}/CIC(\theta) \quad (5.17)$$

The curve  $CIC$  is given by  $CIC(\theta) = 1 + ax + bx^2$  that is a quadratic function of  $x = \cos^2 \theta - \cos^2 38^\circ$  ( $a$  and  $b$  are parameters [97]). The uncertainty in  $S_{38}$  is estimated, by summing in quadrature the three contributors: the uncertainty in the  $CIC$  curve, the uncertainty in the  $S_{1000}$  and the angular accuracy of the event.

With the  $S_{38}$  parameter, we can calibrate the energy of the SD with the energy measured by the FD and we

have a calibration of the form:

$$E = a S_{38}^b \quad (5.18)$$

In section 5.3.1, we can see the latest results of the hybrid calibration. For angles above  $60^\circ$  [70] however, this method is not appropriate because the shower particles will be deflected by Earth's magnetic field, becoming with an asymmetrical profile, which means it should depict a different dependency on the distance to the shower axis. So the energy resolution of hybrid events is less than 6%, while in SD events is 15%.

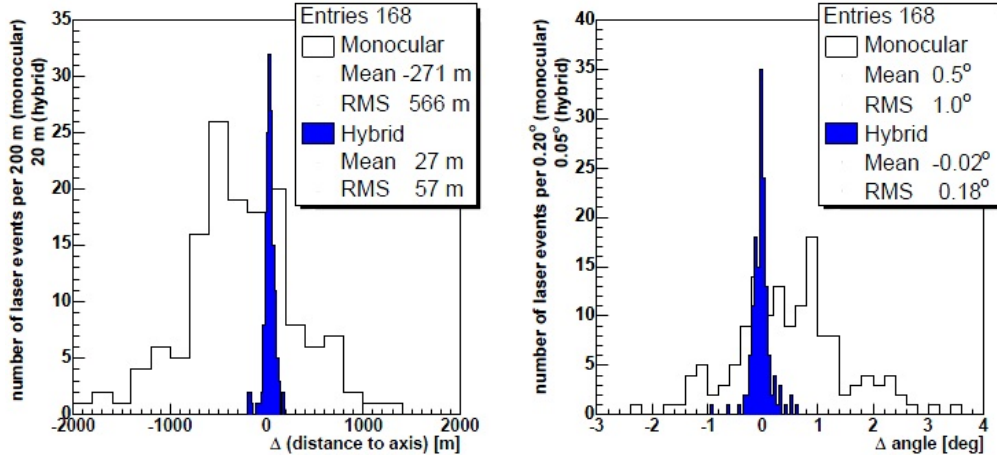


Figure 5.10: In the left is plotted the difference between the real and the reconstructed distance from the eye to the laser beam for monocular and hybrid techniques, the laser beam position is known with 5m error (see text). In right, is the difference between the real and the reconstructed direction of the laser beam for monocular and hybrid techniques, the laser beam angle is known with  $0.01^\circ$  error (taken from [96]).

## 5.3 Recent results

### 5.3.1 Energy spectrum

To obtain the energy spectrum, first we have to calibrate the parameter  $S_{38}$  as a function of energy in the hybrid reconstruction. In figure 5.11, are represented 795 hybrids selected events in the area of energy where the detector is fully efficient for  $E > 3EeV$ . We can see the  $S_{38}$  parameter as a function of FD energy  $E_{FD}$  and fit to equation 5.18. The parameters obtained are [95]:

$$\begin{aligned} a &= ((1.51 \pm 0.06(stat) \pm 0.12(syst)) \times 10^{17} eV \\ b &= 1.07 \pm 0.01(stat) \pm 0.04(syst) \end{aligned} \quad (5.19)$$

with a reduced  $\chi^2 = 1.01$ . The accuracy of the calibration for higher energies is dependent on the number of showers recorded (which means it becomes worst), the more energetic shower has an energy  $6 \cdot 10^{19} eV$ . Total systematic uncertainties are about 22% in the reconstruction of energy, in the hybrid method (to see the factors discriminated see [98]).

Using this calibration, we can study the spectrum of the Pierre Auger Observatory. In figure 5.11, is shown the energy spectrum with the data until the end of 2008. The exposure is then of  $12790 km^2 sr yr$  and again uses only the data with a zenith angle less than  $60^\circ$ , with over 35000 events selected. In figure 5.12 left, we have the CR fluxes with the hybrid data, in the right we have the SD data, which are consistent with one another. To analyse the features, we do fits with a broken power law with the shape  $J(E) = const \cdot E^{-\gamma}$  and get the indexes  $\gamma$  for each zone (figure 5.12). Instead of a simple power law, they also used a power law with a smooth function of the form:

$$J(E; E > E_{ankle}) \propto \frac{E^{-\gamma}}{1 + \exp\left(\frac{\log_{10} E - \log_{10} E_{1/2}}{\log_{10} W_c}\right)} \quad (5.20)$$

In figure 5.11 right, the combined spectrum of Auger is compared to the one from HiRes stereo instrument measures. The flux of HiRes has a shift in relation to the Auger flux that may be due to systematic uncertainties of one or both experiments. However, the ankle is much more defined in the Auger data than in HiRes. It should be noted that from  $\log_{10}(E/eV) = 19.61 \pm 0.03$  there is a large suppression in the flux. For example, a continuation of the power law above the ankles to higher energies can be rejected with  $20\sigma$  [99]. The suppression in flux is similar to what is expected from the GZK effect, but that does not exclude the possibility of being related to the change of the shape of the average injection spectrum at the sources.

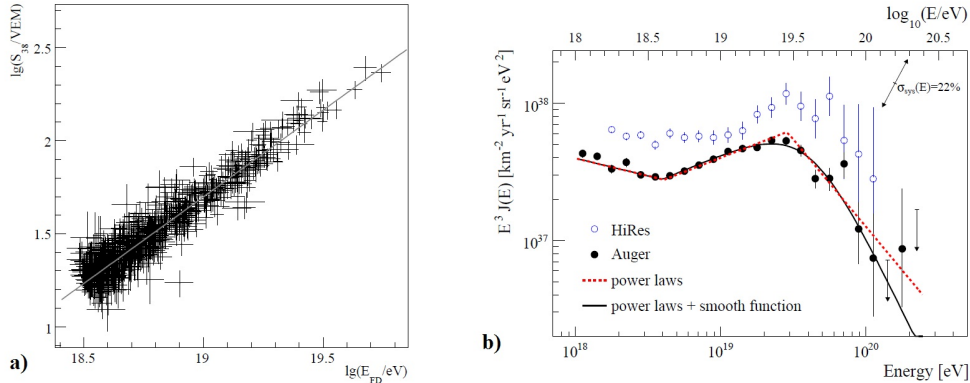


Figure 5.11: a) calibration between the parameter  $S_{38}$  and FD energy  $E_{FD}$  with 785 hybrid events (from [95]). b) The spectrum of HiRes and Auger, the Auger data are fit to a broken power law and to equation 5.20 (from [99]).

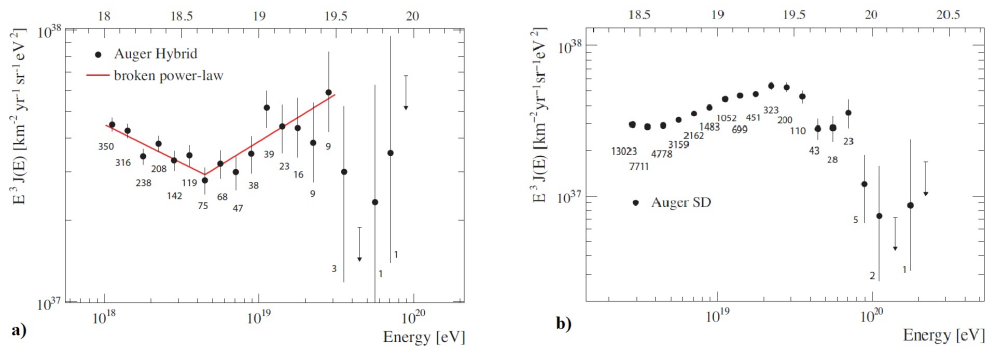


Figure 5.12: a) spectrum of hybrid events in Auger data and b) spectrum of SD events in Auger Data (from [99]).

### 5.3.2 Sources and anisotropies

In section 2.2, we saw that considering the intergalactic magnetic fields in nanogauss, protons with an energy of 100EeV have almost rectilinear trajectories and we can use them for astronomy. In figure 5.13, is represented the sky map in galactic coordinates with the 69 most energetic events (with  $E > 55EeV$ ) from 1 January 2004 until 31 December 2009 [100]. Auger events are represented by black dots, the solid line is the PAO field of view for zenith angles smaller than  $60^\circ$ . The Blue circles with  $3.1^\circ$  are center position of 318 AGNs from Véron-Cetty and Véron (VCV catalogue) that lie within 75 Mpc, or a redshift  $z < 0.018$ . This upgrade the previous results in [101][102]. We must not forget that about 90% of protons with 60EeV energy

at a distance of 200Mpc are expected to fail to reach the Earth due to the GZK effect. That means we have something similar to a GZK horizon for the sources that we associate with UHECR.

According to [101], we can see that we have more events in the line of the supergalactic plan than in other areas. There are two overlapping events to less than  $3^\circ$  of Centaurus A. So it is likely that the UHECR are protons.

It should be noted that the extragalactic magnetic fields are still unknown and the differences between positions can be related to the existence of magnetic dipoles, quadrupoles, or other magnetic structures that deflect the particles. Currently, attempts to infer various scenarios for the magnetic structures in the nearby universe are doing based on deflections of the CR (see [103]).

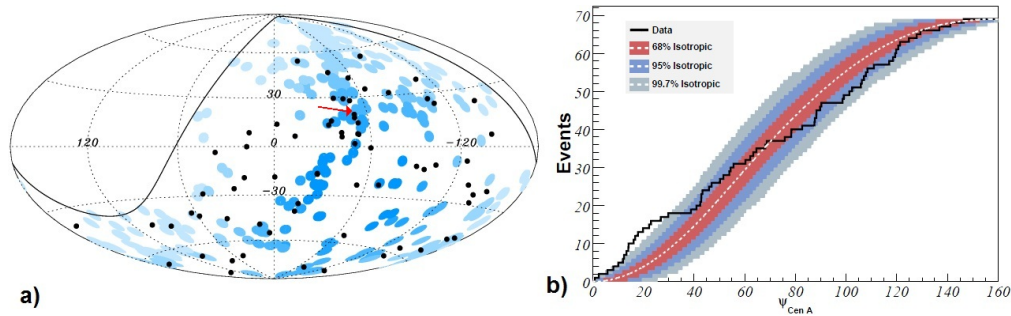


Figure 5.13: a) The 69 PAO events with  $E \geq 55EeV$  until 31 December 2009 are represented with black dots, in the sky with galactic coordinates. The solid line is the PAO field of view for zenith angles smaller than  $60^\circ$ . The Blue circles with  $3.1^\circ$  are center in the position of 318 AGNs from VCV catalogue, the blue scale represents the relative exposure of AGN, the total AGN weighted exposures, covers a fraction of 21% of the full exposure sky. The red arrow points Centaurus A. b) is represented the cumulative number of events as function of the angle  $\Psi_A$ , with relation to the position of Centauros A. [100]

Since we have an excess of events around Centaurus A, we could try to study the the isotropy as function of this location. So in the figure 5.13b), we have the number of CR with an arrival direction within an angle  $\Psi_A$  from the Cen A location, compared with the expected for an isotropic distribution. As we see, the less isotropic region is until  $18^\circ$ , where we detect 13 events, while 1.1 is expected for isotropic flux.

Apparently, the events seem to be anisotropic, but we need an analytical method to study the isotropy. To do so, we minimizes the probability  $P$  that  $k$  or more events at a maximum angular distance  $\phi$  with respect to any collection of sources in  $N$  isotropic events are correlated by chance with the selected objects at the chosen angular scale [104][102]:

$$P = \sum_{j=k}^N \binom{N}{j} p_{iso}^j (1 - p_{iso})^{N-j} \quad (5.21)$$

where  $p_{iso}$  is the exposure-weighted fraction of sky available to the PAO, which is within the  $3.1^\circ$  degrees of the selected potential sources. For an isotropic distribution has  $p_{iso} = 0.21$  (with VCV catalogue). Another method is likelihood ratio  $R$ , ie, basically is the ratio of the binomial probability of the correlation and the binomial probability in the isotropic case. defined by:

$$R = \frac{\int_{p_{iso}}^1 p^k (1 - p)^{N-k} dp}{p_{iso}^k (1 - p_{iso})^{N-k+1}} \quad (5.22)$$

In figure 5.14, it appears that in an initial period the data were completely anisotropic, however, now the directions of the events approach the isotropy hypothesis and stabilize in those very close values. The correlation decreases from  $69_{-13}^{+11}\%$  (in the first 13 events) to  $38_{-6}^{+7}\%$ [100], with the 55 events. Given  $p=0.21$  for isotropic flux, the cumulative binomial probability that the recent flux be isotropic is  $P = 0.003$ . We should note that 9 of the 55 events comes from angle lower than  $10^\circ$  in relation to the galactic plane (none has correlation within  $3.1^\circ$ ). The VCV catalogue could be very incomplete in this region, because of the obscuration by the Milky Way or the magnetic fields are bigger than what is expected, which could explain this differences. If we neglect this 9 events, we get  $46 \pm 6\%$  (  $24\%$  in isotropic). Still, it is possible to reject

the hypothesis of isotropy with 99% [105], which means that this distribution of directions could only be isotropic with a probability of 1% (can not be update with the new statistics).

Since the VCV catalogue, could be incomplete and don't have all possible sources, the analysis of the 69 events is repeated for the 2MASS Redshift Survey and Swift Burst Alert Telescope catalogue, but for now the study is not sufficiently for better conclusion (see [100] for details).

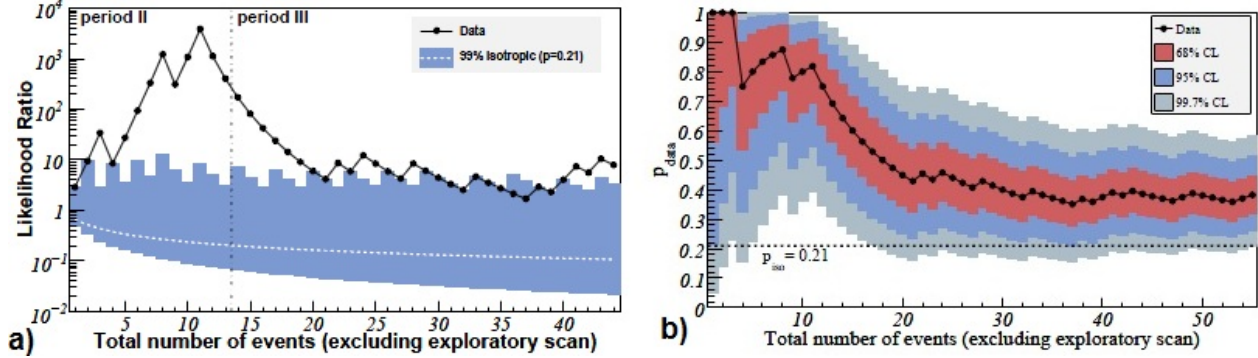


Figure 5.14: a) the sequential analysis of the likelihood ratio of CR with energy greater than 55EeV after 27 May 2006, values outside the blue area have less than 1% chance to arise from an isotropic distribution (with  $P_{iso} = 0.21$ ), b) the most likely value for the binomial parameter  $p_{data} = k/N$ , the current values is  $p_{data} = 38^{+7}_{-6}\%$ , the coloured areas corresponds to  $1\sigma$  and  $2\sigma$  uncertainties. (from [105] and [100])

### 5.3.3 Elongation Rate

In Section 3.1.2, we wrote about the elongation rate, this is a method to infer the composition of cosmic rays. Basically,  $X_{max}$  (section 3.1.2) of the development of a cascade depends on the energy and type of particle that initiate the cascade. If the CR is a proton, then the  $X_{max}$  is larger than that of iron for the same energy. Moreover, the  $X_{max}$  also varies with energy and by definition, the elongation rate corresponds to the rate of change of the average  $X_{max}$  with energy. In figure 5.15, it depicts the recent data of PAO and the lines correspond to the predictions of various models for protons and iron. Up to energies of  $10^{18}eV$ , the data are close to the lines of protons, and therefore the composition of the CR is becoming lighter. However, as shown in the figure 5.15, from  $10^{18}eV$  on, the data is approaching iron and looking to the RMS of  $X_{max}$  instead of  $\langle X_{max} \rangle$ , this behaviour is even more evident. We can conclude that the composition starts to get heavier approaching the mass of iron. These results contradict the previous section of the anisotropy, where due to correlations of the directions to the areas of AGN, it is expected to have lighter particles such as proton.

Indeed, the lines of the figure for proton and iron in the different models are not obtained analytically, because it is still not possible, but they came from simulation. Because the models use data from accelerators at energies far below the energies of the CR, extrapolations are needed (section 4) and we still know very little, so we conclude that their predictions are not the most correct. Therefore, this opens up many possibilities for particle physics.

### 5.3.4 Photon and neutrino fluxes

In section 3.1, it was shown that showers initiated by photons are really different from the started by heavy nuclei. The development of a cascade initiated by a photon is even more slower than for protons, and so the  $X_{xmax}$  is much deeper in photons than in nuclei. The signal of SD detector is also very different, it will only come from electron cascades since the photons have almost no hadronic or muonic component. Based on these characteristics, we can study the fractions of events initiated by photons and it was found that no photon has been detected. Thus, we define maximum limits for the primary flux of photons. In figure 5.16 on the left, these fluxes are represented in blue for hybrids data and in black there are the SD data. With these results, we can already reject several models that predicted the production of UHE photons (see [108]).

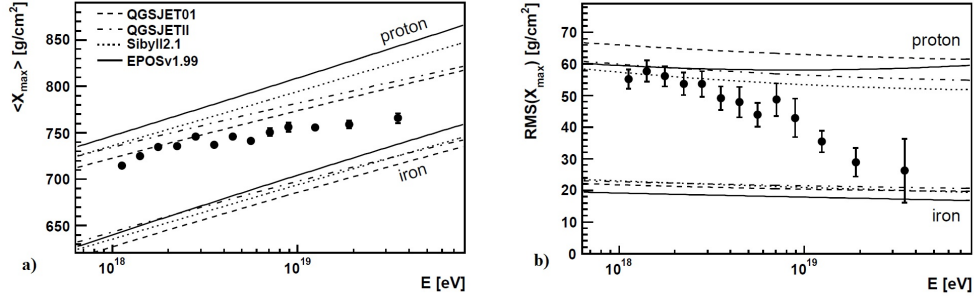


Figure 5.15: a)  $\langle X_{max} \rangle$  b) RMS ( $X_{max}$ ) from PAO data, from December 2004 until March 2009, compared with simulation predictions (from [106] [107])

It is also possible to reject some models Top-down production of CR.

The neutrinos are a very different and since the PAO has a vertical depth less than  $1000g/cm^2$ , then there isn't enough matter for neutrinos to interact. However, if the neutrino arrives on horizontal direction, it could cross Andes mountains, which will increase the depth crossed by about 20 times [107]. These events will have a weak horizontal electromagnetic component, but the muonic component would be well defined and could be detected by the SD detectors. A very interesting case is tau neutrino (and the others), they could cross the Earth or the Andes interacting and producing showers oriented from ground to space. It still not been detected such events and we may establish limits on the maximum flux (see figure 5.16right). The PAO design is very clean for this events and the results are comparable to experiments dedicated only to neutrinos.

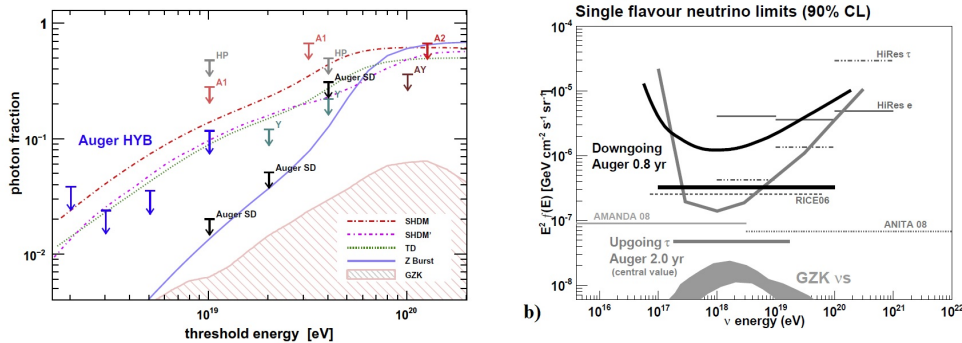


Figure 5.16: a) Upper limits on the photon fraction in the integral cosmic-ray flux for different experiments, the blue limits came from PAO hybrid data and black limits came from SD data, the shadow region is the expected GZK photon fraction. The models considered are the decay or annihilation of primordial relics such as topological defects (TD) or super heavy dark matter (THDM) and Z-burst scenarios (ZB). (taken from [109]) b) Differential and integrated upper limits for the flux of down-going  $\nu$  and up-going  $\nu_\tau$ , from [110]

## Chapter 6

# How exotic are standard events

The standard events are expected to have a longitudinal profile like a Gaisser-Hillas (GH) function. However, even though most of the showers are close to the GH, their shape could be really different (see fig. 6.1). The shower could be more deep in atmosphere (higher  $X$ ) or had developed sooner, and it can be higher and thinner or lower and larger. These differences come from the statical fluctuations in the development of the shower, i.e. it comes from the statistical behaviour of the decaying and interacting particles in the shower. As a consequence, we can not have two equal showers and we measure a distribution of  $X_{max}$  and other variables instead of a single value. These variations are expected to be restrained in the 4 degrees of freedom of GH function. Using simulations with the hadronic models we can predict the fluctuations of these quantities (which are expected to have a Gaussian statistical behaviour with respect to GH) that come from standard physics.

Knowing those normal shapes, we can look for exotic physics by studding strange events that are not accounted in the simulation or even expected from the simulation. For example, we can see some profile with two peaks of  $X_{max}$  instead of one (see next chapter). These are predicted in scenarios like a mini black-hole formation or could be signatures of creation of a new undiscovered particle that decays deeper in atmosphere causing a double-bang (and other scenarios). To know if we are dealing with exotic events we have to quantify the background that comes from normal events. In this way, we need to study if we have shapes (from standard physics) that differ from GH with gaussian fluctuations. We will try to find how many events have more fluctuations than what was expected.

In this chapter, we make simulations of EAS with CONEX[111] program, and use a sample with 64000 events, with  $10^{19}eV$  proton primaries. To increase the statistics we also use a new sample with 122000 events at  $10^{18}eV$  (which will be important in next chapter).

### 6.1 Universal Shower Profile

To study the cosmic rays, we can analyse the cascade development of the primary particle in atmosphere by detecting the electromagnetic sub-showers in fluorescence detectors. We are interested in determining if the primary CR spectrum consists in protons, irons or even a mixed composition, and usually we study the longitudinal profile of electromagnetic component. However, the characteristic electromagnetic features of the shower, could give us also access to some information and "hidden" hadronic features about the first interactions. As we have seen in section 4.3.4, different parametrizations of hadronic interaction in ultra high energy regime would give different features in the shower development. So, in section 3.2 we saw that the longitudinal profile can be parametrized by the Gaisser-Hillas function and I write it again in equation 6.1. To parametrize the electromagnetic component we need the shower maximum  $X_{max}$  together with the total number of particles  $N_{max}$  at  $X_{max}$  in depth, that can be easily obtain from data. Instead of using the  $N_{max}$ , we could use the  $dE/dX_{max}$  since they are proportional. Apart from these, we also need more two parameters to describe the shower (eq. 6.1), the  $\lambda$  gives an indication about the interaction length and the  $X_0$  is an effective first interaction length. The last two, must be extracted from data fitting the equations

and are correlated.

$$N_e(X; N_{max}, X_{max}, X_0, \lambda_{GH}) = N_{max} \left( \frac{X - X_0}{X_{max} - X_0} \right)^{\frac{X_{max} - X_0}{\lambda_{GH}}} e^{-\frac{X_{max} - X}{\lambda_{GH}}} \quad (6.1)$$

Figure 6.1 shows some shower profiles for the same energy. They look very different from each other, since some of them developed more or less quickly and have a bigger or smaller  $X_{max}$ . They have different  $N_{max}$  too, since they only should have equal  $\int dE/dX_{max} dX$ . This shapes can be very similar if we translate the shower maximum and normalize the maximum. We can write the Universal Shower Profile (USP) as a function of  $N' = N/N_{max}$  and  $X' = X - X_{max}$  ( $X'_0 = X_0 - X_{max}$ ) with the form:

$$N' = \left( \frac{X'}{X'_0} - 1 \right)^{\frac{X'_0}{\lambda}} \exp\left(-\frac{X'}{\lambda}\right) \quad (6.2)$$

In figure 6.1 we can see some events in USP profile and normal profile. In the USP, we see that most of the showers presents the same characteristics and a few have different shapes (wider or thinner) and even less have a very different behaviour. In this chapter I'm concerned to analyse the strange behaviour of these events.

The USP equation can be expanded around  $X' \sim 0$  (around the  $X_{max}$ ) and we have [113]:

$$\begin{aligned} N' &\sim \exp\left(-\frac{X'^2}{2|X'_0\lambda|}\right) \prod_{n=3}^{\infty} \exp\left(\frac{1}{n} \frac{X'_0}{\lambda} \left(\frac{X'}{X'_0}\right)^n\right) \\ &= \exp\left(-\frac{1}{2} \left(\frac{X'}{L}\right)^2\right) \prod_{n=3}^{\infty} \exp\left(\frac{R^{n-2}}{n} \left(-\frac{X'}{L}\right)^n\right) \\ N' &= \left(1 + \frac{RX'}{L}\right)^{R-2} \exp\left(-\frac{X'}{LR}\right) \end{aligned} \quad (6.3)$$

With the Taylor expansion, we get something like a gaussian with width  $L = \sqrt{|X'_0\lambda|}$  and distorted by  $R = \sqrt{\lambda/|X'_0|}$ . So with these parameters less correlated (see ref. [113]),  $L$  will be something like the width and  $R$  will be a rotation of the shower (see fig. 6.2).

The  $L$  parameter will be related with the electromagnetic interactions and it should not vary much either with primary particle type or its energy. The energy deposited ( $dE/dX$ ) along the shower is proportional to the number of particles  $N$ , so the integral of the distribution is used to compute the electromagnetic shower energy. The integral of a USP is:

$$\begin{aligned} E/\frac{dE}{dX}_{max} &= \lambda A^A \exp(A) \Gamma(A+1) \\ E/\frac{dE}{dX}_{max} &\sim \lambda \sqrt{2\pi A} = \sqrt{2\pi} L \end{aligned} \quad (6.4)$$

where  $A = R^{-2}$  and the approximation results in an small underestimation of the integral (by  $< 1\%$  for  $R < 0.35$  and  $\sim 9\%$  for  $R = 1$ [113]). In the table A.1 we have the values for  $R$  and  $L$  in different energies. This means that  $L$  can be calculated as a function of the total energy, and as we can see in figure A.3 the distribution of  $L$  are very close and for the presented simulations have variation less than 2%. The  $L$  variable has a smaller particle type dependence and small event-by-event fluctuation.

Nevertheless, the variable  $R$ , for the rotation of the shape is related with the rate at which the energy is transferred from hadronic to the electromagnetic component. At same energy, a heavier nucleus will interact sooner and more efficiently than a proton, so  $R$  will be bigger for iron which means that the hadronic component transforms more quickly into electromagnetic component. The  $R$  presents around 15% ( $\sigma/mean$  see table A.1) of variations. An interesting feature is that the  $R$  can be related with  $\Delta_0 = X_{max} - X_1$ , where  $X_1$  is the the depth of the first interaction. So  $\Delta_0$  decreases linearly as  $R$  increases (see [112]).  $R$  can be used in a event-by-event basis to study the showers and the first interactions.

## 6.2 Tool to separate standard from exotic events

Consider that a standard event can be parametrized by a Gaisser-Hillas function, then we can see how good this function fits to a sample of simulated events. In this section we use the sample with 64000 events at

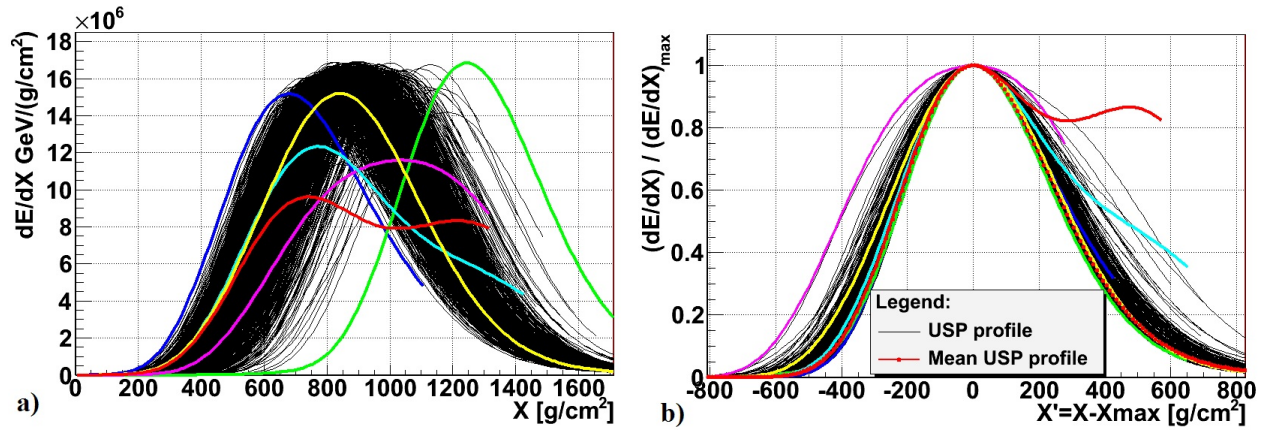


Figure 6.1: a) normal shower profile, b) universal shower profile normalized and translated with  $X' = X - X_{max}$ . In the two plots we have some events in other colours. The green one is a very deep shower, but in b) we can see that its shape is quite normal, while the red one has two peaks and the pink is much larger than the others. In our samples, the profiles have bins of  $10g/cm^2$

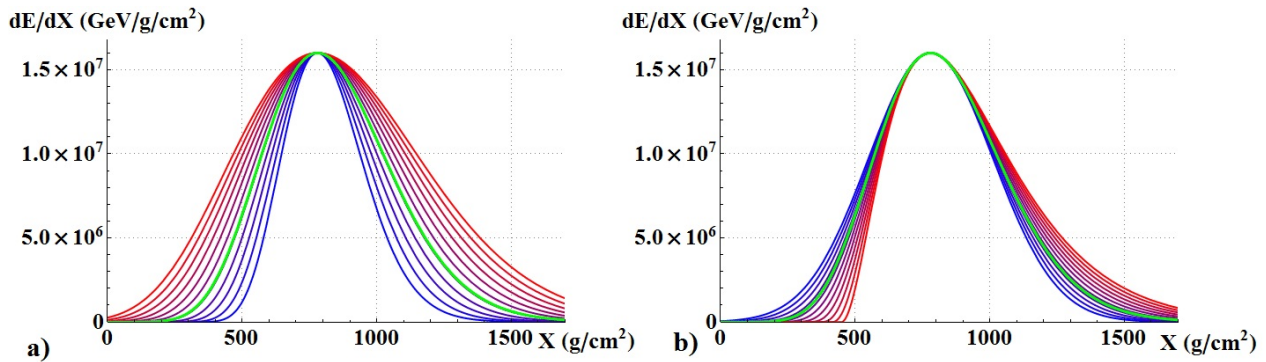


Figure 6.2: a) Geisser-Hillas profiles with  $L$  varying between  $150g/cm^2$  (blue) to  $350g/cm^2$  (Red), b) GH profile with  $R$  varying between  $0.01$ (blue) and  $0.7$ (red). In green we have a GH with  $L = 232g/cm^2$  and  $R = 0.15$ (mean values at  $10^{19}eV$ ), are used  $X_{max} = 780g/cm^2$  for all GH. We can see that  $L$  is related with the width and  $R$  is a rotation of the profile.

$10^{19}eV$ . In the figure 6.3, there is plotted a random event with its fit. This event has a  $\chi^2/ndf = 2162$  (from now on  $\chi^2/ndf \equiv \chi^2$ ), despite its high value, it looks like the fit is good, indeed, the parameters errors are very small. The main reason for the high  $\chi^2$  is that the error considered in each bin (or point  $X$ ) is underestimated (and the fit can't have that precision, see section 6.2.1).

In the figure 6.3, we have the  $\chi^2$  distribution of the 64000 events. We obtain a mean value of 2162, and we can see that the shape is not the normal  $\chi^2$  distribution. It has two peaks, and a smooth peak in the right tail. In addition to the underestimate error, we should see from where comes the main error. In this way, we plot the  $\chi_i^2 = \chi^2(X_i)$  in the fig. 6.4 b) and c).

We can observe that a big  $\chi_i^2$  component comes from the right tail of the shower development and another comes from the initial development. The initial development of a shower is unique for each shower and we need a higher number of particles (or begin in a higher development stage of the shower) to have a GH. Besides this region is more unstable and the two big terms in Geisser-Hillas equation 6.3 will diverge, so the fit will be more difficult.

The decay of the shower presents the biggest problem since the muonic component at some point will be higher than the electromagnetic (see picture 6.4 a). Consequently, if during the shower evolution, the  $dE/dX$  from

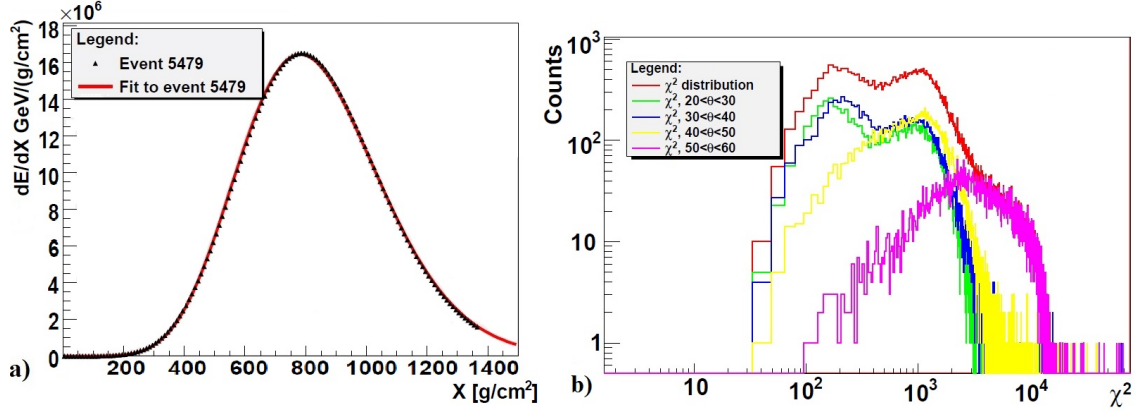


Figure 6.3: a) event 5479 with it's fit to 1GH, we have the  $\chi^2 = 2357$ ,  $N_{max} = 1.6 \times 10^7$ ,  $X_{max} = 781g/cm^2$ ,  $L = 230g/cm^2$  and  $R = 0.24$ , it is a nomrla events with a good fit, but have a very high  $\chi^2$ . b) the  $\chi^2$  distribution are plotted and we have the various contribution in angle too. In red we have all events, in green events with  $20 < \theta < 30$ , blue for  $30 < \theta < 40$ , yellow for  $40 < \theta < 50$  and pink for  $50 < \theta < 60$ .

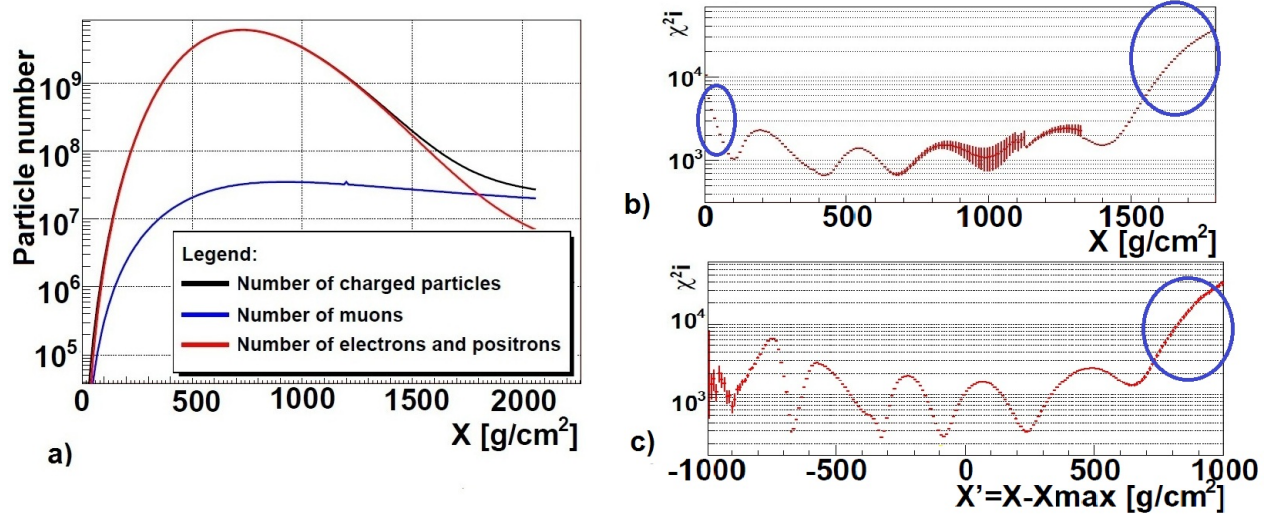


Figure 6.4: a) the number of charge particles in a longitudinal profile, most of the particles are electrons and positron, but at the end of the development the number of muon is higher. b) is display the mean  $\chi^2_i$  as function of  $X$  and  $X'$ , the initial and final state of development have the major problems.

the muonic shower is negligible, in the end of the shower it becomes a big factor and we don't have one GH, but two GH functions (so the fit goes wrong). In the simulation, it was been consider the sea level as the point where the shower development stops. So a shower will be longer in depth if it is a more horizontal shower (with bigger zenite angle  $\theta$ ). If the shower is longer, it's more probable that we reach the evolution zone with an important muonic component. In the figure 6.3, we separate the  $\chi^2$  with  $\theta$  interval and we see that the higher  $\chi^2$  comes from bigger  $\theta$ .

We have to note that the initial and final evolution of the shower can not be detected with fluorescence techniques, since the luminosity in very small. Therefore, if the big problems comes from the birth and death of the shower, we should simple cut these points in the fits.

We remove the points with  $X \leq 100g/cm^2$  (10 first points in samples) and if we see the picture 6.4 c) and compare with 6.1, we see that we can cut the point at which the development decreases bellow  $\sim 30\%$  of the  $N_{max}$ . The new result for the fits are expressed in the figure 6.5. Now our  $\chi^2$  distribution have normal

shape, but the mean value of the  $\chi^2$  is 235.7. This value is still a big number, since the  $\chi^2$  (over number of degree of freedom) should be one.

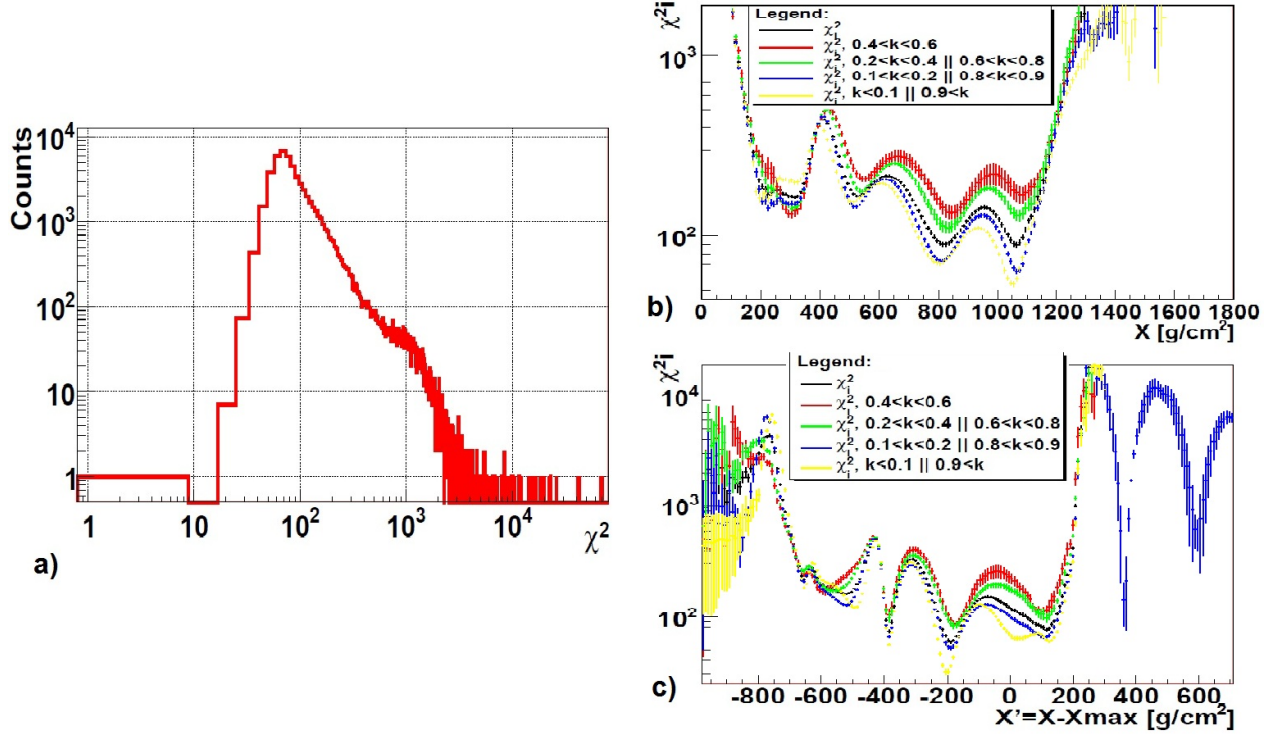


Figure 6.5: a)  $\chi^2$  distribution without the end and the initial state of the shower. b) mean  $\chi_i^2$  values in function of  $X$  and  $X'$  for several sample, each sample is characterized by the inelasticity  $K$  of the first interaction.

### 6.2.1 Fluctuation in CONEX and $\chi^2$ definition

What is the reason behind the high values of  $\chi^2$ ? To reduce the computation time, the simulation programs like CONEX have some interesting features.

If we are at relatively low energies like 1GeV, it's considered that we understand quite well the particle behaviours with standard physics. So, instead of continuing to follow each particle, with its interaction/decays and subsequent multiple particles produced, we say that a particle development below some energy threshold can be obtained analytically. If a produced hadron have an energy less than 1GeV, then we don't follow its development but we use the predicted analytical evolution.

In CONEX, the threshold used depends on the particle and on the energy, so we will have a  $\xi_p E$  as a threshold for proton (protons with fraction  $\xi_p$  of the primary energy  $E$ ) and so on for others particles. Suppose all particle energies decrease at the same rate, so at a  $X_a$  depth, all of them cross the threshold. In this way for  $X > X_a$  we will have  $N(X) = N_a * N_f(\xi_i E; X)$ , the particles will not be followed, and each one gives a contribution to the total profile given by  $N_f(\xi_i E; X)$ . Since  $\xi_i$  depends on the particle type, we consider that we have an effective  $N_f \propto E^\gamma f(X)$  (see chapter A.0.0.1, where we see  $N \propto E$ ). We can find this effect on  $\chi^2$  and in this approach, we have

$$\chi^2 = \sum_X \left( \frac{N(X) - GH}{\sqrt{N(X)}} \right)^2 = \sum_X \left( \frac{N_a E^\gamma f(X) - GH}{\sqrt{N_a E^\gamma f(X)}} \right)^2 = \sum_X \left( \frac{N_a f(X) - GH/\sqrt{E^\gamma}}{\sqrt{N_a f(X)}} \right)^2 E^\gamma \propto E^\gamma \quad (6.5)$$

In the figure 6.6, we see that  $\chi^2$  is proportional to the energy.

This means that in  $X_a$  we have  $\sqrt{N_a}$  fluctuations, than at higher  $X$  we will not have  $\sqrt{NX}$  but  $\sqrt{N_a} \times \sqrt{E^\gamma f(X)}$ , so the precision  $\sqrt{N(X)}$  we consider for the fit is smaller than it should be with  $\sqrt{N_a}$ .

Our result gives a  $\chi_{mean}^2 = 233.5$ , but this distribution could be divided according to the figure 6.6 and than we should have a mean value around one. This follows the approach given in CONEX, where we could divide the chi-square over  $\sqrt{N_{max}} \propto \sqrt{E}$ . Here instead, we make  $\sigma = \sqrt{N(X)} \times \sqrt{\chi_{norm}^2}$ , where  $\chi_{norm}^2$  is a constant obtained from eq. A.7. We will get  $f(\chi^2) \simeq \sum_k^n \chi_k^2 / \sqrt{\chi_{norm}^2}$  and obtain the distribution in the figure 6.8, since  $\chi_{norm}^2 \propto N_{max} \propto (dE/dX)_{max}$  it's more or less the same thing done at CONEX.

We could note that the  $\chi^2$  is not exactly proportional to the energy since at lower energies the previous discussion is not so important. Above  $10^{17} eV$  we have a linear function, but at lower energies this features begin to disappear.

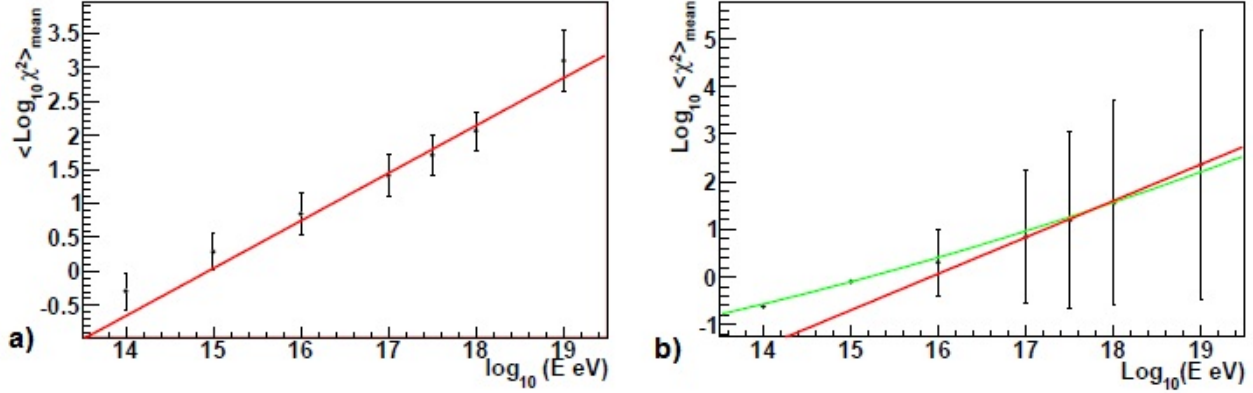


Figure 6.6: a) mean  $\text{Log}_{10} \chi^2$  values using all points, with linear fit. b)  $\text{Log}_{10}$  mean  $\chi^2$  values without using the initial and final points of the profile, with linear fit. see appendix A.0.0.6

## 6.2.2 Chi-square tests

The shower fluctuations are considered to come from the statistical behaviour of the shower development, then if the GH function describes the cascade, we will have a normal  $\chi^2$ . On other hand, if there are some physics that cause extra fluctuations, then we will see a bigger tail in  $\chi^2$  (more events in that area than expected). One way to study if the fluctuations are mainly statistical is the  $\chi^2$  test.

Given a  $\chi^2$  distribution, we can calculate the  $\chi^2$  probability defined as  $P(\chi_k^2) \equiv P(\chi^2 \geq \chi_k^2) = \int_{\chi_k^2}^{\infty} f(\chi^2) d(\chi^2)$ , for each event  $k$  with  $\chi_k^2$  (fig. 6.7),  $f(\chi^2)$  is the chi-square distribution function. If the considered  $\chi^2$  are obtained from gaussian fluctuations around a GH, they will follow a  $\chi^2$  distribution function and P will be flat (fig. 6.7). An excess of events with low probability, means we have extra events with high fluctuations i.e., fluctuations are larger than the normal values for the  $\chi^2$  distribution.

After having computed the  $f(\chi^2)$  with mean value around one, we can calculate the probability distribution. Now, we should note that our  $\chi^2/ndf$  distribution is very good to compare events, but to calculate the probability, this is not good. In the next figure, we can quickly see that the  $\chi^2$  distribution change with the number of degrees of freedom. In this way, we can not use the shape of fig. 6.7 left directly with one degree of freedom,  $f(1df; \chi_{1df}^2) \neq f(\frac{Ndf}{Ndf}; \frac{\chi_{Ndf}^2}{Ndf})$ . Beside, each event has different degrees of freedom. To calculate the probability, we should compare the  $\chi^2$  of each event with the distribution of it's corresponding number of degrees of freedom ( $Ndf$ ). We will have for each event  $P(\chi_k^2) = P(Ndf; \chi_k^2 \times Ndf)$ .

Our probability distribution has not the expected flat behaviour (black line). As we can see, in the central probabilities we have a flat distribution, but with much less events. At the ends of the probability we have excess of events.

In one hand, at very high probabilities, we have high peak with a great excess of events, this means that we have more events with a shape close to a GH than what is expected. Or, we can conclude that the error considered is overestimated.

In the other hand, we have another excess of events in the peak at low probability. This events will have a big  $\chi^2$ , so we have more events with shapes different from a normal GH than what is expected. Or the error

is underestimated, contradicting the previous one.

So even with the possibility that the errors are overestimated, we will have much more events behaving differently from a GH than that would be expected with gaussian fluctuations. We are interested, precisely in this events of the extremely high tale of the  $\chi^2$ .

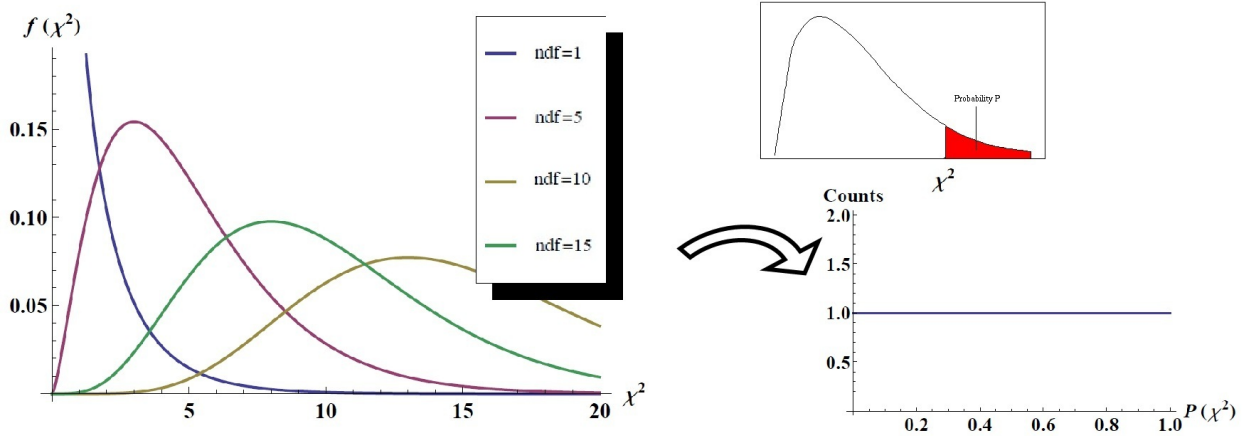


Figure 6.7: In left we have several  $\chi^2$  distributions, if we calculate  $\int_{\chi_k^2}^{\infty} f(\chi^2)d(\chi^2)$  we have the  $\chi^2$  probability, which is a flat distribution as we see in the left.

### 6.3 Extreme fluctuations

Since we are interested in not normal events, we will estimate the rate of extra events with high fluctuations. For that purpose, we plot a zoom of the  $P(\chi^2)$  distribution in the low probabilities area. In the figure 6.10, we have the probability from 0 to 0.006, the black line is the expected density consider for the 64000 events. We can see that we have a big excess of events in the peak around zero and if we make a zoom in this area (fig. 6.10b), we obtain again, a peak around zero, which means that basically the peak has not structure. So this events have  $\chi^2$  well above to what it should be.

In the beginning of the left figure, we have an excess and in the final we have less events than what is expected. The turning point where we move from an excess to a lack of events is  $P(\chi^2) \sim 0.0034$ . The number of events obtained with  $P(\chi^2) < 0.0034$  is 8792, while we expect  $n(P(\chi^2) < 0.0034) = 221$ . Therefore, we have 8571 more events with high fluctuations (events in the  $\chi^2$  tail), which amount for approximately  $\sim 13.4\%$  of the total events as extra strange events compared with normal statistical fluctuations.

We can repeat for the  $10^{18}eV$  sample and we have 17228 events with  $P(\chi^2) < 0.0034$  for  $n(P(\chi^2) < 0.0034) = 428$  events expected. We have approximately 16800 extra event or  $\sim 13,8\%$ .

We can also see how many events are extra good fitted. In the figure 6.8, we can see that the turning point from lack to excess of event is approximately at  $P(\chi^2) > 0.985$  and we have 41730 extra events (42957 counted events with 1227 expected events). At  $10^{18}eV$  we have 82575 extra events (84444 events counted less 1869). So the extra good events with this error definition are  $\sim 65\%$  and  $\sim 67\%$  for  $10^{19}eV$  and  $10^{18}eV$  respectively.

#### 6.3.1 What are the extreme fluctuations

The event excess with low probability should have profiles with shapes very different from a GH function. So in the figure 6.11a, we plot the mean profile for the events in each zone. In blue we have the events with  $P(\chi^2) > 0.985$ , in red are the events with  $P(\chi^2) < 0.00345$ , in green are the events between the two areas. In violet and light blue we have the very bad and very good GH shape events respectively. Since we are look at mean profiles, we can not see much difference, but if we normalize all mean profiles to the mean profile of

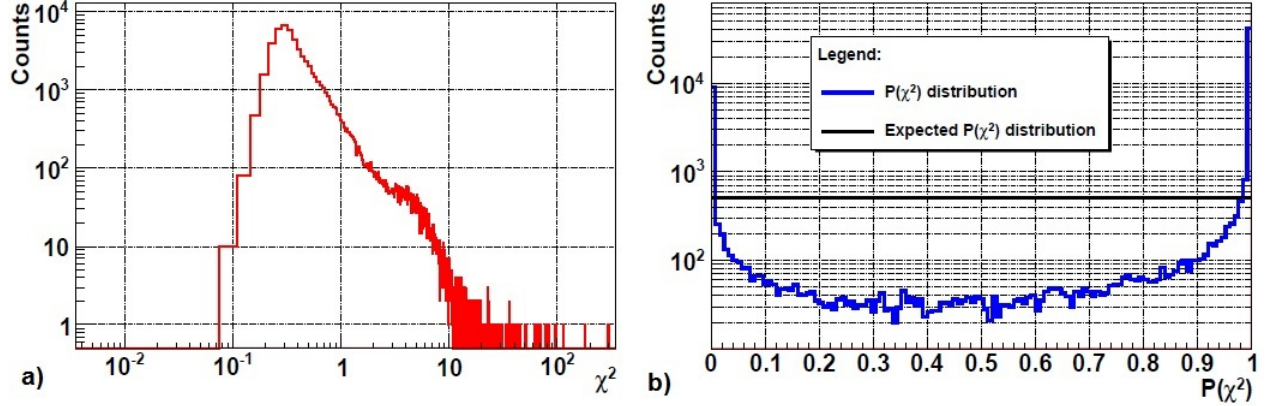


Figure 6.8: a)  $\chi^2$  distribution for the sample with  $10^{19}eV$ , b)  $P(\chi^2)$  for the same events, the black line represents the expected distribution for events with gaussian fluctuations.

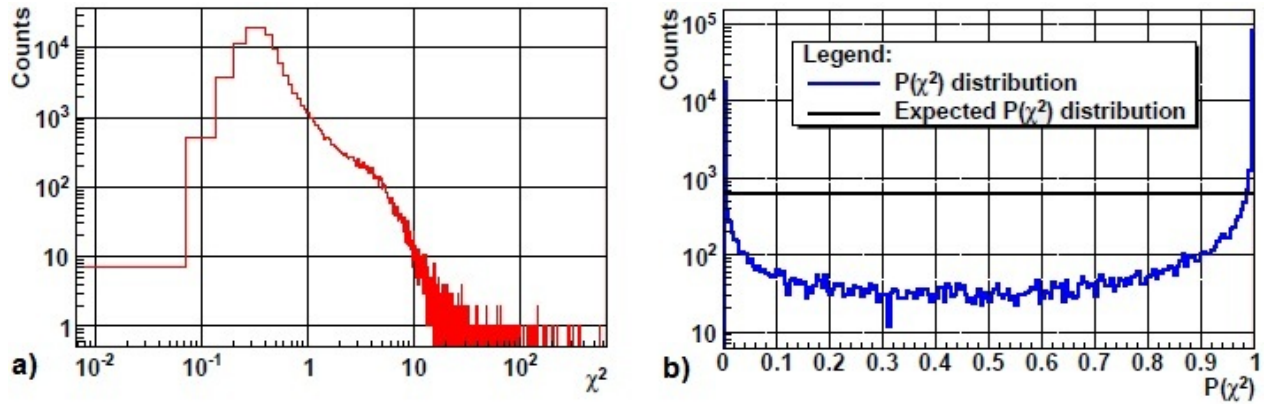


Figure 6.9: a)  $\chi^2$  distribution for the sample with  $10^{18}eV$ , b)  $P(\chi^2)$  for the same events, the black line represents the expected distribution for events with gaussian fluctuations.

the  $P(\chi^2) > 0.985$ , in the figure 6.11b we can see some differences.

For example, events with central probabilities are wider than the considered good events (with  $P(\chi^2) > 0.985$ ). The extreme event are even more wider than the normal events. In order to see exactly the differences we can plot the density of all profile. In the figure 6.11c, we have the density of the profiles with low probabilities in colour scale and with the black lines we have the density of the good events. The normal events, besides being many more they are concentrated around the normal mean profiles. The extreme profile have big variations between each other and strange profiles. For example, the red, light blue and pink profiles in figure 6.1 are some of these profiles.

The extreme profiles are wider and sometimes even have two peak, which are called double bangs. The main reason of this shapes in simulation is the production of particle in the first interactions with a big fraction of the total energy. If this particle travels a big distance before interacts again, we will have shape as a sum of two GH (one from the energetic particle produced and other from the remaining particles), see next chapter for further detail.

In real data, besides this statistical feature, we could have another exotic scenarios that could produce such different behaviour. For example, a production of a mini black hole with a big multiplicity in it's evaporation, or a production of new kinds of particle with that could interact more weakly.

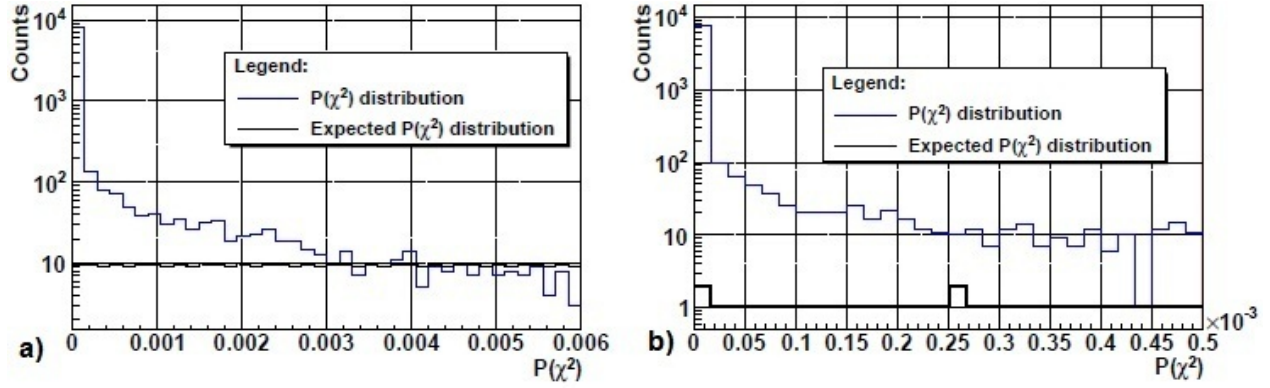


Figure 6.10: Zoom of the low  $\chi^2$  probability zone for the sample of  $10^{19}eV$ . We see that even with a big zoom (left) we still have a peak of events around the zero. The excess of events are at about  $P \lesssim 0.035$ .

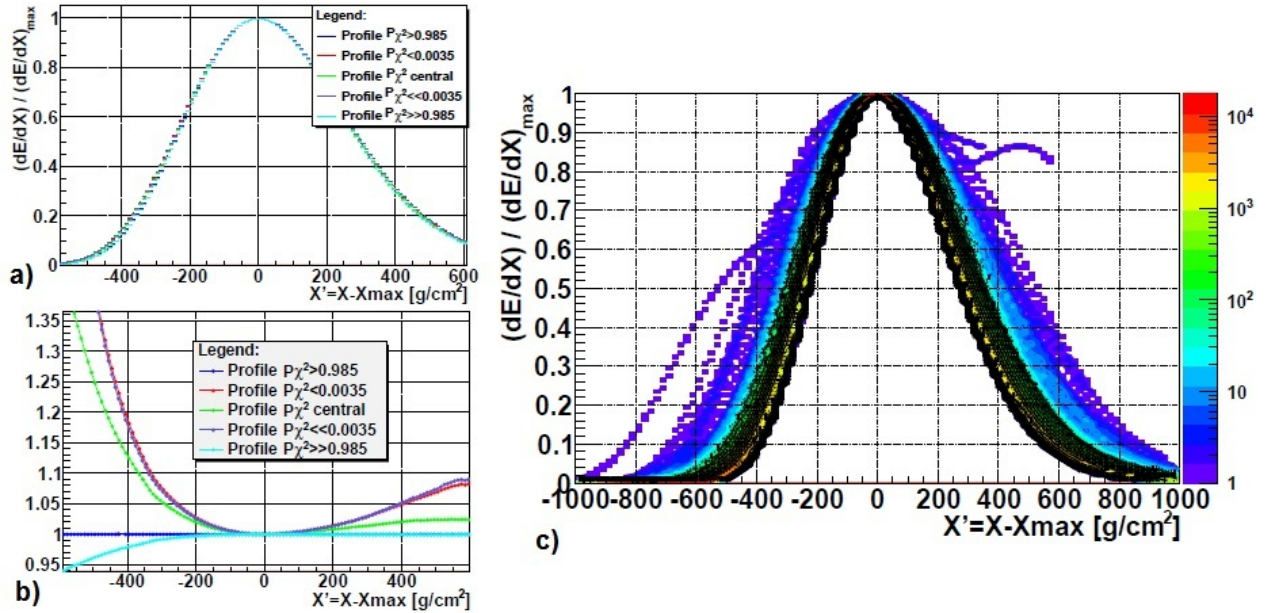


Figure 6.11: a) are plotted the mean profiles for several samples of the  $10^{19}eV$  sample. In blue the events of the peak with high probability, in red the events with low probability and in green the events between the two. In violet and light blue we have the events with very low and high probability respectively. b) we present the mean profiles normalized to the profile for the peak with high probability (which are assumed to be the good events). c) in colour we have the density of shower profiles for low probability and above in black are the density for high probability.

## 6.4 Full Simulation

To really understand real events we have to simulate the detectors. With the Offline framework [114], we can simulate the events, in the figure 6.12, we have the reconstruction of the red event in the figure 6.1. If we look at the events in fig. 6.1a) we see that we need  $\sim 1300g/cm^2$  slant depth ( $X$ ) crossed to catch the shape of the interesting events. The red one, has the second peak at  $\sim 1250g/cm^2$ , the change of the down slope in the light blue event are notorious at  $\sim 1300g/cm^2$  and to catch all pink event we need this big slant depth too. So if Auger is at  $\sim 1400m$  above the sea level, in vertical showers we will cross  $\sim 875g/cm^2$ , this is very far from the minimum slant depth we need. In this way, vertical shower will hide many information

of the shower profiles and we need to read showers at higher angles, increasing  $X$ . The minimum angle at which we could see the all interesting shape is  $\sim 47$  degrees. It's obviously that we could have more verticals showers that we can see the total shape but at this angle, we should see most of the shower behaviour.

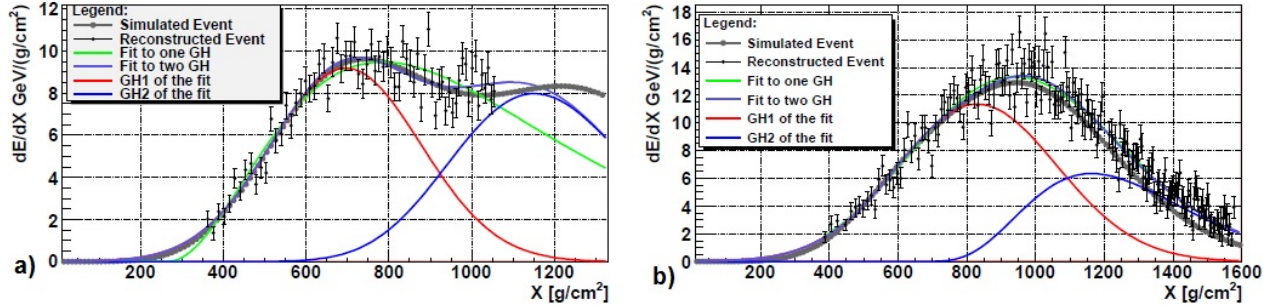


Figure 6.12: In gray we have the simulated event, in black is the reconstructed, in green is the fit to a GH and in violet is the fit to two GH (sum of the red and the blue one). The characteristics of the reconstructions are expressed bellow. The development of event a) was cut by the ground, so we are less sensitive to it's features, the events have  $E = 10^{19} eV$ .

	simulated event	reconstructed event
Event a)		
$\chi_{1GH}^2$	302.8	1.87
$\chi_{2GH}^2$	0.22	1.43
$\Delta X_{Rec}(g/cm^2)$	561.0	455.0
$K_{Rec}$	0.58	0.54
Event b)		
$\chi_{1GH}^2$	51.8	1.40
$\chi_{2GH}^2$	0.56	1.36
$\Delta X_{Rec}(g/cm^2)$	311.3	334
$K_{Rec}$	0.49	0.64

## Chapter 7

# Sensitivity to the leading particle

A most important result from the study of EAS are the indirect results about the interactions at very high energies (well above accelerators energies). The  $X_{max}$  and the muon number are values very important to infer the characteristics of the first interactions (which are at UHE). The muon number is related with the relative production between pions and baryons and their energies, while from the  $X_{max}$ , we can obtain the elongation rate, which is related to the interaction length (or cross section).

Despite this variables, in this chapter we will try to find a way to study the features of the first interaction using two Gaisser-Hillas function. We use the same simulations samples of the previous chapter.

### 7.1 Two Gaisser-Hillas approximation

The primary particle (cosmic ray) will interact in atmosphere producing particles, which in turn produce more particles and then the cosmic ray develops into an air shower. The shower's longitudinal shape is described by a Gaisser-Hillas function (GH).

The primary particle interacts at the mean value  $X_0 \equiv \lambda_0 \sim 43g/cm^2$  in slant depth (this is the first interaction, see table 7.6). This particle will produce  $n$  particles (see multiplicity in section 4.3.4.2), in which the most energetic particle is called the leading particle and it has in average  $\sim 45\%$  (fig. 4.9) of the primary energy. So if the primary particle has  $10^{19}eV$ , then the leading could have  $\sim 4.5 \times 10^{18}eV$  and the sum of the other particles will be  $\sim 5.5 \times 10^{18}eV$ . This means that the leading particle has enough energy to produce a big air shower. Since the leading has such high energy, it will have a long life, so it has to interact with the atmosphere. This leading interacts at  $X_1$ , see fig. 7.1. The distribution of the  $\Delta X_{Gen} \equiv \Delta X = X_1 - X_0$  is given by  $f(\Delta X) \sim e^{-\Delta X/\lambda}$ , where  $\lambda$  is the interaction length.

The particles produced by the development of the leading will slightly interact with the particles coming from the development of the non-leading particles. However, since the energy of the leading development has higher energy, then we can consider that the particles coming from the leading will be almost independent from the rest, and then we can assume that the leading produces an air shower with energy  $E = E(leading)$  and with approximately GH shape. The other particles, since they are also independent from leading's evolution, then they will develop another air shower with GH shape and energy of  $E = E(primary) - E(leading)$ . The result is that we don't have one GH, but two GH.

We also can continue with this assumptions at higher order, and say that when the leading interacts at  $X_2$  (called second interaction), we will have again a second leading particle of the first leading particle, see figure 7.1.

Here we write again the GH shape, but in R and L variables (from 6.3) we have:

$$dE/dX(X) = (dE/dX)_{max} \left(1 + \frac{R(X - X_{max})}{L}\right)^{R-2} \exp\left(-\frac{X - X_{max}}{LR}\right) \quad (7.1)$$

where  $dE/dX(X) \propto N(X)$ . In this chapter, we will work with a longitudinal profile defined as (see figure 7.1 for an example)

$$dE/dX(X) = \{dE/dX(X)\}_{leading} + \{dE/dX(X)\}_{rest} \quad (7.2)$$

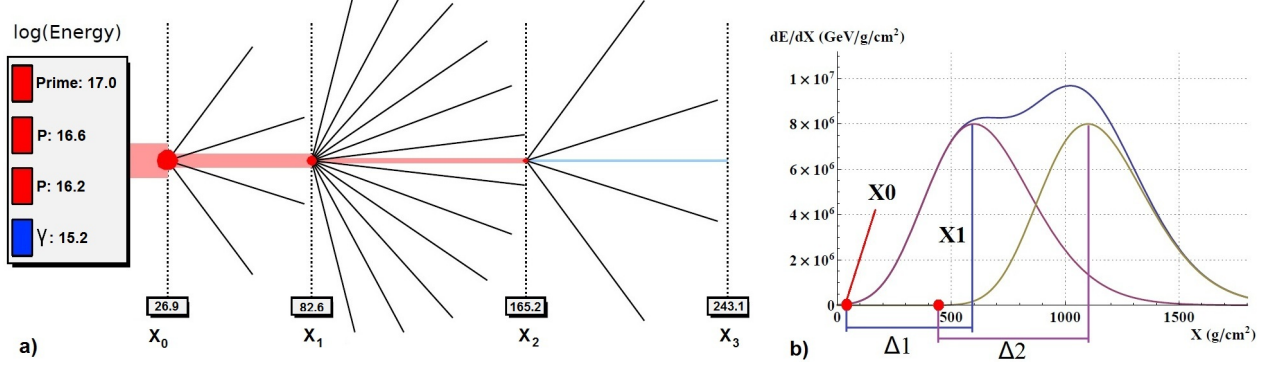


Figure 7.1: a) draft of the initial development of an air shower, the primary particle interacts at  $X_0$  producing multiple particles, in red we have the leading particle with  $\sim 0.6$  of the total energy ( $K \sim 0.4$ ), at  $X_1$  the first leading interacts producing a second leading and so on (adapted from [117]). b) we have a scheme of a sum of 2GH with  $\Delta X = 500g/cm^2$  and  $K = 0.5$ .

Since the leading will travel a distance before developing, we consider that the second GH (with higher  $X_{max}$ ) will be the leading GH. The  $(dE/dX)_{max}$  of a GH is  $(dE/dX)_{max} \propto E_{primary}$  (fig. A.2), so we considered that  $\{(dE/dX)_{max}\}_{leading} \propto E_{leading}$  and the same for the other GH. For now on the second GH will be the leading ( $\{(dE/dX(X))\}_{leading} = \{(dE/dX(X))\}_2$ ). Using the inelasticity, defined as  $k = 1 - \frac{E_{leading}}{E}$ , we can say that:

$$K_{Rec} = 1 - \frac{\{(dE/dX)_{max}\}_2}{\{(dE/dX)_{max}\}_1 + \{(dE/dX)_{max}\}_2} \quad (7.3)$$

Besides this value, we want to measure  $\Delta X_{Rec} = (X_{max})_2 - (X_{max})_1$ . We have that  $X_{max,i} = X_i + \Delta i$  (see fig. 7.1b), in this way, we want that  $\Delta X_{Rec} \simeq \Delta X_{Gen}$  and then:

$$\Delta X_{Rec} = (X_1 + \Delta 2) - (X_0 + \Delta 1) = X_1 - X_0 + (\Delta 2 - \Delta 1) \quad (7.4)$$

We need that  $\Delta 2 \simeq \Delta 1$ , to have  $\Delta X_{Rec} \simeq \Delta X_{Gen}$ .

In cosmic rays with  $10^{19}eV$ , we have a  $\langle X_{max} \rangle = 781.6g/cm^2$  and at  $10^{18}eV$  we have  $\langle X_{max} \rangle = 736.1g/cm^2$ , they have a difference of  $45.5g/cm^2$  ( $\sim 6\%$ ). Now consider that we have a leading particle with 90% or 10% of the total energy ( $10^{19}eV$ ), and the leading interacts in approximately the same slant depth that the first interaction, so in average value, the difference from the two  $X_{max}$  will be  $< 45.5g/cm^2$ .

In this way, even if the leading carry in average  $\sim 50\%$  of the energy (the others particle carries  $\sim 50\%$  too), than in this condition the two  $X_{max}$  will be almost equal. With those consideration, we have that  $\Delta X_{Rec}$  is equals to the interaction distance of the leading ( $\Delta X_{Gen} = X_1 - X_0 \sim \Delta X_{Rec}$ ). So to simplify, we need to have  $\Delta 1 = \Delta 2$  in the figure 7.1 b), but the fluctuations will give us some extra error in the  $\Delta X_{Gen}$  value.

### 7.1.1 Two Gaisser-Hillas approach test

To study the first interaction we proceed to fit the simulations to the equation 7.2. One GH function has 4 degrees of freedom,  $(dE/dX)_{max}$ ,  $X_{max}$ ,  $L$  and  $R$ . The two GH approximation will have 8 degrees of freedom, with so much freedom it is very difficult that the fit converge and the fitting result could be unstable and ambiguity.

In order to stabilize the fit, we will decrease the number of degrees of freedom, parametrizing one variable. We are mainly interested in  $(dE/dX)_{max}$  and  $X_{max}$ , we only could parametrize  $L$  and/or  $R$ . As we can see in appendix A, at  $10^{19}eV$  we have  $\langle L \rangle = 232.8g/cm^2$  with RMS (root mean square) of  $6.9g/cm^2$  and  $\langle R \rangle = 0.253$  with RMS of 0.019. The same behaviour can be observed until  $10^{16}eV$ , so L have much less fluctuations than R and we should parametrize L and expect that R absorbs the L fluctuation.

Again in appendix A, we have the parameter values at several energies and we can find the L by the

parametrization:

$$L = 5.734 \times \log_{10}((dE/dX)_{max}) + 190.83 \quad (7.5)$$

Without L parameter, we end up with 6 degrees of freedom in two GH approximation.

Consider that we could approximate the profile to two GH, we still have the problem of the convergence of the fits or if the fit procedure is adequate to reconstruct the 6 parameters (specially the 4 parameters that interest us). In this way, instead of using the simulations, in this section we sum two Gaisser-Hillas (with known parameters), and apply the fitting procedure to see if we can recover the original parameter.

Therefore we sum two GH with  $\Delta X$  ranging from 0 to  $600g/cm^2$  (with interval of  $50g/cm^2$ ), inelasticity  $k$  from 0.1 to 0.9 in 0.1 steps.  $L$  and  $R$  have gaussian fluctuation around the values parametrized by equation 7.5 and A.5 respectively. For further explanation see appendix B. In the figure 7.2, we see two examples of the fit with two GH and in the figure 7.3 are present the results for  $\Delta X$  and  $K$  from the fits compared with input. We divide the each results into two groups.

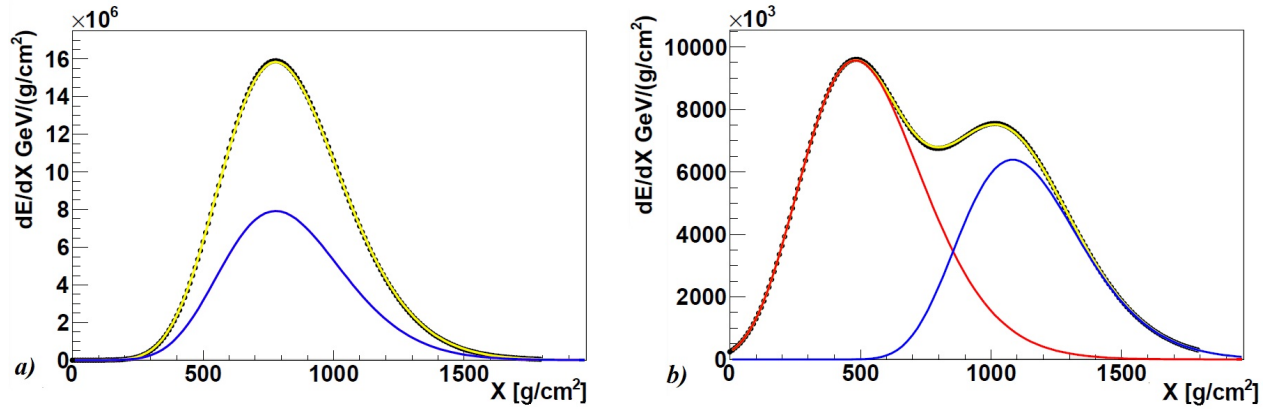


Figure 7.2: Two example of a 2GH fit to a sum of two known GH. a) original values of  $\Delta X_{Gen} = 50g/cm^2$ ,  $K_{Gen} = 0.6$ ,  $R = 0.255$  and  $0.245$  and  $L = 226.5$  and  $229.8g/cm^2$ , for the reconstruction values of  $\Delta X_{Rec} = 0.0g/cm^2$ ,  $K_{Rec} = 0.5$ ,  $R = 0.25$  and  $L = 230g/cm^2$ . b) original values of  $\Delta X_{Gen} = 600g/cm^2$ ,  $K_{Gen} = 0.6$ ,  $R = 0.272$  and  $0.300$  and  $L = 231.2$  and  $227.1g/cm^2$ , for the reconstruction values of  $\Delta X_{Rec} = 601g/cm^2$ ,  $K_{Rec} = 0.6$ ,  $R = 0.273$  and  $0.286$  and  $L = 230.6$  and  $229.3g/cm^2$ . As we see, by parametrizing  $L$  we introduce a little error in the results.

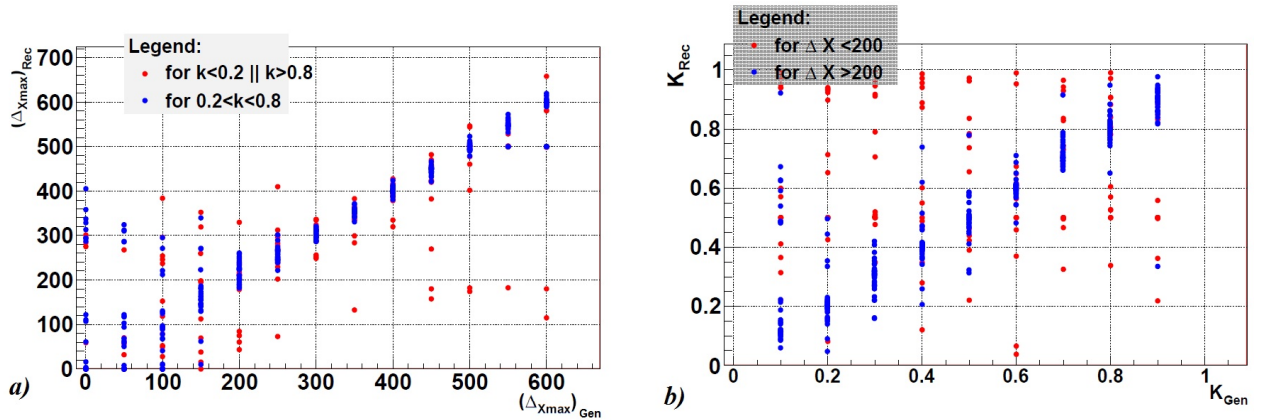


Figure 7.3: a) The  $\Delta X_{Rec}$  in function of  $\Delta X_{Gen}$ , b)  $K_{Rec}$  in function of  $K_{Gen}$ . We have better reconstruction with  $\Delta X_{Gen} > 200g/cm^2$  and  $0.2 < K_{Gen} < 0.8$ , see appendix A.

If the leading particle has very low energy compared with the primary, this means that the leading GH will be a small contribution to the overall GH shape, if it has almost all energy, then the final GH shape will come mainly from the leading GH, and the other GH will be a correction. Keeping this in mind, we make two groups in the  $\Delta X$  plot, in the figure 7.3 a) we can see that the events with  $0.2 < K_{Rec} < 0.8$  have a better  $\Delta X$  reconstruction (see the extra red points with bad reconstruction at  $\Delta X_{Gen} > 200g/cm^2$ ). Since we use a parametrization of  $L$ , if  $R$  and  $L$  input values for sum the two GH was a direct result from parametrization, the fits will converge very well. However in the reality the  $R$  and  $L$  have fluctuations and here we introduce some fluctuation too. In this way, since  $L$  has a distribution, by parametrizing  $L$  with equations, we introduce an error. This is the reason why the blue points make a band and not a line for  $\Delta X_{Gen} > 200g/cm^2$ . The slight difference in  $X_{max}$  carry some of the fluctuations in  $L$ . For  $\Delta X_{Gen} < 200g/cm^2$ , we see that the results are very bad. We have to note that if we sum two GH with the same parameters ( $X_{max}$  equals too) and  $K = 0.5$  ( $GH_1 = GH_2$ ) we obtain a normal GH with the same parameters and double  $(dE/dX)_{max}$ , ( $GH = GH_1 + GH_2 = 2 * GH_1$ ). In this condition if  $K$  varies, we find the same final result and the fit have difficulty to converge. Since we have fluctuation and  $L$  fixed,  $K_{Rec}$  and  $\Delta X_{Rec}$  will absorb the fluctuations too, but here with worst consequences. We can say that the procedure doesn't have so small resolution. If we think that the GH have a width, then only when  $\Delta X_{Rec}$  is bigger than this width, we could have such resolution. As we told before,  $L$  is approximately the longitudinal width of a GH, so the resolution will be something like  $\Delta X_{Rec} > L \sim 200g/cm^2$ . The events with different  $\Delta X$  don't have the same probability, being the probability given by  $f(\Delta X) = \frac{1}{\lambda} e^{-\frac{\Delta X}{\lambda}}$ . Since we want events with  $\Delta X > \Delta X_{cut}$ , than the total probability of this kind of event is  $P(\Delta X > \Delta X_{cut}) = \int_{\Delta X_{cut}}^{\infty} \frac{1}{\lambda} e^{-\frac{\Delta X}{\lambda}} d\Delta X = e^{-\frac{\Delta X_{cut}}{\lambda}}$ . In the figure 7.4 we see the rate of expected double bumps events considering  $\lambda \sim 45g/cm^2$ . we can see that we would have a very low statistics with high  $\Delta X$ .

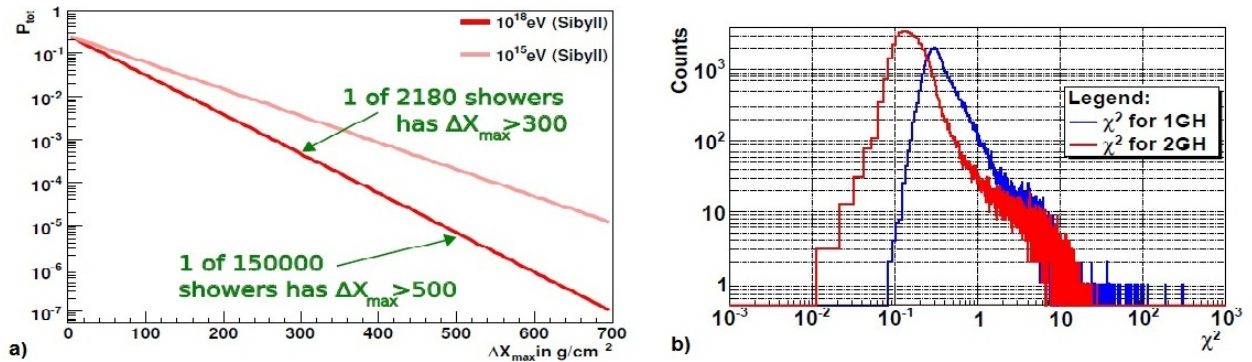


Figure 7.4: a) Probability of having a shower with a given  $\Delta X_{max} \equiv \Delta X_{Gen}$  taken from [117]. b)  $\chi^2_{1GH}$  and  $\chi^2_{2GH}$  distributions of the  $10^{19}eV$  sample,  $\langle \chi^2_{1GH} \rangle = 1.00$ ,  $\langle \chi^2_{2GH} \rangle = 0.75$ .

## 7.2 Two Gaisser-Hillas approach results

In this section we will analyse the result of the two GH fit to simulated events. Our sample has 64000 events with energy  $10^{19}eV$ , it is the same used in chapter 6. In this sample, we cut only 20 events, because they hit the Earth ground (in simulation it is the sea level), before reaching the shower maximum, or the 2GH fit doesn't converge.

Another feature is that we want to measure the interaction length, so for now we only consider the leading particle that interacts, and don't consider the particles that decay. In this way, we loose 12608+20 events and we use only 51372 events. The fitting method is the same used in section 7.1.1, we fix  $L$  parameter with equation 7.5.

The  $\chi^2$  results of the fit with one and two GH, in our final sample, are plotted in figure 7.4. We obtain the expected value of  $\langle \chi^2_{1GH} \rangle = 1$  for one GH fit, and for the two GH fit, we expect a lower mean value,

since we have more degrees of freedom and the points can be better fitted. The value for two GH is now  $\langle \chi_{2GH}^2 \rangle = 0.75$ .

### 7.2.1 Selections

In section 7.1.1, we see that we can not use all range of the parameter to analyse the fit results, since for example at small  $\Delta X$  we don't have resolution to really trust the results.

To see in what regions we should or not consider the results we make some plots of the fraction  $(\Delta X_{Rec} - \Delta X_{Gen})/\Delta X_{Gen}$ . In the figure 7.5a), we have  $(\Delta X_{Rec} - \Delta X_{Gen})/\Delta X_{Gen}$  with the color scale, in function of  $\Delta X_{Rec}$  and  $\Delta X_{Gen}$ , in b) we plotted the number of events in the color scale. This plot is very trivial since the events within the straight line ( $y = x$ ) will be the optimums events. But we can also see that if we cut the region with  $\Delta X_{Gen} < 150g/cm^2$  and  $\Delta X_{Rec} < 150g/cm^2$ , we eliminate the most problematic events (but we reduce considerably the statistics). This is the Selection 1 with 932 in 51376 event selected.

In the figure 7.6, at  $\Delta X_{Gen} \gtrsim 150g/cm^2$  we have good events, but at  $K_{Gen} \gtrsim 0.9$  and  $K_{Gen} \lesssim 0.1$  the events are worst, so as we told before we should cut on  $K_{Gen}$ .

We have to note that in the real data we don't have access to the  $K_{Gen}$  or  $\Delta X_{Gen}$  and we should see only the reconstructed values. In the fig. 7.7 we plot this values obtaining a picture more difficult to interpret. We should note that, the events with small  $\Delta X_{Rec}$  are almost all distributed in the  $K_{Rec} \sim 0.5$  region. This happens, because we should have one GH and not two, the two GH that are summed will have very similar parameter to form one GH, so the value  $K_{Rec}$  doesn't make much sense in this region (see section 7.1.1).

In figure 7.8, we plot the  $\chi^2$  for one GH ( $\chi_{1GH}^2$ ) and for two GH ( $\chi_{2GH}^2$ ). It is interesting to note that we have a very pronounced transition in this plot, where for  $\chi_{1GH}^2 > \chi_{2GH}^2$  we have bad fits. This means that if the events don't behave like one GH, then it's behave better like two GH. So we should include a security cut rule with  $\chi_{1GH}^2 > \chi_{2GH}^2$ .

To better understand the reconstruction behaviour of our selections we should study the distribution of  $\Delta X_{Rec}/\Delta X_{Gen}$  and  $K_{Rec}/K_{Gen}$ , the selections we choose must have a pick at 1. In this way, we plotted the pictures in fig. 7.9 for the selections considered.

The Selection 1 as already explained. The 2nd selection will be in the generator parameters and it should be the golden cut, besides it can be used in real events. According to section 7.1.1, we only have good resolution in  $\Delta X \gtrsim L$  and  $0.2 < K < 0.8$  and in fig. 7.7, we see that this selection could be open. So being  $L \sim 230g/cm^2$ , from the figure, we can cut at  $\Delta X_{Gen} \lesssim 200g/cm^2$ . In K we should keep our original cut in  $0.2 < K_{Gen} < 0.8$ , because we will not have shore of the results with higher or lower  $K$  and include the security cut.

However, the important cuts will be in reconstruction parameters and selection 3 and 4 will be in this parameters. Selection 3, has a trivial cut in K of  $0.2 < K_{Rec} < 0.8$ , in  $\Delta X$ , since we introduce some error in the parametrization of  $L$  we should increase the cut to  $\Delta X_{Rec} > 250g/cm^2 > L$  (which is a little higher than  $L$ ). This selection has a cut in  $P(\chi_{1GH}^2) < 0.0035$ , based on previous chapter and even if an event has an higher  $\chi_{1GH}^2$  (or lower  $P(\chi_{1GH}^2)$ ), it still could have a bad fit to 2GH. So we cut in  $\chi_{2GH}^2 < 2.5$  to get rid of the spread point in fig. 7.8 that have similar  $\chi_{1GH}^2$  and  $\chi_{2GH}^2$ .

Since the extreme events with very high  $\chi_{1GH}^2$  are supposed to be good, we make the selection 4 with  $\chi_{1GH}^2 > 15$  and  $\chi_{2GH}^2 < 2.5$ . The selections are written in table 7.1. The 4 selections rules are independent from each other.

In the figure 7.9, we can see that the selection 2 have a very narrow peak around 1, how it should, since the reconstruction is consider to be good in this region. The selection 3 for it's hand, have a peak around 1 too, with very few event with  $\Delta X_{Rec}$  underestimated, but have many events with this value overestimated.

In figure 7.10 we plot  $K_{Rec}$  in function of  $K_{Gen}$  and  $\Delta X_{Rec}$  in function of  $\Delta X_{Gen}$  for the selection 3 in the left and for selection 2 in the right. In left (selection 3), we see too many event with  $\Delta X_{Rec}$  high, while  $\Delta X_{Gen}$  is very small. The blue points are the slope of the graphic points, from the point where the blue point is, until the end of the graphic (or end of  $\Delta X_{Gen}$ ), the slope is multiplied by 200 in order to be seen. From them, we conclude that we have approximately a linear relation between the two if  $\Delta X_{Gen} > 200g/cm^2$ . In graphic for  $K$ , we see a very weak relation. We should note that we have big  $\Delta X_{Rec}$  for small  $\Delta X_{Gen}$  and small  $\chi_{2GH}^2$ , so we should conclude that the first interaction don't makes the two GH behaviour, but other thing should do it.

On the other side, in selection 4 we see an almost perfect relations between generated values and reconstructed

ones for  $\Delta X$  and for  $K$ . The reconstruction seems to work at input parameters cut, but not in reconstructed parameters cut. However, if the selection 3 only have good fits with small  $\chi_{2GH}^2$ , so why this seems to do not work at selection 3? In section 7.3, we will see that. We also make this selections to the  $10^{18}eV$  sample.

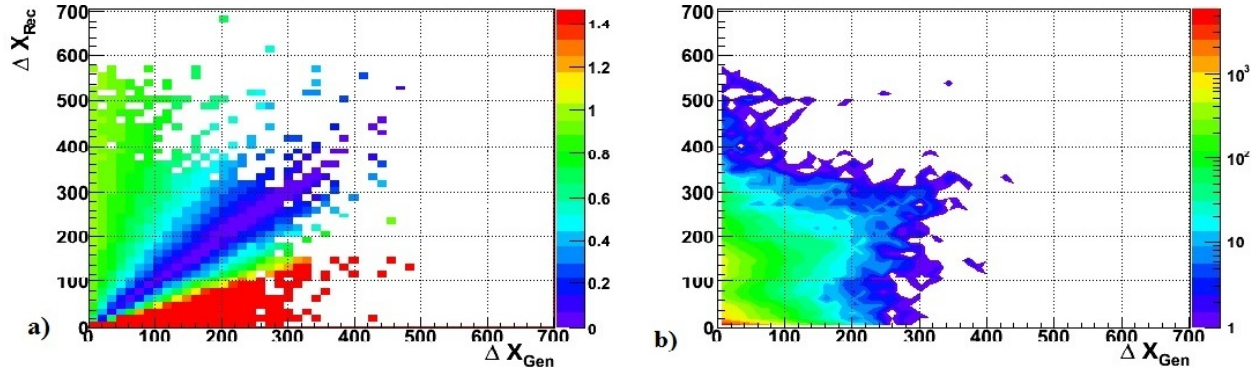


Figure 7.5: a)  $(\Delta X_{Rec} - \Delta X_{Gen})/\Delta X_{Gen}$  in colour scale and b) number of event in colour scale, in function of  $\Delta X_{Rec}$  and  $\Delta X_{Gen}$ .

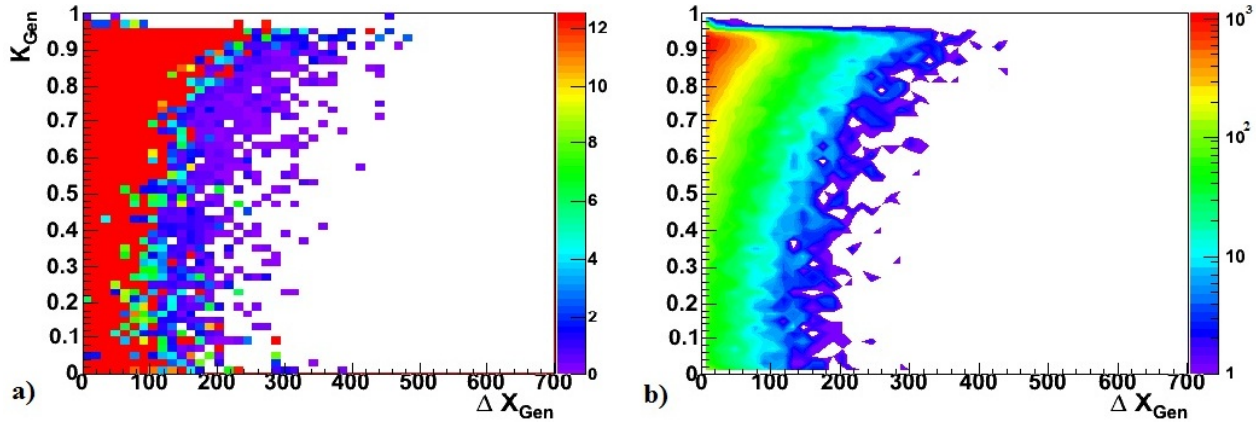


Figure 7.6: a)  $(\Delta X_{Rec} - \Delta X_{Gen})/\Delta X_{Gen}$  in colour scale and b) number of event in colour scale, in function of  $\Delta X_{Gen}$  and  $K_{Gen}$ .

Selections	number of events		
	(sample $10^{19}eV$ )	(sample $10^{18}eV$ )	
All events	with > 1 interactions saved	51376/64000	103084/122000
Selection 1	$\Delta X_{Gen} > 150 \wedge \Delta X_{Rec} > 150$	932	2570
Selection 2	$\Delta X_{Gen} > 200 \wedge K_{Gen} > 0.2 \wedge K_{Gen} < 0.8$ $\wedge \chi_{1GH}^2 > \chi_{2GH}^2$	261	830
Selection 3	$\Delta X_{Rec} > 250 \wedge K_{Rec} > 0.2 \wedge K_{Rec} < 0.8$ $\wedge \chi_{1GH}^2 > \chi_{2GH}^2 \wedge P(\chi_{1GH}^2) < 0.034 \wedge \chi_{2GH}^2 > 2.5$	174	625
Selection 4	$\chi_{1GH}^2 > 15 \wedge \chi_{2GH}^2 < 2.5$	101	391

Table 7.1: Number of events selected with the selection rules.

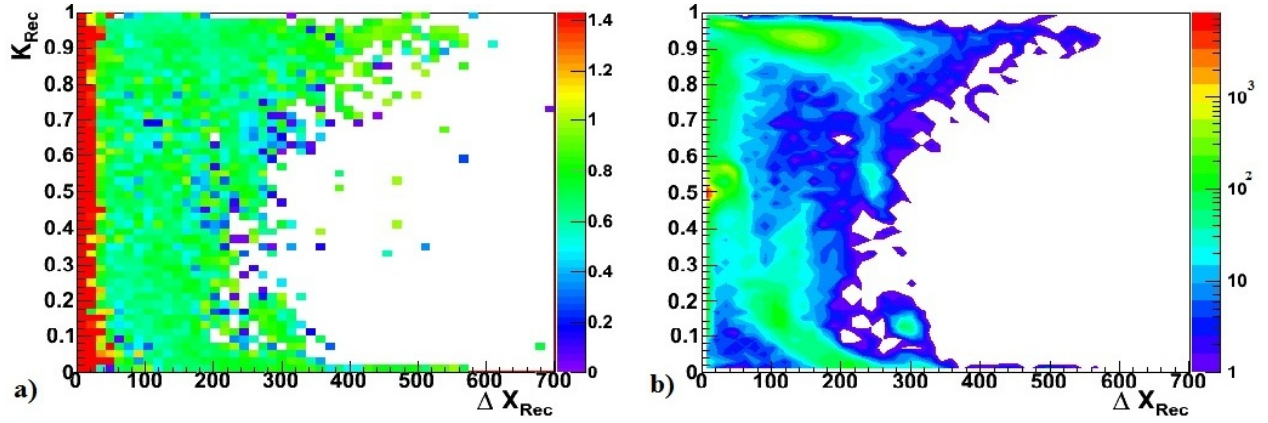


Figure 7.7: a)  $(\Delta X_{Rec} - \Delta X_{Gen})/\Delta X_{Gen}$  in colour scale and b) number of event in colour scale, in function of  $\Delta X_{Rec}$  and  $K_{Rec}$ .

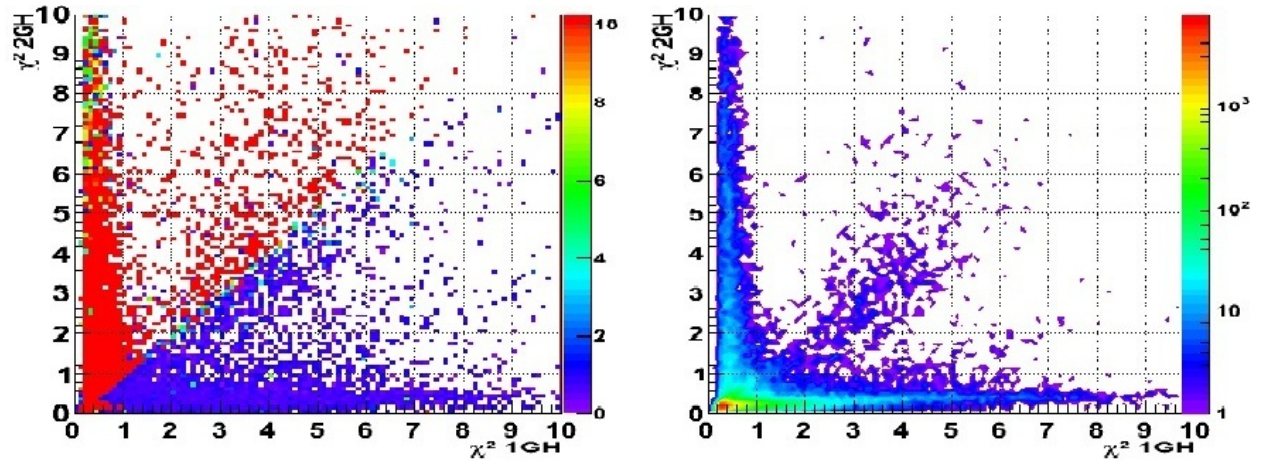


Figure 7.8: a)  $(\Delta X_{Rec} - \Delta X_{Gen})/\Delta X_{Gen}$  in colour scale and b) number of event in colour scale, as function of  $\chi^2_{1GH}$  and  $\chi^2_{2GH}$ .

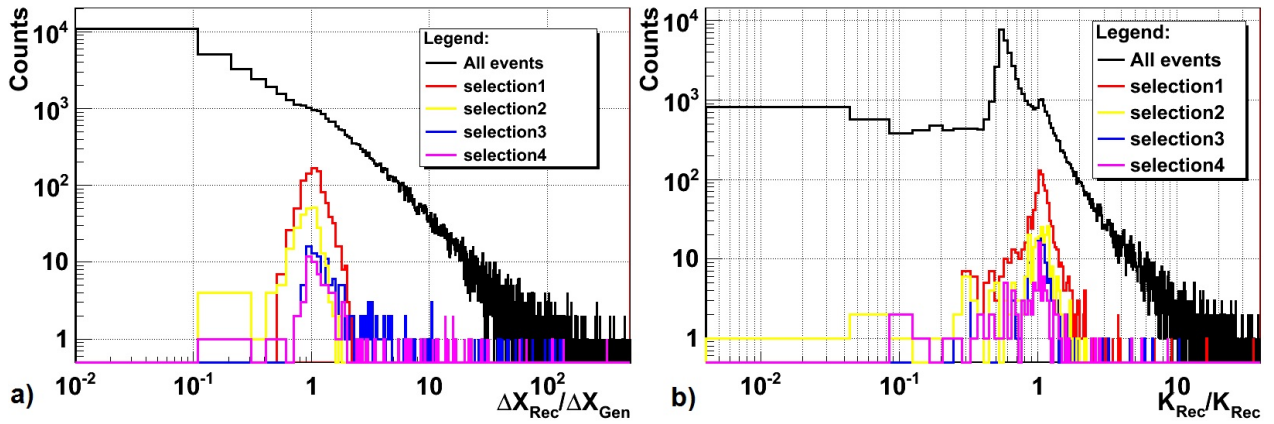


Figure 7.9: a)  $\Delta X_{Rec}/\Delta X_{Gen}$  distribution, b)  $K_{Rec}/K_{Gen}$  distribution for the 4 selection. The Selection 5 is Selection 1 +  $\chi^2_{1GH} < \chi^2_{2GH}$ , where we can see that we lost many events.

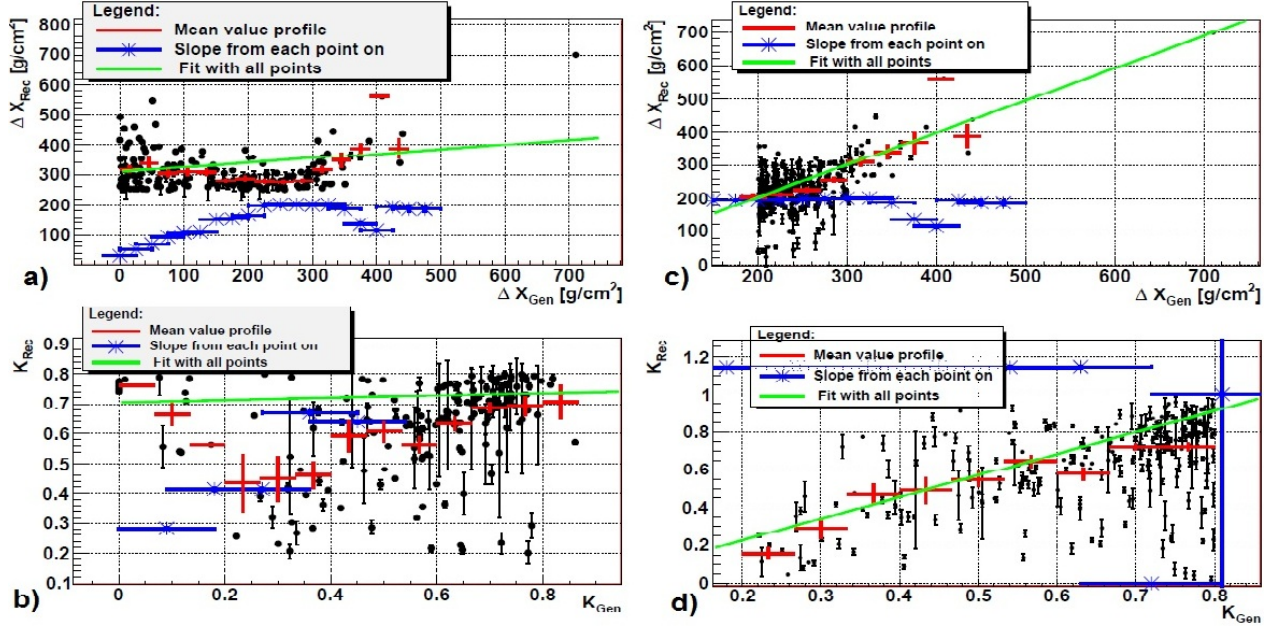


Figure 7.10: a) and c)  $\Delta X_{Rec}$  in function of  $\Delta X_{Gen}$ , b) and d)  $K_{Rec}$  in function of  $K_{Gen}$ . a) and b) for selection 3 and c) and d) for selection 2. The blue points are the slope of the points (in a) and b) multiplied by 200), in red is the mean profile of the points, in green is the linear fit ( $a * x + b$ ) with all point. a)  $a = 0.135 \pm 0.002$  b)  $a = 0.001 \pm 2.10^{-5}$  c)  $a = 0.973 \pm 0.003$  and d)  $a = 1.141 \pm 0.001$ . We have a good response in selection 2, but in a) if  $\Delta X_{Rec} \gtrsim 250 \text{g/cm}^2$  the slope is approximately 1.

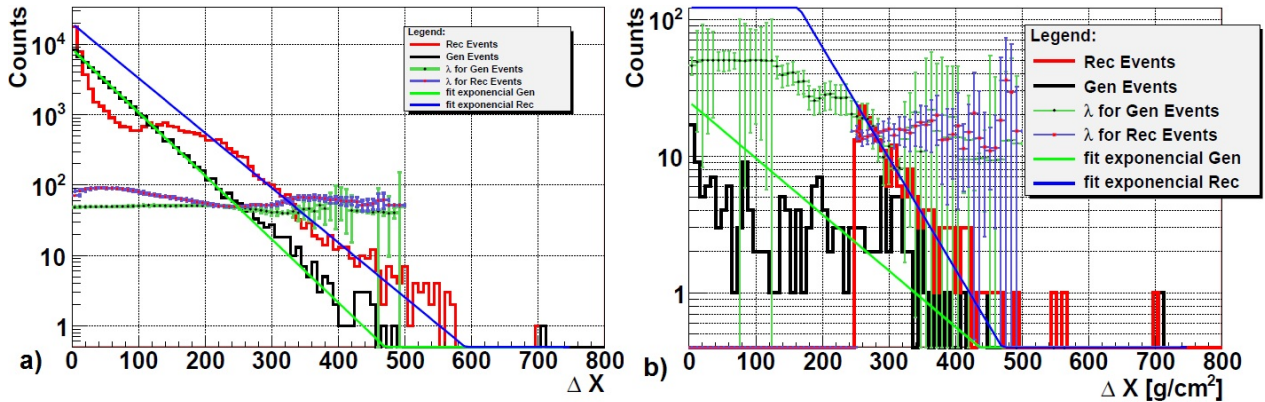


Figure 7.11:  $\Delta X$  distributions for a) all events and b) events of selection 3. In green and blue we have the fit to equation  $conste^{-\Delta X/\lambda}$  for  $\Delta X_{Rec}$  and  $\Delta X_{gen}$  respectively (blue fit it for  $X > 250 \text{g/cm}^2$ ), green and blue points are the  $\lambda$  values for  $X$  bigger than the  $X$  point.

## 7.2.2 Interaction length and Inelasticity

We assume that  $\Delta X_{Rec} \sim X_1 - X_0$  and that  $K_{Rec} \sim 1 - E_{leading}/E_{primary}$ , so in the figure 7.11 and 7.12, we plot their distribution.

In fig. 7.11 we have the distribution of  $\Delta X_{Rec}$  (in red) and  $\Delta X_{Gen}$ (in black). With black point and green error bars, we have the  $\lambda$  for the generated values, each point is the  $\lambda$  corresponding to the points from where

it's plotted to the end of the distribution. The result for the generated values are very constant, but for reconstructed ones they change with  $\Delta X$ . In the reconstructed  $\lambda$  distribution, we see that it is unstable for  $\Delta X < 200g/cm^2$  since as was been told, for small  $\Delta X$  our fit doesn't work well. However at high  $\Delta X$  they have a good behaviour with systematic higher  $\Delta X$  than the generated one as we see in previous section.

In the figure, with black point and green error bars, we have the  $\lambda$  for the generated values, each point is the  $\lambda$  corresponding to the points from where it's plotted to the end of the distribution. The result for the generated values are very constant, but for reconstructed ones they change with  $\Delta X$ . In the reconstructed  $\lambda$  distribution, we see that it is unstable for  $\Delta X \lesssim 250g/cm^2 \sim L$  since as was been told, for small  $\Delta X$  our fit doesn't work well. However at high  $\Delta X$  they have a good behaviour with systematic higher  $\Delta X$  than the generated one and it looks like a exponential dislocated from the generated values.

In b) are the events of selection 3, as we see, the reconstructed distribution does not correspond to the generated one, but without any doubt, we still have a good exponential from where we could extract an interaction length (see table 7.5).

The inelasticity distribution is plotted at fig. 7.12. In a) we see a big peak at  $K = 0.5$ , we already talk about these events in section 7.2.1, they are the event with very small  $\Delta X$ , where the fits tends to make two similar GH. We are not sensitive to the diffractive peak at  $K = 0$  as we expected. In b) we see the distribution for the selection 3 events, where the reconstructed values in mean have bigger  $K$ .

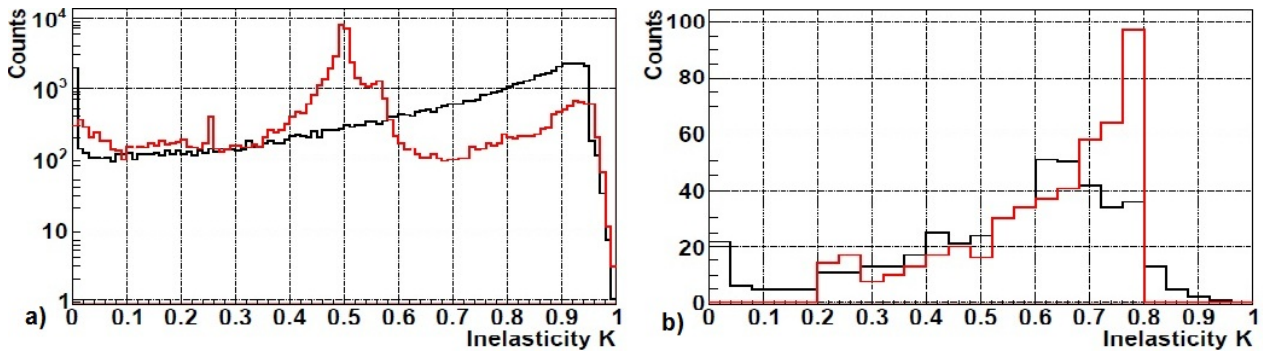


Figure 7.12: The inelasticity ( $K$ ) distribution for a) all events and b) selection 3. In red is  $K_{Rec}$  and in black is  $K_{Gen}$ .

### 7.3 Results interpretation

In this section, we try to study the real meaning of the reconstructed values.

In the previous section, we see that using the same cutting rules in the  $K_{Rec}$  and  $\Delta X_{Rec}$  as in the generated ones, we have some good events, but a great number of them have a much higher value of  $\Delta X_{Rec}$  than  $\Delta X_{Gen}$  and since they have good fit with low  $\chi^2_{2GH}$  we shall conclude that in some cases we are not measuring the  $\Delta X_{Gen}$  but other thing with the same effect. For example, in the figure 7.13 we see two event with low  $\Delta X_{Gen}$  but high  $\Delta X_{Rec}$ . The fits have a good  $\chi^2_{2GH}$ , so what's the reason for such different  $\Delta X$ ?

The second event has  $\Delta X_{Rec} = 446.7g/cm^2$  but  $\Delta X_{Gen} = 14.1g/cm^2$ . However,  $K_{Gen} = 3.2 \times 10^{-8}$  so this is a diffractive interaction and we will not measure it, we will measure the second leading until the third interaction. The second leading carries 0.26 of the total energy ( $K = 0.74$ ) and travels  $\Delta X = 529.6 - 54.5 = 475.0 \pm 10.24g/cm^2$  until the third interaction. This is exactly what we measure, and the  $K_{Rec} = 0.77 \pm 0.04$  which is very close to what is expected.

The first example is more difficult, we have  $\Delta X_{Rec} = 440.7g/cm^2$ , but  $\Delta X_{Gen} = 155.1g/cm^2$ . The first leading carries 0.68 of the primary energy, while the second leading travels  $\Delta X_{L2,Gen} = X_2 - X_1 = 485.0 - 188.5 = 296.6g/cm^2$  with 0.72 of the first leading energy.

The first leading travels  $155g/cm^2$ , this value is around the width of a GH, so we will have difficult to distinguish the 32% energy of the 1GH from the 68% of the second. Moreover, since the second leading carries much energy and travels a distance higher than the GH width, than those 2GH should have 19% of

the energy. We can conclude that the first and second GH will be seen as only one GH with  $19\% + 32\% = 51\%$  and the second leading particle will produced a observable second GH with  $68\% * 72\% = 49\%$  of the energy. This is exactly what we see, with  $K_{Rec} = 0.59 \pm 0.04$ .

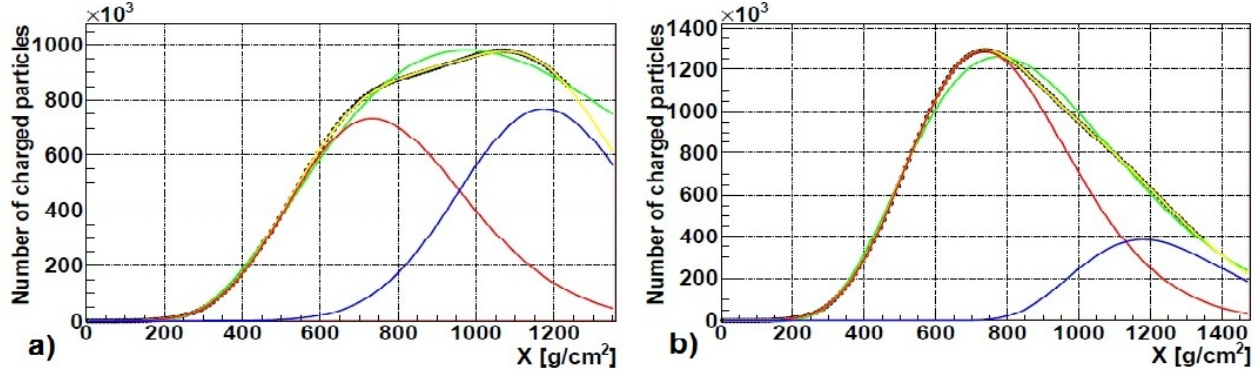


Figure 7.13: Examples of two events from  $10^{18}eV$  sample. In green we have 1GH fit, in yellow the 2GH fit (and sum of the blue and red GH).

a)  $\chi^2_{1GH} = 4.49$  vs  $\chi^2_{2GH} = 0.04$ ,  $\Delta X_{Rec} = 440.7g/cm^2$  vs  $\Delta X_{Gen} = 155.1g/cm^2$  and  $\Delta X_{L2,Gen} = 296.6g/cm^2$ ,  $K_{Rec} = 0.488$  vs  $K_{Gen} = 0.324$  and  $K_{L2,Gen} = 0.280$  ( $X_0 = 33g/cm^2$ ,  $X_1 = 188g/cm^2$  and  $X_2 = 485g/cm^2$ ).

b)  $\chi^2_{1GH} = 6.41$  vs  $\chi^2_{2GH} = 0.01$ ,  $\Delta X_{Rec} = 446.7g/cm^2$  vs  $\Delta X_{Gen} = 14.1g/cm^2$  and  $\Delta X_{L2,Gen} = 475.1g/cm^2$ ,  $K_{Rec} = 0.771$  vs  $K_{Gen} = 3.2 \times 10^{-8}$  and  $K_{L2,Gen} = 0.743$  ( $X_0 = 40g/cm^2$ ,  $X_1 = 55g/cm^2$  and  $X_2 = 530g/cm^2$ ).

In the figure 7.12 we see the inelasticity distribution, we have a diffractive pick at  $K \sim 0$  with lots of events, so if we have one of this events, we could have for example  $\Delta X_{Gen} \sim 50g/cm^2$  and  $\Delta X_{Gen} \sim 0.95$ . In this case we will not be able to see the shower with 5% of the energy. But when the leading particle with 95% of the energy interacts in a second interaction (at  $X_1$ ), we could produce a second leading, this second leading will behave almost like the normal first leading. It can have  $K \sim 0.5$  and if it travels a great distance before interacts again (in  $X_2$ ) we will have a shower that develops from  $X_1$  (with half energy) and another that develops from  $X_1$  (with half energy too). In this way, instead of measuring the first leading interaction length, we measure the second one in  $\Delta X_{Rec}$ . These picture of measuring one leading or the other is not completely independent. We could have a leading with 0.8 of the energy which travels  $100g/cm^2$  and produces a second leading with 0.5 of the initial energy. If this second leading travels a big distance, than we will see a  $\Delta X_{Rec}$  as a convolution of the two distances. In our simulations sample we only have access to the particles produced in the 1st interaction and the particles produced by the first leading in the 2nd interaction and so on. Besides that, for now, we don't have access to information about the leadings that don't interact with the atmosphere. Therefore from our 64000 events at  $10^{19}eV$  we only can use 21493 which, with the selection cuts, gives very small statistics. We become with 95 events in selection 3. In order to solve this problem, we use now the sample with 122000 events at  $10^{18}eV$  (see table 7.1).

With this new sample we have approximately 50000 events with 3 interaction saved. In this sub-sample, we select 492 events (in selection 3), from these, we have 153 events that corresponds to the same  $\Delta X_{Gen}$  and  $K_{Gen}$  (see table 7.2). Part of the remaining events could come from the second leading, so we define  $K_{L2} = 1 - E_{secondleading}/E_{primary}$ , and  $\Delta X_{L2,Gen} = X_2 - X_1$ . If the events don't pass the previous selection in the first leading, than we are measure a more important contribution from the second leading if  $\Delta X_{L2,Gen} > 200g/cm^2$  and  $0.2 < K_{L2,Gen} < 0.8$ . This selection B contribute with 129 events. But what happens with the remaining 210 events?

We should not forget that in the first interaction there are produced more than one particle, so if one leading interacts with very small  $\Delta X_{Gen}$ , we still could have a second particle with a considerable amount of the initial energy (with high limit of 0.5). If the leading carries 0.45 of the energy, than a second particle can have until 0.45 of energy. So if this 2nd energetic particle in the 1st interaction travels a large distance, than we will see it in the 2GH shape and not the leading. In the table 7.2 we see that we have 69 events in this

conditions (selection C), which the second more energetic particle have  $K_{2,Gen} < 0.8$ . But we don't know how many of them can pass through the cut in  $\Delta X_{2,Gen}$ .

Besides these events, we still could have a second most energetic particle in the second interaction. If the first interaction is diffractive or at least almost diffractive, then this second more energetic particle could again have an energy until 0.5 of the primary. We have 12 events in these conditions (selection D).

Probably we could have other terms to explain the remaining events. In Appendix C, we plot the distribution of some variables for the new selections of the table 7.2 and see that they are very similar between each other, so if Selection 3C, looks like Selection 3A and Selection 3B, there is no reason to think that the fit works for these two, but not for the first one. The same applies to the selection 3E (with the remaining events). In this way, probably, most of the 210 events really have some physical information.

Consequently we can use the selection 3 as a good selection rule, but we are not measuring the leading properties, but instead, we are measuring a complicated convolution of the first leading, second leading and second particles with high energy and high  $\Delta X$ . If we are measuring something like  $\Delta X_{Gen} + \Delta X_{2L,Gen} + \dots$  this means that we measure a distribution of  $\lambda > \lambda_{1leading}$ . In this way we can give an upper limit for  $\lambda_{1leading}$ . Since we are not sensitive to the diffractive peak at 1st interaction, we will measure the second interaction. As the 1st leading will have basically the primary energy, then we can see the 2nd interaction like it was the first. Nevertheless, we will have extra events with high  $\Delta X$  compared to what we would measure only with one interaction, like in fig. 7.4 a). In the next table we plot the new selections of the sub-sample, selection 3.

	Selections	number of events (sample $10^{18}eV$ )
All events	with > 1 interactions saved	49736/122000
Selection 3	$\Delta_{Rec} > 250 \wedge 0.2 < K_{Rec} < 0.8$	492
	$\wedge \chi_{1GH}^2 > \chi_{2GH}^2 \wedge \chi_{1GH}^2 > 2.5 \wedge \chi_{2GH}^2 > 2.5$	
Selection 3A	$Selection3 \wedge \Delta_{Gen} > 200 \wedge 0.2 < K_{Gen} < 0.8$	153(426)
Selection 3B	$Selection3 \wedge \neg(Selection3A)$	129 (219)
	$\wedge \Delta_{L2,Gen} > 200 \wedge 0.2 < K_{L2,Gen} < 0.8$	
Remains	$Selection3 \wedge \neg(Selection3A) \wedge \neg(Selection3B)$	210
Selection 3C	$E_{2nd \ leading \ 1st \ interaction} > 0.2$	69
Selection 3D	$E_{2nd \ leading \ 2nd \ interaction} > 0.2$	12
Selection 3D	remaining events	129

Table 7.2: Number of events of sub selections of selection 3, see text for further explanation. In selection A and B, between parentheses is the number of event that pass the condition in  $K$ .

In the table 7.3, we separate the conditions of the selection 3 in several steps and plot the efficiency and purity of each step. The efficiency is defined as:

$$\begin{aligned}
\varepsilon_{Selection} &= \frac{\#selected \ events}{\#all \ events} \\
\varepsilon_{A(B)} &= \frac{\#A(B) \text{selection in the selection step}}{\#A(B) \text{selection in all events}} \\
P_{A(B)} &= \frac{\#A(B) \text{selection in the selection step}}{\#all \ events}
\end{aligned} \tag{7.6}$$

In this table we can see that the efficiency decreases as we add more cuts, but by its way, the purity has an increase in each step, so our selection rules are good. The last selection ( $\chi_{1GH}^2 > \chi_{2GH}^2$ ) has a very small impact, but it is important to keep, because it prevents events with a behaviour between 1GH and 2GH, that could be misleading.

In the end we can consider  $\sim 57.3\%$  as good events,  $\sim 16\%$  of events that are probably good and  $\sim 26\%$  of events that could be background.

Events with > 2 interactions saved						
Selections	# events	$\varepsilon_{Selection}$	$\varepsilon_A$	$\varepsilon_B$	$P_A$	$P_B$
All events	49736	1.0000	1.000	1.000	0.010	0.017
$P(\chi_{1GH}^2 < 0.034)$	7413	0.1490	0.722	0.569	0.050	0.064
$\wedge \chi_{2GH}^2 > 2.5$	6391	0.1285	0.695	0.560	0.056	0.073
$\wedge \Delta X_{Rec} > 250$	1343	0.0270	0.359	0.226	0.138	0.140
$\wedge K_{Rec} > 0.2 \wedge K_{Rec} < 0.8$	496	0.0100	0.299	0.156	0.310	0.262
$\wedge \chi_{1GH}^2 > \chi_{2GH}^2$	492	0.0099	0.297	0.154	0.311	0.262

Table 7.3: The efficiency and purity of the several steps in selection 3.

## 7.4 Interaction length and Inelasticity

### 7.4.1 Interaction length

In the figure 7.11 in section 7.2.2, we plot the  $\lambda$  distribution and see that we reconstruct a  $\Delta X$  with the exponential shape:

$$f(\Delta X) = const \times e^{-\Delta X/\lambda} \quad (7.7)$$

, from where we can extract the  $\lambda$  parameter, which is the interaction length. This figure is for the  $10^{18}eV$  sample, the distribution of the other sample is more or less the same, but with less statistics.

In section 7.3 we see that we can measure a complicated convolution of the first leading, second leading and second particles with high energy and high  $\Delta X$ . So we can have an upper limit for the  $\lambda_{1leading} < \lambda$ . In the table 7.5, we write the  $\lambda$  values and in table 7.6 we write the  $\lambda$  for each type of particle and effective values. We have to note that the  $\Delta X$  distribution are made for all type of particle that the leading could have and for all energies of those leading, which could vary from 5% to 100% of the total energy. As a result, the  $\lambda$  will be an effective value. With our cutting rules, we should have a leading with energy approximately from 0.2 to 0.8 of the total energy.

We have an input value of  $\lambda = 52.4 \pm 0.2g/cm^2$ , while in the reconstructed, we have higher  $\lambda$ . As should happen, the  $\lambda$  at  $10^{19}eV$  is lower than at  $10^{18}eV$ , since the cross-section is higher for the first one.

### 7.4.2 Cross section

With the interaction length  $\lambda$ , we can calculate the cross section  $\sigma$  using:

$$\sigma = \frac{1}{n \cdot \lambda} \quad (7.8)$$

$n$  is the number of target particles per unit volume. Since we have  $\lambda$  in  $g/cm^2$ , we could re-write it in  $m$  and we could use  $n$  in  $[m^{-3}]$ . Nevertheless the value of  $n$  and the density of atmosphere in  $g/cm^2$  change with altitude(see figure 3.3). In this way, is better to use  $n$  as the number of particles per unit gram, which is the same, but is independent of the altitude of the atmosphere. According to [31] and [115] the atmosphere have 78.09%  $N_2$ , 20.95%  $O_2$  and 0.96% others compositions (we will consider to be mainly argon). The mass numbers are  $A(N_2) = 2 * 14.01 = 28.02g/mol$ ,  $A(O_2) = 2 * 16.00 = 32.00g/mol$  and  $A(Ar) = 39.95g/mol$ , so the effective value will be  $A_{eff} = 28.97g/mol$ . In this way  $n$  will be:

$$n = \frac{N_A}{A_{eff}} = 2.08 \times 10^{22} \text{ particles per gram } [g^{-1}] \quad (7.9)$$

Where  $N_A = 6.022 \times 10^{23}mol^{-1}$  is the Avogadro constant.

In the table 7.5, we have the cross section results. This cross-section value is an effective value over the different compositions and energy of the leadings. The value is higher for higher energy as it should be and

we can obtain a lower limit for the cross section.

For the selection 3, we have  $\lambda_{3,eff} = 56.8g/cm^2$  and  $58.4g/cm^2$  at  $10^{18}eV$  and  $10^{19}eV$  respectively. If we compare this result to the  $\lambda_{eff,L1}$  ( $\lambda_{eff}$  of the 1st leading) with cut in  $K$  values, we see that we obtain a value  $\sim 14\%$  higher than it should be (table 7.6 7th line), which is not a big problem since we have said that we will get an upper limit to  $\lambda$ . Probably this value should be compared to the  $\lambda_{eff,L1+L2}$ , but this value is much higher than ours (so we are not measuring a direct sum of the two exponential,  $\lambda_{eff,L1}$  and  $\lambda_{eff,L2}$ ). In our selection 3A, we impose that the 1st leading has a big component, but we don't say anything about the second leading, so we will have the sum of the two leadings. The result in this sub selection is  $\lambda_{eff,3A} = 67.8 \pm 5.4g/cm^2$  which is very close to the value of  $\lambda_{eff,L1+L2}$  (with respective cuts, table 7.6 11th line).

The selection 3B, have a 1st leading less important and thus, we see the second leading. Since the second leading could also have a 3rd leading we should see some  $\lambda$  close to the value of selection 3 itself. We get  $\lambda_{eff,3B} = 56.9 \pm 5.2g/cm^2$ . In next section we will see the type of the first leading.

### 7.4.3 Leading type

Since we have several types of leading, in the table 7.4 we write the number of leadings that are mesons and baryons and in figure 7.14 we plot its distribution.

In figure, in blue we have the events that we save the 2nd interaction, for example, all  $\gamma$  leadings (with number 1) will decay and we don't consider them. With the cut in the leading inelasticity ( $K$ ), we get  $\sim 18\%$  of mesons and  $\sim 82\%$  baryons. The cut in inelasticity change the composition, since the mesons tend to leave less energy than the baryons.

	sample $10^{18}eV$		sample $10^{19}eV$	
	# events	fraction	# events	fraction
All events	103135	1.00	51386	1.00
mesons	37638	0.36	20135	0.39
pions	30993	0.30	16571	0.32
kaons	6645	0.06	3564	0.07
hadrons	65497	0.64	31251	0.61
protons	40461	0.40	19112	0.37
not protons	25036	0.24	12139	0.24
mesons/baryons	-	0.57	-	0.64

	with cut in K			
	# events	fraction	# events	fraction
All events	46733	1.00	21051	1.00
mesons	8602	0.18	3684	0.18
pions	6977	0.15	2985	0.15
kaons	6645	0.03	699	0.03
hadrons	38131	0.82	17367	0.82
protons	22737	0.49	10296	0.49
not protons	15394	0.33	7071	0.33
mesons/baryons	-	0.23	-	0.21

Table 7.4: Leadings number per particle type.

### 7.4.4 Meson-Baryon fraction

Our effective  $\lambda$  should have the form  $\lambda_{eff} = f_{baryons}\lambda_{eff,baryons} + f_{mesons}\lambda_{eff,mesons}$ , where  $f_{baryons}$  and  $f_{mesons}$  are the baryon and meson fraction. For the selection 3, we have  $\lambda_{eff} = 56.8g/cm^2$  ( $58.3g/cm^2$ ) at

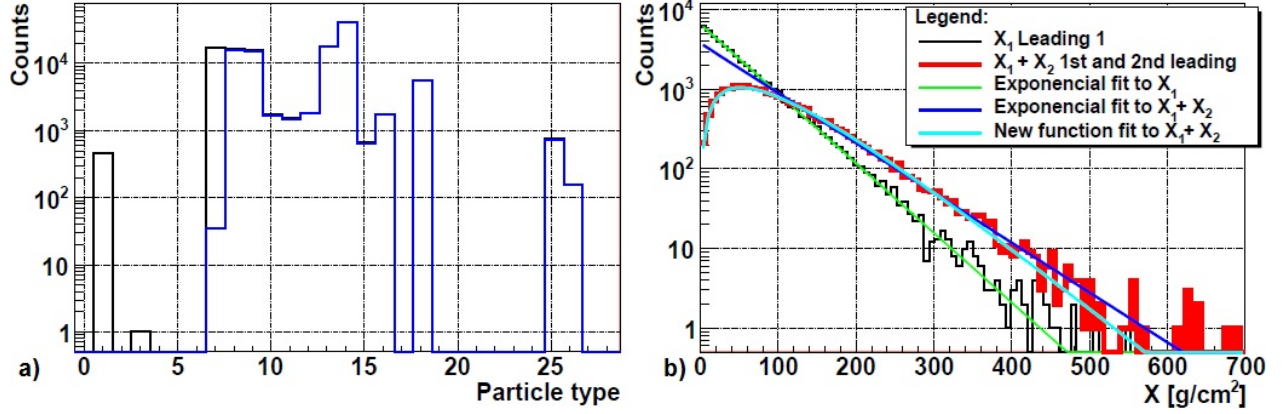


Figure 7.14: a) in black we have all events, in blue the event with 1st interaction saved. Definitions: 1-  $\gamma$ ; 3-  $e^-$ ; 7-  $\pi^0$ ; 8-  $\pi^+$ ; 9-  $\pi^-$ ; 10-  $K_L^0$ ; 11-  $K^+$ ; 12-  $K^-$ ; 13-  $n$ ; 14-  $p$ ; 15-  $\bar{p}$ ; 16-  $K_S^0$ ; 18-  $\Lambda$ ; 25-  $\bar{n}$ ; and 26:  $\bar{\Lambda}$  [115]. b) in black the  $\Delta X_{Gen}$  and in red the  $\Delta X_{Gen} + \Delta X_{L2,Gen}$  distributions, with green line the fit of eq. 7.7 to  $\Delta X_{Gen}$ , blue line for the fit of eq. 7.7 to  $\Delta X_{Gen} + \Delta X_{L2,Gen}$  ( $\Delta X > 200g/cm^2$ ) and light blue the fit of eq. 7.14 to  $\Delta X_{Gen} + \Delta X_{L2,Gen}$

Selections	$\lambda$ ( $g/cm^2$ )		$\sigma_{inf}$ (barn)	
	sample $10^{18}eV$	sample $10^{19}eV$	sample $10^{18}eV$	sample $10^{19}eV$
All events (reconstructed) with $\Delta X_{Rec} > 250g/cm^2$	$64.8 \pm 0.6$	$55.6 \pm 0.8$	$0.742 \pm 0.007$	$0.865 \pm 0.012$
selection 3 (reconstructed)	$56.8 \pm 2.6$	$53.4 \pm 6.1$	$0.846 \pm 0.039$	$0.900 \pm 0.103$
effective energy (eV)	$(0.62 \pm 0.16) * E_p$	$(0.62 \pm 0.16) * E_p$	$(0.63 \pm 0.16) * E_p$	$(0.62 \pm 0.15) * E_p$
Events 3A	$67.8 \pm 5.4$	-	$0.709 \pm 0.056$	-
Events 3B	$56.9 \pm 5.2$	-	$0.845 \pm 0.077$	-
effective energy ( $*E_p$ eV)	0.61	-	0.61	-

Table 7.5: The  $\lambda$  and  $\sigma$  effective for the selections.

$10^{18}eV$  ( $10^{19}eV$ ), this values are almost equal to the mesons  $\lambda$ , then we should have a big fraction of mesons. Nevertheless, as we see in previous section, most of the particles are baryons and not mesons. The reason behind this too high  $\lambda_{eff}$  comes from the fact that it's exact form should be

$$\lambda_{eff} = f_{baryons}\lambda_{eff,baryons} + f_{mesons}\lambda_{eff,mesons} + f_{L2}\lambda_{L2} \quad (7.10)$$

, where  $\lambda_{L2}$  is the effective  $\lambda$  for the 2nd leading and  $f_{L2}$  is it's weight for the total lambda.

At first look, we can think that the  $\lambda$  of a distribution of  $\Delta X = \Delta X_{L1} + \Delta X_{L2}$ , should be  $\lambda_{eff,L1+L2} = \lambda_{eff,L1} + \lambda_{eff,L2}$ , but in fact, if we look at  $\lambda_{eff,L1+L2}$  we have the value  $69.3g/cm^2$  which is different from  $49.7 + 51.9g/cm^2$  ( $\lambda_{eff,L1} + \lambda_{eff,L2}$ , tab. 7.6 11th, 7th and 9th line). In the figure 7.14 b) we see the distribution of  $\lambda_{eff,L1+L2}$ . This result is quite obvious, since in the distribution we will not add two equals  $\lambda_{eff,L1}$  and  $\lambda_{eff,L2}$ , but we can add a small  $\lambda_{eff,L1}$  and an higher  $\lambda_{eff,L2}$  or vice-versa and the final  $\lambda$  will increase with a weight  $f_{L2}$  less than 1.

In this way, we can get:

$$\begin{aligned} \lambda_{eff} &> f_{baryons}\lambda_{eff,baryons} + f_{mesons}\lambda_{eff,mesons} = f_{mesons}(\lambda_{eff,mesons} - \lambda_{eff,baryons}) + \lambda_{eff,baryons} \Leftrightarrow \\ \Leftrightarrow f_{mesons} &< \frac{\lambda_{eff} - \lambda_{eff,baryons}}{\lambda_{eff,mesons} - \lambda_{eff,baryons}} \end{aligned} \quad (7.11)$$

We have a lower limit for baryon fraction and a upper limit to meson fraction. We get  $(f_{baryons})_{lower\ limit} = 0.11 \pm 0.33$  at  $10^{18}eV$  besides the high error, we are far from the real value, but as we said, this is a lower limit. In next section we will upgrade this result.

Selections	$\lambda$ ( $g/cm^2$ )		$\sigma_{eff}$ (barn)	
	sample $10^{18}eV$	sample $10^{19}eV$	sample $10^{18}eV$	sample $10^{19}eV$
$X_0$ proton	$46.5 \pm 0.1$	$42.8 \pm 0.2$	$1.035 \pm 0.003$	$1.124 \pm 0.004$
$\Delta X_{Gen}$ mesons (cut K) effective energy ( $*E_p$ eV)	$58.0 \pm 0.6$ $0.30 \pm 0.09$	$49.9 \pm 0.9$ $0.30 \pm 0.09$	$0.829 \pm 0.009$ $0.30 \pm 0.09$	$0.963 \pm 0.016$ $0.30 \pm 0.09$
$\Delta X_{Gen}$ barions(cut K) effective energy ( $*E_p$ eV)	$47.4 \pm 0.2$ $0.42 \pm 0.16$	$44.2 \pm 0.3$ $0.42 \pm 0.16$	$1.013 \pm 0.005$ $0.42 \pm 0.16$	$1.087 \pm 0.008$ $0.42 \pm 0.16$
$\Delta X_{Gen}$ pions (cut K) effective energy ( $*E_p$ eV)	$57.5 \pm 0.7$ $0.30 \pm 0.09$	$49.3 \pm 1.0$ $0.30 \pm 0.09$	$0.837 \pm 0.010$ $0.30 \pm 0.09$	$0.976 \pm 0.019$ $0.30 \pm 0.09$
$\Delta X_{Gen}$ protons(cut K) effective energy ( $*E_p$ eV)	$47.3 \pm 0.3$ $0.43 \pm 0.16$	$43.7 \pm 0.4$ $0.42 \pm 0.16$	$1.017 \pm 0.006$ $0.43 \pm 0.16$	$1.099 \pm 0.011$ $0.42 \pm 0.16$
$\Delta X_{Gen}$ effective effective energy ( $*E_p$ eV)	$52.4 \pm 0.2$ $0.32 \pm 0.26$	$48.2 \pm 0.2$ $0.27 \pm 0.23$	$0.917 \pm 0.003$ $0.32 \pm 0.26$	$0.997 \pm 0.005$ $0.27 \pm 0.23$
$\Delta X_{Gen}$ effective (cut K) effective energy ( $*E_p$ eV)	$49.7 \pm 0.2$ $0.40 \pm 0.16$	$45.6 \pm 0.3$ $0.40 \pm 0.16$	$0.968 \pm 0.004$ $0.40 \pm 0.16$	$1.054 \pm 0.007$ $0.40 \pm 0.16$
$\Delta X_{L2,Gen}$ effective effective energy ( $*E_p$ eV)	$51.6 \pm 0.3$ $0.16 \pm 0.15$	$45.7 \pm 0.4$ $0.15 \pm 0.15$	$0.932 \pm 0.005$ $0.16 \pm 0.15$	$1.052 \pm 0.008$ $0.15 \pm 0.15$
$\Delta X_{L2,Gen}$ effective (cut K) effective energy ( $*E_p$ eV)	$51.9 \pm 0.3$ $0.19 \pm 0.17$	$46.5 \pm 0.4$ $0.18 \pm 0.16$	$0.926 \pm 0.005$ $0.19 \pm 0.17$	$1.033 \pm 0.009$ $0.18 \pm 0.16$
$\Delta X_{Gen} + \Delta X_{L2,Gen}$ effective	$70.4 \pm 0.4$	$62.5 \pm 0.7$	$0.682 \pm 0.004$	$0.769 \pm 0.008$
$\Delta X_{Gen} + \Delta X_{L2,Gen}$ effective (cut K)	$69.3 \pm 0.7$	$62.5 \pm 0.7$	$0.682 \pm 0.004$	$0.769 \pm 0.008$

Table 7.6: Several important  $\lambda$  and corresponding  $\sigma$  effective, from the input values.

### 7.4.5 Convolution of Leadings

In figure 7.14 b), we see that  $f(\Delta X_{L1} + \Delta X_{L2}) \neq const \times e^{-(\Delta X_{L1} + \Delta X_{L2})/\lambda}$ , consequently we should find another distribution to fit the results. Observing the previous distribution we can conclude that the rate of double bangs will be much higher than what was initial thought in the figure 7.4 a).

If we have a distribution with the shape  $f(\Delta X) = C \times e^{-\Delta X/\lambda}$ , in a discrete plot we have  $f(\Delta X_k) = C \times e^{-\Delta X_k/\lambda}$  where k is the bin number (from 1 to n). This is the distribution for the 1st leading, the 2nd leading alone will have the same shape. In bin 1 the first leading travels  $X_1$ , adding the 2nd leading contribution we will have  $f_{L1+L2}(\Delta X_1) \equiv f'_{L1+L2}(\Delta X_1, \Delta X_1) = A(X_1) \times f_{normalized,L2}(\Delta X_1) = C_1 \cdot e^{-\Delta X_{L1,1}/\lambda_1} \times C_{norm} \cdot e^{-\Delta X_{L2,1}/\lambda_2}$ , where the amplitude of distribution of the second leading will be constrained by the number of 1st leading particles that have travel  $X_1$ . The  $C_1$  constant comes from the number of particle, but since  $f_{L1}(\Delta X_1)$  will be the amplitude of the second leading, then we need  $C_{norm,2}$  to normalize the second distribution (basically, the second term will be a probability). In  $f'_{L1+L2}(\Delta X_j, \Delta X_k)$ ,  $\Delta X_j$  and  $\Delta X_k$  is the distance travels by 1st and 2nd leadings. From the 1st bin of 1st leading we will have more terms for others

higher bins in 2nd leading in the form  $f'_{L1+L2}(\Delta X_1, \Delta X_k)$ .

The second bin of the total distribution will have a contribution from the 1st bin and 2nd bin of the first leading and it will be  $f_{L1+L2}(\Delta X_2) \equiv f'_{L1+L2}(\Delta X_1, \Delta X_2) + f'_{L1+L2}(\Delta X_2, \Delta X_1)$ , and so on. Bellow we can see the construction scheme:

$$\begin{aligned}
f_{L1+L2}(\Delta X_1) &= f'_{L1+L2}(\Delta X_1, \Delta X_1) = C_1 \times e^{-\Delta X_{L1,1}/\lambda_1} \times e^{-\Delta X_{L2,1}/\lambda_2} \\
f_{L1+L2}(\Delta X_2) &= f'_{L1+L2}(\Delta X_1, \Delta X_2) + f'_{L1+L2}(\Delta X_2, \Delta X_1) = \\
&= C_1 \times e^{-\Delta X_{L1,1}/\lambda_1} \times e^{-\Delta X_{L2,2}/\lambda_2} + C_2 \times e^{-\Delta X_{L1,2}/\lambda_1} \times e^{-\Delta X_{L2,1}/\lambda_2}
\end{aligned} \tag{7.12}$$

...

$$f_{L1+L2}(\Delta X_n) = \sum_{k=1}^n f'_{L1+L2}(\Delta X_k, \Delta X_{n-k}) = \sum_{k=1}^n C_k \times e^{-\Delta X_{L1,k}/\lambda_1} \times e^{-\Delta X_{L2,n-k}/\lambda_2}$$

where we define  $C_k = C_k \times C_{norm}$ . Now, we can do  $limit_{bins\ spacing \rightarrow 0} \sum_{k=1}^n \rightarrow \int_0^{X_n}$ . Therefore, for the new distribution we get the shape:

$$f_{L1+L2}(\Delta X_n) = \int_0^{\Delta X_n} C \times e^{-\Delta X/\lambda_1} \times e^{-(\Delta X_n - \Delta X)/\lambda_2} d\Delta X = C \frac{e^{-\Delta \Delta X_n/\lambda_1} - e^{-\Delta X_n/\lambda_2}}{1/\lambda_2 - 1/\lambda_1} \tag{7.13}$$

If  $\lambda_2 = \lambda_1$ , than we get:

$$f_{L1+L2}(\Delta X_n) = C e^{-\Delta X_n/\lambda} \times \Delta X_n \tag{7.14}$$

From equation  $const \times e^{-x/\lambda}$ , now we have  $const \times e^{-x/\lambda} \cdot x$ . In light blue, at fig. 7.14b) we have the fit of  $\Delta X_{L1+L2}$  distribution to equation 7.14. To keep the same number of parameters, we consider that  $\lambda_1 \sim \lambda_2$  (which is acceptable by table 7.6). We obtain here a  $\lambda_{eff} = 51.5 \pm 0.4 g/cm^2$ , which is  $\sim \lambda_{eff,L1} \sim \lambda_{eff,L2}$  (cutting in  $K$  parameter). If we don't cut in  $K$  we get  $\lambda_{eff} = 52.5 \pm 0.3 g/cm^2$ . The  $\chi^2 = 97.0/85$  using equation 7.7 and is  $\chi^2 = 68.2/100$  with eq. 7.14. With the new distribution we get a better fit and have a interaction length very close to the input.

In figure 7.15, we repeat the  $\Delta X$  distribution for all events (a) and selection 3 (b) with the fit to the new function. The results for this new fit and posterior meson-baryon fraction calculation are in table 7.7.

Selections	$\lambda$ ( $g/cm^2$ )		$\sigma_{inf}$ (barn)	
	sample $10^{18} eV$	sample $10^{19} eV$	sample $10^{18} eV$	sample $10^{19} eV$
$\Delta X_{Gen} + \Delta X_{L2,Gen}$ effective	$52.6 \pm 0.3$	$47.3 \pm 0.4$	$0.914 \pm 0.005$	$1.017 \pm 0.010$
$\Delta X_{Gen} + \Delta X_{L2,Gen}$ effective with cut in $K$	$51.6 \pm 0.4$	$46.4 \pm 0.7$	$0.931 \pm 0.008$	$1.035 \pm 0.015$
All events (reconstructed) with $\Delta X_{Rec} > 250 g/cm^2$	$53.0 \pm 0.4$	$46.3 \pm 0.6$	$0.906 \pm 0.007$	$1.038 \pm 0.013$
selection 3 (reconstructed) effective energy (eV)	$48.8 \pm 1.9$ $(0.62 \pm 0.16) * E_p$	$45.8 \pm 4.6$ $(0.62 \pm 0.16) * E_p$	$0.984 \pm 0.039$ $(0.63 \pm 0.16) * E_p$	$1.050 \pm 0.104$ $(0.62 \pm 0.15) * E_p$
	<i>meson fraction</i>		<i>#meson/#baryon</i>	
All events (reconstructed) with $\Delta X_{Rec} > 250 g/cm^2$	$0.42 \pm 0.04$	$0.17 \pm 0.07$	$0.74 \pm 0.10$	$0.20 \pm 0.10$
selection 3 (reconstructed)	$0.13 \pm 0.18$	$0.28 \pm 0.80$	$0.15 \pm 0.20$	$0.38 \pm 1.10$

Table 7.7: The  $\lambda$  and corresponding  $\sigma$  effective for the new fitting equation (eq. 7.7) and corresponding meson/baryon fraction.

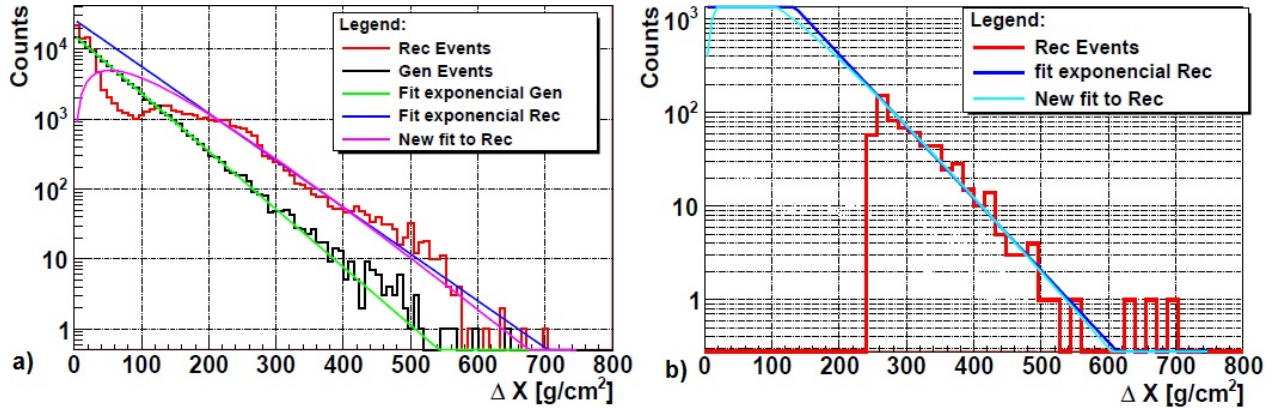


Figure 7.15: The new fit (of eq. 7.14) to the  $\Delta X$  distributions of all reconstructed events (a) and selection 3(b).

We can see that if we compare the new values of the effective  $\lambda$  with the obtained from the same method for  $\Delta X_{Gen} + \Delta X_{L2,Gen}$ , they are very close and compatible within the errors. Comparing this values to the values in table 7.6, the results are very accurate. For the selection 3 we have  $\lambda_{eff,3} = 48.8 \pm 1.9 g/cm^2$  (tab. 7.7 4th line), while  $\lambda_{eff,L1} = 49.7 \pm 0.2 g/cm^2$  at  $10^{18} eV$  (tab. 7.6 7th line). At  $10^{19} eV$ , we have  $\lambda_{eff,3} = 45.8 \pm 4.6 g/cm^2$  ( $\sim 10\%$ ), while  $\lambda_{eff,L1} = 45.6 \pm 0.3 g/cm^2$ . The values are close, but we have large uncertainties. Here we can repeat the calculation for meson-baryon fraction. Compared with the table 7.4, the results are not too good, beside being compatible with the errors. The error in this case are extremely high since equation 7.11 is very sensitive to small changes.

The experiment of LHCf will detect something similar to this fraction, it will allow the measure of neutral particle produced in the forward direction of ATLAS (see [118]). In the quote [119] we find a study of the variation of the number of muons in EAS with percolation, which will be related with this value.

The interesting result of this thesis is that using this new fit or even the previous one (more conservative), at least we can obtain a lower limit for cross section. This can be applied to data and be compared with the preview by Monte Carlo models.

#### 7.4.6 Inelasticity

Besides the  $\Delta X$ , we have the information of  $K$  too. In the figure 7.12, is plotted the inelasticity distribution for all events in a) and for selections 3 in b). The mean values are plotted in the table 7.8. Looking at the figure, we see that in reconstruction we have smaller  $K$  than in  $K_{Gen}$  and as we told many times, we are not sensitive to the diffractive peak. Our result is a complicated convolution of several leadings with several energies. Consequently if we can not measure the first leading (because  $\Delta X_{Gen} \lesssim L$ ) but we measure the 2nd leading or other most energetic particle, we will decrease the energy of what we are measuring. In this way, we tend so measure a lower value of  $K$ .

In the table we see that the mean  $K$  reconstructed is smaller than the input of 1st leading.

### 7.5 Real Events

In real events is more difficult to follow this procedure, since we could have reconstruction problems or even atmospheric condition that deteriorate our FD signal. We could think that we are seeing some double bang event, but we are actually seeing a normal event.

In the figure 7.16 a), we have a good example where we can fit 2GH. The  $\chi^2_{1GH} = 1.50$  and  $\chi^2_{2GH} = 0.68$  this shows that this event has a behaviour of two GH, and not 1GH. The event is a very good event since it doesn't have clouds, and the Mie, Rayleigh and Cherenkov component of the light that arrives at the FD is very small.

Selections	Inelasticity $K$	
	sample $10^{18} eV$	sample $10^{19} eV$
All events (generated values)	$0.68 \pm 0.26$	$0.70 \pm 0.26$
All events (reconstructed values) for $\Delta X < 200 g/cm^2$	$0.53 \pm 0.22$	$0.52 \pm 0.20$
selection 3 (reconstructed values)	$0.61 \pm 0.16$	$0.61 \pm 0.16$
effective energy( $*E_p eV$ )	$0.62 \pm 0.16$	$0.62 \pm 0.16$

Table 7.8: Values of the effective inelasticity  $K$ .

In b), we have a normal event, where we don't expect 2GH, so the  $\chi_{1GH}^2 = 0.46$  while  $\chi_{2GH}^2 = 0.51$ . It's interesting to note that we obtain  $\Delta X_{Rec} = 33.0 g/cm^2$ , and  $L$  and  $X_{max}$  have very similar results, so the two  $N_{max}$  don't mean anything, since it tries to have 1GH. If we have 1GH, as we told before, we can divide it in two GH with similar parameter and the two  $N_{max}$  can change almost in an arbitrary way, giving more or less the same result.

In the figure 7.17, we have more two examples where we can fit 2GH better than 1GH. Nevertheless, this new events are in very bad condition. In figure 7.18, we see that the 4th event has a cloud in half of the development of the shower, which could cause the double bang shape. Meanwhile, the 3th and 4th events have a big direct Cherenkov component which could compromise the good reconstruction of the longitudinal profile.

In real events, in this way, is much more difficult to use the 2GH fit in order to obtain information about the shower. In many of the events we will have two GH because of clouds, or problems of reconstruction, with a second GH coming from Cherenkov and scatter light. In this context, a careful pre-selection of the data is needed, hence the PAO has a very good control of atmosphere conditions, we may achieve a clean data selection.

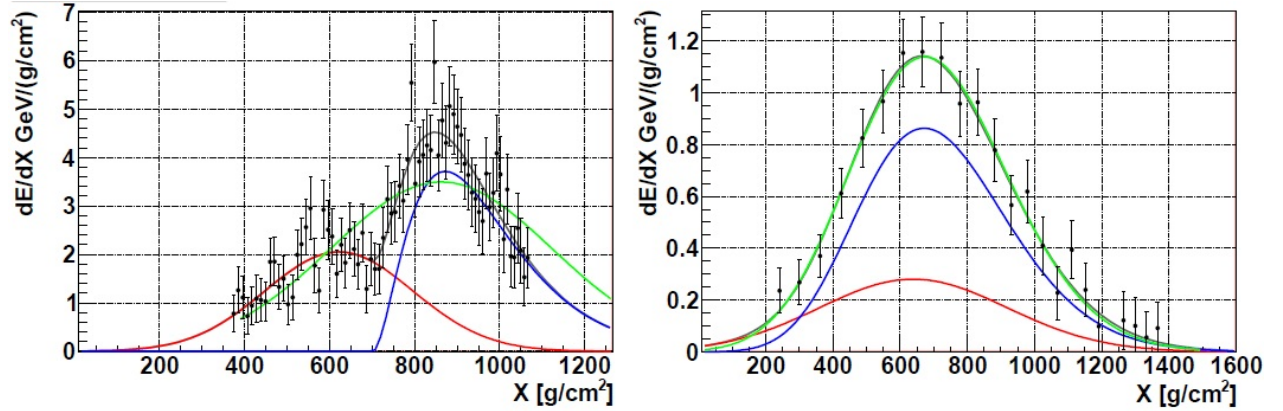


Figure 7.16: a) EventId 7274947 (2009/02/21, Los Morados)

$$E = 2.93 \pm 0.20 \cdot 10^{18} eV, \chi_{1GH}^2 = 1.50, \chi_{2GH}^2 = 0.68$$

$$\Delta X = 250.1 g/cm^2, K = 0.36$$

b) EventId 7274947 (2009/02/21, Coihueco)

$$E = 7.57 \pm 0.35 \pm 0.31 \cdot 10^{17} eV, \chi_{1GH}^2 = 0.47, \chi_{2GH}^2 = 0.51$$

$$\Delta X = 33.0 g/cm^2, K = 0.25$$

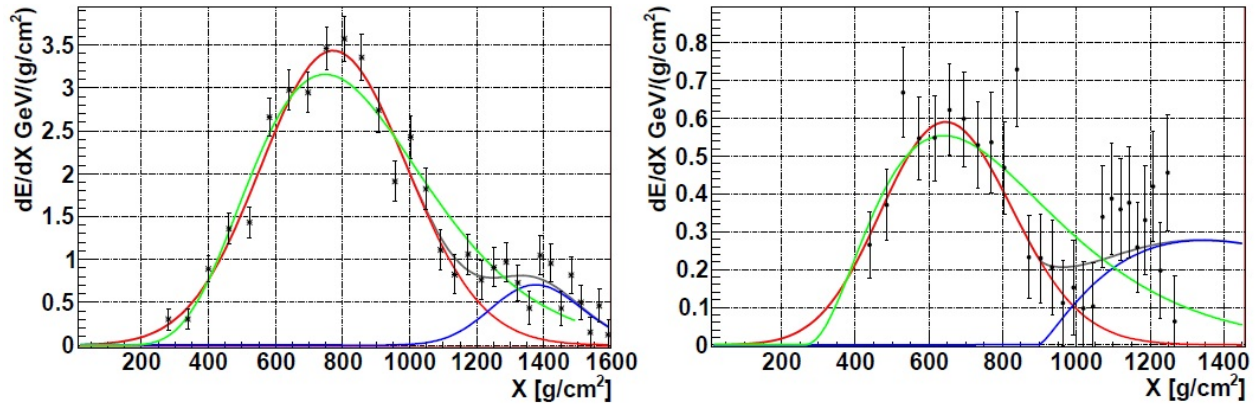


Figure 7.17: a) EventId 7269175 (2009/02/20, Los Leones)  
 $E = 2.39 \pm 0.09 \pm 0.15 \cdot 10^{18} eV$ ,  $\chi_{1GH}^2 = 2.34$ ,  $\chi_{2GH}^2 = 1.10$   
 $\Delta X = 603.2 g/cm^2$ ,  $K = 0.83$   
 b) EventId 7270194 (2009/02/20, Los Leones)  
 $E = 4.46 \pm 0.33 \pm 0.22 \cdot 10^{18} eV$ ,  $\chi_{1GH}^2 = 1.55$ ,  $\chi_{2GH}^2 = 0.81$   
 $\Delta X = 222.4 g/cm^2$ ,  $K = 0.68$

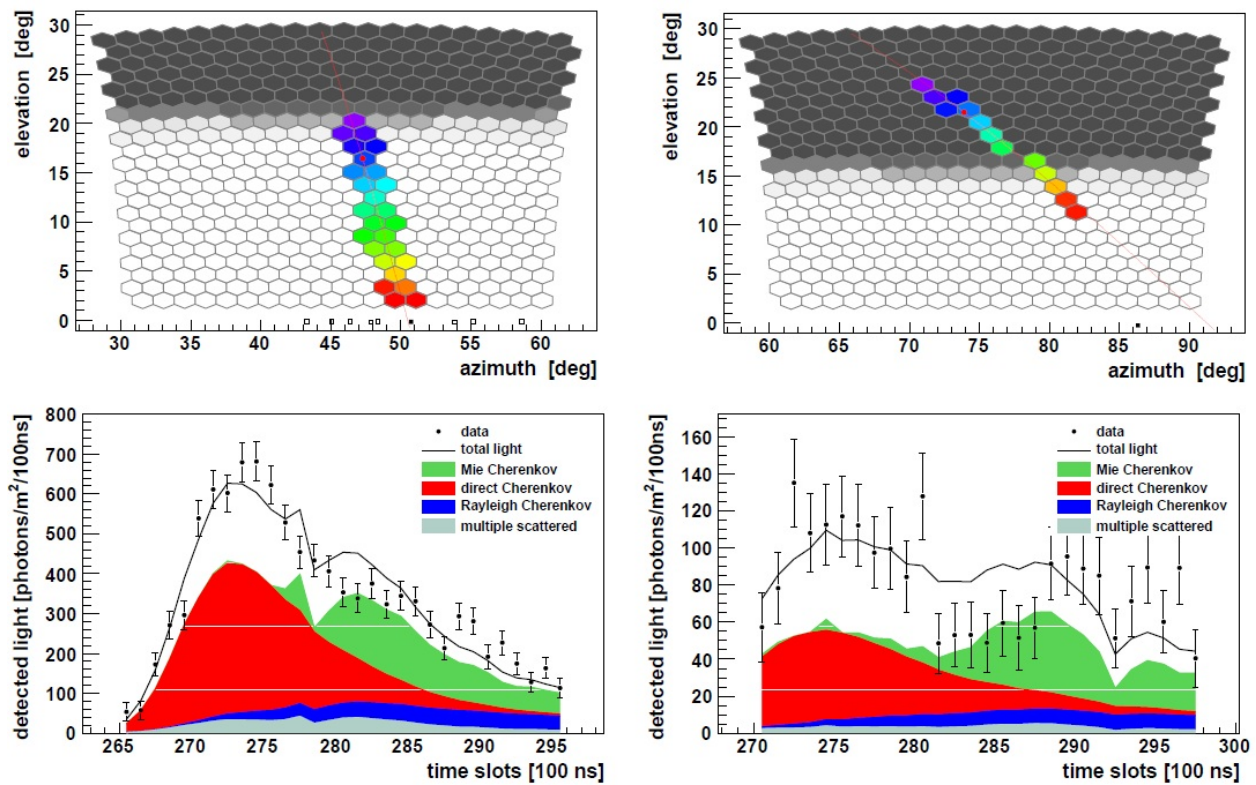


Figure 7.18: a) EventId 7269175 (event a in fig. 7.17) b) EventId 7270194 (event b in fig. 7.17). Above we have the camera pixels that were activated with the colour, the pixels in the shadow correspond to pixels that were pointed at clouds during the event, below we have the detected light at the camera divided in several components.



## Chapter 8

# Conclusion and prospects

The main purpose of this thesis was to study the events with extreme fluctuations and apply a new method to recover the interaction length of first interaction from the extensive air shower.

In the study of events with extreme fluctuations, we observed that there is a large excess of events with high  $\chi^2$ , or we have a tail in the  $\chi^2$  distribution of too large. This means that these events have more fluctuations compared to the profile of a GH, than expected for Gaussian fluctuations. In order to understand the number of events with more fluctuations than expected, we studied the probability of  $\chi^2$ . Based on the probability, we found an excess of low probability events. Thus, we have at  $10^{19}eV$  about 13.4% of events with extra fluctuations and at  $10^{18}eV$  we have about 13.8%. This sample of events is marked by, on average, be wider than the events with good  $\chi^2$ . Besides being on average wider, in event by event we have enough distance, we get a shape very different from a GH, and even we can get two maximums in the shower.

The events where we had troubles to adjust one GH to the points of the event, were the best events for applying the new method. Basically, the method considers that one of the leading from first interactions, carrying a large fraction of the energy might be developed separately from the other particles produced. Thus, if the leading interacts very close to the point where it was produced, then its development in a GH will be superimposed on the GH of the other particles. If the leading travels a large distance before interact, it was found that both GH developments are spaced (double bang) and we can be sensitive enough to recover its shape. If the event does not have a profile similar to 1GH, then it should be something similar to the sum of two GH. The optimum zone is to use method for distances between GH( $X$ ) larger than the value of  $L$  (it is approximately the width of 1GH) and leading that carries a fraction of energy between 0.2 and 0.8. The distance between the two  $X_{max}$  of the two GH, is corresponding to the distance travelled by the leading.

It was found that a major difficulty comes from the fact that, we not always measure the leading of the first interaction, we have cases where the leading of the second interaction carries a larger fraction of the total energy and travels a larger distance, or even have a 3rd leading particles or a high energy particle produced in the interactions and are not the leading, but are under the above conditions. We can still be measuring the sum of two leading. This means that we measure a fit of all those leadings obtaining a interaction length that is higher than expected, we get  $\lambda_{eff} = \lambda Leading1 + \lambda Leading2$ . With this upper limit, we can calculate a lower limit for the cross section.

Using Monte Carlo simulation programs, at  $10^{18}eV$  we find an upper limit on the length of interaction of  $56.8 \text{ pm}2.6g/cm^2$ , one would expect a value about  $49.7g/cm^2$ . It was noted that the distribution for the interaction length with the accumulation of leadings was not exactly an exponential. On the approach of two leadings with equal interaction length, we have a distribution with the shape  $conste^{-x/\lambda} * x$ . With it was possible to find a value for  $\lambda$  that in principle was not supposed to be superior. For  $10^{18}eV$  get  $48.8 \text{ pm}1.9g/cm^2$ , about 3.9% of uncertainty, the expected value of  $49.7g/cm^2$  would be a difference of 1.8%, so the results are compatible. For  $10^{19}eV$ , we have  $45.8 \text{ pm}4.6$  to  $45.7 \text{ pm}0.3g/cm^2$ . With the second shape for the distribution it is possible to recover very close value.

For the calculation of the fraction of meson-baryons, it was found to be very sensitive to errors in the interaction length, so although the results being compatible with expected values, due to large statistical uncertainties, they are not very accurate.

The main goal of this thesis was to find a distribution for the  $\Delta X_{max}$  compatible with an exponential and that it corresponds to the distribution of a leading or/or overlapping of several. With this it appears that the method can be accurate.

Finally it was found that there are real events which are candidates for double bang, however, extra care is needed for the atmospheric conditions that can cause a similar effect.

In the future, we intend to initially apply the model to the reconstruction of simulated events and then apply it to real data. This model could emerge as a way to strongly constrain hadronic models.

# Bibliography

- [1] V. Hess, *Über Beobachtungen der durchdringenden Strahlung bei sieben Freiballonfahrt*, *Physikalische Zeitschrift* 13, p. 1084-1091, 1912.
- [2] B. Rossi, *On the magnetic deflection of cosmic rays*, *Physical Review* 36, p. 606, 1930.
- [3] P. Auger, P. Ehrenfest et al., *Extensive cosmic-ray showers*, *Review of Modern Physics* 11, p. 288-291, 1939.
- [4] H. J. Bhabha and W. Heitler, *The passage of fast electrons and the theory of cosmic showers*, *Royal Society of London Proceedings Series A* 159, p. 432, 1937.
- [5] C. M. G. Lattes, H. Muirhead, G. P. S. Occhialini and C. F. Powell, *Processes involving charged mesons*, *Nature* 159, p. 694-697, 1947.
- [6] C. Anderson and S. Neddermeyer, *Note on the nature of cosmic-ray particles*, *Physical Review* 51, p. 884, 1937.
- [7] J. Linsley, *Evidence for a primary cosmic-ray particle with energy  $10^{20}eV$* , *Physical Review Letters* 10, p. 146-148, 1963.
- [8] A. Hillas, *Cosmic rays: Recent progress and some current questions*, *Cosmology, Galaxy Formation and Astroparticle Physics on the pathway to the SKA*, Oxford, April 2006. arXiv:astro-ph/0607109v2
- [9] J. Cronin, *Cosmic rays: the most energetic particles in the universe*, *Reviews of Modern Physics*, 71(2), p. 165-172, 1999.
- [10] A. Olinto, *Ultra high energy cosmic rays and the magnetized universe*, *Journal of the Korean Astronomical Society*, 37, p. 413-420, 2004.
- [11] T. Stanev, *High Energy Cosmic Rays*, Springer Praxis Books, 2004.
- [12] U.S. standard atmosphere parameters: <http://faculty.virginia.edu/ribando/modules/xls/USStandAtmos.xls>
- [13] R. Abbasi et al., *Observation of the ankle and evidence for a high-energy break in the cosmic ray spectrum*, *Physics Letters B* 619, p. 271-280, 2005. arXiv:astro-ph/0501317
- [14] D. Allard et al., *On the transition from galactic to extragalactic cosmic-rays: spectral and composition features from two opposite scenarios*, *Astroparticle Physics* 27, p. 61-75, 2007.
- [15] J. Cronin, *The highest-energy cosmic rays*, *Nuclear Physics B (Proceedings Supplements)* 138, p. 465-491, 2005.
- [16] K. Greisen, *End to the cosmic-ray spectrum?*, *Physical Review Letters* 16(17), p. 748-750, 1966.
- [17] G. Zatsepin and V. Kuzmin, *Upper limit of the spectrum of cosmic rays*, *Journal of Experimental and Theoretical Physics* 4(3), p. 78-80, 1966.
- [18] L. Bergström and A. Goobar, *Cosmology and Particle Astrophysics*, John Wiley & Sons, 1999.

- [19] A. Hillas, *The origin of ultra-high energy cosmic rays*, Annual Review of Astronomy and Astrophysics 22, p. 425-444, 2009.
- [20] L. Anchordoqui et al., *Ultra-high energy cosmic rays: The state of the art before the Auger Observatory*, International Journal of Modern Physics A 18, p. 2229-2366, 2003. arXiv:hep-ph/0206072v3
- [21] E. Fermi, *On the origin of the cosmic radiation*, Physics Review 75, p. 1169-1174, 1949.
- [22] P. Bhattacharjee and G. Sigl, *Origin and propagation of extremely high-energy cosmic rays*, Physics Report 327, p. 109-247, 2000.
- [23] J. Blumer, *Cosmic rays at the highest energies and the Pierre Auger Observatory*, Journal of Physics G: Nuclear and Particle Physics, 29(5), p. 867-879, 2003.
- [24] R. Blandford and J. Ostriker, *Particle acceleration by astrophysical shocks*, Astrophysical Journal, Part 2 - Letters to the Editor 221, p. L29-L32, 1978.
- [25] V. Scherini, *Study of the performance of the Pierre Auger Observatory and search for primary cosmic ray photons*, PhD thesis at Fachbereich C - Physik Bergische Universität Wuppertal, 2007.
- [26] F. Aharonian and j. Cronin, *Influence of the universal microwave background radiation on the extragalactic cosmic ray spectrum*, Physics Review D 50, p. 1892-1900, 1994.
- [27] D. D'Urso, *Pierre Auger Observatory: Fluorescence detector event reconstruction and data analysis*, PhD thesis at Universita' Degli Studi Di Catania, 2007.
- [28] C. Wileman, *The spread in the arrival times of particles in air-showers for photon And anisotropy searches above 10 EeV*, PhD thesis at The University of Leeds School of Physics and Astronomy, 2008.
- [29] L. Anchordoqui et al., *High energy physics in the atmosphere: phenomenology of cosmic ray air showers*, Annals of Physics 314, p. 145-207, 2004.
- [30] C. Amsler et al., *Particle Data Group*, Physics Letters B 667, p. 1, 2008.
- [31] D. Lide, *Handbook of Chemistry and Physics, 89th Edition*, CRC Press, 2008.
- [32] M. Risse, *Photon air showers at ultra-high energy and the photonuclear cross-section*, Czechoslovak Journal of Physics 56, p. A327-A336, 2006.
- [33] W. Heitler, *The Quantum Theory of Radiation*, Oxford University Press, London, 1944.
- [34] J. Mathews, *A Heitler model of extensive air showers*, Astroparticle Physics 22, p. 387-397, 2005.
- [35] P. Assis, *Data acquisition and performance studies in cosmic ray experiments*, PhD thesis at Universidade Técnica de Lisboa, Instituto Superior Técnico, 2009.
- [36] K. Greisen, *Cosmic ray showers*, Annual Review of Nuclear Science 10, p. 63-108, 1960.
- [37] K. Kamata and J. Nishimura, *The lateral and the angular structure functions of electron showers*, Progress of Theoretical Physics Supplement 6, p. 93-155, 1958.
- [38] H. Koch and J. Motz, *Bremsstrahlung cross-section formulas and related data*, Review of Modern Physics 31, p. 920-955, 1959.
- [39] F. Kakimoto et al., *A measurement of the air fluorescence yield*, Nuclear Instruments and Methods in Physics Research Section A 372, p. 527-533, 1996.
- [40] A. Donnachie and P. Landshoff, *New data and the hard pomeron*, Physics Letters B 518, p. 63-71, 2001.
- [41] P. Colin et al., *Measurement of air and nitrogen fluorescence light yields induced by electron beam for UHECR experiments*, Astroparticle Physics 27, p.317-325, 2007. arXiv:astro-ph/0612110v1

- [42] F Boley, *Atmospheric Cherenkov radiation from cosmic ray air showers*, Reviews of Modern Physics 36, p. 792-808, 1964.
- [43] J. Diaz, *Weakly interacting particles viewed by fluorescence detectors*, Note GAP-2000-058.
- [44] F. Nerling, *Description of Cherenkov light production in extensive air showers*, Note GAP-2005-063.
- [45] F. Halzen and A. Martin, *Quarks and Leptons: An Introductory Course in Modern Particle Physics*, Jonh Wiley & Sons, First Edition, 1984.
- [46] H. Drescher et al., *Parton-based Gribov-Regge theory*, Physics Reports 350, p. 93-289, 2001.
- [47] O. Nachtmann, *Pomeron physics and QCD*, Contribution to the Ringberg Workshop on HERA Physics, 2003. arXiv:hep-ph/0312279v1
- [48] K. Werner et al., *Gribov-Regge theory, partons, remnants, strings - and the EPOS model for hadronic interactions*, Nuclear Physics B (Proceedings Supplements) 196, p. 36-43, 2009.
- [49] K. Werner, *Physics of Event Generators*, lecture at Pan-American Advanced Study Institute "New States of Matter in Hadronic Interactions", Campos de Jordao, Brazil, January 7-18, 2002. arXiv:hep-ph/0206111v1
- [50] S. Ostapchenko, *Non-linear effects in high energy hadronic interactions*, proceedings of the Interdisciplinary Workshop "QCD at Cosmic Energies", Ettore Majorana Centre, Erice, Italy, August 15 - September 5, 2004. arXiv:hep-ph/0501093v1
- [51] K. Werner, *The string model for ultra relativistic nuclear scattering*, International School/Workshop for Young Physicists on Relativistic Heavy-Ion Physics, in Prague (Czech Republic), pp.591-609, 1994. arXiv:nucl-th/9412006v1
- [52] K. Werner, F. Liu and T. Pierog, *Parton ladder splitting and the rapidity dependence of transverse momentum spectra in deuteron-gold collisions at RHIC*, Physics Review C 74, 044902, 2006.
- [53] F. M. Liu, J. Aichelin et al., *Constraints on models for proton-proton scattering from multi-strange baryon data*, Physics Review D 67, 034011, 2003.
- [54] R. Ulrich, R. Engel et al., *Proton-air cross section and extensive air showers*, Nuclear Physics B (Proceedings Supplement) 196, p. 335-340, 2009.
- [55] N. Kalmikov, S. Ostapchenko and A. Pavlov, *Quark-Gluon-String model and EAS simulation problems at ultra-high energies*, Nuclear Physics B (Proceedings Supplement) 52(3), p. 17-28, 1997.
- [56] S. Ostapchenko, *Non-linear screening effects in high energy hadronic interactions*, Physics Review D 74, 014026, 2006.
- [57] S. Ostapchenko, *QGSJET-II: towards reliable description of very high energy hadronic interactions*, Nuclear Physics B (Proceedings Supplement) 151, p. 143-146, 2006.
- [58] S. Ostapchenko, *QGSJET-II: results for extensive air showers*, Nuclear Physics B (Proceedings Supplement) 151, p. 147-150, 2006.
- [59] E. Ahn, R. Engel, T. Gaisser et al., *Cosmic ray event generator Sibyll 2.1*, Physics Review D 80, 2009.
- [60] R. Fletcher, T. Gaisser et al., *SIBYLL: An event generator for simulation of high energy cosmic ray cascades*, Physics Review D 50, p. 5710-5731, 1994.
- [61] K. Werner, T. Pierog et al., *Extended air shower simulation based on EPOS*, 12th International Conference on Elastic and Diffractive Scattering: Forward Physics and QCD, DESY, in Hamburg (Germany), p. 21-25, 2007. arXiv:0707.3330v1
- [62] T. Pierog, *Forward Physics: from SPS to LHC, What can we learn from air showers?*, presentation at XLIIIth Rencontres de Moriond QCD and high Energy Interactions, in La Thuile (Italy), 2009.

- [63] R. Engel, *Phenomenology of hadronic Showers*, Corsika School at Lauterbad, Germany, 2008.
- [64] T. Pierog et al., *Latest results from the air shower simulation programs CORSIKA and CONEX*, 30th International Cosmic Ray Conference, in Merida (Mexico), 2007.
- [65] D. Heck, *The Influence of Hadronic Interaction Models on Simulated Air-Showers: A Phenomenological Comparison*, Corsika School at Lauterbad, Germany, 2008.
- [66] J. Friedman, *Deep inelastic scattering: Comparisons with the quark model*, Nobel Lecture, December 8, 1990.
- [67] M. Takeda et al., *Energy determination in the Akeno Giant Air Shower Array experiment*, Astroparticle Physics 19, p. 447-462, 2003.
- [68] L. Wiencke, *Extracting first science measurements from the southern detector of the Pierre Auger Observatory*, Nuclear Instruments and Methods in Physics Research Section A 572, p.508-510 ,2007.
- [69] R. U. Abbasi et al., *Measurement of the flux of ultrahigh energy cosmic rays from monocular observations by the High Resolution Fly's Eye Experiment*, Physics Review Letter 92, 151101, 2004.
- [70] J. Abraham et al., *Properties and performance of the prototype instrument for the Pierre Auger Observatory*, Nuclear Instruments and Methods in Physics Research Section A 523(1-2), p. 50-95, 2003.
- [71] T. Waldenmaier, J. Blümera and H. Klages, *Spectral resolved measurement of the nitrogen. Fluorescence yield in air induced by electrons*, Astroparticle Physic 29(3), p. 205-222, 2008.
- [72] The Pierre Auger Collaboration, *The fluorescence detector of the Pierre Auger Observatory*, Nuclear Instruments and Methods in Physics Research Section A 620, p. 227-251, 2010.
- [73] E. Cantoral et al., *Proposal for the optical system of the fluorescence detectors of the Auger Project*, Note GAP-1996-039.
- [74] D. Allard et al., *A new method for the longitudinal profile reconstruction of the auger fluorescence detector events*, Note GAP-1006-026.
- [75] L. Wiencke, *Pierre Auger Observatory recent results & future plans*, presentation at SLAC National Accelerator Laboratory, in Menlo Park (USA), 2009.
- [76] M. Giller et al., *Angular directions of pixels in the FD camera*, Note GAP-2000-032.
- [77] J. Blumer et al., *Atmospheric profiles at the southern Pierre Auger Observatory and their relevance to air shower measurement*, 29th International Cosmic Ray Conference 7, p. 123, 2005.
- [78] B. Wilczynska, D. Góra et al., *Importance of Atmospheric Model in Shower Reconstruction*, 28th International Cosmic Ray Conference, p. 571, 2003.
- [79] M. Mostafa, *Atmospheric monitoring for the Pierre Auger fluorescence detector*, The 28th International Cosmic Ray Conference, p. 465-468, 2003. arXiv:astro-ph/0308442v1
- [80] R. Cester et al., *Atmospheric aerosol monitoring at the Pierre Auger Observatory*, 29th International Cosmic Ray Conference Pune 8, p. 347, 2005.
- [81] A. Filipci et al., *Scanning LIDAR based atmospheric monitoring for fluorescence detectors of cosmic showers*, Astroparticle Physics 18, p. 501-512, 2003.
- [82] S.Y. BenZvi et al., *Measurement of the aerosol phase function at the Pierre Auger Observatory*, Astroparticle Physics 28, p. 312-320, 2007.
- [83] P. Younk et al., *Measurements of SD-FD time offset using inclined laser shots*, Note GAP-2006-005.
- [84] F. Arqueros, J. Bellido et al., *The Central Laser Facility at the Pierre Auger Observatory*, Journal of Instrumentation 1, P11003, 2006. arXiv:astro-ph/0507334v1

- [85] D. Veberic et al., *Offline reference manual: SD reconstruction*, Note GAP-2005-035.
- [86] M. Horvat and D. Veberic, *On shower-front start-time variance*, Note GAP-2007-057.
- [87] M. Unger, *Shower profile reconstruction from fluorescence and Cherenkov light*, Note GAP-2006-010.
- [88] D. Newton et al., *The optimum distance at which to determine the size of a giant air shower*, *Astroparticle Physics* 26, p. 414-419, 2007.
- [89] M. Ave, *Reconstruction accuracy of the surface detector array of the Pierre Auger Observatory*, 30th International Cosmic Ray Conference, in Merida (Mexico), 2007. arXiv:0709.2125v1
- [90] Karl-Heinz Kamperta, *The Pierre Auger Observatory - Status and Prospects*, presentation at XIII ISVHECRI, Pylos (Greece), 2004. arXiv:astro-ph/0501074v1
- [91] P. Sommers, *Capabilities of a giant hybrid air shower detector*, *Astroparticle Physics* 3, p. 349-360, 1995.
- [92] M. Unger et al., *Reconstruction of longitudinal profiles of ultra-high energy cosmic ray showers from fluorescence and Cherenkov light measurements*, *Nuclear Instruments and Methods in Physics Research A* 588, p. 433-441, 2008.
- [93] F. Nerling et al., *Universality of electron distributions in high-energy air showers - Description of Cherenkov light production*, *Astroparticle Physics* 24, p. 421-437, 2006.
- [94] The Pierre Auger Collaboration, *First estimate of the primary cosmic ray energy spectrum above 3 EeV from the Pierre Auger Observatory*, 29th International Cosmic Ray Conference Pune, p. 101-106, 2005. arXiv:astro-ph/0507150v1
- [95] C. Di Giulio, *The cosmic ray energy spectrum and related measurements with the Pierre Auger Observatory*, 31st International Cosmic Ray Conference, in Lodz (Poland), 2009.
- [96] M. Mostafa, *The hybrid performance of the Pierre Auger Observatory*, 29th International Cosmic Ray Conference Pune, p. 101-106, 2005.
- [97] M. Roth, *Measurement of the UHECR energy spectrum using data from the Surface Detector of the Pierre Auger Observatory*, 30th International Cosmic Ray Conference, in Merida (Mexico), 2007.
- [98] B. R. Dawson, *Hybrid performance of the Pierre Auger Observatory*, 30th International Cosmic Ray Conference, in Merida (Mexico), 2007.
- [99] Pierre Auger Collaboration, *Measurement of the energy spectrum of cosmic rays above  $10^{18}$  eV using the Pierre Auger Observatory*, *Physics Letters B* 685, p. 239-246, 2010.
- [100] The Pierre Auger Collaboration, *Update on the correlation of the highest energy cosmic rays with nearby extragalactic matter*, *Astroparticle Physics* 34(5), p. 314-326, 2010. arXiv:1009.1855v2
- [101] The Pierre Auger Collaboration, *Correlation of the highest energy cosmic rays with nearby extragalactic objects*, *Science* 318, p. 938, 2007. arXiv:0711.2256v1
- [102] The Pierre Auger Collaboration, *Correlation of the highest-energy cosmic rays with the positions of nearby active galactic nuclei*, *Astroparticle Physics* 29, p. 188-204, 2008. arXiv:0712.2843v2
- [103] Yun-Ying Jiang et al., *Do ultra-high energy cosmic rays come from active galactic nuclei and fermi  $\gamma$ -ray sources?*, 2010. arXiv:1004.1877v4
- [104] E. M. Santos, *Anisotropy studies with the Pierre Auger Observatory*, 2009. arXiv:0902.0040v1
- [105] J. D. Hague, *Astrophysical sources of cosmic rays and related measurements with the Pierre Auger Observatory*, 31st International Cosmic Ray Conference, in Lodz (Poland), 2009.

- [106] The Pierre Auger Collaboration, *Measurement of the depth of maximum of extensive air showers above  $10^{18}eV$* , Physics Review Letters 104, 091101, 2010.
- [107] S. Andringa, *Results of the Pierre Auger Observatory on Astroparticle Physics*, conference proceedings of Rencontres de Moriond 2010 (Electroweak). arXiv:1005.3795v1
- [108] M. Risse, *Search for ultra-high energy photons using air showers*, Modern Physics Letters A 22, p. 749-766, 2007.
- [109] The Pierre Auger Collaboration, *Upper limit on the cosmic-ray photon fraction at EeV energies from the Pierre Auger Observatory*, Astroparticle Physics 31, p. 399-406, 2009.
- [110] P. Billoir, *Limit on the diffuse flux of ultra high energy neutrinos using the Pierre Auger Observatory*, Journal of Physics: Conference Series 203(1), 012125, 2010.
- [111] T. Pierog et al., *First results of fast one-dimensional hybrid simulation of EAS using CONEX*, Nuclear Physics B (Proceeding Supplement) 151, p. 159-162, 2006. arXiv:astro-ph/0411260v1
- [112] S. Andringa, R. Conceicao and M. Pimenta, *Increased sensitivity to electromagnetic and hadronic features of air showers from a new parameterization of the longitudinal profiles*, 31st International Cosmic Ray Conference, in Łódź (Poland), 2009.
- [113] S. Andringa, R. Conceicao and M. Pimenta, *Mass composition and cross-section from the shape of cosmic ray shower longitudinal profiles*, Astroparticle Physics, 2010. doi:10.1016/j.astropartphys.2010.10.002
- [114] J. Allen et al., *The Pierre Auger Observatory offline software*, 29th International Cosmic Ray Conference Pune, p. 101-106, 2005.
- [115] D. Heck and T. Pierog, *Extensive Air Shower Simulation with CORSIKA: A User's Guide*, Institut für Kernphysik, Forschungszentrum Karlsruhe, 2010.
- [116] J. Espadanal, *How strange are standard events?*, presentation at Auger Collaboration Meeting March 2010, in Malargue (Argentina), 2010.
- [117] C. Baus, R. Engel, T. Pierog and M. Unger, *Proposal for a shoot-the-shower trigger for double bump showers*, presentation at Lecce analysis meeting, in Lecce (Italy), 2010.
- [118] The LHCf Collaboration et al., *The LHCf detector at the CERN Large Hadron Collider*, Journal of Instrumentation 3, S08006, 2008.
- [119] J. Alvarez-Muniz, P. Brogueira, R. Conceicao, J. Dias de Deus, M. C. Espirito Santo, M. Pimenta, *Percolation and high energy cosmic rays above  $10^{17}eV$* , Astroparticle Physics 27, p. 271-277, 2007. arXiv:hep-ph/0608050v1

# Appendix A

## Showers parametrizations

In this appendix, we present the mean shower characteristics for primary energy from  $10^{16}eV$  to  $10^{19}eV$ . We use the hadronic model QGSJET-II3, since it was used for the simulations in chapter 6 and 7. If you want to see some differences between models, you can look at chapter 4. To reduce computation time, here we use samples of 1000 events for each energy considered (we have 5 samples with  $10^{16}eV$ ,  $10^{17}eV$ ,  $10^{17.5}eV$ ,  $10^{18}eV$  and  $10^{19}eV$ ). In table A.1, the results are displayed. The parameters are obtain by fitting the simulated events to the Gaisser-Hillas equation with the shape of equation 6.1 and with 4 parameters ( $N_{max}$ ,  $X_{max}$ ,  $L$  and  $R$ ). Here we use all points of the profile to fit to one GH, and unlike in the final of section 6.2 or even in chapter 7, where we cut the initial and final tail of the profiles. We use this parametrizations to improve the 2 GH fit, so even if we cut the initial and final tail of the total profile, we will not cut the final tail of the first GH and the initial tail of the second GH (that are summed, see fig. B.5), so it's more correct to use the parametrization with all points of the profiles.

### A.0.0.1 Shower $N_{max}$

In the figure A.1 a), we can see the that the  $N_{max}$  has a very narrow distribution with  $\sigma$  varying from  $\sim 2.7\%$  to  $\sim 7.5\%$  at  $10^{19}eV$  and  $10^{16}eV$  (see tableA.1 for detailed values). If we plot  $Log_{10}N_{max}$  in function of  $Log_{10}Energy$ , we see that they vary almost linearly. So we could parametrize  $N_{max}$  in fig. A.1 b), by:

$$Log_{10}N_{max} = \begin{pmatrix} 0.9970 \\ \pm 0.0089 \end{pmatrix} \times Log_{10}Energy + \begin{pmatrix} -11.74 \\ \pm 0.16 \end{pmatrix} \quad (A.1)$$

Since we will parametrize the other parameters as function of energy, and in chapter 7 we will need  $L$  parameter in function of  $N_{max}$ , so we invert this equation and obtain:

$$Log_{10}Energy = \begin{pmatrix} 1.0030 \\ \pm 0.0090 \end{pmatrix} \times Log_{10}N_{max} + \begin{pmatrix} 11.77 \\ \pm 0.27 \end{pmatrix} \quad (A.2)$$

### A.0.0.2 Shower $X_{max}$

The  $X_{max}$  distribution have more fluctuations than  $N_{max}$ , but we can still see an evolution with energy. This is not so important since we are interested in the  $X_{max}$  value event by event. We can parametrize it by:

$$X = \begin{pmatrix} 49.82 \\ \pm 27.04 \end{pmatrix} \times Log_{10}Energy + \begin{pmatrix} -162.7 \\ \pm 485.2 \end{pmatrix} \quad (A.3)$$

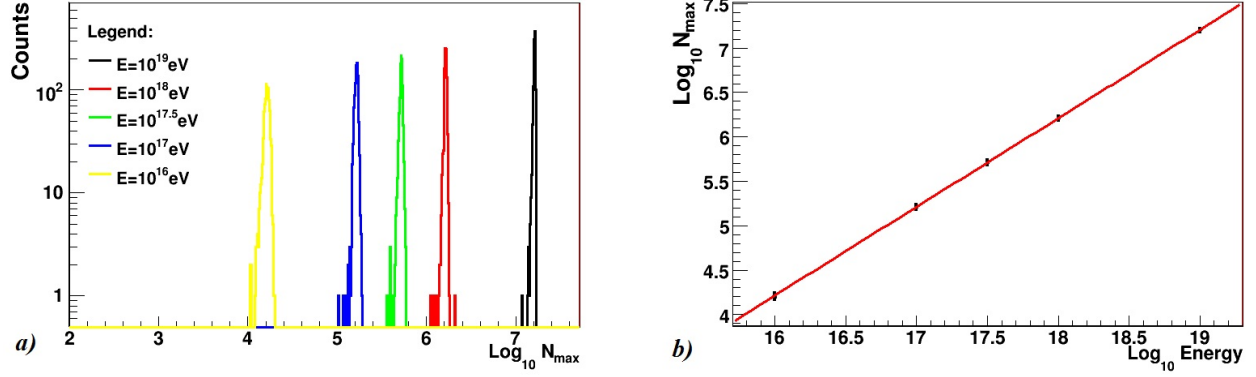


Figure A.1: a)  $N_{max}$  distribution for several energies, b)  $N_{max}$  as a function of Energy, in red we have the linear fit with  $\chi^2 = 0.0003$ .

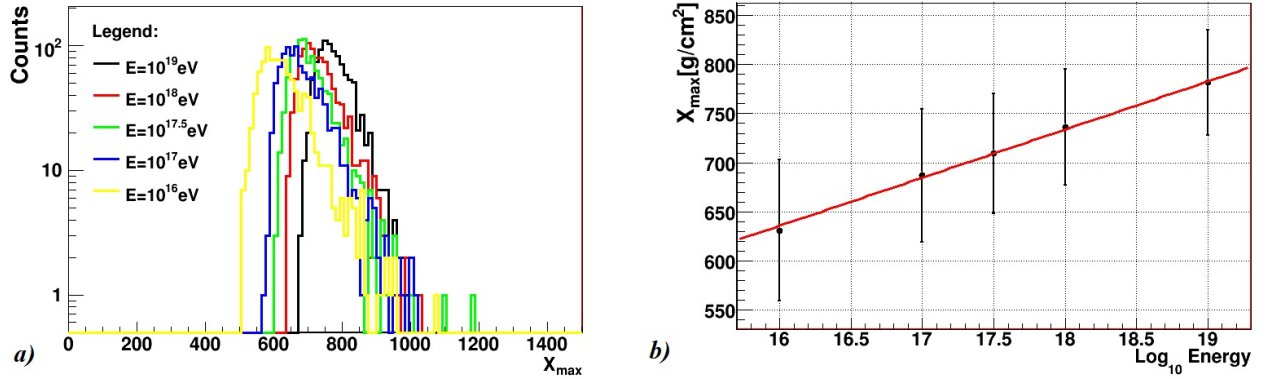


Figure A.2: a)  $X_{max}$  distribution for several energies, b)  $X_{max}$  as a function of Energy, in red we have the linear fit with  $\chi^2 = 0.008$

### A.0.0.3 Shower $L$ parameter

The  $L$  parameter have fluctuations with sigma approximately between 3% and 7%. It can be parametrized by (see fig. A.3):

$$L = \begin{pmatrix} 5.72 \\ \pm 4.17 \end{pmatrix} \times \text{Log}_{10} \text{Energy} + \begin{pmatrix} 123.5 \\ \pm 80.1 \end{pmatrix} \quad (\text{A.4})$$

### A.0.0.4 Shower $R$ parameter

The  $R$  parameter has more fluctuations than  $L$ , which are between  $\sim 7\%$  and  $\sim 14\%$ . It can be parametrized by (see fig. A.4):

$$R = \begin{pmatrix} -0.019 \\ \pm 0.013 \end{pmatrix} \times \text{Log}_{10} \text{Energy} + \begin{pmatrix} 0.619 \\ \pm 0.227 \end{pmatrix} \quad (\text{A.5})$$

### A.0.0.5 Synthesis and conclusion

The mean values for the shower parameters are displayed in table A.1. The previous parametrizations are used in the appendix B.

The two Gaisser-Hillas function method has 8 parameter, and obviously we can not parametrize the  $N_{max}$  and  $X_{max}$ , since they are the values we want to extract (see appendix B). The  $L$  parameter has less fluctuation

with respect to  $R$  so we can parametrize  $L$  parameter by equation A.4. In this way, the two GH method has now 6 parameter, and it is easier to fit events.

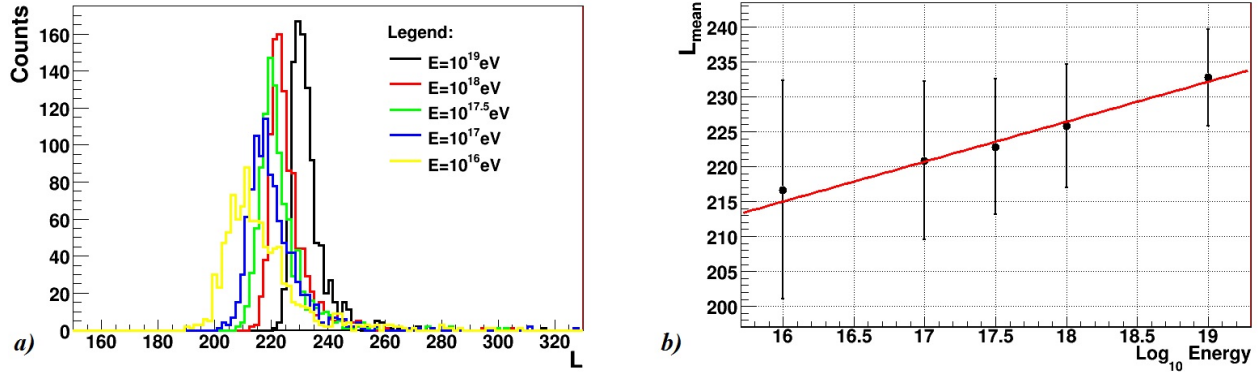


Figure A.3: a)  $L$  distribution for several energies, b)  $L$  as a function of Energy, in red we have the linear fit with  $\chi^2 = 0.03$ .

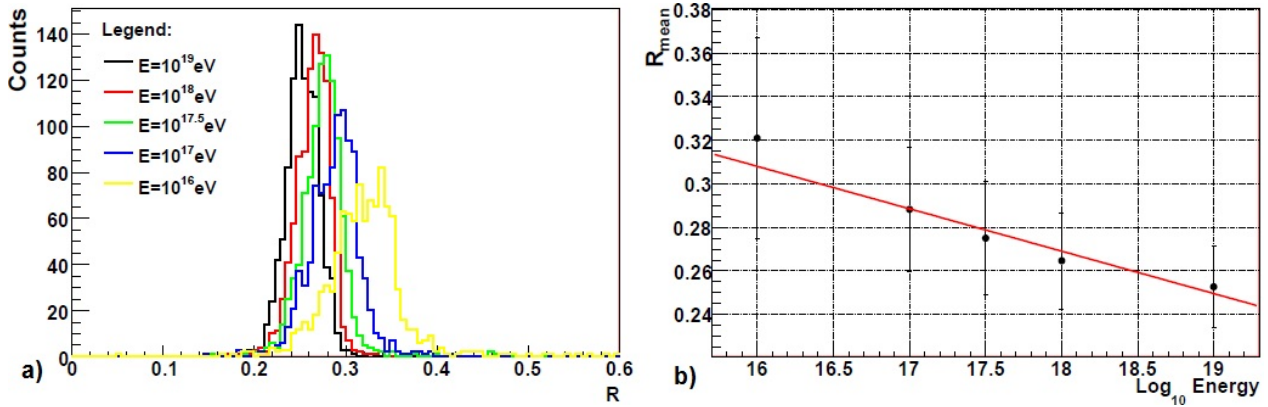


Figure A.4: a)  $R$  distribution for several energies, b)  $R$  as a function of Energy, in red we have the linear fit with  $\chi^2 = 0.17$ .

	$\text{Log}_{10}E$	Mean Value	$\sigma$	$\sigma/\text{Mean}$ (%)		$\text{Log}_{10}E$	Mean Value	$\sigma$	$\sigma/\text{Mean}$ (%)
$N_{max}$ (GeV/ g/cm <sup>2</sup> )	16	16227.3	1218.9	7.51	$X_{max}$ (g/cm <sup>2</sup> )	16	630.5	72.2	11.44
	17	163503	8188	5.01		17	687.2	67.7	9.86
	17.5	518018	22184	4.28		17.5	709.4	61.1	8.62
	18	$1.62944 \times 10^6$	59508	3.65		18	736.1	58.8	7.99
	19	$1.60629 \times 10^7$	437761	2.73		19	781.6	53.6	6.86
L (g/cm <sup>2</sup> )	16	216.6	15.7	2.97	R	16	0.321	0.046	7.42
	17	220.8	11.3	3.92		17	0.288	0.029	8.34
	17.5	222.8	9.7	4.36		17.5	0.275	0.026	9.46
	18	225.8	8.9	5.13		18	0.265	0.022	9.94
	19	232.8	6.9	7.24		19	0.253	0.019	14.43

Table A.1: Mean values for Shower Parameters

### A.0.0.6 $\chi^2$ evolution

Beyond the previous evolutions with energy, we still can see another interesting feature, the  $\chi^2$  depends on energy too. In figure A.5 we see that  $\chi^2 \propto E^\gamma$ , in fact if we observe the points a little better, we see that the exponent  $\gamma$  is higher at  $E = 10^{19}eV$  and smaller at  $E = 10^{14}eV$ . Here we use the same samples of previous section, but we add two new samples with 1000 events with energy  $10^{14}eV$  and  $10^{15}eV$ . We don't use them for the other parametrizations, because they are out of the utility region of chapter 7. The linear fit gives the result:

$$\text{Log}_{10}\chi^2 = \begin{pmatrix} 0.700 \\ \pm 0.158 \end{pmatrix} \times \text{Log}_{10}\text{Energy} + \begin{pmatrix} -10.5 \\ \pm 2.74 \end{pmatrix} \quad (\text{A.6})$$

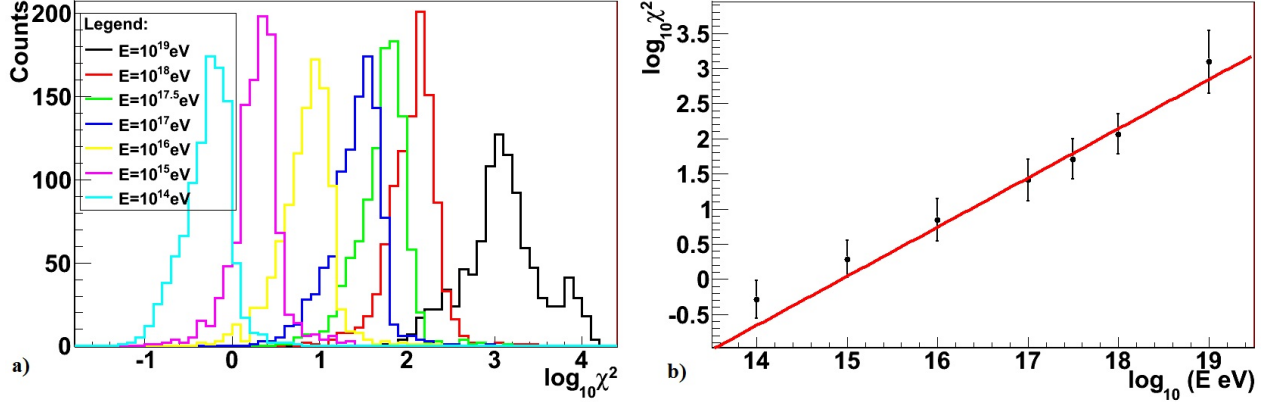


Figure A.5: a)  $\log(\chi^2)$  distribution for several energies, b)  $\langle \log(\chi^2) \rangle$  as a function of Energy, in red we have the linear fit with  $\chi^2 = 0.6$ .

All events in this appendix were fitted using all point of the distributions. Here we repeat the fits but with the initial and final point of the profile cut like in chapter 7 and 6. Since now, we are only interested in the  $\chi^2$ , we only plot this result in fig. A.6. The result of the linear fit is:

$$\text{Log}_{10}\chi^2 = \begin{pmatrix} 0.748 \\ \pm 0.237 \end{pmatrix} \times \text{Log}_{10}\text{Energy} + \begin{pmatrix} -11.9 \\ \pm 24.8 \end{pmatrix} \quad (\text{A.7})$$

The main reason for this dependence can be seen in section 6.2.1.

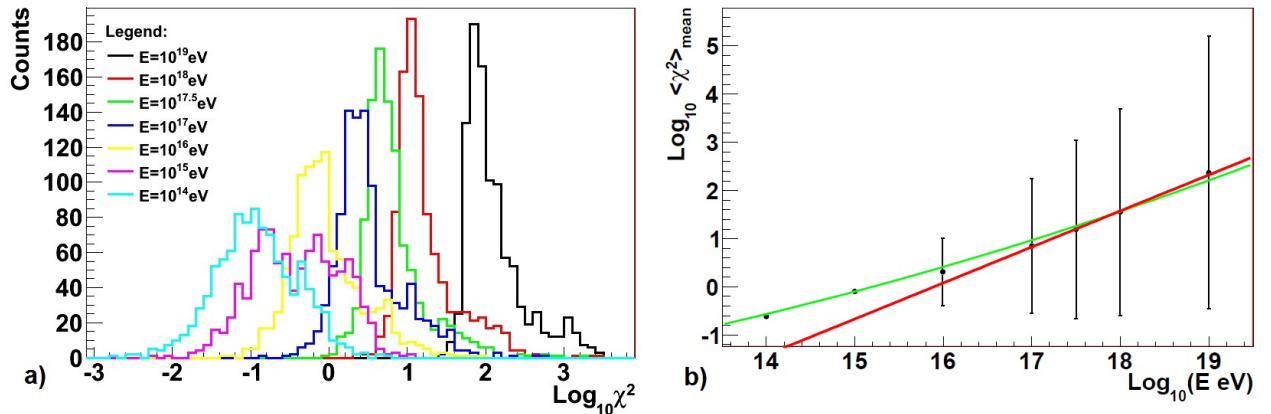


Figure A.6: a)  $\log(\chi^2)$  distribution for several energies, cutting the initial and final points of the profile, b)  $\log(\langle \chi^2 \rangle)$  as a function of Energy, in red we have the linear fit with  $\chi^2 = 0.0024$ , for this fit we only consider the 4 points with higher energy. In green is a fit to a polynomial with degree 2.

## Appendix B

# Two Gaisser-Hillas function fit test

In the section 7.1, we say that a air shower can be view as a sum of two Gaisser-Hillas, one corresponding to the leading particle development, and the other corresponding to the set of the remaining particles development. Considering that this approximation is valid, we should test if given a sum of two GH, we can extract it's original parameters. In this chapter, we sum two GH and fit equation 7.2. We use exactly the same approach as in section 7.1.1, fixing the  $L$  parameter with equations A.2 and A.4.

### B.0.0.7 Parameters fixed

Initially, we fit the profiles obtained from a GH, which are the sum of two GH. We calculate several GH sums, with  $K$  varying in steps of 0.1, from 0.1 to 0.9 and for each  $K$  we have  $\Delta X$  varying from 0 to  $600g/cm^2$  (in steps of  $50g/cm^2$ ). We have then, 117 different profiles ( $9 \times 12$ ).  $K$  is the inelasticity defined by  $K = 1 - \frac{E_{leading}}{E_{primary}} \equiv 1 - \frac{N_{max2}}{N_{max1} + N_{max2}}$  and  $\Delta X = X_{max2} - X_{max1}$ . To reproduce the simulations events we parametrize the parameters with the functions in appendix A.  $N_{max1,2}$  follow  $K$  (with  $N_{max2} = (1 - K)N_{max}$  and  $N_{max1} = K \cdot N_{max}$ ) and  $X_{max1,2}$  follow  $X_{max}$  subtract and summing 25 in each step respectively. Since we parametrize  $L$  in the reconstruction too, the results will be obviously almost perfect. In figure B.1, we have the  $\Delta X$  and  $K$  reconstructed in other to the original.

We can see that the reconstruction is very good, but even in this situation for very small  $\Delta X$  we have problems to recover the  $K$ . This is due to, if we sum two GH with  $\Delta X = 0$  with the same parameters, the  $K$  can vary in all it's range and we still have the same thing. The effect reduces by increasing  $\Delta X$ . Nevertheless, this is not very interesting since in simulation, the parameters have some distribution and will not appear with theirs mean value.

### B.0.0.8 Parameters with fluctuations

Since the  $L$  and  $R$  parameters have fluctuations in real/simulated events, than the previous section does not make much sense and we should introduce some fluctuation in  $L$  and  $R$  in the sum of the two GH. Thus we introduce some Gaussian random fluctuation in these parameters. We use the TRandom3 to obtain a Gaussian random fluctuation with  $\sigma$  given in table A.1. Here we use the  $\sigma$  values for  $10^{19}eV$ .

We have fitted 1170 events, with  $\Delta X$  varying in steps of  $25g/cm^2$  from 0 to  $600g/cm^2$ , and  $K$  varying in steps of 0.1 from 0.1 to 0.9, we repeat each configuration 10 times with different fluctuations ( $9 \times 12 \times 10$ ). In figure, B.2, we have the results for  $\Delta X$  and  $K$  reconstructed.

The new results are a little shuffled, but if we look only at blue points they have much better results. In  $\Delta X$ , the result became better for  $\Delta X > 200g/cm^2$ , since with low  $\Delta X$  we can't distinguish the two showers. For one hand, in the region with small  $\Delta X$ ,  $K$  value can have a big range giving almost the same result. On other hand, since we fixed  $L$  parameter, and now  $L$  parameter has fluctuations, this fluctuations will go not only for  $R$  but also to  $X_{max}$ . For example, if we have a big  $L$ , than the profile will have a big width and since  $L$  was fixed, than we obtain a  $\Delta X$  reconstructed bigger than what is expected. This effect reduces

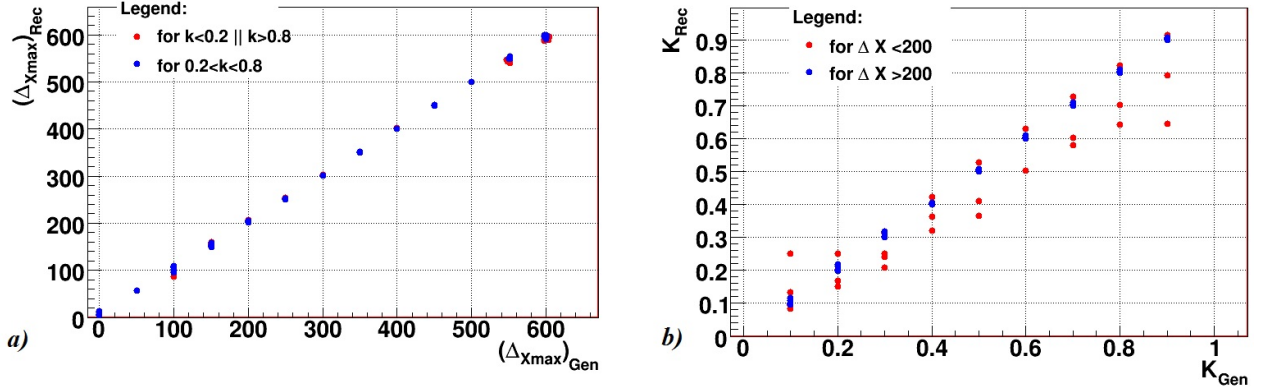


Figure B.1: a)  $\Delta X_{Rec}$  (reconstructed) as a function of  $\Delta X_{Gen}$  (input value), b)  $K_{Rec}$  as a function of  $K_{Gen}$ . These events are made using GH with parameters equals the typical mean values without fluctuations.

in higher  $\Delta X$ . The blue points in  $\Delta X$  picture, corresponds to middle  $K$  (from 0.2 to 0.8) where we have a good reconstruction. If  $K$  is high ( $> 0.8$ ) or small ( $< 0.2$ ), one of the showers will be very small compared to the other, and it will be a small correction to the overall shape. If  $K$  is really close to 1 or 0, than we have almost one shower and the  $L$  fluctuation features become more important. Hence we haven't sensitivity in this region (red points in  $\Delta X$  picture).

In  $K$  figure, we have the same behaviour, but now blue point corresponds to  $\Delta X > 200g/cm^2$  and red points to  $\Delta X < 200g/cm^2$ .

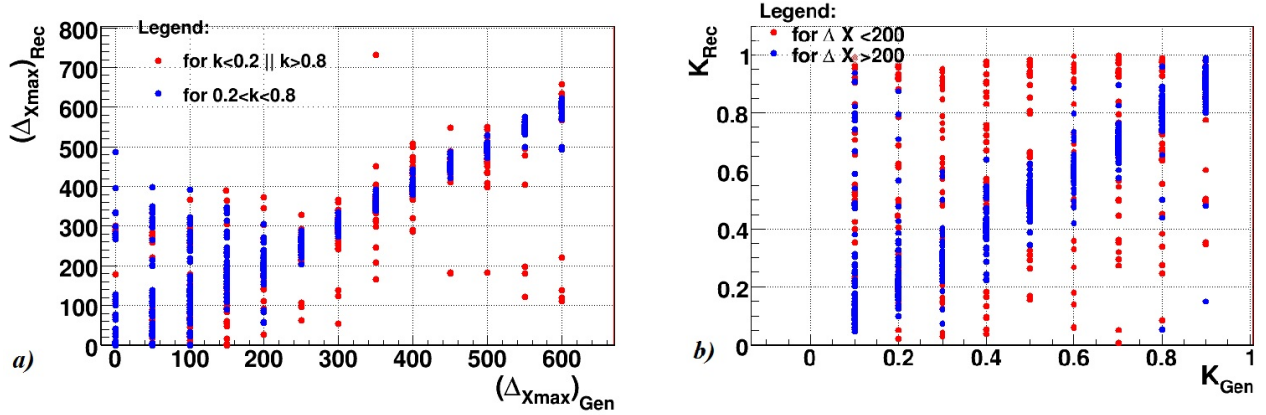


Figure B.2: a)  $\Delta X_{Rec}$  as a function of  $\Delta X_{Gen}$ , b)  $K_{Rec}$  as a function of  $K_{Gen}$ . These events are made using GH with parameters equals the typical mean values with gaussian fluctuations.

In order to see if we have a good reconstruction we can plot the distributions of  $\Delta X_{Rec}/\Delta X_{Gen}$  and  $K_{Rec}/K_{Gen}$  for different selections. In figure B.3, we present these distribution, the best selection is with the previous comments, with  $0.2 < K_{Gen} < 0.8$  and  $\Delta X_{Gen} > 200g/cm^2$ . In this region we have a very narrow distribution around 1. However, these cut is in the input values, which we have not access in the real data, so it's is not a good selection. We could make a translation to selection  $0.2 < K_{Rec} < 0.8$  and  $\Delta X_{Rec} > 200g/cm^2$ . With this new selection we still have a good reconstruction, but in Monte Carlo simulated events we should have more contamination, since we have muons contributions and possibly a second important leading that could change the shape.

Another interesting feature it so see the behaviour of the  $\chi^2$  with the first selection rule. In the figure B.4 we see that the fit with one GH is better in the region that doesn't interest us ( $0.2 > K_{Gen} \wedge K_{Gen} < 0.8$  and  $\Delta X_{Gen} < 200g/cm^2$ ) and it has very bad fits in our region. This means that in our region we don't have the

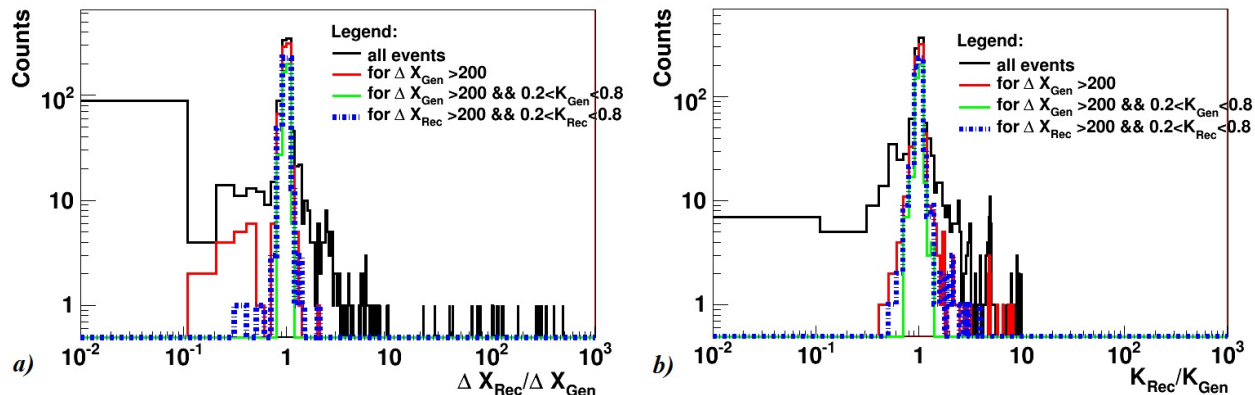


Figure B.3: a)  $\Delta X_{Rec}/\Delta X_{Gen}$  distribution, b)  $K_{Rec}/K_{Gen}$  distribution.

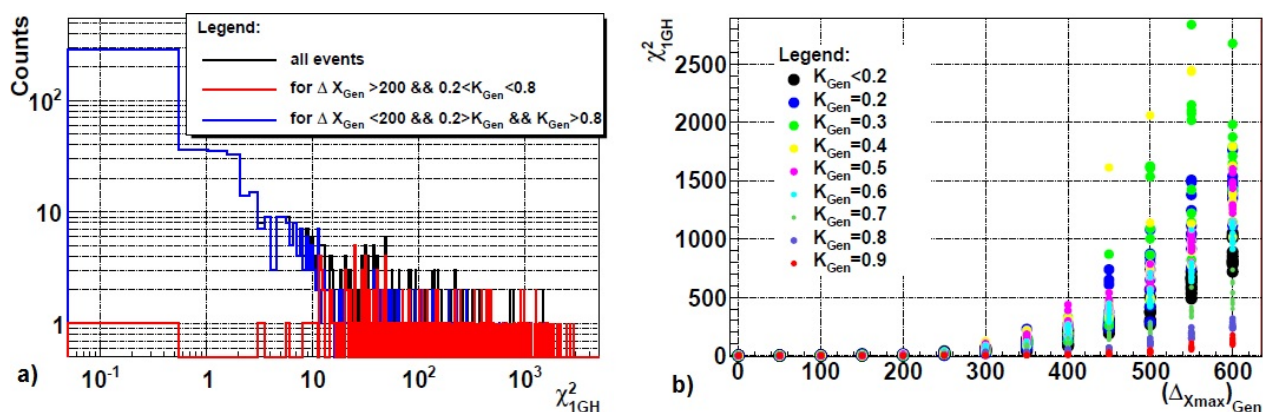


Figure B.4: a)  $\chi^2$  distribution for one GH, we divided the event into a group with  $0.2 < K_{Rec} < 0.8$  and  $\Delta X_{Rec} > 200 g/cm^2$  in red and the rest in blue. the red event have very bad  $\chi^2$  so they don't behave like 1GH. b) We plot the  $\chi^2$  in function of  $\Delta X_{Rec}$  and divided into groups of  $K$ .

one GH behaviour but a two GH is more plausible. At b) in the above figure, we have the  $\chi^2_{1GH}$  evolution with  $\Delta X_{Gen}$ , as we see, the  $\chi^2_{1GH}$  has an exponential growth with  $\Delta X$ , like it was expected. Nevertheless, We expect that the biggest  $\chi^2_{1GH}$  should correspond to the  $K = 0.5$  sample, and the evolution above and below this value should be symmetric. However, we observe an asymmetric evolution with  $K$  and the biggest value of  $\chi^2_{1GH}$  is for  $K = 0.4$ . In fact, this is caused by the asymmetry in the GH function. The raising side of an GH has a bigger slope (in modulo) than the decreasing side. So if we make a change in the raising side (lower  $K$ ), then the GH will have more difficulty to fit a lower slope. If we add some new GH on the right side of the original GH (higher  $K$ ), since here the slope is lower, the change will have a smaller impact on the total shape. With a little lower slope, the GH can fit this perturbation. So our selections with the cut in  $K$ , should be improved in the future to an asymmetric interval, less constrained in the low  $K$ , than in higher  $K$ .

In the figure B.5 and B.6, we have plotted four events from our sample. The event a) in B.6 for example, since it has a  $\Delta X_{Gen}$  small, than the reconstruction can't recover the right values, while event a) in B.5 is almost perfect. Another feature is that the result for events with  $K_{Gen} > 0.8$  are better reconstructed than with  $K_{Gen} < 0.2$ .

The figure B.4 b),

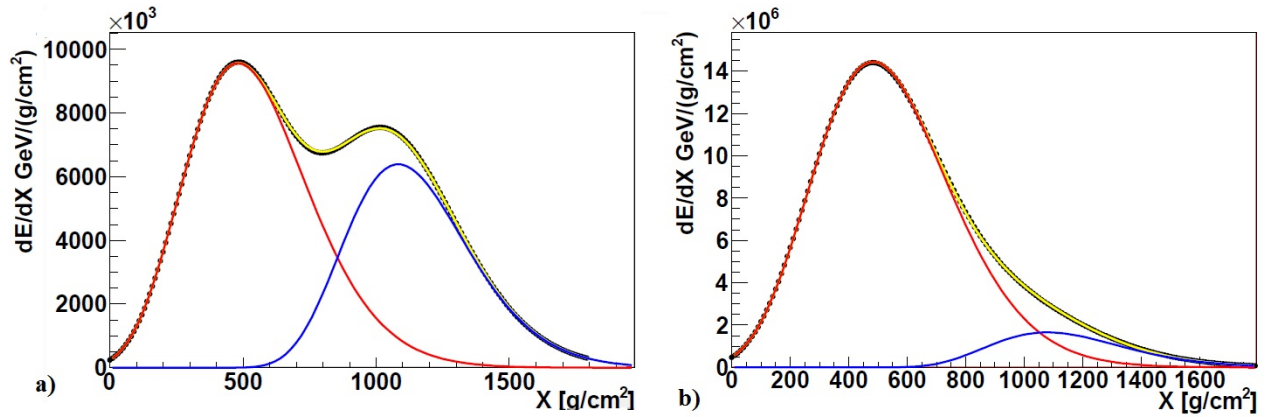


Figure B.5: Two examples of a two GH fit from the previous sample.

a)  $\chi_{1GH}^2 = 984.4$  vs  $\chi_{2GH}^2 = 0.18$ ,  $\Delta X_{Rec} = 601.4g/cm^2$  vs  $\Delta X_{Gen} = 600g/cm^2$ ,  $K_{Rec} = 0.6$  vs  $K_{Gen} = 0.60$ ,  $R_{Rec} = 0.273$  and  $0.286$  vs  $R = 0.272$  and  $0.300$  and  $L_{Rec} = 230.6$  and  $229.3g/cm^2$  vs  $L = 231.2$  and  $227.1g/cm^2$ .

b)  $\chi_{1GH}^2 = 112.7$  vs  $\chi_{2GH}^2 = 0.26$ ,  $\Delta X_{Rec} = 595.3g/cm^2$  vs  $\Delta X_{Gen} = 600g/cm^2$ ,  $K_{Rec} = 0.9$  vs  $K_{Gen} = 0.90$ ,  $R_{Rec} = 0.245$  and  $0.320$  vs  $R = 0.232$  and  $0.231$  and  $L_{Rec} = 231.9$  and  $225.0g/cm^2$  vs  $L = 232.8$  and  $230.8g/cm^2$ .

In b), since the second  $L$  are a little far from the  $L$  parametrization, the  $R$  values are different from the input, because they carry  $L$  fluctuation.

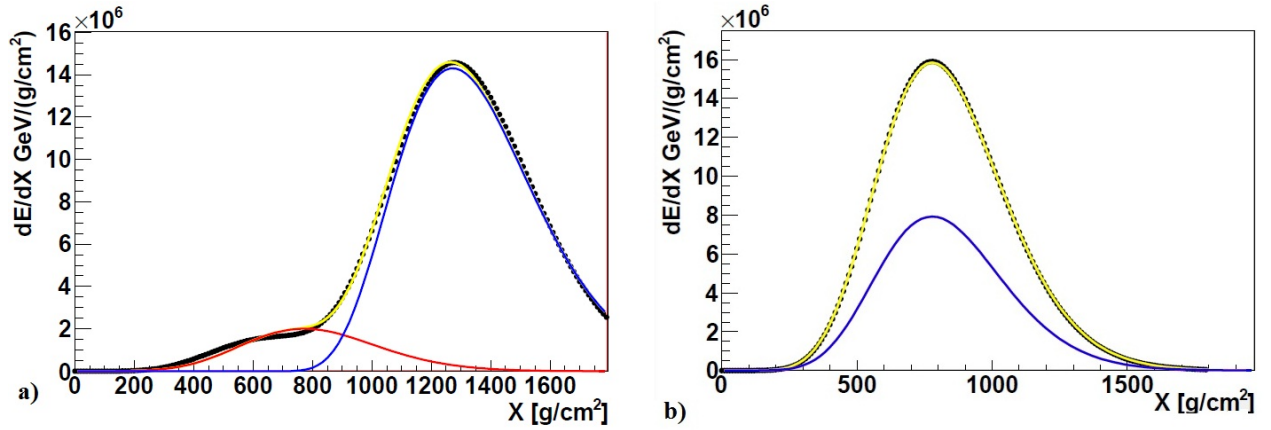


Figure B.6: Two examples of a two GH fit from the previous sample.

a)  $\chi_{1GH}^2 = 1172$  vs  $\chi_{2GH}^2 = 52.1$ ,  $\Delta X_{Rec} = 505.2g/cm^2$  vs  $\Delta X_{Gen} = 600g/cm^2$ ,  $K_{Rec} = 0.6$  vs  $K_{Gen} = 0.60$ ,  $R_{Rec} = 0.273$  and  $0.286$  vs  $R = 0.272$  and  $0.300$  and  $L_{Rec} = 230.6$  and  $229.3g/cm^2$  vs  $L = 231.2$  and  $227.1g/cm^2$ .

b)  $\chi_{1GH}^2 = 0.0037$  vs  $\chi_{2GH}^2 = 1.37$ ,  $\Delta X_{Rec} \sim 0g/cm^2$  vs  $\Delta X_{Gen} = 50g/cm^2$ ,  $K_{Rec} = 0.5$  vs  $K_{Gen} = 0.6$ ,  $R_{Rec} = 0.250$  and  $0.250$  vs  $R = 0.255$  and  $0.245$  and  $L_{Rec} = 230.0$  and  $230.0g/cm^2$  vs  $L = 226.5$  and  $229.8g/cm^2$ .

## Appendix C

### Selection 3 analysis

In this appendix, we describe a characterization of the parameters of the sub-sample of selection 3 of the table 7.2. We will plot the parameters  $\Delta X_{Rec}$ ,  $K_{Rec}$ ,  $\chi^2_{1GH}$ ,  $\chi^2_{2GH}$  and  $X_{max}$ ,  $L$  and  $R$  parameter for both GH in the 2GH fit, for the  $10^{18}eV$  sample. As we see in each plot, there no reason for consider some sample rather than other, since the looks very similar. We should note that  $\lambda$  could change in each selection (fig. C.1a), nevertheless, the selection E, which is supposed to be the worst sample, have the distribution with lower  $\chi^2_{2GH}$ . This means that it shouldn't be neglected.

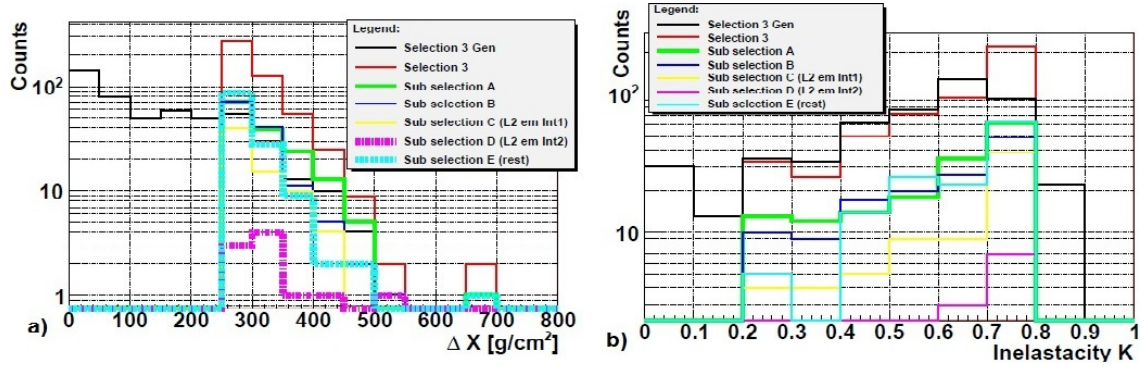


Figure C.1: a) the  $\Delta X_{Rec}$  distribution and b) the inelasticity  $K$  distribution for several sub selections.

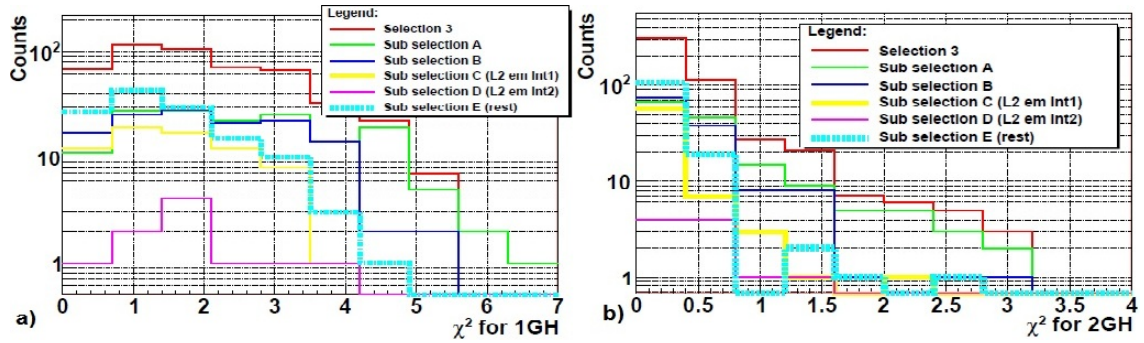


Figure C.2: a) the  $\chi^2_{1GH}$  distribution and b) the  $\chi^2_{2GH}$  distribution for several sub selections.

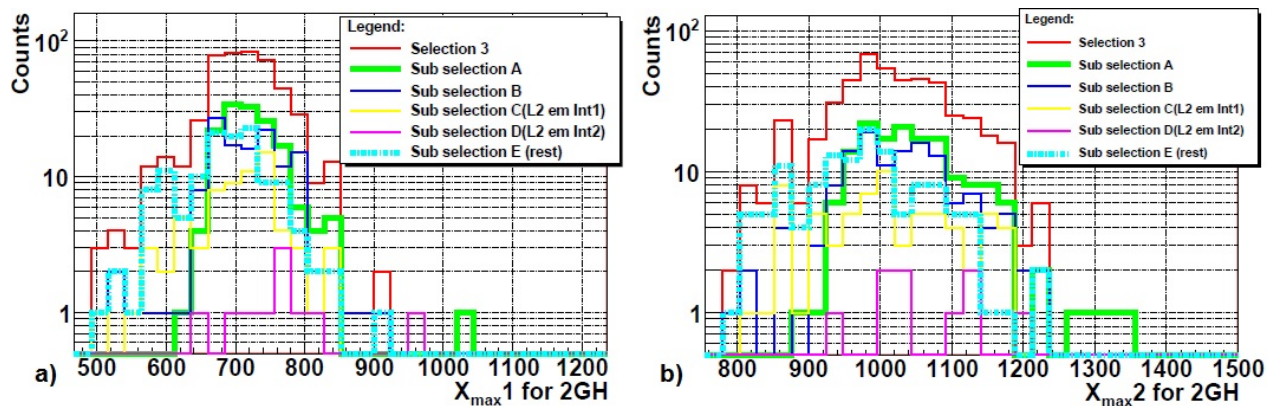


Figure C.3: a) the  $X_{max,1}$  distribution for two GH and b) the  $X_{max,2}$  distribution for two GH for several sub selections.

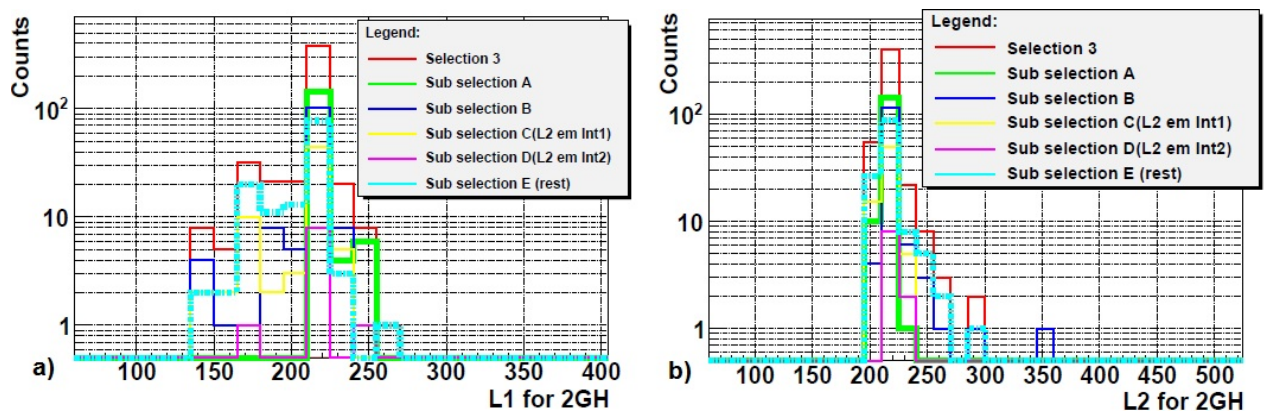


Figure C.4: a) the  $L_1$  distribution for two GH and b) the  $L_2$  distribution for two GH for several sub selections.

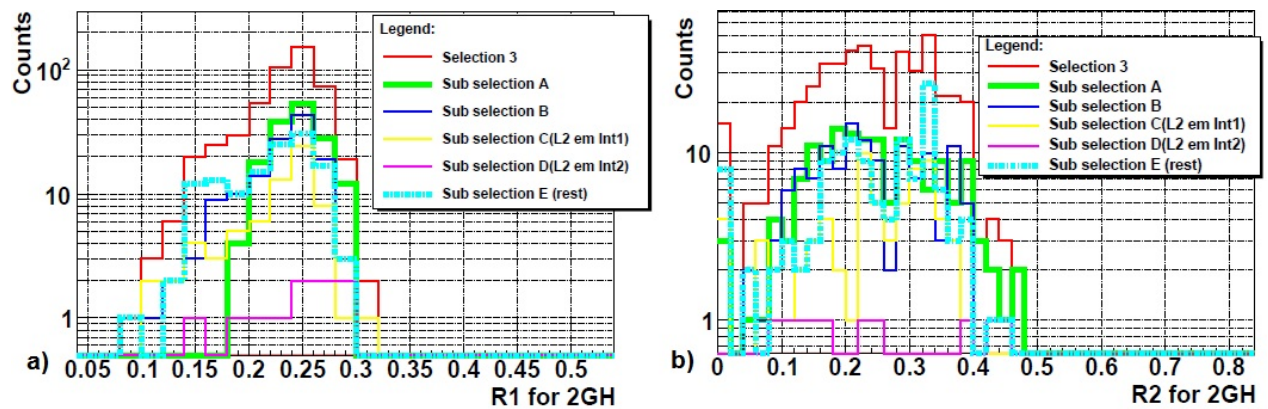


Figure C.5: a) the  $R_1$  distribution for two GH and b) the  $R_2$  distribution for two GH for several sub selections.